Remote sensing of trace gases in the urban and marine boundary layers

Thesis submitted for the degree of
Doctor of Philosophy
at the University of Leicester

by

Louisa Kramer
Earth Observation Science Group
Department of Physics and Astronomy
University of Leicester

February 2008

ProQuest LLC
789 East Eisenhower Parkway
P.O. Box 1346
Ann Arbor, MI 48106-1346

Declaration

I hereby declare that no part of this thesis has been submitted to this or any other University as part of the requirements for a higher degree. The work described here was conducted by the undersigned except for the contributions of colleagues indicated in the text.

Louisa Kramer
February 2008

Acknowledgements

I would first like to thank my supervisors Paul Monks and John Remedios for all their guidance and support throughout my PhD and who have given me the chance to travel to some great places. Secondly, to Roland Leigh who I am indebted to for teaching me the ways of MAXDOAS and who has been with me through the frustration of trying to get the instrument to work and after 3 years finally managed to get me to learn visual basic! I would also like to thank Udo and Gary for their knowledge and input into my research.

I would like to acknowledge the rest of the EOS group members, old and new, who have been great through the last five years during my MPhil and PhD. To Anna, who always seemed to know when I needed a coffee break and to Ann-Marie, who has been a great friend throughout my university life.

A special mention must go to all my friends at Carisbrooke Tennis club, with whom I have had great fun and I will miss immensely. To Jimbo, Alex and Johnno, you guys have been great and kept me entertained on a Saturday night over a few drinks, Johnno, I let you know when your volcano theory comes true.

I would like to thank my parents and brother who have always supported me in my decisions and encouraged me to pursue my goals. Finally, I would like to give a special thanks to Pete and to whom I dedicate this thesis. His continuous support and patience over the last 9 years has kept me going and I am grateful for all his optimism and help.

Remote sensing of trace gases in the urban and marine boundary layers

Louisa Kramer

Abstract

The thesis investigates the application of Concurrent Multi-Axis Differential Optical Absorption Spectroscopy (CMAX-DOAS) for the retrieval of trace gases and aerosols with a particular focus on their spatial and temporal distributions within the urban and marine boundary layers. The CMAX-DOAS technique is a scattered light DOAS instrument with several concurrent viewing directions that is capable of measuring trace gas species and aerosol with fast temporal resolution but also large spatial scale information unlike current *in situ* techniques.

In the urban boundary layer, the capability of the CMAX-DOAS for the retrieval of aerosol optical depth (AOD) measurements has been quantified. Modelled O_4 slant columns calculated using AODs retrieved by a lidar instrument deployed alongside the CMAX-DOAS, showed very good agreement (r=0.98) for cloud free measurements. However, retrieval for AOD from the current CMAX-DOAS was more limited.

CMAX-DOAS NO_2 measurements in the urban boundary layer (UBL) have been used to provide a link between tropospheric NO_2 columns measured by the satellite-based Ozone Monitoring Instrument (OMI) and measurements obtained near-surface. A FOV weighted algorithm has been developed and the agreement is very good between the satellite columns and near-surface NO_2 for spring (r = 0.83) and summer (r = 0.64) months.

Finally, the thesis presents the first measurements of iodine monoxide (IO) in the mid-latitude marine boundary layer (MBL) by a MAX-DOAS instrument, the retrieval of bromine monoxide (BrO) has also been performed. The range of viewing geometries of the CMAX-DOAS instrument provides additional information about the spatial distribution of halogen oxides in a coastal MBL, which has previously not been documented.

Journal publications resulting from this work

Kramer, L. J., R. Leigh, J. Remedios, and P. S. Monks, "Comparison of OMI and ground based *in situ* and MAX-DOAS measurements of tropospheric nitrogen dioxide in an urban area". *Journal Geophysical Research.* doi:10.1029/2007JD009168, in press (accepted 11 February 2008).

Contents

List of Figures

List of Tables

Chapter 1

Introduction

Surrounding the Earth's surface is a thin layer of gas known as the atmosphere. The atmosphere is essential for life as it provides oxygen and water, protects against harmful radiation from the Sun and modulates the thermal energy from the Earths surface. The atmosphere is mainly composed of molecular nitrogen (78.1 %) and oxygen (20.9%), the remaining 1% consists of argon, carbon dioxide and trace gases. Recent human activity has begun to change the composition of the atmosphere, in particular the concentrations of trace gases, resulting in an increase in potentially harmful gases and particulates (atmospheric pollutants) and potential climate change.

Atmospheric pollution is an urgent and fundamental issue in environmental research. The effect of atmospheric pollution on the environment is particularly important in urban areas, as this is where approximately 50% of the world's population resides. Atmospheric pollution has many natural sources, such as particulates and sulphur dioxide from volcanic eruptions and volatile organic compounds (VOCs) from biogenic activity which contribute to tropospheric ozone and photochemical smog. However, the largest sources of atmospheric pollutants are the products of combustion from power generation or motor vehicle traffic, such as NO_x ($NO + NO_2$), CO and particulates. The increase in industrialisation and traffic over the past century has given rise to a significant increase in atmospheric pollution and the effect on human health has become evident [Sandström, 1995, Brunekreef *et al.*, 2002]. Measuring and monitoring the chemistry and dynamics in the urban and marine environment, therefore, is important to understand the changes that have occurred owing to anthropogenic influence and to determine the long-term stability of the climate.

The arrival of satellite based-instruments over the past few decades has enabled global monitoring of the Earths surface and atmosphere. However, remote sensing still requires ground-based monitoring and *in situ* measurements for validation of

the satellite measurements and determining the local and regional effects of atmospheric pollution.

This chapter highlights the important dynamical processes and chemistry that occurs within the urban and marine atmospheres. In the urban atmosphere the reactions leading to the production of tropospheric ozone and photochemical smog are well known. However, the majority of measurements are performed *in situ* and accurate measurements on a regional scale are still in their preliminary stages. In contrast to the urban boundary layer, chemistry in the marine atmosphere, in particular the role of halogens on the oxidative chemistry of the troposphere is still not fully understood and requires further investigation.

1.1 The Earth's atmosphere

The Earth's atmosphere can be classified according to temperature into four distinct layers, known as the troposphere, stratosphere, mesosphere and thermosphere. Each layer is bounded by "pauses", where the maximum changes in the sign of temperature occur (see Figure 1-1).

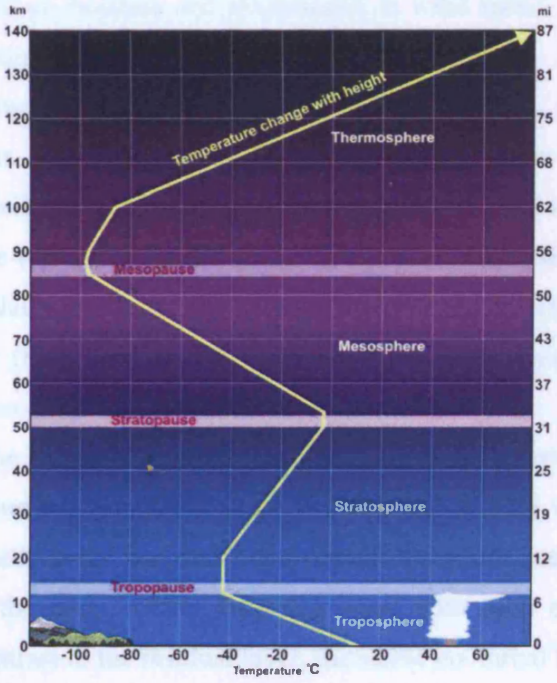

Figure 1-1: Layers of the Earths atmosphere [source: NOAA].

Approximately 99.9% of the atmosphere, by mass, is located below 100 km. The lowest level of the atmosphere, the troposphere, varies in altitude between 10 km at the poles and 18 km at the equator and contains approximately 75% of the total mass of the atmosphere. The lowest kilometre or two of the troposphere, the boundary layer, is directly influenced by the Earth's surface and natural and anthropogenic (human influenced) emissions [Stull, 1988]. It is this region of the atmosphere which is the focus of this thesis.

1.1.1 Planetary Boundary Layer

The planetary boundary layer (PBL) arises from thermal plumes owing to surface heating. In particular over land, the diurnal cycle of surface heating and cooling primarily determines the structure of the PBL. As the thermal plumes rise, they transport moisture, heat, aerosols and gases and expand adiabatically, until a thermodynamic equilibrium is reached at the top of the boundary layer. The top of the PBL ranges in altitude between approximately 100 to 2000 m depending on the time of day and local meteorological conditions and is defined by a sharp decrease in aerosol concentration. The PBL rapidly responds to surface forcing such as temperature as well as moisture and fluctuations in wind speed, all of which allow strong vertical mixing.

Figure 1-2 shows a diagram of the PBL over land. The PBL can be divided into three main regions. The surface or stable layer, at the bottom of the PBL has a thickness of approximately 10% of the total PBL altitude. Above this is the mixed layer (ML), where turbulence is driven by convection. Warm air from the surface meets cool air radiating from the clouds layer above and reaches equilibrium at the entrainment layer (EL). The mixing layer begins to grow just after sunrise and reaches a maximum altitude in the afternoon.

After sunset the thermals decrease and the PBL forms a residual layer above a stable nocturnal surface boundary layer. The gas and aerosol within the residual layer disperse equally in the horizontal and vertical directions and remain within the layer throughout the night, where they may react with each other to form new compounds. In contrast to the residual layer, the stable nocturnal boundary layer has

much weaker turbulence and the vertical dispersion of gas and aerosols is very small.

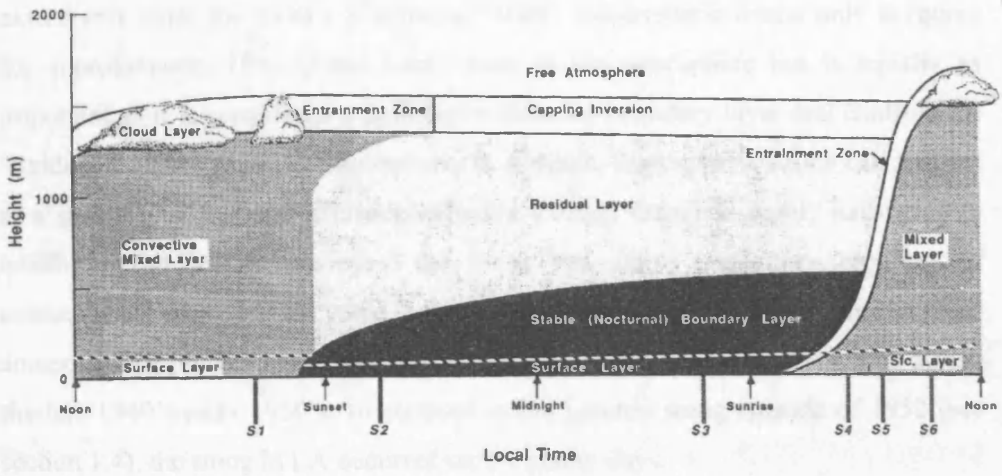

Figure 1-2: Structure of the urban boundary layer [Stull, 1988].

Over the sea and oceans, the surface temperature changes are very small between day and night, owing to the large heat capacity of water which enables water to absorb solar radiation without a large change in temperature. Hence, thermals rising from the surface vary very slowly and the marine boundary layer (MBL) depth stays almost constant and well mixed.

1.2 Urban boundary layer chemistry

Boundary layer chemistry in urban areas is important as the majority of pollutants are emitted from the surface and the entrainment layer acts as a lid and effectively "traps" the pollutants within the boundary layer. In this next section, the photochemical reactions that occur in the urban boundary layer and lead to the formation of photochemical pollution are overviewed.

1.2.1 Tropospheric ozone and nitrogen oxides

The role of the stratospheric ozone layer is well known and has been studied extensively since the 1930's [Chapman, 1930]. Tropospheric ozone only accounts for approximately 10% of the total ozone in the atmosphere but is equally as important as it is considered a pollutant within the boundary layer and controls the "oxidising capacity" of the troposphere. In addition, tropospheric ozone can also act as a greenhouse gas and influence radiative forcing. Ozone is highly hazardous to health; it can irritate the eyes, the lungs and cause respiratory problems if continuously exposed. Elevated concentrations of ozone are also the primary component of photochemical smog. An example of this was in Los Angeles during the late 1940's/early 1950's. In contrast to the London smog episode of 1952 (see section 1.4), the smog in LA occurred on hot sunny days.

NO and NO_2 (NO_x), play an important role in the chemistry of the urban boundary layer. The interconversion between NO and NO_2, first suggested by Blacet [1952] is the main key in the formation of photochemical smog in this region. In high NO_x conditions the reaction of NO with HO_2 leads to the formation of NO_2.

$$OH + CO \rightarrow H + CO_2 \quad (1\text{-}1)$$

$$H + O_2 + M \rightarrow HO_2 + M \quad (1\text{-}2)$$

$$HO_2 + NO \rightarrow OH + NO_2 \quad (1\text{-}3)$$

The photolysis of NO_2 and the subsequent reaction of the photoproducts lead to the production of ozone in the troposphere.

$$NO_2 + h\nu\ (\lambda < 420\ nm) \rightarrow NO + O(^3P) \quad (1\text{-}4)$$

$$O(^3P) + O_2 + M \rightarrow O_3 + M \quad (1\text{-}5)$$

$$\text{NET (1-1 to 1-5): } CO + 2O_2 + h\nu \rightarrow CO_2 + O_3 \quad (1\text{-}6)$$

where M is a third body molecule (N_2 or O_2), which removes excess kinetic energy in the reaction. Pre-existing ozone may also result in the conversion of NO to NO_2.

$$O_3 + NO \rightarrow NO_2 + O_2 \quad (1\text{-}7)$$

A similar reaction sequence involving RO_2 can occur, where R is any organic molecule.

$$RO_2 + NO \rightarrow RO + NO_2 \quad (1\text{-}8)$$

In low NO_x conditions, however, the following reactions (shown for HO_2), resulting in a catalytic destruction of ozone can dominate.

$$OH + CO \rightarrow H + CO_2 \quad (1\text{-}9)$$

$$H + O_2 + M \rightarrow HO_2 + M \quad (1\text{-}10)$$

$$HO_2 + O_3 \rightarrow OH + 2O_2 \quad (1\text{-}11)$$

$$\text{NET (1-9 to 1-11): } CO + O_3 \rightarrow CO_2 + O_2 \quad (1\text{-}12)$$

During the night, when the photolytic production of OH ceases, the NO_3 radical and dinitrogen pentoxide (N_2O_5) can become important [Wayne *et al.*, 1991].

$$NO_2 + O_3 \rightarrow NO_3 + O_2 \quad (1\text{-}13)$$

$$NO_3 + NO_2 + M \leftrightarrow N_2O_5 + M \quad (1\text{-}14)$$

NO_3 is rapidly photolysed (lifetime ~5 s), hence, is only significant at night time. The reaction of NO_2 with NO_3 forms N_2O_5 which acts as reservoir species for NO_x during the night.

The photolysis of NO_2 and reactions of NO and O_3, (reactions 1-4, 1-5 and 1-7) result in a photostationary state, also known as the Leighton relationship, at suitable concentrations and if the sunlight intensity stays constant. The relationship can be expressed as

$$\phi = \frac{j_{1-4}}{k_{1-7}} \frac{[NO_2]}{[NO][O_3]} \qquad (1\text{-}15)$$

Where, j_{1-4} is the photolysis frequency and k_{1-7} is the rate coefficient, for reactions 1-4 and 1-7.

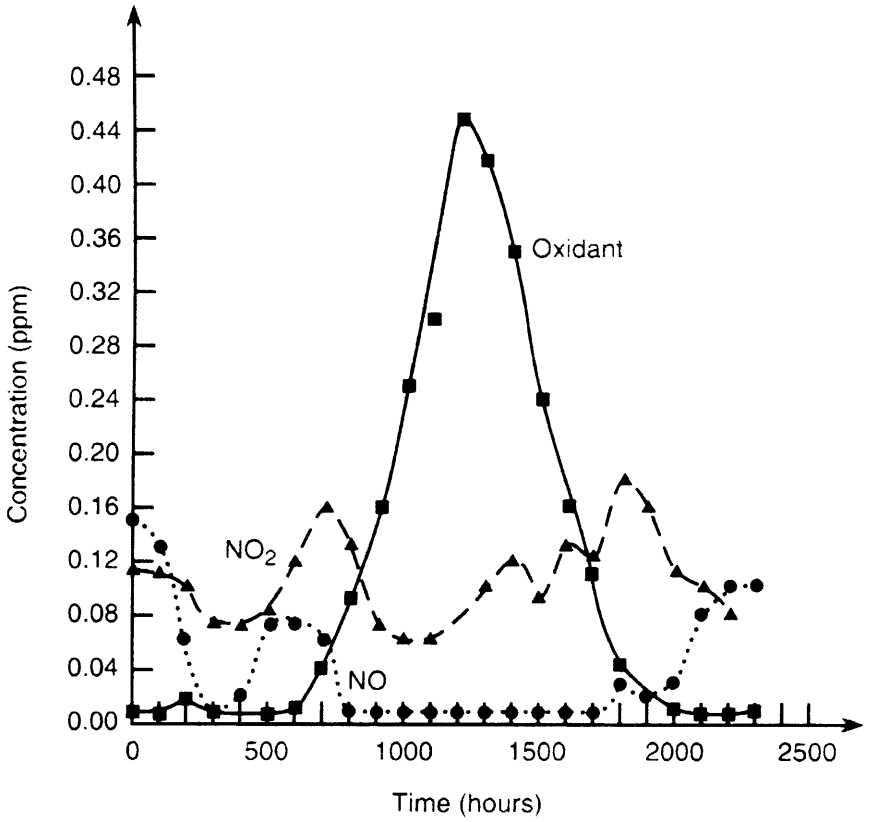

Figure 1-3: Diurnal variation of NO_2, NO and oxidants (including O_3) from 25th July 1973 in Pasadena, California [*Finlayson-Pitts and Pitts*, 1977].

Figure 1-3 shows an example of the diurnal variations of NO_2, NO and oxidant (including O_3) in an urban situation. During the night, N_2O_5 acts as a reservoir species for NO_x. After sunrise the concentration of NO_2 increases, owing to the reaction of NO with HO_2/RO_2, and reaches a peak at approximately 8 am

corresponding to a maximum in traffic emissions, in an urban situation. The NO decreases to a minimum around this point until the evening traffic flow begins. The photolysis of NO_2 and subsequent production of O_3 increases during the day and reaches a maximum in the afternoon. However, the actual time of the peak depends on emissions and transport of pollutants. The NO_2 concentration then increases in the evening owing to reduced photolysis and the reaction of NO with O_3.

The influence of NO_x on the production of tropospheric ozone is dependent on its sources, sinks and reservoir species. The main loss process of NO_2 is the reaction with OH to yield nitric acid (HNO_3).

$$OH + NO_2 + M \rightarrow HNO_3 + M \qquad (1\text{-}16)$$

Nitric acid (HNO_3), with a lifetime of approximately 20 hours, is hence the main sink for tropospheric NO_x and is removed by wet and dry deposition. In the free troposphere, the lifetime of NO_x can be expressed as the time constant for reaction (1-16) which gives a lifetime of the order of a few days in the lower free troposphere. However, in the boundary layer, additional loss and transformation processes results in a NO_x lifetime of approximately 1 hour.

The high photolysis rate and reduced lifetime of NO_2 in the summer months, compared to the long lifetime of NO_2 coupled with increases in residential heating in the winter months, result in a seasonally dependent NO_2 concentration over urban areas. In rural areas, anthropogenic activity is very low and natural emissions dominate, resulting in a different seasonal cycle. In a study by van der A *et al.*, [2006], the seasonal cycle of tropospheric NO_2 columns over China measured by the SCIAMACHY and GOME satellite instruments from 1996 to 2004 was presented. The results indicate that in eastern China, where the population density is high, a winter maximum occurs. However, in the western part of China natural emissions from soil and lightning discharges dominate, resulting in a maximum NO_2 concentration in the summer.

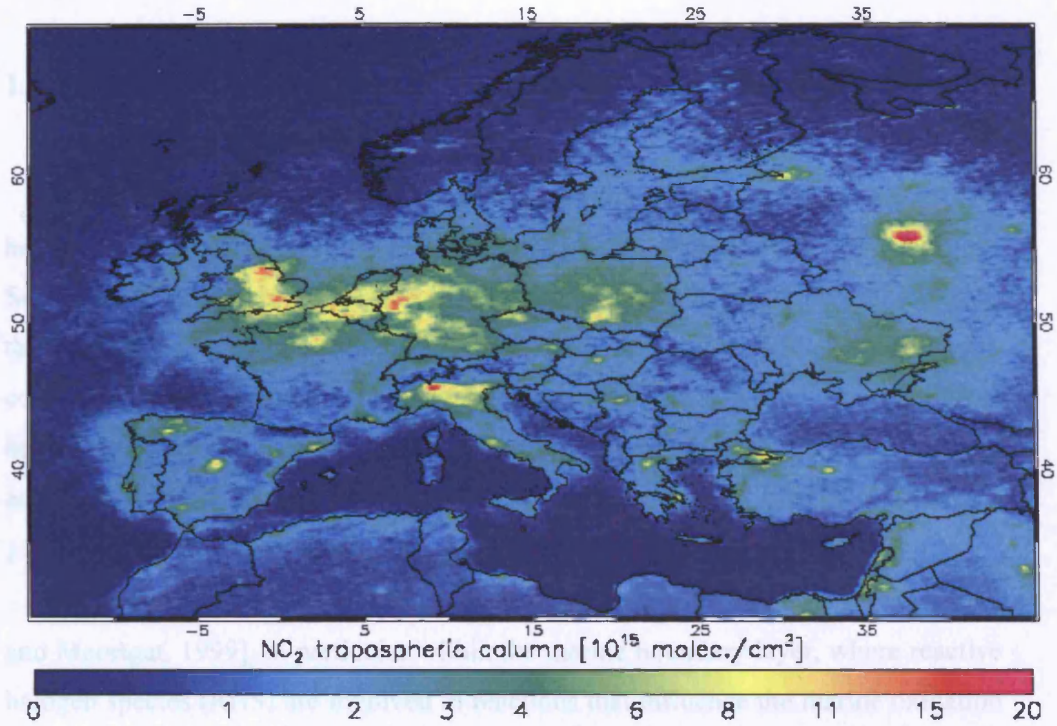

Figure 1-4: Monthly averaged tropospheric NO_2 columns over Europe for September 2007, measured by the OMI on Aura [KNMI/NASA/NIVR].

From the discussion above, it can be observed that nitrogen oxides are important when considering the formation of ozone and photochemical pollution in the urban boundary layer. Figure 1-4, shows monthly averages of tropospheric NO_2 columns over Europe, for September 2007, measured by the OMI on Aura. From Figure 1-4 it can be seen that emissions of NO_2 in the troposphere is particularly high over large cities where anthropogenic sources from industry and vehicles are large.

The Concurrent Multi-Axis Differential Optical Absorption Spectroscopy (CMAX- DOAS) instrument, installed in Leicester, U.K. (see Chapter 3) is capable of measuring NO_2 in the troposphere and urban boundary layer, during daytime, with a temporal resolution of 1 minute. Exploring the monitoring of NO_2 in this regime is one of the main objectives of this thesis.

The second aim of this thesis involves remote sensing of halogen oxides in the MBL with CMAX-DOAS. The next section gives an overview of the main reactions that occur in the MBL, in particular halogen oxides, their precursors, and the role of halogen oxides in the destruction of ozone.

1.3 Marine Boundary layer chemistry

Within the polar regions, the role of halogens in stratospheric ozone destruction has been known for some time [Farman *et al.*, 1985; Molina and Rowland, 1974, Solomon 1990]. However, the role of halogens in ozone depletion events (ODE) in the troposphere is still under debate. Since Barrie *et al.* [1988] first reported high concentrations of bromine compounds during ODE in the polar troposphere a number of studies on halogens in the polar regions have been performed [Hausmann and Platt, 1994; Platt and Janssen, 1996; Tuckermann *et al.*, 1997; Kreher *et al.*, 1997, Frieβ *et al.*, 1999; Frieβ *et al.*, 2001, Platt and Hönninger, 2003].

More recently, however, ODE have been observed in mid-latitude regions [Platt and Moortgat, 1999], in particular within the marine boundary layer, where reactive halogen species (RHS) are involved in reactions that influence the marine oxidation budget, in particular BrO [Platt and Jansen, 1996; Dickerson *et al.*, 1999; Hebestreit *et al.*, 1999; Wagner *et al.*, 2001; Saiz-Lopez *et al.*, 2004; 2006] and IO [Platt and Jansen, 1996; Alicke *et al.*, 1999; Stutz *et al.*, 1999; Carpenter *et al.*, 2001; Allan *et al.*, 2000; Saiz-Lopez *et al.*,2006; Whalley *et al.*, 2007, Wada *et al.*, 2007].

The main reactions which are important in MBL ODE involve the halogens, chlorine (Cl), bromine (Br) and iodine (I) and their monoxides, ClO, BrO and IO [Platt and Jansen, 1996]. The lifetime of halogen atoms in the MBL is very short owing to their reaction with ozone (approximately 0.1 s for Cl and 1 s for Br and I, at background ozone levels).There are two primary sources of halogens in the MBL: the release from sea salt aerosols and the emission of biogenic alkyl halides from seaweed.

Sea salt aerosols are produced from the bursting of air bubbles on the surface of the sea or ocean, which release salt particles into the atmosphere. The sea salt aerosol is generally in aqueous form, unless present in very dry marine regions or the free troposphere. Halide ions (I^-, Br^-, Cl^-) within the aerosol react with HO_x in sufficient acidity (H^+) to form interhalogenated species such as BrCl or Br_2, which are then released into the gas phase and photolysed rapidly to form halogen atoms. Studies of sea-salt aerosols [Ayers *et al.*, 1999, Sander *et al.*, 1999] suggest this may be a primary source of Br atoms.

$$HOX_{(aq)} + H^+ + Br^- \rightarrow BrX_{(aq)} + H_2O \quad (1\text{-}17)$$

$$BrX + h\nu \rightarrow Br + X \quad (1\text{-}18)$$

$$X + O_3 \rightarrow XO + O_2 \quad (1\text{-}19)$$

where X= Cl, Br, I

Another mechanism for the release of halogens from sea-salt aerosol is via the reaction with N_2O_5, or $XONO_2$. However, this process is only expected to occur in regions with high NO_x concentrations. The release of halogen atoms in reaction 1-17 is autocatalytic and can lead to events such as "Bromine explosions" [Barrie *et al.*, 1988].

In contrast to bromine atoms, the main source of iodine atoms in the MBL is thought to be from the photolysis of biogenic alkyl halides (RI_x) such as CH_3I and CH_2I_2 and iodine molecules (I_2) emitted from macro-algae and phytoplankton [Schall and Heumann, 1993, Carpenter *et al.*, 1999, 2001, McFiggans *et al.*, 2004]. It has been suggested that the algae and phytoplankton release iodine compounds as a defence mechanism and a maximum in IO occurs during low tide in the daytime owing to the exposure of the algae and phytoplankton to air and solar irradiance.

$$RI_x + h\nu \rightarrow R + I \quad (1\text{-}20)$$

$$I + O_3 \rightarrow IO + O_2 \quad (1\text{-}21)$$

During the day photolysis of XO or the reaction with NO in polluted regions may lead to the re-generation of halogen atoms.

$$XO + h\nu \rightarrow X + O \quad (1\text{-}22)$$

$$XO + NO \rightarrow X + NO_2 \quad (1\text{-}23)$$

Self reactions of XO, or another halogen oxide may also occur.

$$XO + YO \rightarrow X + Y + O_2 \quad (1\text{-}24a)$$

$$\rightarrow XY + O_2 \quad (1\text{-}24b)$$

$$\rightarrow OXO + Y \quad (1\text{-}24c)$$

where Y= Cl, Br, I.

During high IO events, the self reaction of IO to form OIO results in the nucleation of iodine oxide radicals and the possible growth of aerosols particles which may contribute to local radiative budgets [Murphy *et al.*, 1998].

Reaction 1-24a and 1-24b may lead to a catalytic destruction of ozone *via* reaction 1-19. The photolysis of OXO formed in reaction 1-24c, does not generally lead to a net destruction in ozone as the reaction yields oxygen atoms, which can quickly react with O_2 to from ozone. However, in the case of OIO, a study by Ashworth *et al.* [2002] show that the photolysis of OIO is more likely to lead to the formation of I and O_2, hence the subsequent reaction of iodine with ozone will result in ozone destruction.

Halogen atoms may also react with hydrocarbons or HO_2 to form hydrogen halides [Monks *et al.*, 2005].

$$HCHO + X \rightarrow CHO + HX \quad (1\text{-}27)$$

$$HO_2 + X \rightarrow O_2 + HX \quad (1\text{-}28)$$

However, reaction 1-25 does not occur for iodine atoms. The hydrogen halides are eventually removed from the atmosphere by wet or dry deposition.

A schematic of the primary reactions involving halogens in the MBL is given in Figure 1-5.

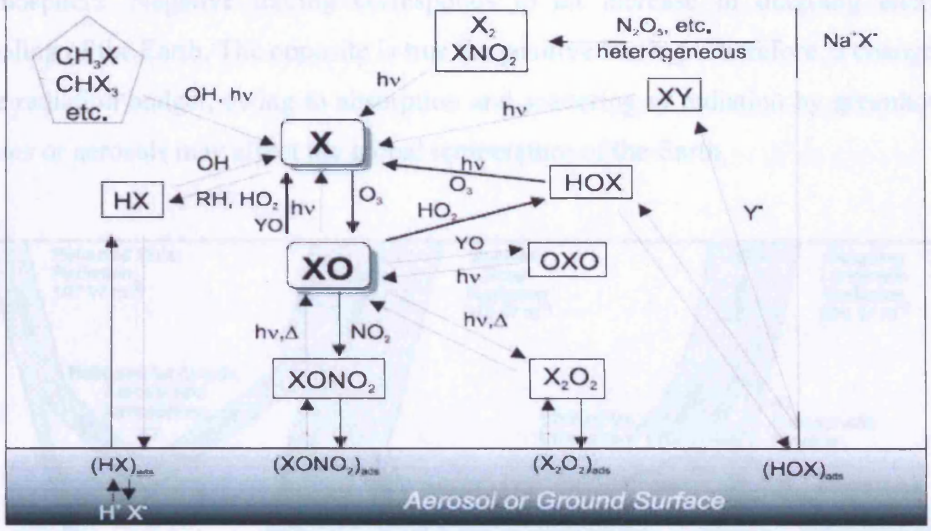

Figure 1-5: Schematic of the primary halogen reactions in the marine boundary layer [Hönninger *et al.*, 2002, modified from Platt and Jansen, 1996].

Along with measurements of trace gases in the urban and marine boundary layers, the CMAX-DOAS instrument is also sensitive to aerosol and clouds within these regions of the atmosphere and is explored further in this thesis. The radiative property of clouds and aerosols are important to determine the radiative forcing of the atmosphere and is explored in the next section.

1.4 Aerosols

Tropospheric aerosol particles or particulate matter (PM) have a direct influence on the climate through absorption and scattering of radiation and indirectly by functioning as cloud condensation nuclei (CCN) [Haywood and Boucher, 2000]. Figure 1-6 shows an illustration of the Earths radiation budget [Kiehl and Trenberth, 1997]. Incoming solar radiation is absorbed by the Earth's surface and water vapour, gases, and aerosols in the atmosphere. The incoming solar radiation is also reflected by the Earth's surface, clouds, and the atmosphere. The energy that is absorbed by the surface and atmosphere is emitted in the form of long-wave radiation. The radiative forcing is defined as the change in the radiation balance at the top of the

atmosphere. Negative forcing corresponds to an increase in outgoing energy, cooling of the Earth. The opposite is true for positive forcing. Therefore, a change in the radiation budget, owing to absorption and scattering of radiation by greenhouse gases or aerosols may affect the global temperature of the Earth.

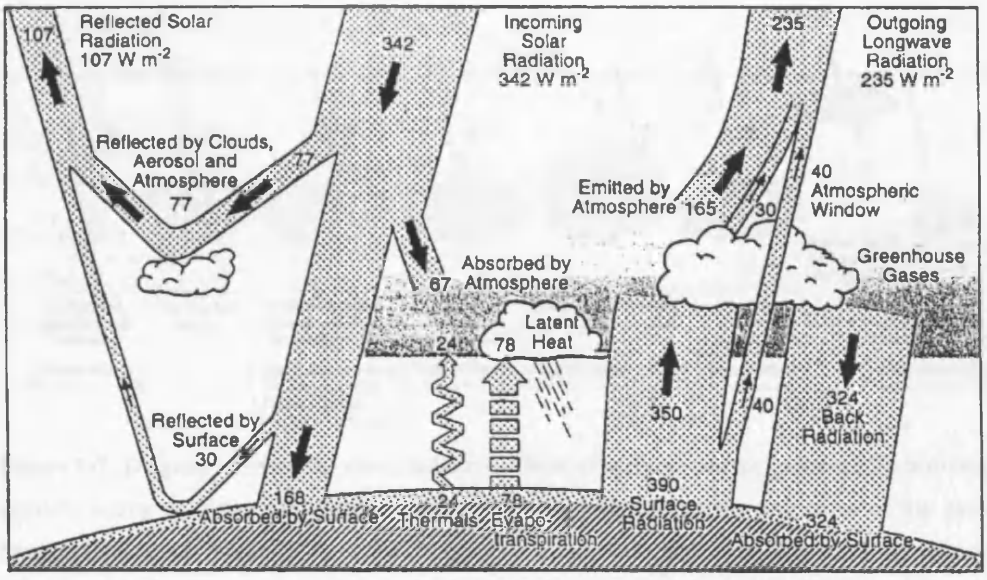

Figure 1-6: Illustration of the Earth's radiation budget [Kiehl and Trenberth, 1997]

Particles in the atmosphere arise from natural sources such as dust, volcanic eruptions and sea salt and also from anthropogenic sources such as the combustion of fuels from industry and traffic. Particulate matter consists of small liquid or solid particles that are suspended in the air which can vary in size from nanometres to micrometers [Seinfeld *et al.*, 1998]. The aerosol surface can provide a site for heterogeneous reactions to occur in the troposphere and stratosphere.

The radiative properties of aerosols are determined by the composition, size and shape of the particle [Stier *et al.*, 2005], resulting in positive or negative radiative forcing in the atmosphere. Anthropogenic aerosol particles in the troposphere, such as black carbon, partially absorb solar radiation leading to a positive radiative forcing effect on the atmosphere and an increase in temperature. Sulphate aerosols, formed from the oxidation of SO_2, and dimethyl sulphide (DMS) in marine atmospheres, scatter short-wave solar radiation back into space, resulting in a negative radiative forcing effect and a decrease in temperature.

Indirect radiative forcing also occurs, owing to aerosol particles acting as cloud condensation nuclei which modify the physical and radiative properties of clouds as well as the cloud lifetime. An increase in cloud droplets due to aerosols may result in an increase in cloud albedo and greater scattering of radiation back into space.

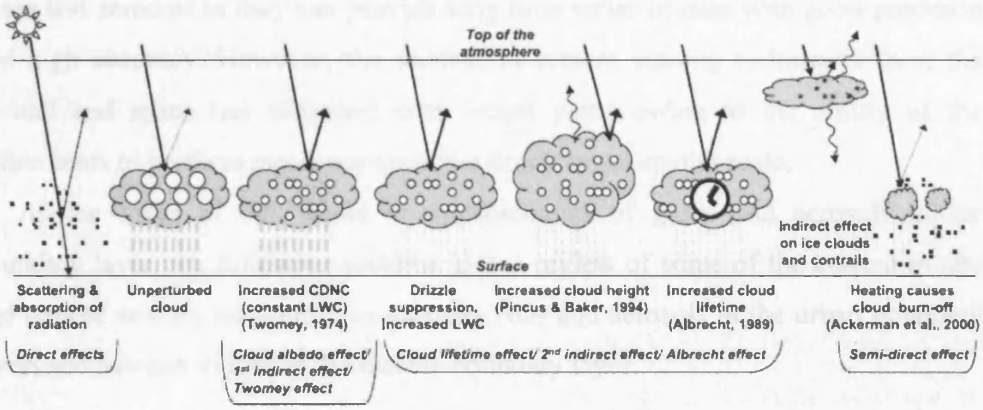

Figure 1-7: Diagram showing the direct radiative effects of aerosols and the indirect effects owing to aerosols acting as cloud condensation nuclei (CCN) which change the properties of the clouds. Straight lines represent the incident and reflected solar radiation, and wavy lines represent terrestrial radiation. Filled white circles indicate cloud droplet number concentration (CDNC) and the black points as aerosols. The vertical grey dashes represent rainfall, and LWC refers to the liquid water content. (IPCC report IV- modified from Haywood and Boucher, 2000).

Aerosols also have an adverse effect on the health of humans and animals. Inhaling particulate matter may allow the smallest particles (< 10 μm) to penetrate deep into the lungs, possibly causing serious respiratory disease. The contribution of SO_2 and PM during December 1952 caused up to 4000 excess deaths in the London "Great Smog" episode. A cold spell caused an increase in coal burning and owing to the dense mass of cold air an inversion layer formed trapping the pollutants near the surface [Wilkins *et al.*, 1952]. Subsequent to this episode a Clean Air Act was passed in 1956 to reduce emissions.

1.5 Monitoring the urban and marine boundary layers

In the previous sections the importance of trace gases and aerosol in the urban and marine boundary layers has been highlighted. Global chemistry and transport

models (CTMs) [Bey *et al*, 2001] are useful tools to study the distribution and transport of tropospheric gases. However they require knowledge of the initial and boundary conditions which are often retrieved from ground based and satellite measurements.

In situ monitoring techniques are widely used to perform measurements of trace gases and aerosols as they can provide long time series of data with good precision and high accuracy. However, the number of remote sensing techniques from the ground and space has increased over recent years owing to the ability of the instruments to perform measurements on a much larger spatial scale.

As the focus of this thesis is measurements of gases and aerosols in the boundary layer, the following sections give a review of some of the current *in situ* and remote sensing techniques to measure NO_2 and aerosols in the urban boundary layer, and halogen oxides in the marine boundary layer.

1.5.1 *In situ* measurement techniques

In situ measurement techniques are often used by local authorities to monitor the levels of pollutants in cities. Chemiluminescence monitors, in particular, are employed as they are inexpensive and can provide measurements of NO_2 in real time with good temporal resolution [Navas *et al.*, 1997]. Chemiluminescence monitors typically operate by routing an air sample to a reaction chamber where the NO reacts with ozone to form an excited state of NO_2 which emits radiation, detected by a photomultiplier tube [Navas *et al.*, 1997]. The total NO_x concentration is also measured by passing the sample stream through a converter containing a catalyst (such as molybdenum) to reduce any NO_2 present to NO. Subtracting the NO from the NO_x value yields a concentration of NO_2. It is known, however, that in monitors with molybdenum oxide catalysts, other compounds such as nitric acid (HNO_3) and peroxyacetyl nitrate (PAN), may also reduce to NO, leading to an overestimation of the NO_2 measurement [Ordóñez *et al.*, 2006, Steinbacher *et al.*, 2007; Dunlea *et al.*, 2007]. Other photolysis techniques, less effected by the interference of other nitrogen compounds, are often used in scientific research to measure NO_2 such and diode based blue light (BLC), photolytic NO_2 converter (NOxy) and laser induced fluorescence (LIF) [Kley and McFarland, 1980]. LIF can

also be used to measure other species such as NO_2, OH and HO_2 radicals and other free-radical species, for example IO and RO_2 [Bloss *et al.*, 2003].

In situ measurements of aerosols are often obtained by trapping the particles on filters. Their chemical composition and mass can be measured by a number of different methods. For example, particle counters operate by measuring scattered light from a single particle and condensation particle counters inject the aerosols into air supersaturate with water, where they act as condensation nuclei and grow into large particles which are passed through a detector and counted.

1.5.2 Ground-based remote sensing technique

To retrieve information on gas species and aerosols at different altitudes and locations, the *in situ* instruments described in section 1.5.1 can be operated on balloons and aircraft. However, ground-based remote sensing instruments may also obtain information at different altitudes above the instrument, for example, light detection and ranging (lidar) systems and Multi-Axis DOAS instruments (MAX-DOAS).

Lidar instruments, in particular, are useful for measuring aerosols as lidar instruments are highly sensitive to particles and clouds and can retrieve aerosol distribution, optical properties and cloud heights from backscatter measurements at multiple wavelengths. The use of lidar instruments to perform measurements of aerosols is explored further in Chapter 4.

Sun photometry measurements are often performed alongside lidar measurements as sun photometry can provide complimentary data for aerosol optical thickness (AOT) and particle size distribution [Takamura *et al*, 1994, Ferrare *et al*, 2000].

Sun photometers measure direct solar light across specific wavelength ranges to determine the quantity of absorption from molecules and aerosols in the atmosphere. A tracker device enables the instrument to constantly point towards the sun, ensuring no scattered light enters the detector. As the light travels through the atmosphere, gases and aerosols scatter and absorb some of this radiation and the difference between the intensity at the top of the atmosphere and that detected by the photometer allows the aerosol and gas properties to be calculated. The

AERONET (AErosol RObotic NETwork) program is a ground based aerosol monitoring system that uses a network of sun photometers around the world to perform measurements of aerosol optical properties for monitoring and the validation of satellite retrievals [Holbern *et al.*, 1998].

Figure 1-8: CIMEL sun photometer operating at the University of Leicester in 2007.

A similar technique to that used by sun photometers is the differential optical absorption spectroscopy (DOAS) method, established by Platt *et al.* [1979]. A detailed description of the method is presented in Chapter 2. The DOAS technique enables simultaneous measurements of both gases and aerosols in the atmosphere. DOAS can be applied to ground-based instruments such as, long path DOAS (LP-DOAS) [Perner and Platt, 1979, Axelson, 1990] and cavity enhanced absorption spectroscopy (CEAS) [Berden *et al.*, 2000], or remote sensing instruments that may be deployed on the ground, air, or on satellites, for example, zenith-viewing [Noxon,1975] and multi-axis DOAS (MAX-DOAS) [Hönninger *et al.*, 2004a] (see section 3.1).

1.5.3 Satellite observations of the atmosphere

Ground-based and airborne instruments provide measurements with good temporal resolution and high precision. However, it was not until instruments were launched onboard satellites that information could be obtained of gas species and aerosols on a global scale. The first operational satellite to produce the images of Earth from space was Explorer 6, a U.S. satellite instrument launched in 1959. Since then, many satellites have been launched with instruments to measure the Earth's atmosphere, land surface and sea-surface.

Retrieving information on gas species and aerosols can be challenging with space-based instruments. Clouds within the line of sight of the instrument can have varying effects on retrievals from space. Clouds may obscure gas located below the cloud, decreasing measurement sensitivity. Secondly, owing to the high albedo of clouds, they generally increase the sensitivity to gas above the cloud layer.

Satellite instruments perform measurements with different viewing geometries. Nadir viewing instruments measure the backscattered radiation directly below the instrument to retrieve total vertical column measurements. When performing tropospheric measurements, the stratospheric contribution to the measured column needs to be quantified and subtracted. Performing measurements in limb viewing geometry by either measuring the solar radiation through the limb of the atmosphere or measuring radiation emitted by trace gases, clouds and aerosols allows the retrievals of trace gases in the upper atmosphere with a vertical resolution of typically 1 to 3 km. However, the spatial resolution is much poorer is limb that nadir view owing to the long horizontal path

Satellite instruments that employ the DOAS technique are particularly useful for monitoring tropospheric gas species and aerosols, as multiple species may be retrieved simultaneously. A summary of recent satellite DOAS instruments that perform measurements in the troposphere is given in Table 1-1 and an overview of the target gases shown in Figure 1-9.

Table 1-1: Summary of the satellite DOAS instruments that perform measurements in the troposphere.

Satellite instrument	Platform	Launch year	Limb/ Nadir	Spatial resolution (km)	Spectral range (nm)	Spectral resolution (FWHM nm)
GOME	ERS-2	1995	Nadir	40 x 320	240 to 790	0.2 to 0.4
SCIAMACHY	ENVISAT	2002	Limb/ Nadir	30 x 60	240 to 2380	0.2 to 1.5
OMI	Aura	2004	Nadir	13 x 24	270 to 500	0.45 to 1.0
GOME-2	MetOp	2006	Nadir	80 x 40	240 to 790	0.2 to 0.4
TROPOMI*	TRAQ	2014/ 2015	Nadir	10 x 10	270 to 2380	0.25 to 0.45

* proposed future mission

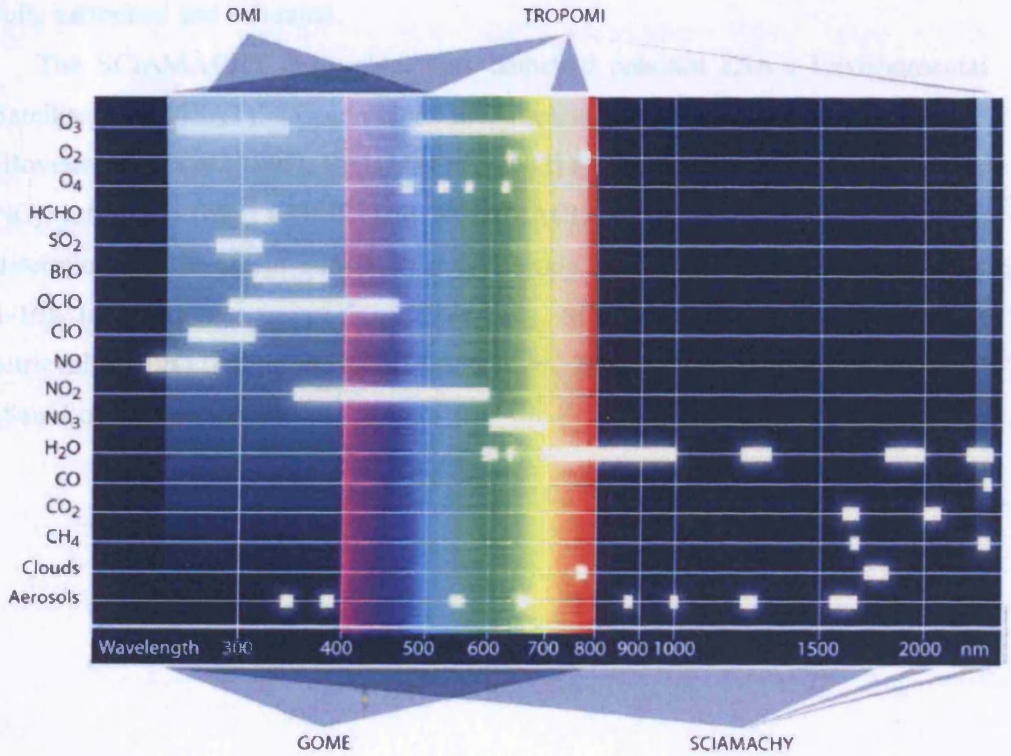

Figure 1-9: Overview of the spectral range and trace gas products from GOME, SCIAMCHY, OMI and TROPOMI (proposed future mission) [de Vries *et al.*, 2007].

The Global Ozone Monitoring Experiment (GOME) has a large swath width of 960 km across track which enables global coverage to be achieved in three days. GOME was originally designed to measure the global distribution of ozone along with other trace gases which play a role in ozone chemistry, such as NO_2 [Burrows *et al*, 1999, Richter *et al.*, 2002; Balis *et al.*, 2007]. However, in addition to the operational products, GOME has also performed measurements of other trace gases such as OClO [Wagner *et al.*, 2002], SO_2 [Eisinger *et al.*, 1996], BrO [Hegels *et al.*, 1998; Chance, 1998; Richter, 2002] and HCHO [Burrows *et al*, 1999, Chance *et al.*, 2000]. NO_2 measurements from GOME have also been compared to ground based instruments with good agreement [Petritoli *et al.*, 2004; Ordóñez *et al.*, 2006, Schaub *et al.*, 2006] and used to determine weekly cycles of tropospheric NO_2 vertical columns for different regions of the world [Beirle *et al.*, 2003].

More recently, the second generation GOME-2 instrument on MetOp was launched on October 19, 2006. GOME-2 will continue the long-term monitoring of atmospheric gases started by GOME, although, currently the spectra are not yet fully calibrated and validated.

The SCIAMACHY instrument was launched onboard ESA's Environmental Satellite (ENVISAT) to continue the measurements performed by GOME [Bovensmann *et al.*, 1999]. Richter *et al.* [2003] used a combination of tropospheric NO_2 retrievals from GOME and SCIAMACHY between 1996 and 2004 to determine the change in emissions over Europe the U.SA and China (see Figure 1-10). In addition to measurements of NO_2, SCIAMACHY has also performed retrievals of BrO [Afe *et al.*, 2004; Piters *et al.*, 2004, Rozanov *et al.*, 2005 and IO [Saiz-Lopez *et al.*, 2007].

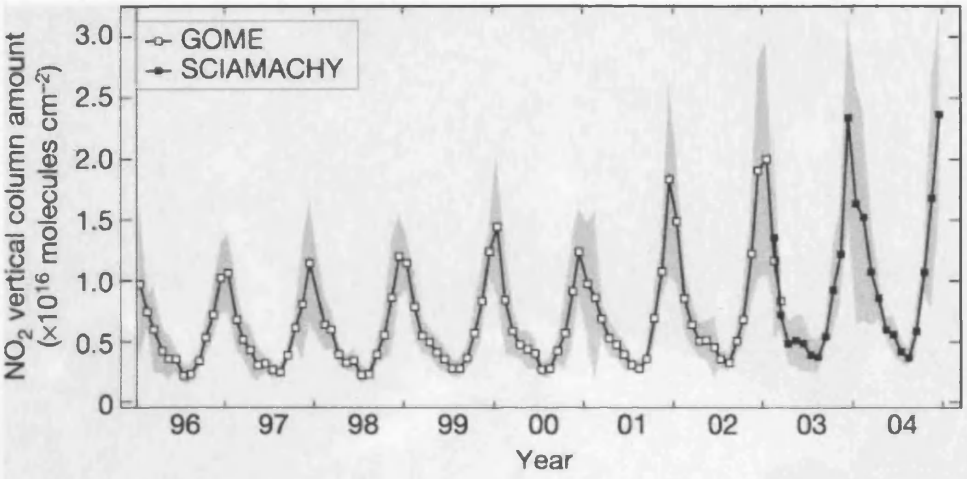

Figure 1-10: Monthly averages of tropospheric vertical columns of NO_2 over East Central China from GOME and SCIAMACY for 1996 to 2004 [Richter *et al.* 2003].

The Ozone Monitoring Instrument (OMI) instrument was designed to obtain column measurements of gases important to ozone chemistry and air quality. OMI has a ground pixel size of 13 km × 24 km at nadir and can achieve global coverage in one day, making it ideal for measurements of tropospheric gas species on an urban scale (see section 5.4). OMI was launched onboard Aura, which is a member of the "A-train" (Figure 1-11). The A-train presently consists of five satellites (Aura, PARASOL, CALIPSO, CloudSat and Aqua) flying in low polar orbits a few minutes apart. Two additional satellites, OCO and Glory, are to be launched in late 2008 and will join the rest of the A-train. All the satellites will cross the equator around 1.30 UT. By combining the different sets of observations, we will be able to gain a better understanding of the parameters related to pollution and climate change.

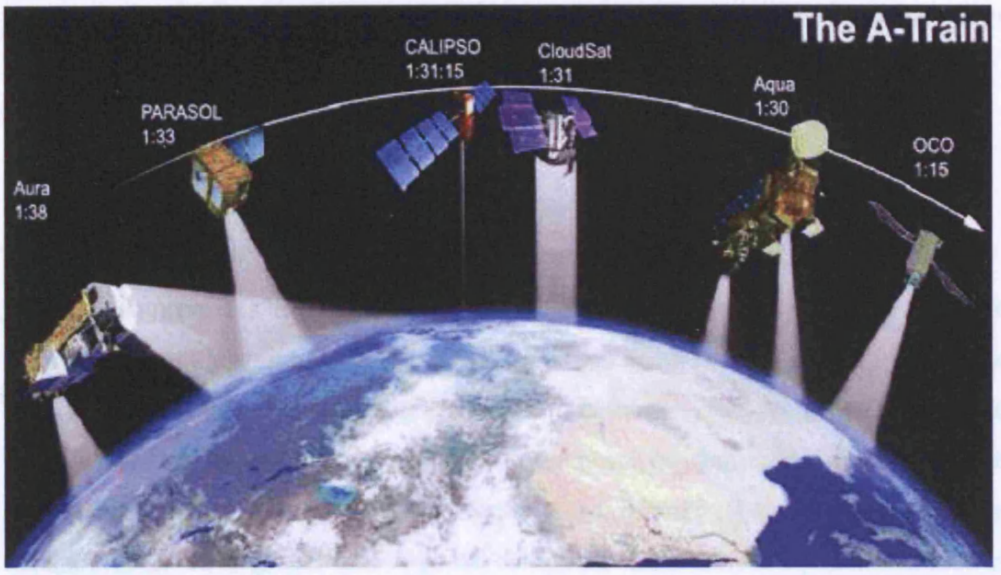

Figure 1-11: The"A Train" satellites (cloudsat.atmos.colostate.edu/ images/)

1.6 Summary

In Chapter 1, an introduction to some of the dynamical processes and chemistry that occur within the urban and marine boundary layers were given, in particular, photochemical reactions leading to the production of tropospheric ozone and urban pollution and the role of halogens on the oxidative chemistry of the troposphere.

Monitoring pollutants in the urban boundary layer is very important to determine their effect on the environment and human health. In this chapter, details of the current *in situ* and remote sensing techniques employed for this purpose have been presented. In the marine boundary layer, the current theories on the role of halogen oxides on the oxidative chemistry of the troposphere have been discussed and a need for further investigations in this area noted.

The recent use of remote sensing techniques, such as MAX-DOAS and space-based instruments enable simultaneous measurements of a number of trace gases and aerosols on a regional and global scale. It has been noted, however, that it is important that the retrieved quantities from these instruments, in particular satellite instruments, are validated with ground-based or airborne measurements to ensure

that geophysical quantities inferred from the in-orbit radiometric measurements meet requirements for the intended scientific studies and applications.

1.6.1 Motivation for this work

The requirements for additional measurements of trace gases and aerosols to improve our understanding of the processes that occur in the urban and marine boundary layers have been highlighted in this chapter. Current techniques are based on *in situ* measurements that provide good temporal resolution but cannot provide information on a large spatial scale. Satellite instruments, however, can perform measurements on a global and regional scale but their sensitivity near-surface is poor. The need to perform measurements on a larger spatial scale with information on the near-surface and free troposphere is evident and the CMAX-DOAS instrument developed at the University of Leicester has the capability of performing long term measurements of trace gases and aerosols with a good temporal resolution. It also provides information on the vertical and horizontal distribution of gases within two diverse regions of the atmosphere.

In this thesis, the CMAX-DOAS instrument was employed to perform measurements of trace gases in an urban and marine atmosphere during two measurement campaigns. The results from the campaigns and the additional work on the validation of a satellite-based instrument, provides interesting results that have previously not been documented in the literature.

Chapter 2

Differential Optical Absorption Spectroscopy

Spectroscopy has become widely used to infer information about gases and particles in the atmosphere. Continuous spectra arise from the emission of radiation over a broad range; this can be in the form of UV or visible radiation such as the radiation the Sun emits or in the case of the Earth, infrared radiation. Discrete spectra are the result of interactions between radiation and atoms/molecules. The outcome is specific energy changes depending on whether a photon is absorbed by an atom or molecule, resulting in a transition from a lower energy state to an exited state or if a transition occurs from an excited state to a lower energy state, producing emission spectra.

In this chapter, an introduction to absorption spectroscopy and its applications is given, in particular DOAS. The DOAS technique, used to perform the retrievals of trace gases in this thesis, utilises absorption spectroscopy to determine concentrations of gases in the atmosphere. The DOAS principle was first introduced by Platt [Platt *et al.*, 1994] and has since been used for ground based and satellite measurements using both active and passive instruments. The process involved in retrieving slant column densities (SCDs) of trace gases from the measured spectra will be explained here, along with information on the radiative transfer in the atmosphere and the calculation of air mass factors required to determine concentrations of the retrieved species within the atmosphere.

2.1 The Beer-Lambert Law

Figure 2-1 shows a demonstration of radiation incident on a gas sample with a concentration, c. As the radiation travels through the sample it is scattered and absorbed by gas molecules. The absorption of radiation by matter is wavelength dependent and is defined by the Beer-Lambert law. Assuming a single absorber, and that the dependence of the absorption cross section on pressure and temperature is negligible, the Beer-Lambert Law can be written as:

$$I(\lambda) = I_o(\lambda)\exp\left(\int_{l=0}^{l=L}(\sigma(\lambda)c(l))dl\right) \qquad \textbf{Equation 2-1}$$

where, $I_0(\lambda)$ and $I(\lambda)$ are the incident and transmitted intensities at a wavelength λ, L, is the path length of the light, c, is the concentration of the absorbing species at point l, and $\sigma(\lambda)$ is the wavelength dependent absorption cross section of the gas species. The absorption cross-section refers to the probability of a molecule to absorb a photon as a function of photon wavelength. It is therefore a measure of the effective surface area of the molecule and is expressed in units of area.

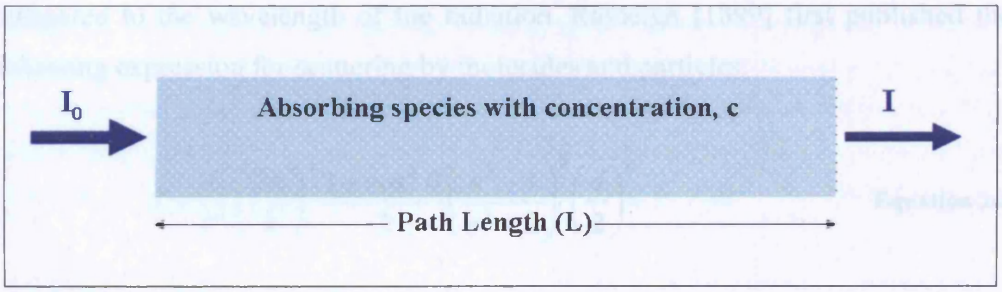

Figure 2-1: Absorption of radiation by a gas sample with concentration, c.

The optical density, τ of the absorbing species is defined as the logarithm of the ratio of the transmitted and incident intensities:

$$\tau = \ln\left(\frac{I_0(\lambda)}{I(\lambda)}\right) = L\,\sigma(\lambda)\,c \qquad \textbf{Equation 2-2}$$

In reality, there are a number of absorbing species in the atmosphere and the absorbing cross sections are not only wavelength dependent but temperature and pressure dependant too. Rayleigh and Mie scattering can also act like an absorption process by scattering radiation away from the line-of-sight of the detecting instrument. The scattered radiation may follow a multiple of paths through the atmosphere. In addition, the sensitivity of the instrument and the detector noise will also have an effect on the measured intensity.

2.2 Scattering

The scattering behaviour of radiation depends on the size of the molecules or particles relative to the wavelength of the radiation. The main forms of elastic scattering are Rayleigh and Mie scattering.

2.2.1 Rayleigh scattering

Rayleigh scattering occurs when the radius of the molecule or particle is small compared to the wavelength of the radiation. Rayleigh [1899] first published the following expression for scattering by molecules and particles:

$$I = \frac{I_0}{r^2}\left(\frac{2\pi}{\lambda}\right)^4 \frac{1+\cos^2\theta}{2}\left(\frac{n^2-1}{n^2+2}\right)^2\left(\frac{d}{2}\right)^6 \qquad \textbf{Equation 2-3}$$

where I and I_0 are the incident and scattered intensities, r is the distance to the particle, d is the diameter of the particle, n is the refractive index of air and θ is the scattering angle.

The intensity of the scattered radiation actually depends on the polarisation of the incident radiation. For radiation polarised perpendicular to the incident direction the scattering is isotropic. With plane polarised light however, the scattering is a function of $1+\cos^2\theta$. Integrating over the sphere surrounding the particle gives the Rayleigh scattering cross section (σ_R),

$$\sigma_R = \frac{2\pi^5}{3}\frac{d^6}{\lambda^4}\left(\frac{n^2-1}{n^2+2}\right)^2 \qquad \textbf{Equation 2-4}$$

The strong wavelength dependence Rayleigh scattering (λ^{-4}) results in the shorter blue wavelengths being scattered much more than the red end of the visible spectrum. It is this effect that gives the sky a blue appearance in a clean atmosphere.

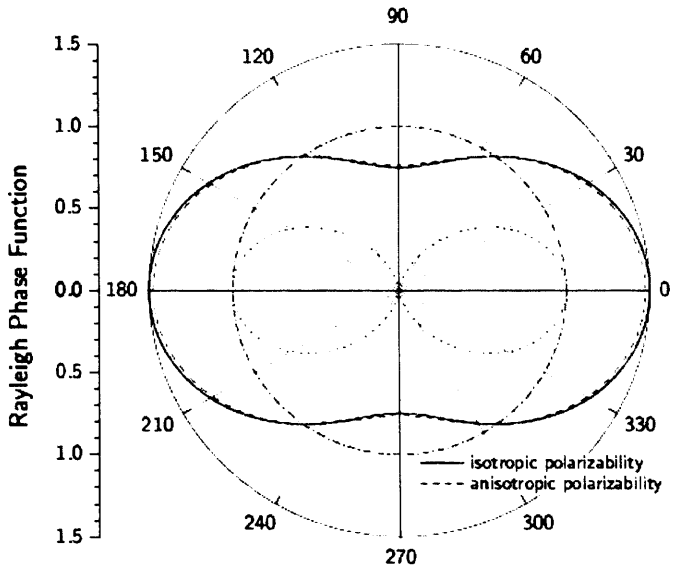

Figure 2-2: Polar diagram of the Rayleigh scattering phase function for isotropically unpolarised incident radiation, represented by a blue line. The dotted line shows the contribution of light polarised parallel to the incident plane, while the dot-dashed line shows the contribution from light polarised perpendicular to the incident plane. The red dashed line represents the Rayleigh scattering phase function for anistropically unpolarised incident radiation [Hönninger: *et al.*, 2002].

2.2.2 Mie scattering

Mie theory describes the solution to Maxwell's equations for spherical particles. First developed by Gustav Mie in 1908 [Mie, 1908] it defines the interaction of radiation with wavelengths comparable to or larger than the size of the particle. Calculation of the Mie scattering cross section is much more complicated than for the Rayleigh cross section, but it can be expressed simply as:

$$\sigma_m = \frac{\lambda^2}{2\pi}\sum_{n=0}^{\infty}(2n+1)\left(|a_n|^2 + |b_n|^2\right) \qquad \textbf{Equation 2-5}$$

where a_n and b_n are the Mie scattering coefficients, determined by the boundary conditions on the surface of the sphere.

The Mie phase function is different to the Rayleigh phase function in that the Mie scattering has weaker wavelength dependence but a large dependence on the size parameter,

$$\alpha = \frac{d\pi}{\lambda} \qquad \textbf{Equation 2-6}$$

The scattering of radiation is asymmetrical with most of the radiation scattering forwards, along the plane. The Rayleigh and Mie contributions to the absorption can be included in the Beer-Lambert law (Equation 2-1) to give

$$I(\lambda) = I_o(\lambda)\exp\left(\int_{l=0}^{l=L}\left(\sigma(\lambda)\ c(l)\right) + \varepsilon_m(\lambda) + \varepsilon_R(\lambda)\ dl\right) + A(\lambda) \qquad \textbf{Equation 2-7}$$

where, and ε_m and ε_R are the Mie and Rayleigh extinction coefficients, which are the products of the Mie and Rayleigh cross sections with the number density of air (n_{air}) and A is the attenuation function which describes the broad wavelength dependence transmission of the detector optics.

2.3 Differential Optical Absorption Spectroscopy

The application of DOAS to the measurements of atmospheric gases was first performed in the 1970's when Noxon [1975, 1979] used absorption spectroscopy to retrieve NO_2 in the troposphere and stratosphere with an instrument that measured scattered sunlight in the zenith direction. Since then the DOAS technique has been employed in a number of different applications. Platt *et al.* [1979] used DOAS to retrieve gas species using an artificial light source. The application of the Beer-

Lambert law to measurements in the atmosphere, in comparison to measurement in a laboratory is much more demanding as the absorption cannot be directly determined, owing to the lack of information on the intensity in the absence of the atmosphere (I_0). The DOAS technique was developed to circumvent the requirement for an absolute intensity measurement, by separating the broad and narrow band structures in the spectra.

Mie and Rayleigh scattering effects result in broadband structures in the measured spectra. Using the DOAS method the broad band structures are removed from the measured spectra and the absorption due to gases with structured cross sections can be isolated. The broad band structure can be approximated by fitting a polynomial of the appropriate order to the spectra. The order of the polynomial will depend on the width of the wavelength window used for the fitting and the width of the broadest gas absorption feature.

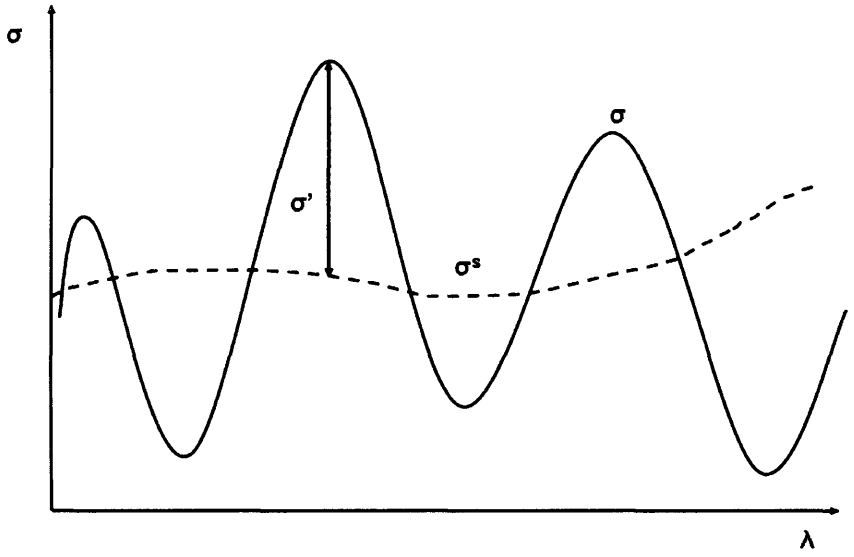

Figure 2-3: Example of the separation of the slow and rapidly varying components of the absorption cross section. The dashed line represents a polynomial fitted to the spectra. σ^s and σ' represent the slow and rapid varying components of the absorption cross section, respectively.

Figure 2-3 shows an example of how the absorption cross section can be separated into two components, one which varies slowly with wavelength (σ^s), mainly owing to scattering in the atmosphere and the attenuation function (A) and another which varies rapidly with wavelength (σ') owing to gases in the atmosphere; σ' is known as the differential cross section. A new quantity $I'_0(\lambda)$, can

be derived from the intensity of light in the absence of gases in the atmosphere by only applying the slowly varying cross section to the Beer-Lambert law.

$$I_0'(\lambda) = I_o(\lambda)\exp\left(\int_{l=0}^{l=L}\left(\sigma_i^s(\lambda)c_i(l)\right) + \varepsilon_m(\lambda) + \varepsilon_R(\lambda)dl\right) + A(\lambda) \quad \textbf{Equation 2-8}$$

where, *i* denotes the atmospheric gas species.

The derived incident intensity $I'_0(\lambda)$ and the differential cross section are then substituted for $I_0(\lambda)$ and σ in equation 2-7 to calculate the differential optical density τ' and the differential slant column density (DSCD) for each gas species, *i*.

$$\tau'(\lambda) = -\ln\frac{I(\lambda)}{I_0'(\lambda)} = L\sum_i c_i\sigma_i'(\lambda) \quad \textbf{Equation 2-9}$$

$$SCD_i = \int_0^L c_i dl = \frac{\tau_i'}{\sigma_i'} \quad \textbf{Equation 2-10}$$

$$DSCD_i = SCD_i - SCD_{i\,(ref)} \quad \textbf{Equation 2-11}$$

where, $SCD_{i\,(ref)}$ is the slant column density of the trace gas in the reference spectrum. For passive DOAS systems the reference spectrum is usually measured at solar noon by a zenith viewing telescope as this is the shortest path the light travels through the atmosphere, therefore, the influence from absorbing species can be minimised. The SCD is an integration of the trace gas concentration along the photon path length and can be expressed as the ratio of the differential optical density and the differential absorption cross section.

2.4 Spectral fitting algorithm

2.4.1 WinDOAS

Various techniques can be used to analyse DOAS spectra, most of these are based on least-squares fitting routines. Linear fitting methods involve minimising the difference between the measured and fitted functions. In the case of DOAS, cross sections, polynomials and other parameter such as stray light corrections are all fitted to the spectra simultaneously.

Owing to spectral misalignments and uncertainties in the wavelength calibration, a non-linear least squares fitting method is preferable for DOAS retrievals. In this project spectra are analysed using the WinDOAS software which was developed at the Belgian Institute for Space Aeronomy (BIRA) (Fayt and Roozendael, 2001). The WinDOAS software uses the Marquardt-Levenberg non-linear least-squares algorithm [Levenberg, 1944; Marquardt, 1963]. The WinDOAS software also incorporates a "shift" and "squeeze" of the spectra into the fitting routine which allows for slight adjustments to the spectra (see section 3.4.1) owing to differences in the wavelength calibration applied to the spectra. The Marquardt-Levenberg non-linear least-squares fitting algorithm is an iterative process where the parameters that are included in the fitting routine are adjusted slightly between each fitting process to reduce the residual between the fitted and measured differential optical density, until an optimum solution is obtained. The residual consists of random noise and features owing to errors and incorrect fitting of parameters. The residual can give an estimate of the quality of the fit hence, the detection limit of the instrument (see section 3.5.3).

2.4.2 Instrument line shape

The instrument line shape (ILS) of a spectrometer and detector is defined as the response of the instrument to a monochromatic signal at a given wavelength. To perform a DOAS fit, the absorption cross sections are convolved to the line shape of the instrument. The line shape can, however, become distorted, arising from the

variation across the focal plane of the instrument and effect of misalignments of the optical components and depends on the path length, grating, slit width wavelength and many other instrument properties. The ILS for a particular wavelength can be calculated by measuring spectra of a calibration light source such as a mercury lamp. The WinDOAS software enables a wavelength dependent slit function to be calculated by convolving the spectrum with a high resolution solar spectrum or theoretical spectrum and fitting a polynomial through individual sub windows.

In addition to the polynomial and absorption cross sections of trace gases, other parameters are included in the fitting routine, such as a Ring cross section and the application of filtering techniques, I_0 and temperature corrections. The additional parameters and applications are described in the following sections.

2.4.3 The Ring Effect and Raman scattering

Rotational Raman scattering has a strong effect on the measured spectra through filling in of the Fraunhofer lines [Fish and Jones, 1995]. Rotational Raman scattering is an inelastic scattering process which occurs when a photon interacts with a molecule, normally O_2 or N_2, in such a way that the frequency of the photons change, which can broaden the Fraunhofer structure. The effect is also present for strong gas absorptions lines. The amount of rotational Raman scattering increases as the path length through the atmosphere increases, therefore, the ratio of a twilight spectrum to the reference spectrum at noon does not fully remove the Fraunhofer structure. This is known as the Ring effect after Grainger and Ring [1962].

A number of methods have been proposed to compensate for the Ring effect, this is especially important when measuring weak absorbers with narrow band features, as they can be masked by the Ring structure. The Ring structure can be thought of as an absorber with a cross section. The WinDOAS software calculates Ring cross sections using the method described by Chance and Spur [1997]. Briefly, a reference high resolution solar spectrum [Kurucz, 1995] is convolved using calculated rotational Raman scattering cross sections to produce a rotational Raman spectrum. A Ring cross section is then calculated from the ratio of the rotational Raman spectrum to the reference solar spectrum. The Ring cross section is then convolved to the line shape of the instrument to produce a cross section that can be

included in the fitting routine. Figure 2-4 shows an example of a Ring cross section (bottom figure) calculated using the WinDOAS software from a convolved reference solar spectrum.

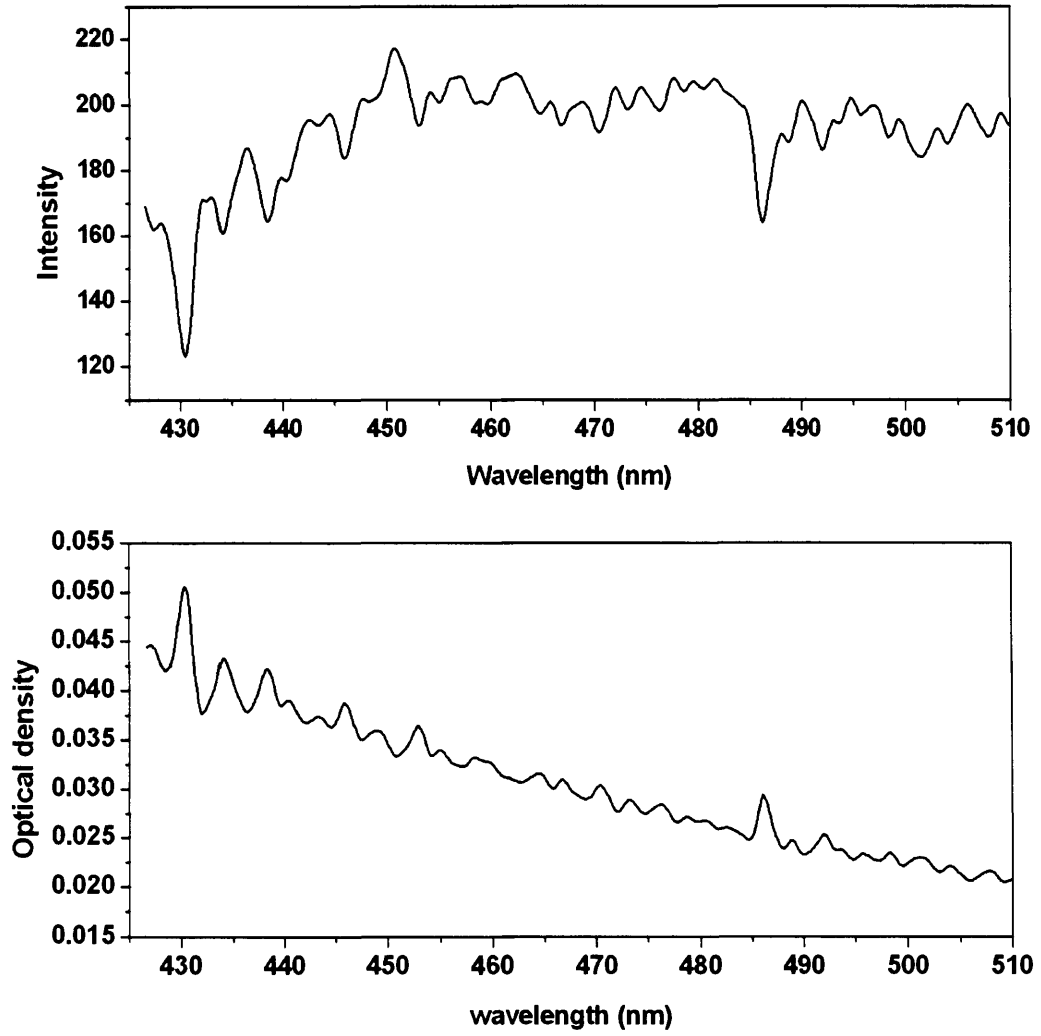

Figure 2-4: Top figure shows the reference solar spectrum [Kurucz, 1995] convoluted to the ILS of the CMAX-DOAS instrument. The bottom figure shows the Ring cross section calculated using the method described in the text.

A Ring spectrum may also be measured directly, from the polarization properties of light [Solomon *et al.*, 1987]. Rayleigh scattering is highly polarized, however, rotational Raman scattering is only weakly polarised. By measuring scattered spectra from different viewing angles the intensity of the Rayleigh and Raman scattering can be determined and the Ring intensity calculated as:

$$I_{Ring} = \frac{I_{Raman}}{I_{elastic}}$$ **Equation 2-12**

This method, however, may result an unknown amount of absorption in the retrievals as the light paths are different depending on the polarisation. Therefore, a calculated Ring spectrum will be used in this thesis.

2.4.4 The Solar I_0 effect

The solar spectrum is highly structured, owing to Fraunhofer lines. The DOAS technique attempts to remove the Fraunhofer structure by calculating the log ratio of two spectra at different solar zenith angles, leaving the absorption due to gases and scattering effects in the atmosphere. However, both spectra have been filtered by the ILS previous to applying the DOAS method; therefore, complete removal of the Fraunhofer structure is not possible resulting in errors when fitting the laboratory cross sections, which have been measured using a smooth light source. The errors arising from the Fraunhofer structure are known as the 'I_0 effect' [Platt *et al.*, 1997].

A correction for the I_0 effect can be performed using a reference high resolution solar spectrum (I_0) which is convolved with the ILS. An effective absorption spectrum ($I_{modelled}$) is then derived using the high resolution solar spectrum and absorption cross section both convolved with the ILS. A correction to the cross section ($\sigma_{corrected}$) can now be derived:

$$\sigma_{corrected}(\lambda, S) = \frac{-\ln\left(\frac{I_{modelled}(\lambda, S)}{I_0(\lambda)}\right)}{SCD}$$ **Equation 2-13**

where SCD is an assumed slant column density for the absorber.

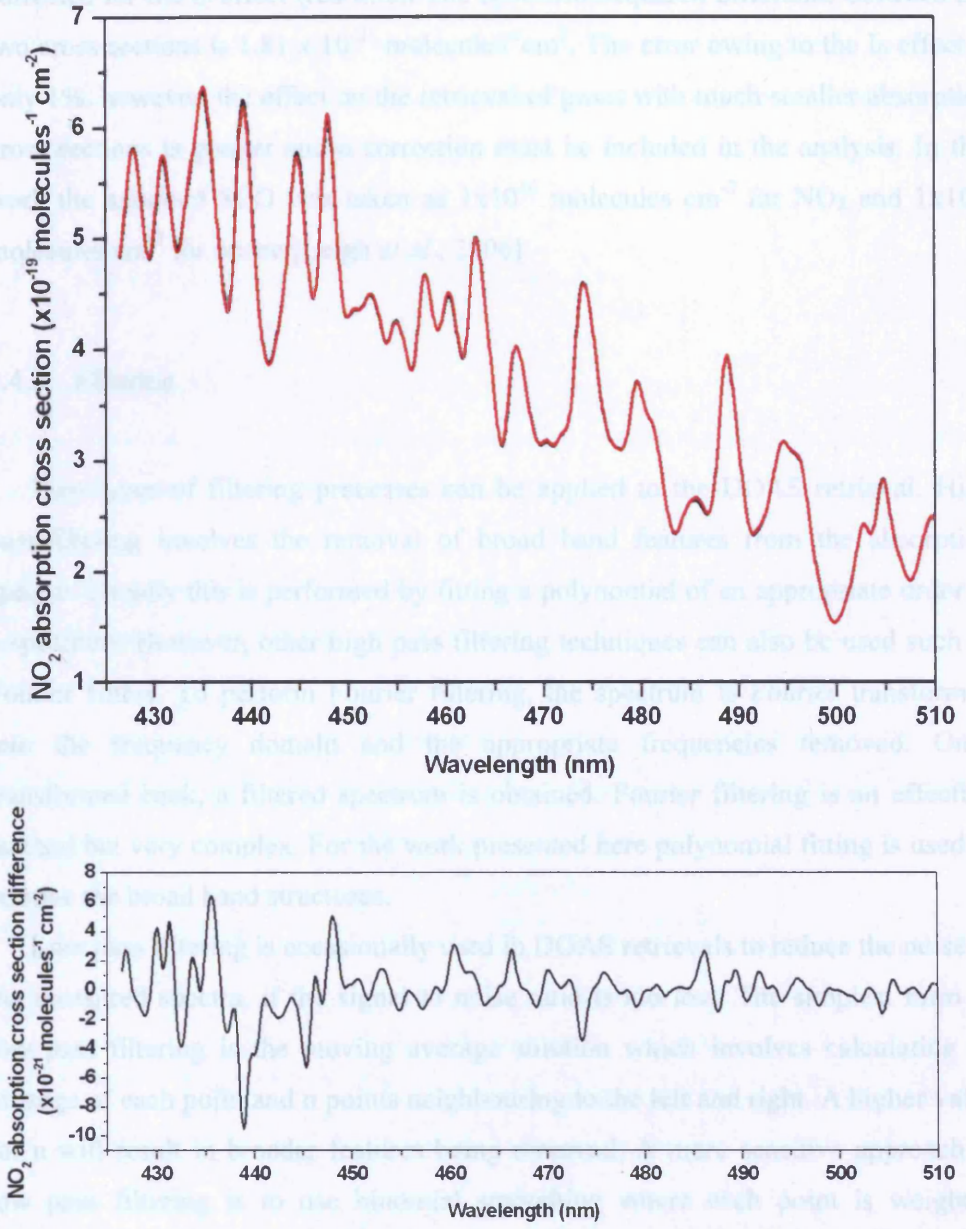

Figure 2-5: NO_2 absorption cross section with an I_0 correction applied (red line) and without an I_0 correction applied (black line). The bottom figure shows the difference between the two cross sections.

The value for the SCD is usually taken as the typical SCD for that particular absorber in the local atmosphere. For many atmospheric absorbers the I_0 effect is weak and can be neglected, but for strong absorbers like NO_2 and ozone the I_0 effect can have an impact on the retrieval of weak absorbers. In Figure 2-5, the absorption cross section for NO_2 is plotted along with the absorption cross section that has been

corrected for the I_0 effect (red line). The root-mean-squared difference between the two cross sections is 1.81 x 10^{-21} molecules^{-1}cm^2. The error owing to the I_0 effect is only 1%, however, the effect on the retrieval of gases with much smaller absorption cross sections is greater and a correction must be included in the analysis. In this work the assumed SCD was taken as 1x10^{16} molecules cm^{-2} for NO_2 and 1x10^{20} molecules cm^{-2} for ozone [Leigh *et al.*, 2006].

2.4.5 Filtering

Two types of filtering processes can be applied to the DOAS retrieval. High pass-filtering involves the removal of broad band features from the absorption spectra. Usually this is performed by fitting a polynomial of an appropriate order to a spectrum. However, other high pass filtering techniques can also be used such as Fourier filters. To perform Fourier filtering, the spectrum is Fourier transformed into the frequency domain and the appropriate frequencies removed. Once transformed back, a filtered spectrum is obtained. Fourier filtering is an effective method but very complex. For the work presented here polynomial fitting is used to remove the broad band structures.

Low pass filtering is occasionally used in DOAS retrievals to reduce the noise in the measured spectra, if the signal to noise ratio is too low. The simplest form of low pass filtering is the moving average solution which involves calculating an average of each point and n points neighbouring to the left and right. A higher value for n will result in broader features being removed. A more sensitive approach to low pass filtering is to use binomial smoothing where each point is weighted according to the binomial distribution; therefore, those values that are further away from the original point contribute less to the average.

2.5 Trace gas cross sections

In this section the trace gas absorption cross sections used in the DOAS retrieval are presented. Where appropriate, cross sections measured at different temperatures

are included in the DOAS fitting routine and orthogonalised to each other to correct for the temperature dependency of absorption species. This is important as residual effects resulting from using a cross section measured at a different temperature can mask the presence of other species.

2.5.1 Retrieval of gases in urban boundary layer

Within the urban boundary layer the main target species for this work are NO_2 and O_4. However, other species are also included in the analysis. The cross sections used in the fitting routine are summarised in Table 2-1.

Table 2-1: A summary of the absorption cross sections used in the urban boundary layer retrievals.

Cross Section	**Temp. (K)**	**Convolution**	**Reference**
Ring	-	Wavelength dependent Gaussian	WinDOAS (calculated)
NO_2	220	Wavelength dependent Gaussian ,I_0 correction ($5x10^{16}$ mol/cm^2)	Vandaele *et al.*, 1998
NO_2	294	Wavelength dependent Gaussian, I_0 correction ($5x10^{16}$ mol/cm^2)	Vandaele *et al.*, 1998
O_3	223	Wavelength dependent Gaussian , I_0 correction ($1x10^{20}$ mol/cm^2)	Bogumil *et al.*, 2003
O_4	296	Wavelength dependent Gaussian	Greenblatt *et al.*,1990 (with Burkholder - 0.2nm shift)
H_2O	273	Wavelength dependent Gaussian	Hitran Database (Rothman *et al.*, 2003)

2.5.1.1 NO_2

In the UV/visible region the NO_2 cross section is composed of broad and narrow band absorption structures. A spectral fitting window in the wavelength range 431 to 508 nm was chosen for the retrieval of NO_2 as the ozone absorption features in this window are small; therefore, spectral interference effects are reduced.

The temperature dependence of NO_2 in this region is significant, as show in Figure 2-6. Therefore, two temperature dependent cross sections were included for the NO_2 retrieval, one at 294 K and the other at 220 K to represent the tropospheric and colder, stratospheric conditions.

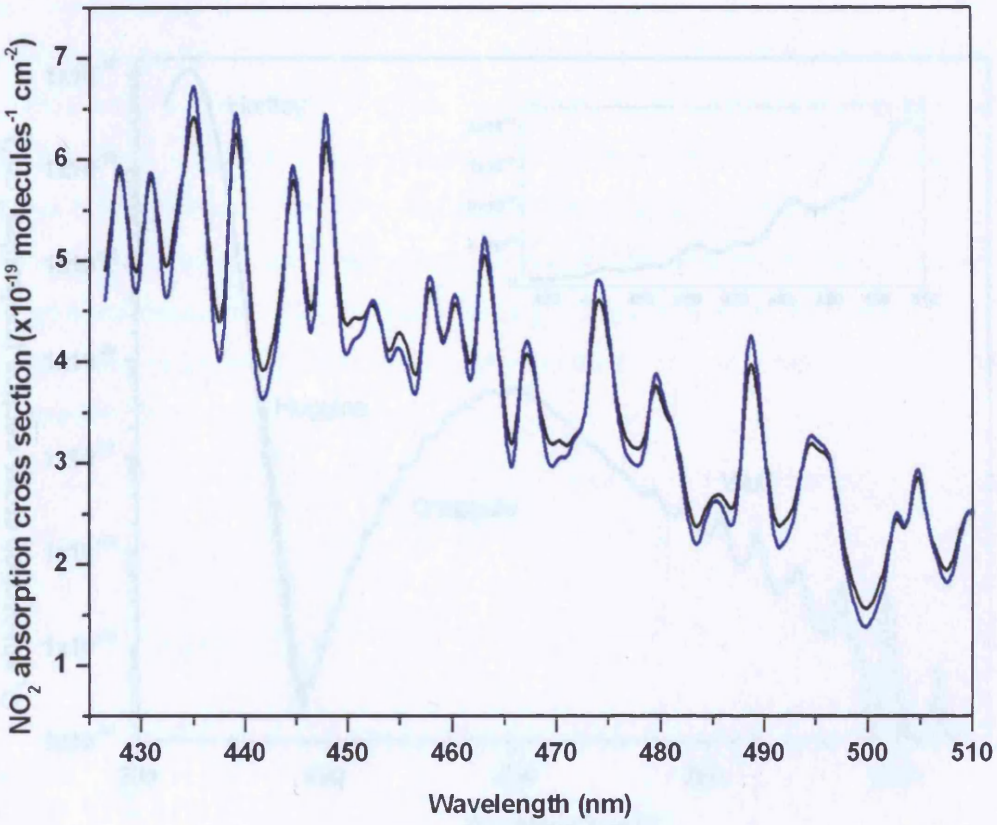

Figure 2-6: NO_2 absorption cross sections measured by Vandaele *et al.*, [1998] at 294 K (black line) and 220 K (blue line).

2.5.1.2 O_3

The O_3 absorption cross section is shown in Figure 2-7. The strongest feature is a broad band structure from the Hartley band observed in the UV. For the retrievals performed in this thesis the narrow band structures in the Huggins and Chappuis bands are the most significant. The majority of ozone absorption by sunlight occurs in the stratosphere, owing to the high concentration in the ozone layer. A separation between the tropospheric and stratospheric ozone absorption is often performed by using temperature dependent cross-sections Therefore, an absorption cross section of 223 K was used in the analysis to represent the warmer tropospheric conditions.

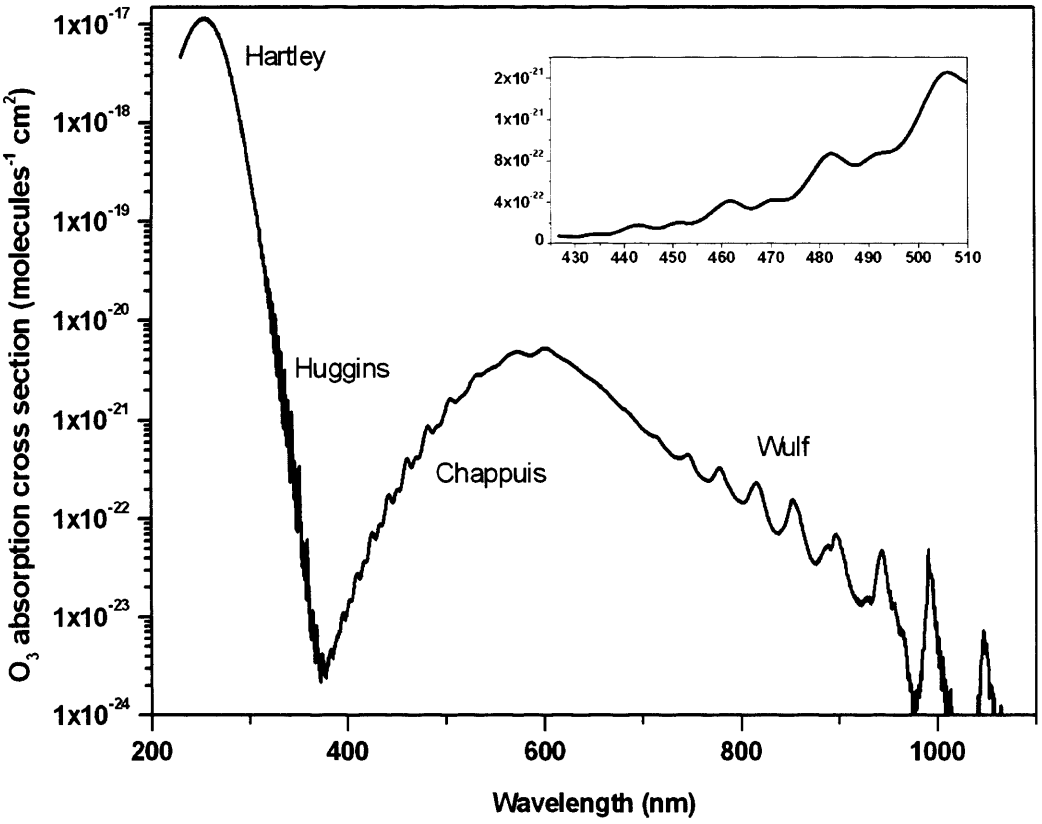

Figure 2-7: O_3 absorption cross section measured by Bogumil *et al.*, [2003] at 223 K. The inset shows the Chappius bands used in the retrieval between 431 to 508 nm.

2.5.1.3 O_4

The O_4 absorption bands in the UV and visible spectrum arise from the collisional complex of molecular oxygen (O_2) [Perner and Platt, 1980]. The concentration of O_4 is proportional to the square of the concentration of O_2 and both have a small dependence on atmospheric pressure. The vertical profile of O_4 in the atmosphere is well known [Pfeilsticker *et al.*, 1996]. Therefore, the retrieval of O_4 can give information on the radiative transport through the atmosphere, in particular, the detection of cloud and aerosol loads (see Chapter 4).

The O_4 absorption features are relatively broad with widths of a few nanometres and are easily resolved with DOAS instruments. Figure 2-8 shows the O_4 cross section used in this thesis. In a study by Pfeilsticker *et al.* (2001), O_4 absorption profiles were inferred from a direct sun DOAS instrument onboard a balloon gondola, for a temperature range between 203 K and 250 K and an atmospheric pressure from 500 hPa to 40 hPa. The results show that the O_4 band shapes do not change with pressure and temperature; however, the absorption intensities are temperature dependent. In this thesis, a single cross section at a temperature of 296K is used in the analysis; therefore, errors in the O_4 retrieval may arise from the temperature dependence.

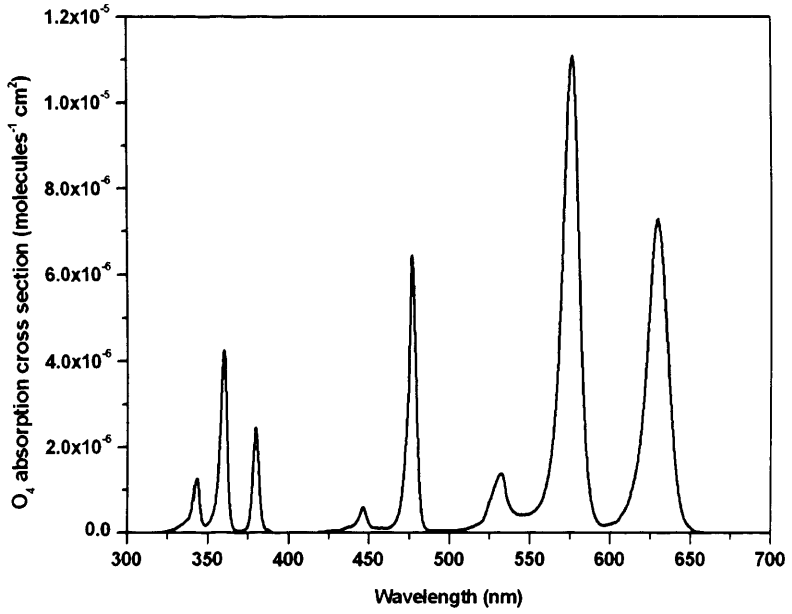

Figure 2-8: O_4 absorption cross section at 296 K measured by Greenblatt *et al.* [1990] with a shift of 0.2 nm.

The DSCD of O_4 derived from the spectral analysis is not directly associated with the concentration of O_4 in the atmosphere as the equilibrium constant between O_2-O_2 and O_4 is not known. The concentrations of both species is proportional to the square of the O_2 concentration; therefore, the "O_4 DSCD" is given instead as the integrated quadratic O_2 concentration, with units of molecules^2 cm^{-5} [Greenblatt *et al.*, 1990]

2.5.1.4 H_2O

Water vapour is a weak absorber in the visible wavelength region and only has a small effect on the spectral retrieval of the target gas species. However, it is still included in the fitting routines here for the visible region to remove any structure in the residual. The cross section of water vapour was obtained from the HITRAN data base [Rothman *et. al.*, 2003].

2.5.2 Retrieval of gases in the marine boundary layer

When performing measurements in the marine boundary layer (MBL) the main target species were IO and BrO. In addition to the cross sections listed in Table 2-2, the halogen species were included in the analysis (see Table 2-2). The absorption cross section of OClO was also included when retrieving BrO in the UV region, to remove any remaining structure from the residual.

Table 2-2: A summary of the cross sections used in the marine boundary layer retrievals, in addition to the cross sections in Table 1.

Cross Section	Temp. (K)	Convolution	Reference
IO	298	Wavelength dependent Gaussian	Spietz *et al.*, 2005
BrO	298	Wavelength dependent Gaussian	Wilmouth *et al.*, 1999
OClO	213	Wavelength dependent Gaussian	Kromminga *et al.*, 2003

2.5.2.1 IO and BrO

For the retrieval of IO a wavelength window between 434 and 459 nm has been chosen as it includes three strong absorption bands of IO at 436, 445 and 456 nm (see Figure 2-9). There are also four more IO bands below this wavelength region; however, the strong Fraunhofer structure between 425 and 433 nm may result in errors in the retrieval if the Ring spectrum is not fully resolved. Therefore, a window at larger wavelengths is used to avoid the Fraunhofer structure.

BrO absorption occurs in the UV wavelength region and a window between 341 to 364 nm is used to retrieve BrO in the marine boundary layer. The strongest absorption features occur at lower wavelengths, however, the DOAS instrument used to retrieve trace gases in this project is a passive instrument which uses sunlight as a light source, therefore, the signal is very low when observing in the UV region.

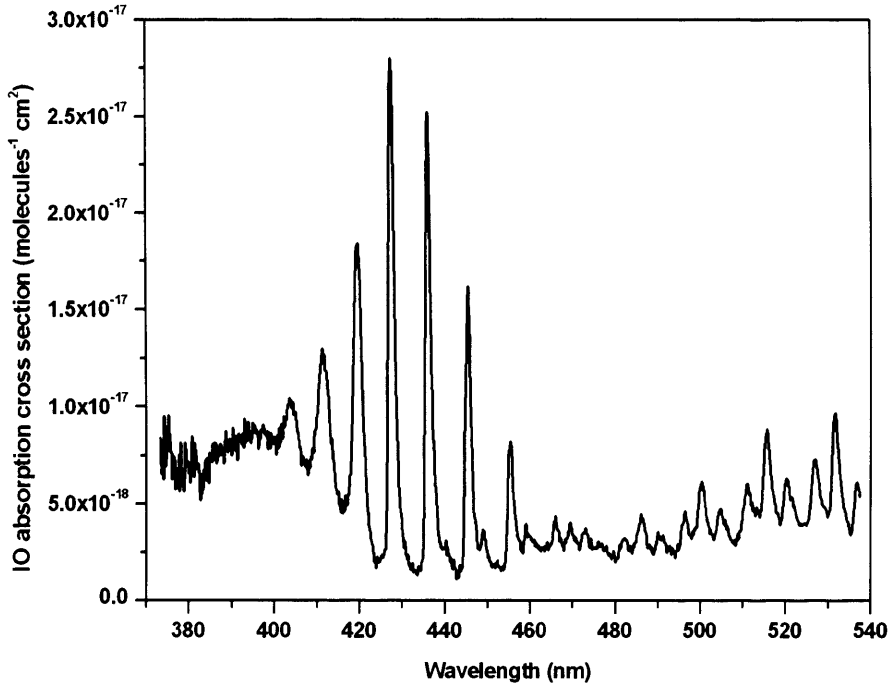

Figure 2-9: IO absorption cross section measured by Spietz [2005].

2.5.2.1 IO and BrO

For the retrieval of IO a wavelength window between 434 and 459 nm has been chosen as it includes three strong absorption bands of IO at 436, 445 and 456 nm (see Figure 2-9). There are also four more IO bands below this wavelength region; however, the strong Fraunhofer structure between 425 and 433 nm may result in errors in the retrieval if the Ring spectrum is not fully resolved. Therefore, a window at larger wavelengths is used to avoid the Fraunhofer structure.

BrO absorption occurs in the UV wavelength region and a window between 341 to 364 nm is used to retrieve BrO in the marine boundary layer. The strongest absorption features occur at lower wavelengths, however, the DOAS instrument used to retrieve trace gases in this project is a passive instrument which uses sunlight as a light source, therefore, the signal is very low when observing in the UV region.

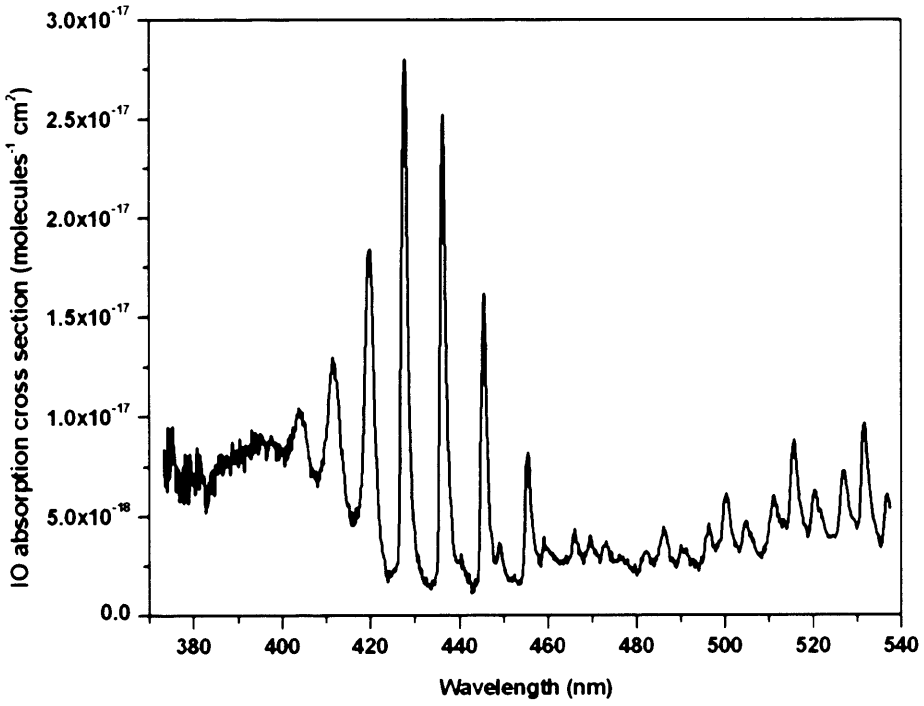

Figure 2-9: IO absorption cross section measured by Spietz [2005].

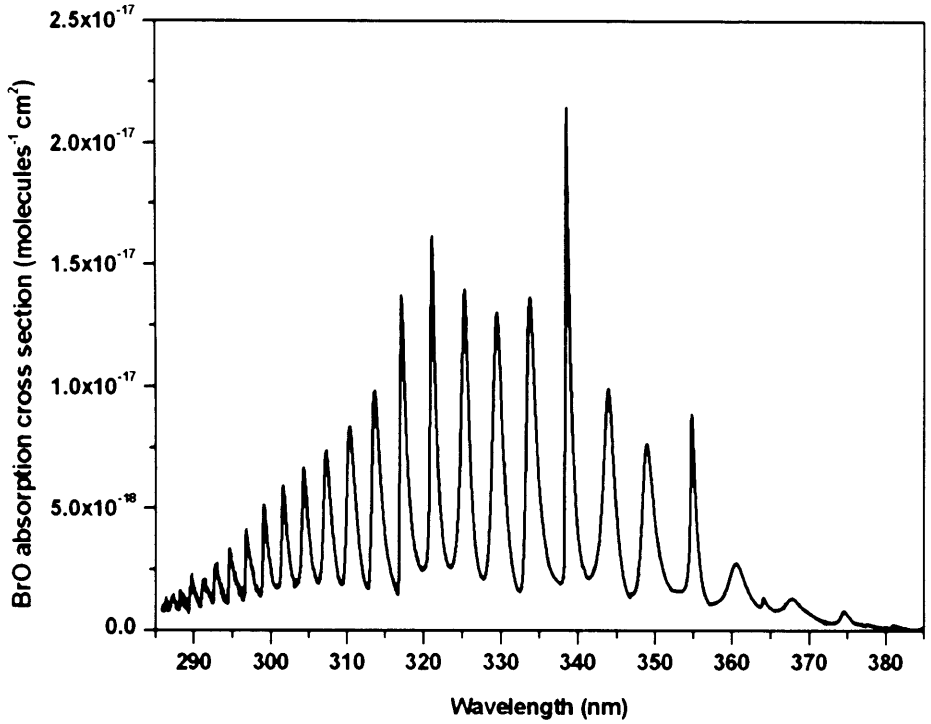

Figure 2-10: BrO absorption cross section measured by Wilmouth *et al.* [1999]

2.6 Radiative transfer

The DOAS retrieval described in section 2.3, for scattered sunlight DOAS instruments, yields differential slant column densities (DSCDs) for each absorber included in the fitting routine. These DSCDs give a measurement of the amount of increased absorption compared to that measured in the reference spectrum, for photon path lengths through the atmosphere. In order to perform comparisons between measurements at different SZA and viewing geometries and also to model data, it is more convenient to express the values in terms of the vertical column density (VCD), which is defined as the trace gas concentration integrated along a vertical path through the atmosphere. The vertical column density can also be expressed as the ratio of the DSCD to the air mass factor (AMF).

$$VCD = \frac{DSCD}{AMF}$$ **Equation 2-14**

In order to perform this process it is required to fully understand the path the radiation has taken through the atmosphere. The AMF describes the effective absorption path of the light and depends on the distribution of the particular atmospheric gas and also the solar zenith angle, cloud cover, aerosol properties and surface albedo.

2.6.1 Air Mass Factors

AMFs may be calculated using a simple geometric approach if a single scattering approximation is employed [Hönninger *et al.*, 2004a].

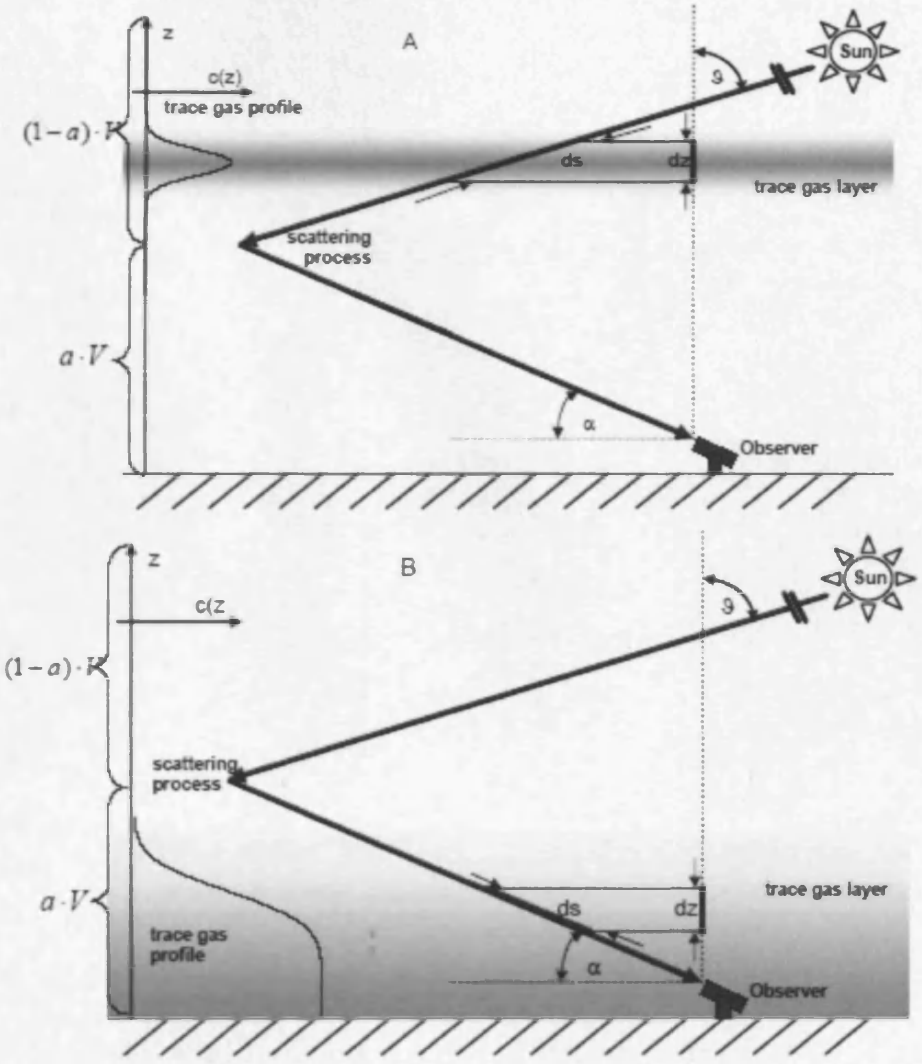

Figure 2-11: Single scattering approximation for a trace gas a) above the scattering point and b) below the scattering point. [*Honninger et al.*, 2004].

The AMFs for the stratosphere, where the absorber is above the scattering altitude, is mainly dependent on the SZA, owing to the increase in path length through the stratosphere as the SZA becomes larger. The AMF for a stratospheric absorber can, therefore, be expressed as 1/cos (φ), where φ is the SZA. For absorbers below the scattering altitude, the AMF is dependent on the elevation angle, as the sensitivity to tropospheric absorbers increases with lower elevation angles owing to an increase in photon path length within the troposphere. AMFs for tropospheric absorbers, using a single scattering approximation can be defined as 1/sin (α), where α is the elevation angle of the viewing telescope. This method can only be taken as an approximation of the AMFs. For a precise calculation, multiple scattering must be taken into account [Perliski and Solomon, 1993] and is usually performed with a radiative transfer model (RTM).

2.6.2 Radiative transfer models

To calculate a precise AMF for an absorber in the atmosphere, multiple scattering of photons in the atmosphere can be modelled with a RTM. At high sun the Earth can be treated as a plane-parallel scattering layer, however, for large SZAs a correction for the sphericity of the Earth, must be applied. This can be in the form of a pseudo-spherical correction, where the direct radiation is corrected for sphericity of the Earth, but the multiple scattering approximation is applied in plane-parallel only, or a full-spherical correction can be applied.

There are many radiative transfer models that can be used to calculate AMFs for DOAS observations. In a study by Hendrick *et al.*, [2006] an intercomparison was performed between six RTMs for interpreting zenith sky and MAX-DOAS observations. SCD simulations for BrO, NO_2 and OClO in the zenith sky and NO_2 and BrO for the multi-axis geometries were performed using identical settings for each RTM. The results from the study show that the model agrees well, especially for zenith sky, when the SZA is below 90° . At higher SZAs, the differences between the models become much larger, with discrepancies between 2 and 14%. For multi-axis observations the agreement is also good, with SCDs of NO_2 and BrO only differing by 5% or less for the SZAs and elevations angles investigated. More recently, a comparison exercise was performed between nine RTMs from various

research groups [Wagner *et al.*, 2007]. A number of different scenarios were performed in each comparison exercise, such as wavelength changes and aerosol loads. The RTM datasets agreed within 5% in most cases. The largest differences were observed when the path length along the line-of-site was very large, between those models which include full-spherical geometry and those using plane-parallel geometries.

2.6.3 AMF dependence

The calculation of AMF's from RTMs for retrievals from space and ground based instruments are very sensitive to the input parameters, such as solar azimuth, multiple scattering, and aerosol and trace gas profiles. In a study by Wittrock *et al.* [2004] the sensitivity of O_4 retrievals from a DOAS instruments using AMFs calculated by the RTM SCIATRAN were assessed. The results show that multiple scattering is an important feature in RTMs; however, refraction in the atmosphere has less of an effect and is considered trivial. The relative azimuth between the instrument viewing direction and the sun has a large effect on the AMFs, in particular at high elevation angles and small relative azimuth angles. The study compared AMFs calculated with surface albedo values of 0.9 and 0.01 and compared these to AMFs with an albedo value of 0.5. The vertical columns of O_4 are underestimated with an albedo of 0.01 and overestimated for a too high albedo when observing at a low elevation angle of 3 or a higher elevation at 18 degrees. The albedo has the strongest effect when the instrument is pointing directly towards the sun (see Figure 2-12)

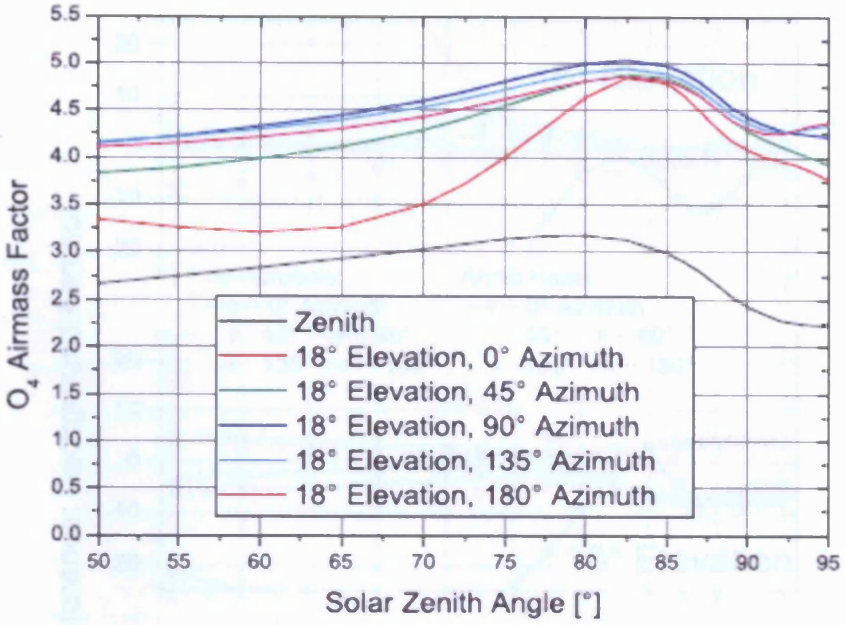

Figure 2-12: AMFs for O_4 calculated with SCIATRAN for an elevation angle of 18 degrees and various azimuth angles. The strongest effect is observed when pointing directly toward the sun [Wittrock *et al.*, 2004].

The distribution and type of aerosols in the atmosphere is important in DOAS retrievals. An increase in aerosol extinction does not have a large effect on the zenith view, but will reduce the path length of the light when viewing at lower elevation angles. Figure 2-13 demonstrates the importance of using the correct aerosol profile when calculating AMFs. The results show the error in retrieved O_4 VCD for different aerosols scenarios in the AMF calculations. The aerosol extinction profile was changed from a scenario with no aerosols to a background level and finally to an arctic haze event. In the lowest elevation angle the light path decreases with increasing extinction and can lead to an overestimation in the retrieved trace gas vertical column. The effect decreases as the elevation angle increases. The azimuth effects play a part here too as the sensitivity of aerosols increases when the instrument is pointing towards the sun.

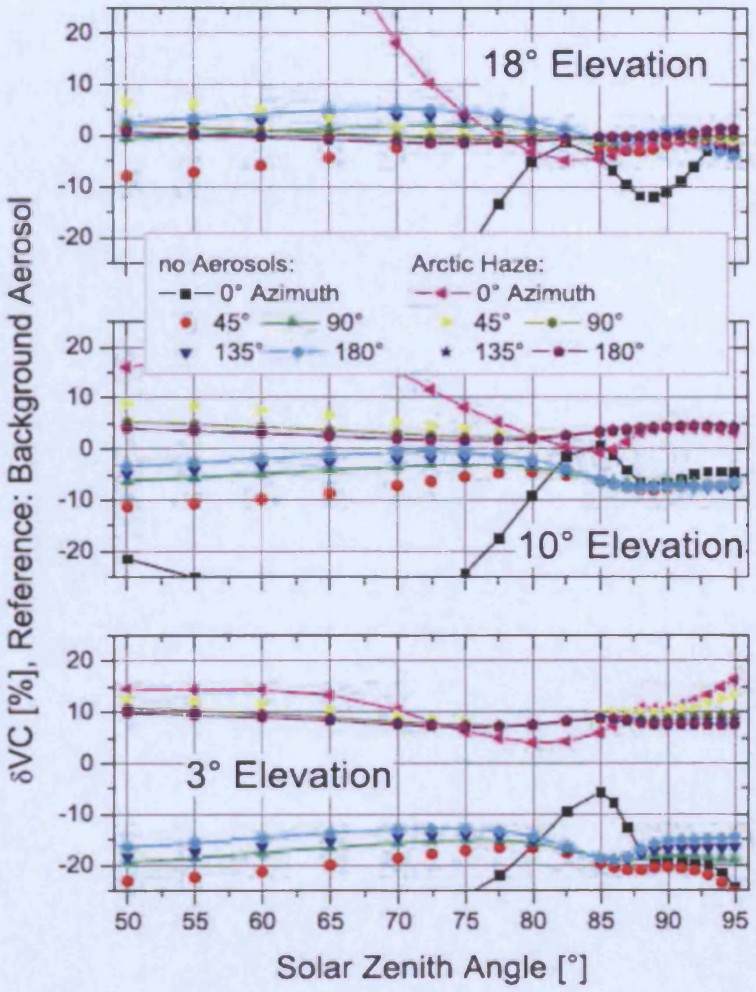

Figure 2-13: The error on O_4 VCDs owing to the difference in aerosols extinction profiles input into the SCIATRAN AMF calculations for elevation angles of 18, 10 and 3 degrees and various azimuth angles [Wittrock *et al.*, 2004].

In this thesis, the SCIATRAN RTM, which includes a spherical treatment of single scattered light with multiple scattering initialized by a pseudo-spherical model, is used to perform calculations of AMFs for the target gas species. The advantage of this technique over others is the reduced computational time. A summary of the main features of SCIATRAN are given in Section 4.4.2.

2.7 Summary

In this chapter an overview of absorption spectroscopy was given, in particular the application of the DOAS technique to the retrieval of gases in the atmosphere. DOAS instruments are very useful when measuring gases within the atmosphere as simultaneous measurements can be performed for many gases with highly structured absorption cross sections, within a chosen wavelength window. The DOAS method reduces measurement time and allows an analysis of the chemistry with a high temporal resolution.

An overview of the target trace gases in this thesis is given, along with a description of the absorption cross sections applied in the DOAS fitting routine, to retrieve DSCDs of each gas. Converting the slant columns to vertical columns requires knowledge of the photon path through the atmosphere. The last section of this chapter describes the calculation of AMFs used to determine the radiative transfer, using a geometrical approach and by modelling with RTMs, including a comparison of RTMs currently used for DOAS retrievals.

Chapter 3

The CMAX-DOAS instrument

The measurements presented in this thesis have been performed with the Leicester based UV/visible Concurrent Multi-Axis DOAS (CMAX-DOAS) instrument. In this chapter an overview of the different types of DOAS instruments will be given and the advantages of CMAX-DOAS instruments discussed. During the research project a number of the instrument components were altered. Here, the initial set up will be described in detail and the alterations will be highlighted in the appropriate chapters.

3.1 Introduction to DOAS instruments

As discussed in the previous chapter, DOAS instruments have been employed for many years to perform retrievals of trace gases in the atmosphere. DOAS instruments can be classified into two different types. Active instruments, such as Long Path DOAS (LP-DOAS), use artificial light sources and can perform localised measurements of trace gases in the lower troposphere (see section 6.6). Passive DOAS instruments, however, use the sun or moon as a light source, either directly or via scattered light, in the case of the sun.

Scattered light DOAS instruments initially comprised of a ground based instrument with a single telescope directed towards the zenith. UV/visible measurements of scattered light were used to retrieve atmospheric column measurements of many trace gases in the atmosphere, such as O_3 [Platt 1994, Solomon *et al.*, 1987], NO_2 [Noxon 1975; 1979; Van Roozendael *et al.*, 1994], BrO [Hausmann and Platt 1994; Van Roozendael *et al.*, 2002; Aliwell *et al.*, 2002], IO

[Alicke *et al.*, 1999; Wittock *et al.*, 2000; Frieβ *et al.*, 2002] and OClO [Solomon *et al.*,1988 Tørnkvist *et al.*, 2002].

Measurements performed by zenith scattered light DOAS are sensitive to stratospheric absorbers. More recently, however, the development of DOAS instruments incorporating "off-axis" telescopes pointing towards the horizon has enabled monitoring of tropospheric gas species and provided information for the distinction between tropospheric and stratospheric column measurements.

Off-axis DOAS is essentially a version of zenith scattered light DOAS. A telescope pointing towards the zenith will observe gas absorption indirectly via the scattering of sunlight through different layers of the atmosphere. As the sun moves across the sky the solar zenith angle (φ), SZA and the solar azimuth angle (ζ), SAA, will change, which will alter the path that the solar radiation takes as it passes through the atmosphere, with the minimum path length occurring at solar noon. The off-axis geometries increase the sensitivity of the instrument to absorption in the troposphere due to the increase in photon path lengths at lower elevations angles. The stratospheric component to the absorption is comparable for each elevation angle and the zenith view, therefore, can be distinguished from the tropospheric signal. In addition to retrieving concentrations of gases in the troposphere MAX-DOAS instruments may also provide information on their vertical profiles.

Sanders *et al.* [1993] first introduced off-axis measurements when observing OClO over Antarctica during twilight. The off-axis technique has been advanced by several groups over the last few years to include scanning telescopes that can switch between several viewing geometries and/or multiple telescopes set to different angles. An overview of the measurements currently performed by ground based MAX-DOAS systems is shown in Table 3-1.

A MAX-DOAS instrument consisting of a scanning telescope (S) has the advantage of using only a single optical set-up. However, the telescope needs to be re-positioned to different elevation angles for each measurement. MAX-DOAS instruments with multiple telescopes (M), also known as CMAX-DOAS instruments, image concurrently onto different sections of the detector for each view. Therefore, they remove the time scanning delay and can retrieve gas species with very good temporal resolution. With the concurrent system, attention does

need to be paid to the variability of the line shape and wavelength calibration between the individual views.

Table 3-1: Overview of ground based MAX-DOAS instruments (adapted from Hönninger *et al.*, 2004a)

Measurement	**No. of axes**	**References**
Trace Gases	2-4,M	Löwe *et al.* [2002], Oetjen *et al.*, [2002], Heckel [2003], Wittrock *et al.* [2003]
Tropospheric BrO	4,S	Hönninger and Platt [2002], Hönninger *et al.* [2004c]
NO_2 plumes	8, M	von Friedeburg (2003), Leigh *et al.*, [2006]
BrO in MBL	6,S/M	Leser *et al.*, [2003], Bossmeyer [2002]
BrO, SO_2, volcanoes	10,S	Bobrowski *et al.* [2003]
BrO, Salt lakes	4,S	Hönninger *et al.* [2004b]
Gas and aerosols	5,S	Sinreich *et al.* [2005], [2006]
Tropospheric NO_2	5,M	Leigh *et al.* [2006], [2007]
Tropospheric and Stratospheric BrO	5,S	Theys *et al.* [2007]
HCHO	5,S	Heckel *et al.*, [2004]
Aerosols	6,S	Irie *et al.*, [2007]

S=Scan, M=Multiple telescopes

The instrument employed in this thesis is a CMAX-DOAS system [Leigh *et al.* 2006] with five 5 cm diameter telescopes positioned at elevation angles of 90° (zenith), 15°, 10°, 5° and 2°, in normal operation mode The use of a single charge coupled device (CCD) with an imaging spectrometer and a multi-track fibre-optic cable, gives an instrument that offers temporal resolution of a minute or less.

3.2 The CMAX- DOAS setup

The CMAX-DOAS instrument was initially set up on the roof of the Space Research Centre at the University of Leicester. The measurement site is located south of the city, with the telescopes directed in a northerly direction towards the city centre. The location of the site is ideal in that it allows the measurement of trace gases over an urban polluted region.

The CMAX-DOAS instrument has previously been assembled and tested during the NAMBLEX (North Atlantic Marine Boundary Layer Experiment) in Ireland in 2002 and more recently formed part of the NDSC inter-comparison campaign in Andøya, Norway in 2003. More recently the instrument has been used for long term measurement of stratospheric ozone and tropospheric NO_2 over Leicester [Leigh *et al.* 2006; 2007].

3.2.1 The Head Unit

The head unit of the CMAX-DOAS instrument is designed to house the viewing telescopes in a stable position and to protect them from atmospheric conditions which can effect the retrievals, such as condensed water on the optics. A container of silica gel desiccant is placed inside the head unit and during the winter, heating pads were wrapped around the frame and telescopes to avoid freezing of optical parts. The head unit is attached to a mast that can be moved up and down *via* a pulley system to allow access to the telescopes.

A schematic of the head unit is shown in Figure 3-1. Each telescope is made from aluminium alloy tubes with a diameter of 5 cm. To ensure only the radiation from each view is directed onto the telescope and there are no stray light issues, every part of the head unit is black anodised and an alloy tube is placed between the entrance window and the telescope.

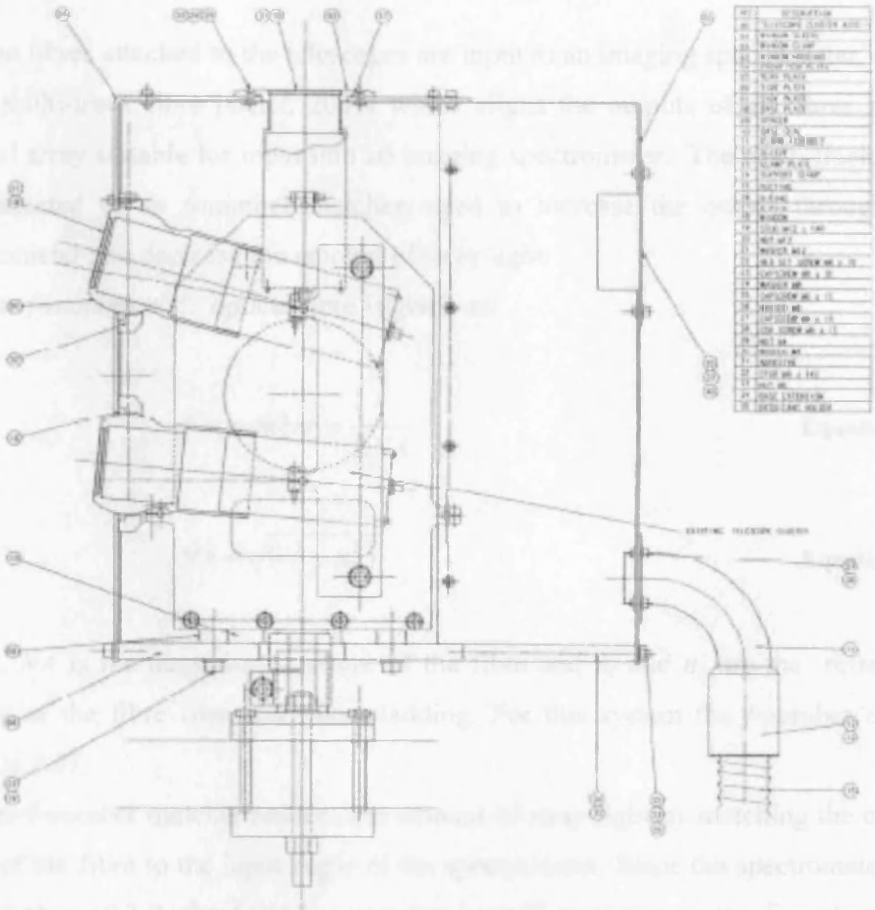

Figure 3-1: Schematic diagram of the head unit housing the viewing telescopes of the CMAX-DOAS instrument (Image courtesy of Barry Towell, University of Leicester).

Each telescope is connected to a 200 μm diameter fibre optic cable. The field of view of the telescopes (θ) is given by:

$$\theta = 2\arcsin\left(\frac{d}{2f}\right) \approx 0.12° \qquad \textbf{Equation 3-1}$$

where, d is the diameter of the fibre entrance (d = 200μm) and f is the focal length of the lens (f=100 mm).

3.2.2 The spectrometer

The fibres attached to the telescopes are input to an imaging spectrometer *via* an Oriel multi-track fibre [Oriel, 2001] which aligns the outputs of all fibres into a vertical array suitable for input into an imaging spectrometer. The multi-track fibre is connected to an *f*-number matcher, used to increase the output through the spectrometer and decrease the amount of stray light.

The *f*-number of an optical fibre is given as:

$$f-number = \frac{1}{2NA} \qquad \textbf{Equation 3-2}$$

$$NA = \sqrt{\left(n_1^2 - n_2^2\right)} \qquad \textbf{Equation 3-3}$$

where, NA is the numerical aperture of the fibre and n_1 and n_2 are the refractive indices of the fibre core and fibre cladding. For this system the *f*-number of the fibres is 2.27.

The f-number matcher reduces the amount of stray light by matching the output angle of the fibre to the input angle of the spectrometer. Since the spectrometer has an *f*-number of 3.9, the *f*-number matcher is used to converge the *f*-numbers and maintain the vertical separation of each fibre in the spectrometer.

The imaging spectrometer is a Czerny-Turner design (Oriel MS257™) [Oriel, 2001] with a multiple grating turret which can hold up to four gratings. A schematic diagram of the spectrometer is shown in Figure 3-2. The optics of the spectrometer are especially designed to enable many sources to be simultaneously diffracted and resolved as separate images on a CCD, which makes it suitable for use in CMAX-DOAS systems. Table A-1 in the Appendix lists the specifications of the three gratings incorporated into the spectrometer. The light, transmitted from the multi-track fibre is incident onto a plane-parallel mirror and directed towards a collimating mirror. The collimating mirror focuses the light onto a diffraction grating. A second collimating mirror then focuses the dispersed light from the grating onto the detector.

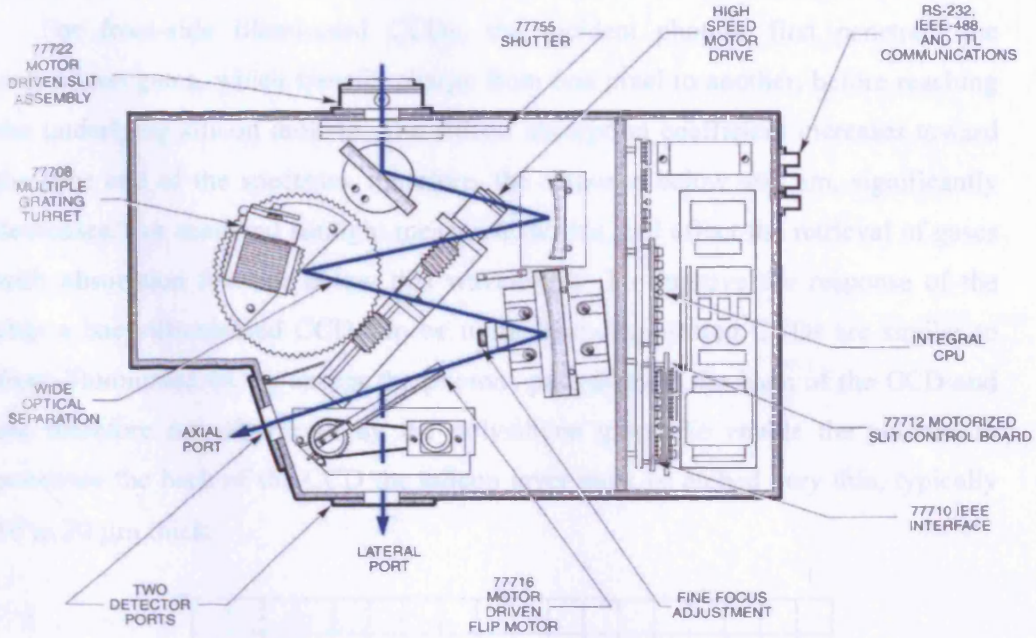

Figure 3-2: The Oriel MS257™ use in the CMAX-DOAS system [Oriel 2001].

3.2.3 The CCD

The spectrometer is connected to a custom built CCD camera and the image from each fibre produces a spectrum dispersed over the horizontal direction of the CCD chip. The detector is a Marconi 48-20 back illuminated, frame transfer UV coated CCD and has 1033 rows and 1072 columns of pixels each of which is 13 μm in height and by 13 μm in width.

The CCD measures the intensity of the incident photons by the use of metal-oxide-semiconductor (MOS) chips. The photon excites an electron in the silicon band which is then transferred into the conduction band, forming an electron/hole pair. The electrons are then stored in a potential well. A full potential well will result in a good signal to noise ratio, however, overflowing of the potential well may cause saturation of the image. Therefore it is important to obtain the correct integration time to ensure the potential well is full, but saturation does not occur. A sequence of voltages is applied to the rows and columns of the CCD to transfer the

charge from one pixel to another which is then read out at the end. An analogue-to-digital converter (ADC) converts the voltages into data numbers (DN).

For front-side illuminated CCDs, the incident photons first penetrate the polysilicon gates, which transfer charge from one pixel to another, before reaching the underlying silicon dioxide. The silicon absorption coefficient increases toward the blue end of the spectrum, therefore, the response below 400 nm, significantly decreases. For scattered sunlight measurement this will effect the retrieval of gases with absorption features below this wavelength. To improve the response of the chip a back-illuminated CCD can be used. Back-illuminated CCDs are similar to front-illuminated CCDs except the photons pass through the back of the CCD and are therefore not obstructed by the polysilicon gates. To enable the photons to penetrate the back of the CCD the silicon layer must be etched very thin, typically 10 to 20 μm thick.

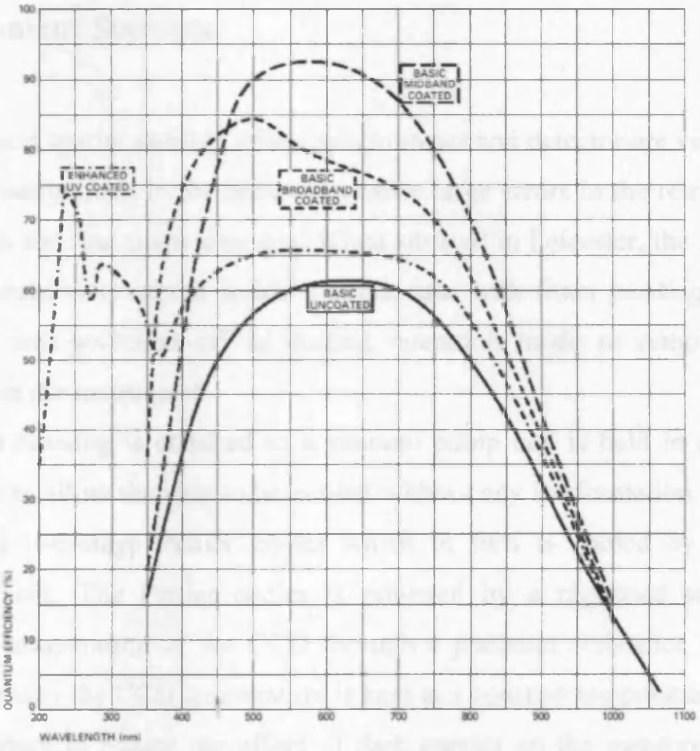

Figure 3-3: Quantum Efficiencies of a typical 48-20 CCD with different coatings (Marconi, 48-20 technical notes). The CCD used in this work was coated with the enhanced UV coating, shown as a dot-dashed line in the figure.

The Marconi 48-20 is a frame transfer CCD, which can operate without a shutter at a high frequency. The CCD has an opaque layer, often aluminium, on which the image can be stored. From this storage area the image can be read slowly, while a new image is being created. The UV coating on the CCD increases the efficiency of the CCD in producing cascades of electrons for each photon incident on the surface. This is known as the Quantum Efficiency (QE). The QE is dependent on wavelength and is different for each detector. The QE for the CCD used in this work is shown in Figure 3-3. For a CCD with enhanced UV coating the QE is between 50% and 65% for the wavelength regions important in this work (approximately 320 to 550nm), whereas, without any coating the QE drops considerably below 450 nm.

3.3 Instrument Stability

Thermal and spatial stability of the spectrometer and detector are very important as a slight misalignment in the optics can cause large errors in the retrievals owing to wavelength and line shape changes. When situated in Leicester, the spectrometer and CCD system were stored inside a flight case with foam padding lining. The spectrometer was switched off in normal operation mode to remove any heat generated from the instrument.

The CCD housing is attached to a vacuum pump and is held in a vacuum of $\sim 5 \times 10^{-4}$ mbar to allow the chip to be cooled without any ice formation. The CCD is attached to a two-stage Peltier cooler which in turn is cooled by an external refrigeration unit. The Peltier cooler is powered by a regulated supply which monitors the temperature of the CCD through a platinum resistance thermometer (PRT). In this way the CCD temperature is kept at a constant temperature of ~40 °C. This is important to reduce the effect of dark current on the measured spectra as described in the following section.

3.3.1 Dark Current

The dark current (DC) is an offset from zero that arises from thermal energy within the CCD creating electrons independent of the photons falling on the CCD. Dark current varies from pixel to pixel and can also vary slowly with time. The dark current can be limited by reducing the temperature of the CCD, as the number of excited electrons increases exponentially with the temperature.

$$D_R(e^-) = CT^{1.5}e^{\frac{-E_g}{(2kT)}} \qquad \textbf{Equation 3-4}$$

where $D_R(e^-)$ is the average dark current measured in e^- pixel^{-1} s^{-1}, T is the operating temperature of the CCD (K), k is Boltzmann's constant (8.62×10^{-5} eV/K) and E_g, is the band gap energy of silicon (eV).

$$E_g = 1.1557 - \frac{7.021\times10^{-4}T^2}{1108+T} \qquad \textbf{Equation 3-5}$$

C is a constant and the solution can be found at room temperature (300 K).

$$C = \frac{D_{FM}P_S}{qT_{RM}^{1.5}e^{\frac{-E_g}{(2kT_{RM})}}} \qquad \textbf{Equation 3-6}$$

where P_S is the pixel area in cm^{-2} and D_{FM} is the "dark current figure of merit" at 300 K (in units of nAcm^{-2}) which is different for each CCD.

The final dark current can be expressed as:

$$D_R(e^-) = 2.5\times10^{15}P_S D_{FM}T^{1.5}e^{\frac{-E_g}{(2kT)}} \qquad \textbf{Equation 3-7}$$

Figure 3-4 shows the relationship between the CCD temperature and the dark current for the CCD chip used in this work. A temperature of -40 °C results in a dark current of approximately 100 to 150 e^- $pixel^{-1}$ s^{-1}. The method for the removal of the dark current from the measured spectra is discussed in section 3.3.3.

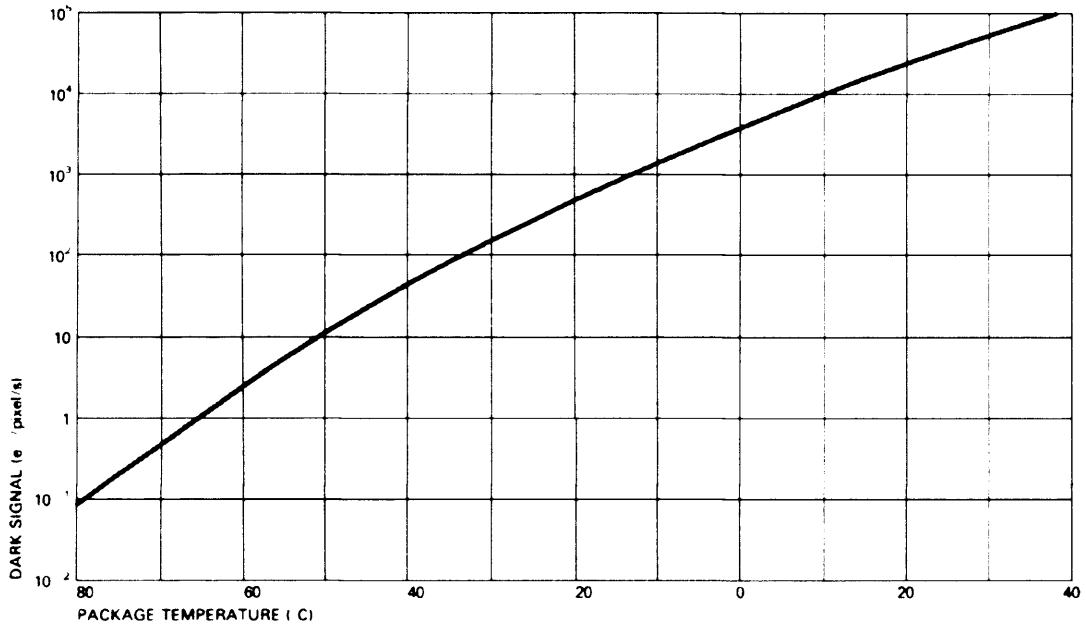

Figure 3-4: Relationship between CCD temperature (°C) and dark current (e^- $pixel^{-1}$ s^{-1}) for the 48-20 CCD chip (Marconi, 48-20 technical notes).

3.3.2 Stray light

Instrument stray light can originate from the incident photons reflecting off the optical components such as mounts and other surfaces and also from higher order diffraction and can interfere with the retrievals if detected by the CCD.

The stray light effects for this instrument have previously been quantified during the intercomparison of ground-based zenith-sky viewing UV-visible spectrometers at Andøya, Norway [Vandaele *et al.*, 2005]. A set of Schott filters was used to determine the magnitude of the stray light for the CMAX-DOAS system. The filters block the radiation below a certain wavelength, reducing the amount of stray light. A ratio of two zenith spectra, one obtained with a filter in the 350 to 370 nm wavelength region and one without a filter, should yield a zero ratio, if there are no stray light effects. For the CMAX-DOAS instrument, a ratio less than 0.5 % was

calculated at 360 nm. The Network for the Detection of Stratospheric Change (NDSC) class those instruments, for which the ratio was found to be smaller than 0.5 % as having a very good stray light rejection capability.

3.3.3 Instrument noise and offset

The input into the CCD is determined by the number of photons striking the detector, however, the output is a digital number produced by the analogue to digital converter (ADC). An offset can occur when there are no photons detected, owing to an artificial signal added to each measurement in case a negative signal is detected which cannot be converted by the ADC.

In addition to the offset, random noise in the spectra may also occur. Random noise is the dominant source of error and determines the detection limit of the retrieval. It is primarily caused by photoelectron and detector noise [Stutz, 1991]. The photoelectron noise (shot-noise) is associated with the random arrival of photons as some pixels interact with more photons than others. The shot noise (σ_S) has a Poisson distribution, and is proportional to the square root of the number of incident photons.

$$\sigma_S \propto \sqrt{N_{photons}} \qquad \textbf{Equation 3-8}$$

The detector noise is produced by the electronics in the system, for example, the variability on the dark current and the readout noise. The readout noise is proportional to the square root of the number of CCD images averaged for each spectrum. In the CMAX-DOAS system the number of CCD images changes throughout the measurement period of one day as it depends on the integration time, which is determined by the intensity of the scattered light. The detector noise, for current CCD systems is very small and the shot noise dominates here.

All sources of offset and errors described in section 3.4 will affect the DOAS retrievals, therefore, they must be removed or minimised as much as possible. To increase the signal to noise ratio, the spectra are averaged over a number of rows and scans. Each fibre image is dispersed over approximately 30 rows and all of these rows are included to obtain averaged spectra. In order to reduce the noise even

further, multiple images were averaged within a specific time period. The time period chosen should allow for a significant number of images to be obtained, without reducing the ability of the instrument to detect sudden changes in concentrations of trace gas species. In the case of NO_2, the absorber is strong; therefore, some noise on the spectra does not affect the retrievals considerably. Images were averaged over a one minute period, which enabled small changes in NO_2 to be detected. At noon this corresponds to approximately 20 images, but decreases towards dusk and dawn when the integration time for each image is much longer.

The offset due to the ADC, random noise and dark current can vary easily with each scan and need to be measured frequently. Figure 3-5 shows a standard CCD image with the zenith image at the top of the CCD followed by the 15, 10, 5, and 2 degree elevation angles. The images from each telescope are spaced approximately 100 rows apart. The gaps between each fibre image give a good approximation of the dark current and offset for the scan, together creating a background level. The background spectrum is obtained by averaging over 10 rows centred on the 50^{th} row either side of the central peak of each image. The average of these two spectra was calculated, which give a value for the background signal for each section of the CCD. Each background spectra can then be subtracted from the appropriate measured spectra.

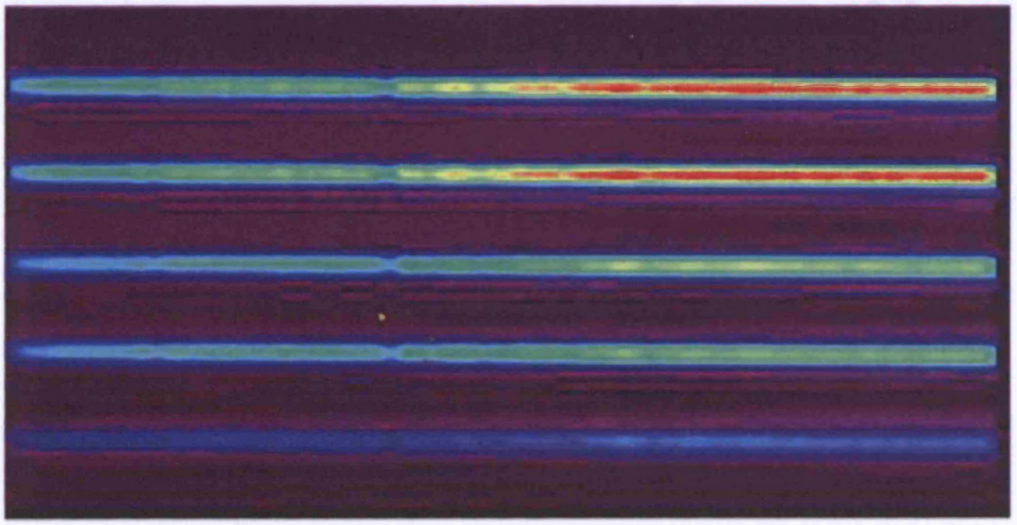

Figure 3-5: CCD image of scattered sunlight, the image from the zenith telescope is at the top of the CCD followed by the 15, 10, 5, and 2 degree elevation angles.

The variability in the signal obtained from the background spectra gives an estimate of the electronic noise. The root mean squared value of the mean daily variability is 2.5 counts. For average signal strength of 1500 on each fibre, this gives an error of approximately 0.2%. The error owing to electronic noise is very small in comparison to the error from the DOAS fitting routine which will be discussed in section 3.5. The 2 degree fibre, however, has a low intensity which increases the error due to electronic noise, particularly at twilight and the error can be as high as 5.3% in these cases [Leigh *et al.*, 2006].

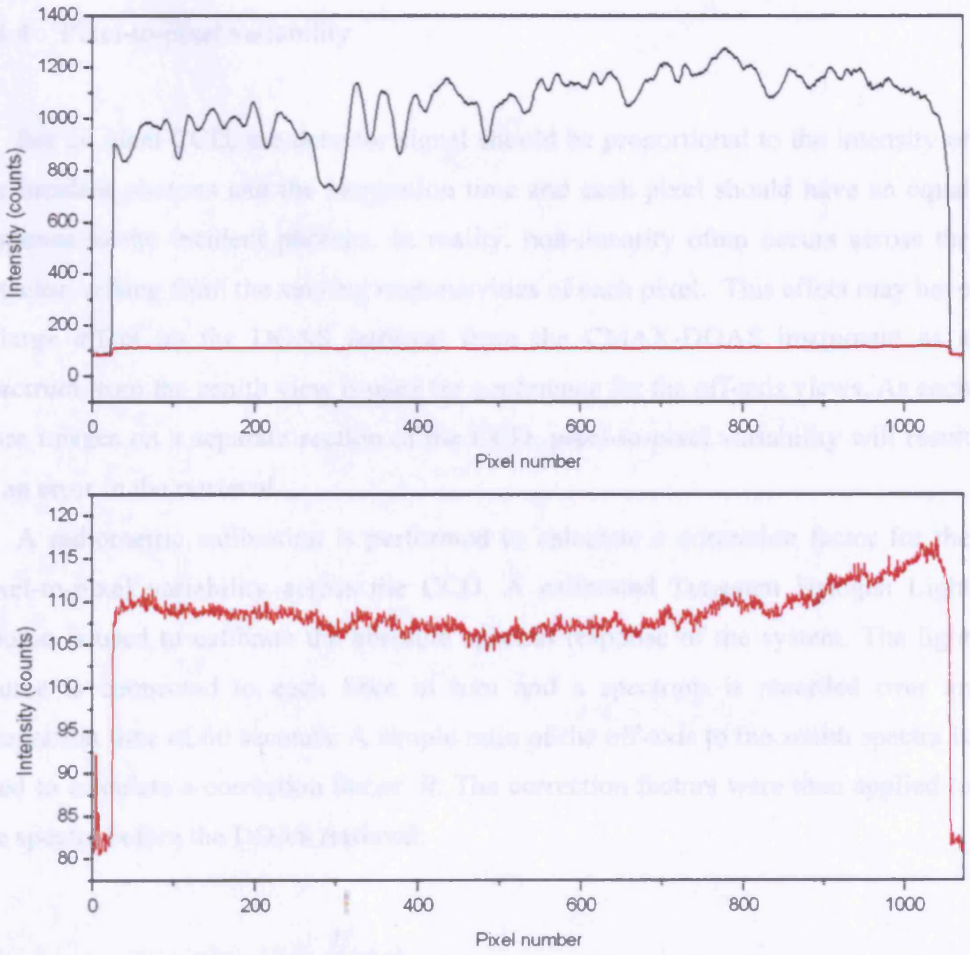

Figure 3-6: Absorption (black line) and background spectra (red line) measured by the CMAX-DOAS instrument. The background spectrum was obtained from the average of 10 rows either side of the absorption spectrum. Bottom figure shows a zoomed in plot of the background spectrum.

Figure 3-6 gives an example of an absorption spectrum extracted from the CCD image (black line) and a background spectrum obtained from the average of 10 rows either side of the absorption spectrum (red line). The observed background intensity is approximately 10% of the absorption spectrum. The bottom plot in Figure 3-6 shows a zoomed in version of the background spectrum. The variability on the background intensity due to electronic noise can be observed. The final spectrum used in the DOAS retrieval is the result of the background spectrum subtracted from the absorption spectrum.

3.3.4 Pixel-to-pixel variability

For an ideal CCD, the detector signal should be proportional to the intensity of the incident photons and the integration time and each pixel should have an equal response to the incident photons. In reality, non-linearity often occurs across the detector, arising from the varying responsivities of each pixel. This effect may have a large effect on the DOAS retrieval from the CMAX-DOAS instrument as a spectrum from the zenith view is used for a reference for the off-axis views. As each fibre images on a separate section of the CCD, pixel-to-pixel variability will result in an error in the retrieval.

A radiometric calibration is performed to calculate a correction factor for the pixel-to-pixel variability across the CCD. A calibrated Tungsten Halogen Light Source is used to calibrate the absolute spectral response of the system. The light source is connected to each fibre in turn and a spectrum is recorded over an integration time of 60 seconds. A simple ratio of the off-axis to the zenith spectra is used to calculate a correction factor, R. The correction factors were then applied to the spectra before the DOAS retrieval.

$$R_{(\alpha,n)} = \frac{I^{c}_{(zen,n)}}{I^{c}_{(\alpha,n)}} \qquad \textbf{Equation 3-9}$$

where, $I^{c}_{(zen,n)}$ is the intensity of the zenith spectrum at a pixel and $I^{c}(\alpha,n)$ is the intensity of the off-axis spectrum.

Figure 3-7 demonstrates the spectral response of the CCD to a calibrated light source and the associated correction factors calculated from Equation 3-7 for each off-axis view. Broad features are observed below pixel 600 in all fibres, in particular the 2 ° view, most likely owing to smears on the surface of the CCD. The edges of the CCD are dominated by noise, owing to low signals. These pixels are not included in the DOAS retrieval. A radiometric calibration is performed each time the wavelength range is changed or the images are re-focused.

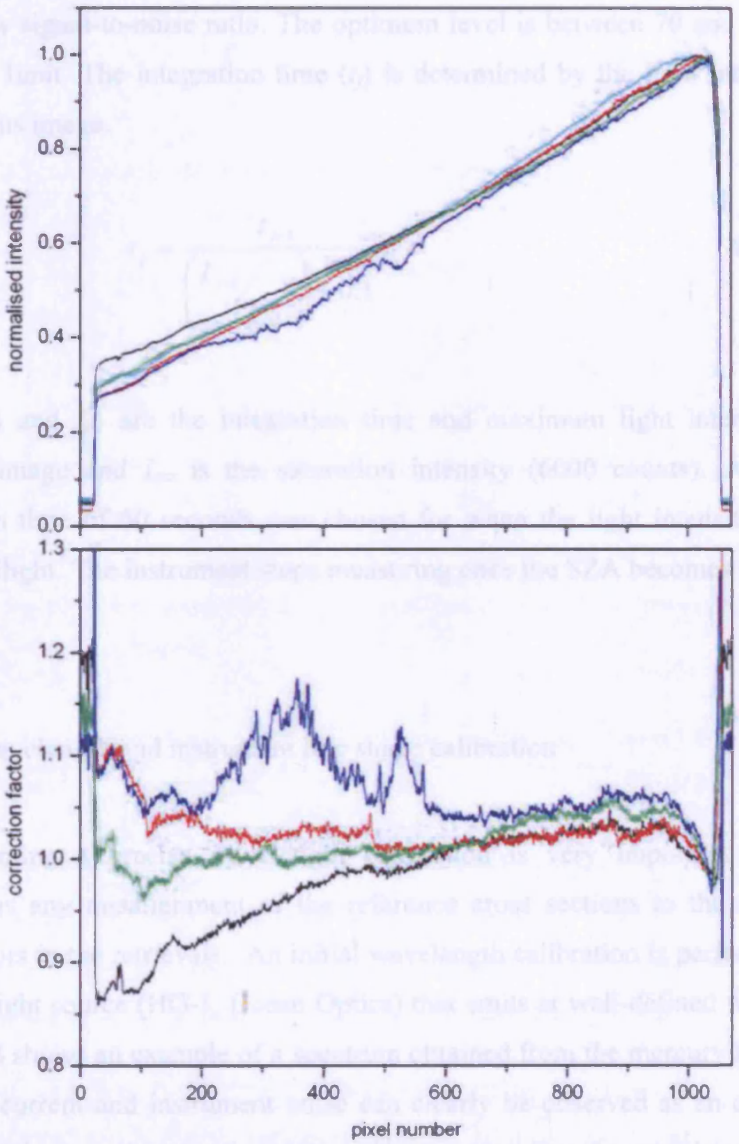

Figure 3-7: a) Spectral response of the CCD chip measured with a calibrated Tungsten Halogen Light Source for the 15° (black), 10° (red), 5° (green), 2° (blue), zenith (light blue) view and b) the associated correction factors for the off-axis views.

3.4 Measurement software

The spectrometer and CCD electronics are all controlled by a personal computer via USB and high speed-data cables. A Visual Basic™ (VB) program developed at the University of Leicester enabled the instrument to run autonomously. An important feature of the VB program is the ability to vary the integration time depending on the light intensity. The CCD image should not become saturated or have a low signal-to-noise ratio. The optimum level is between 70 and 90% of the saturation limit. The integration time (t_j) is determined by the light intensity from the previous image.

$$t_j = \frac{t_{j-1}}{\left(\frac{I_{j-1}}{I_{sat}}\right) + 0.1} \qquad \textbf{Equation 3-10}$$

where, t_{j-1} and I_{j-1} are the integration time and maximum light intensity for he previous image and I_{sat} is the saturation intensity (6000 counts). A maximum integration time of 60 seconds was chosen for when the light intensity decreases during twilight. The instrument stops measuring once the SZA becomes greater than 93°.

3.4.1 Wavelength and instrument line shape calibration

Performing a precise wavelength calibration is very important for DOAS retrieval as any misalignment of the reference cross sections to the spectra will create errors in the retrievals. An initial wavelength calibration is performed with a mercury light source (HG-1, Ocean Optics) that emits at well-defined wavelengths. Figure 3-8 shows an example of a spectrum obtained from the mercury light source. The dark current and instrument noise can clearly be observed as an offset in the spectrum. The wavelength of each mercury emission line detected here is listed in Table 3-2. Associating the wavelengths of each emission line with a pixel number allows an initial wavelength calibration to be performed. A disadvantage of using an emission light source to perform a wavelength calibration, however, is the difficulty

in accurately determining the position of the emission line centre if neighbouring emission lines are not completely resolved by the instrument or the ILS is asymmetric.

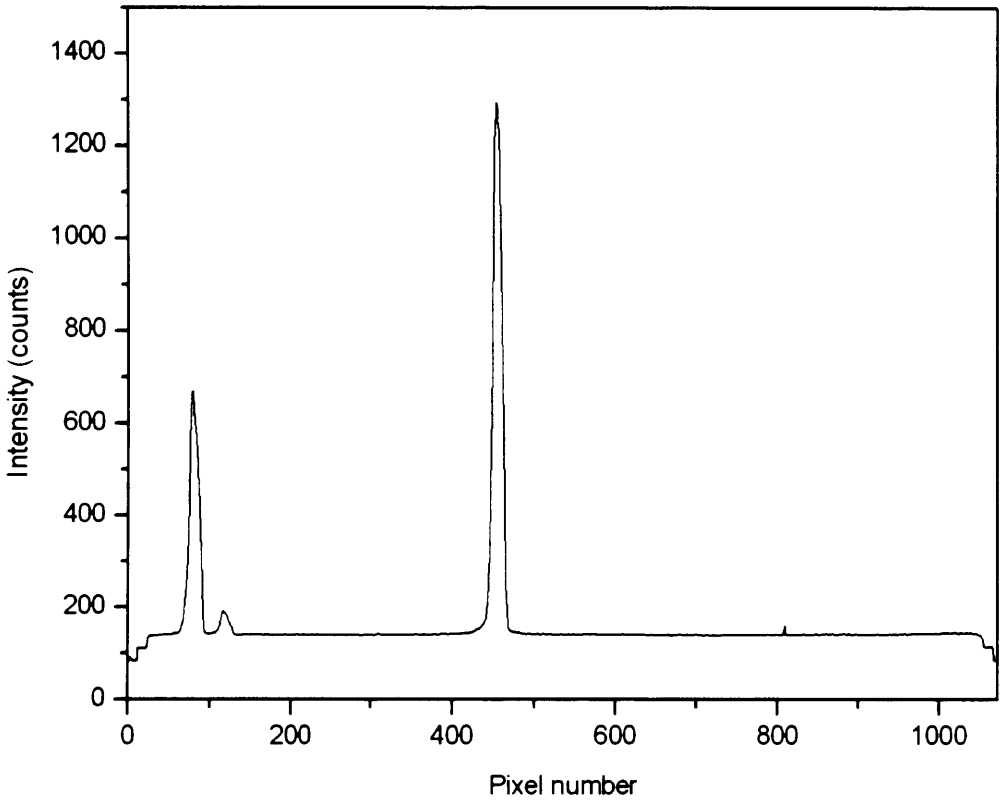

Figure 3-8: Emission line spectra from a Mercury calibration lamp (HG-1, Ocean Optics) measured by the CMAX-DOAS instrument.

Table 3-2: List of mercury lines [Ocean Optics] and pixel numbers from Figure 3-8.

Pixel number	**Wavelength (nm)**	**FWHM (pixels)**	**FWHM (nm)**
80	404.656	10.75	0.90
117	407.783	10.93	0.91
454	435.833	10.98	0.91

The ILS can also be determined from the mercury emission lines (see section 2.4.2). However, the ILS may vary across the CCD; therefore, it is more accurate to calculate a wavelength dependent ILS. The WinDOAS software can calculate a wavelength dependant ILS, by fitting a pre-selected line shape to the spectrum with the appropriate full width half maximum (FWHM).

The WinDOAS software includes a wavelength calibration feature which performs a calibration over the whole wavelength range of the instrument. The procedure utilises the strong Fraunhofer lines in a high resolution reference solar spectrum [Kurucz, 1995], convolved with the ILS, to align the measured spectra. Using non-linear least squares fitting, a calibration is performed by shifting and stretching the spectra to fit the solar Fraunhofer lines to those in the reference spectrum obtained at noon from each view.

$$\Delta = a + b.(\lambda - \lambda_0) + c.(\lambda - \lambda_0)^2, \qquad \textbf{Equation 3-11}$$

where, λ is the preliminary wavelength calibration (performed using the mercury lamp.), λ_0 the centre wavelength of the current spectral window, a the fitted shift, b the fitted stretch (first order) , c the second order fitted stretch (if used).

Figure 3-9 gives an example of the output from the WinDOAS wavelength calibration and ILS feature. A wavelength calibration window was chosen between 431 and 508 nm to incorporate the wavelength fitting window for the NO_2 analysis. The wavelength calibration window was then divided into 12 sub-windows and a wavelength and ILS calibration performed on each of these sub-windows. The red line in Figure 3-9a represents the spectrum to which the calibration has been applied and the black line is the high resolution solar spectrum which has been pre-convoluted with the ILS. The difference in optical intensity between the two spectra, shown in Figure 3-9b provides an indication of the quality of the wavelength calibration.

Figure 3-9c is the result of the ILS fitting routine. A Gaussian slit function with a specific FWHM is fitted to the absorption features in each sub-window (black points in figure) and a 2^{nd} order polynomial (red line) is fitted to the points to calculate the variability across the wavelength window. The ILS FWHM ranges between approximately 1.32 and 1.20 across the CCD for a Gaussian slit function.

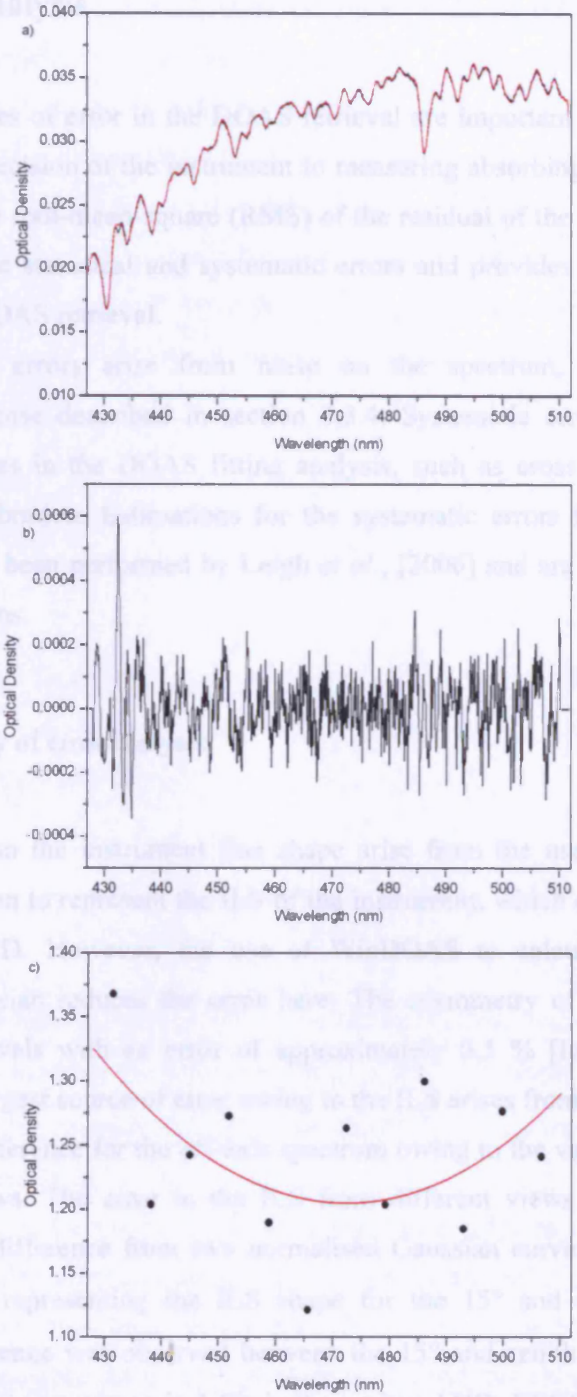

Figure 3-9: WinDOAS wavelength and ILS calibration and using non-linear least squares fitting between 431 and 508 nm. The wavelength region was divided into 12 micro-windows and the analysis performed separately in each window. The top figure shows the convolved solar spectrum (black) along with a zenith viewing spectrum (red). The middle figure shows the residual structure from the non-linear least squares fitting routine and the bottom figure show the Gaussian FWHM for the ILS in each micro-window and a 2nd order polynomial (red) fitted to the data.

3.5 Error analysis

The sources of error in the DOAS retrieval are important in determining the accuracy and precision of the instrument to measuring absorbing gas species in the atmosphere. The root-mean-square (RMS) of the residual of the fitting algorithm is a measure of the statistical and systematic errors and provides an estimate of the quality of the DOAS retrieval.

Statistical errors arise from noise on the spectrum, mainly owing to photoelectron noise described in section 3.3.4. Systematic errors are introduced from inaccuracies in the DOAS fitting analysis, such as cross sections, ILS and wavelength calibration. Estimations for the systematic errors for this instrument have previously been performed by Leigh *et al.*, [2006] and are summarised in the following sections.

3.5.1 Summary of error analysis

The errors on the instrument line shape arise from the use of a pre-selected Gaussian function to represent the ILS of the instrument, which can vary across the columns of CCD. However, the use of WinDOAS to calculate a wavelength dependent Gaussian reduces the error here. The asymmetry of the ILS may also effect the retrievals with an error of approximately 0.5 % [Leigh *et al.*, 2006]. However, the largest source of error owing to the ILS arises from the use of a zenith spectrum as a reference for the off-axis spectrum owing to the variability in the ILS across CCD rows. The error in the ILS from different views was estimated by calculating the difference from two normalised Gaussian curves with FWHMs of 1.14 and 1.38, representing the ILS shape for the 15° and zenith views. The maximum difference was observed between the 15° and zenith views at 470 nm, giving an error of approximately 3.5% in the retrieved NO_2 DSCDs.

The wavelength calibration, performed by the WinDOAS software is assumed to be accurate within a half pixel, which corresponds to 0.04 nm when using the grating with 600 lines mm^{-1}. Errors associated with shifts in wavelength correspond to an error of approximately 0.8%, with a Gaussian line shape of 1.4 FWHM.

Additional errors arise from the calculation of the cross sections from the literature, which differs for each cross section used. Leigh *et al.*, [2006] calculated a total fit error from the RMS residual of approximately 5% on the retrieved NO_2 slant columns for a spectrum analysed with a zenith reference spectrum. As the integration time is determined by the maximum signal on the CCD, the 2° consistently observes lower signal to noise ratios compared to the other views, therefore, the error on the 2° view is much higher at approximately 10.3%. A summary of the error sources and estimates for the CMAX-DOAS instrument is given in Table 3-3.

3.5.2 Detection limit

The detection limit ($\overline{D}_{\text{lim}}$) of the instrument to determining the differential optical depth an individual gas species can be approximated using the following equation [Stutz and Platt, 1996]:

$$\overline{D}_{\text{lim}} \approx \sigma . \frac{6}{\sqrt{n-1}} \qquad \textbf{Equation 3-12}$$

where n is the number of pixels within the fitting window and σ is the instrument noise level. To calculate the detection limit of the instrument for a slant column amount of the gas species, the detection limit $\overline{D}_{\text{lim}}$, is simply divided by the absorption cross section.

This expression for the detection limit was validated with calculations from a Monte-Carlo model which calculates the errors associated with each fitting routine. The estimated detection limits are within 10 to 20% of the Monte-Carlo values. This is an acceptable level and reduces the need for long time-consuming calculations. In this thesis, the RMS residual is used as an estimate of the noise on the spectra and to determine the detection limit. However, the residual may also show systematic structures and in these cases the detection limit has to be treated with care. Typical detection limits for retrieval of NO_2 in the 5°, 10° and 15° views are 4.7×10^{15}, 4.2×10^{15}, 3.2×10^{15} molecules cm^{-2} respectively, when using a zenith

reference spectrum. The detection limits for the target species in this thesis are given in the appropriate chapters.

Table 3-3: Summary of the error sources and estimates for the CMAX-DOAS instrument [Leigh *et al.*, 2006]

Error Source	Error Estimate (%)
Wavelength calibration	0.8
Electronic noise	0.2
Stray light	Negligible
ILS	3.5
Fitting error	5 (10.3 for 2° view)

3.6 Summary

In this chapter, an introduction to different DOAS systems was given, in particular the use of Multi-Axis DOAS to perform retrievals of tropospheric gas species. A description of the design and operation of the CMAX-DOAS system, installed on the Space Research Centre at the University of Leicester, was given, including the process involved in extracting spectra from the CCD images and the calibration of the wavelength and ILS using the the WinDOAS software developed by the Belgian Institute for Space Aeronomy (BIRA). Finally a discussion and summary of the errors associated with the instrument were presented.

The following chapters will present results from the retrievals of NO_2, O_4 and halogen oxides by the CMAX-DOAS instrument in the urban and marine boundary layers. The results demonstrate how the instrument can provide important information on concentrations and profiles of gases to understand the chemical process in the atmosphere and the validation of satellite-based instruments.

Chapter 4

CMAX-DOAS measurements of O_4 for the retrieval of aerosol in the urban boundary layer

Understanding air pollution and transport in the urban boundary layer (UBL) is particularly important for assessing the role of anthropogenic emissions and their impact on the wider environment. As described in Chapter 1, the urban boundary layer is a region of the troposphere directly influenced by the Earth's surface. Vertical mixing of trace gases and aerosols within the UBL is generally fast acting, resulting in a well mixed layer with an altitude between 500 and 2000 m, depending on meteorological conditions. Monitoring the trace gas species and aerosols within the UBL, therefore, improves our knowledge and understanding of the dynamic processes and chemical reactions that affect the surface layer.

In this chapter, results from the measurements of NO_2 and aerosols as part of the Leicester Air Quality Measurement Project (LAMP) during summer 2007 are discussed. The determination of the radiative effects of aerosols and their role in atmospheric chemistry are challenging problems and at the forefront of climate research. In addition, an accurate knowledge of aerosol optical depth (AOD) profiles can optimise the AMF calculations and improve the accuracy of DOAS retrievals. Recently, DOAS instruments have begun to be used to determine aerosol optical depths from O_4 measurements in the atmosphere; however, quantitative studies of MAX-DOAS O_4 retrievals for determining the optical properties of aerosols are limited [Wagner *et al.*, 2004; Sinreich *et al.*, 2005; Frieβ *et al.*, 2006; Leigh *et al.*, 2007, Irie *et al.*, 2007]. In this chapter, a number of sensitivity test have been performed to determine the sensitivity of the CMAX-DOAS to the retrieval of aerosol optical depth in the urban boundary layer.

4.1 Leicester Air Quality Measurement Project (LAMP)

4.1.1 Introduction to LAMP and the participating instruments

The LAMP campaign, held at the University of Leicester (52.38° N, 1.08° W) during summer 2007, involved a number of instruments performing measurements of NOx, VOCs and aerosols to enhance our knowledge of air quality in an urban area. A summary of the instruments is given in Table 4-1. The main objectives of the LAMP campaign were:

1. The comparison of measurement techniques for the determination of NO_2 concentrations

2. The derivation of information on radical reactivity, volatile organic compounds, and secondary aerosol formation in the urban boundary layer.

The first of these objectives involve concurrent measurements of NO and NO_2 concentrations from three different *in situ* instruments along with retrievals of NO_2 from the CMAX-DOAS instrument, to compare measurement techniques in an urban area. The chemiluminescence monitors (API M200a analyser, Enviro Technology) run by Leicester City Council use molybdenum oxide catalysts to measure NO_2. Recently, the effect of interference from other nitrogen compounds converting to NO_2 by molybdenum oxide catalysts has been documented [Ordóñez *et al.*, 2006; Schaub *et al.*, 2006 Steinbacher *et al.*, 2007; Dunlea *et al.*, 2007]. The NO_{xy} instrument consists of a single channel, chemiluminescence NO detector with a molybdenum oxide catalyst, NO_y converter and a diode based blue light (BLC) photolytic NO_2 converter, which is reported to limit the interference of other nitrogen compounds and measure NO_2 more accurately. The BBCEAS instrument performs measurements *in situ*, however, the instrument employs the absorption spectroscopy techniques to derive NO_2 concentrations, therefore is not influenced by the interference from other nitrogen compounds [Langridge *et al.*, 2006]. The comparison of measurements from all these instruments allows us to quantify the

influence of other pollutants to the NO_2 measured by the chemiluminescence method.

Two recent studies evaluated the significance of the interference in the chemiluminescence measurements in a rural and urban site. Steinbacher *et al.*, [2007] compared NO_2 measurements from a molybdenum converter to those from a photolytic converter, which are far less effected by interference, at two rural sites of different elevation levels, in Switzerland. The analysis demonstrated that the molybdenum converters overestimate the amount of NO_2 more in summer than winter, owing to the high production of secondary pollutants from photochemistry, such as HNO_3. On a monthly basis only 70 to 83% of the NO_2 measured by the molybdenum converters on the ground can be attributed to "real" NO_2 and even less at the elevated site. Dunlea *et al.* [2007] presents data from field campaigns in Mexico City during 2002 and 2003. Results from a comparison of NO_2 measurements by chemiluminescence detectors, equipped with molybdenum converters, with a Tunable Infrared Laser Differential Absorption Spectroscopy (TILDAS) and a DOAS instrument, showed that the interference resulted in a 22% increase in average measured concentration of NO_2 from the chemiluminescence monitors than co-located spectroscopic measurements.

The second objective includes measurements of radical reactivity, volatile organic compounds, and secondary aerosol formation from a number of instruments including the chemical ionisation reaction-time of flight-mass spectrometer (CIR-TOF-MS) and dual inlet peroxy radical chemical amplifier (PERCA). A lidar instrument was also deployed to perform measurements of AOD from 80 m to 5000 m at a vertical resolution of 7.5 m. In addition, the AOD from the lidar instrument was used to determine the accuracy of the CMAX-DOAS to the retrieval of AOD in the urban boundary layer. Finally, the AOD measurements from the lidar instrument were used to determine NO_2 AMFs and the urban boundary layer height in Leicester. Using this information the concentration of NO_2 in Leicester is determined from the CMAX-DOAS measurements and correlated with data from *in situ* monitors run by the local council.

Table 4-1: Summary of the instruments and their measurements involved in the LAMP campaign.

Instrument	Target Species	Technique	Detection limit	Institution
NOxy	NO, NO_2	Diode based blue light photolytic converter	~3 ppt (NO), 6ppt (NO_2), 3ppt (NOy) (10 minute data cycle)	University of York
BBCEAS	NO_2	Blue LED	50 to 60 ppt	University of Leicester
Chemiluminescence Monitors (on site and city wide)	NO_2, NO, O_3 PM2.5, PM10	Molybdenum oxide catalysts	0.4 ppb (NO_2)	Leicester City Council
Mobile Lidar	AOD, PBL Height	10 minute integration vertical resolution of 7.5 m for AOD		University of Manchester
CMAX-DOAS	O_4, NO_2	Scattered light measurements with 5 elevation angles	~52×10^{40} molecules^2 cm^{-5} (O_4), 8.60×10^{14} molecules cm^{-2} (NO_2)	University of Leicester
FTIR	CO,CO_2	path of 50m, <1 s resolution		University of Edinburgh

Table 4-1: Continued

Sun photometer	AOD	Direct solar irradiance at 440, 670, 870 and 1020 nm.	±0.01 >440 nm	AERONET
Filter samples	Organic aerosol composition	Filter sample once per day		University of York
CIR-TOF-MS	VOC's, sVOCs, OVOCs, SOA	time-of-flight mass spectrometry	10 ppb (1 min)	University of Leicester
Bottle samples	CH_4, CO_2, CO, and CH_4 isotopes	Samples collected ever 3 hours over 48 hour period.		University College London
PERCA	$\sum HO_2+RO_2$	Detection *via* catalytic reaction with NO	2 ppt (1 min)	University of Leicester
2 x Ozone monitor	O_3	UV absorption technique	1 ppb	University of York/ Leicester
CO monitor	CO	Vacuum ultraviolet fluorescence CO analyser	< 1ppb	University of Leicester
Meteorological data	Temperature, wind speed, wind direction, humidity	Measured at 3 m and 10m altitude		University of Leicester
Radiometers	J values, Actinic flux	2π sr view, 0.5 second integration time		University of Leicester

4.2 CMAX-DOAS set-up during LAMP

During the LAMP campaign the spectrometer and camera set up, as described in chapter 3, was replaced with an Acton InSight system (PIActon, which consists of a spectrometer and CCD camera controlled by the PC via a USB cable). The new set up allowed for thermally stable continuous measurements with a much higher S/N than previously attainable.

A multi track fibre, connected to the telescopes in the head unit, which were set to elevation angles of 6°, 8°, 10°, 12° and zenith, was coupled to the spectrometer with an imaging fibre adaptor, (PIActon, model: FC-446-030) designed especially for the spectrometer which enables precise images of the fibres at the entrance slit. The spectrometer contains two gratings with line densities of 600 and 1200 lines per mm. During this campaign only the 1200 lines per mm grating was used, which enabled spectra to be measured over a wavelength range of 67 nm.

The CCD (PIActon, model: Pixis 1024,) is back illuminated and contains 1024 rows and 1024 columns with a pixel size of 13 μm x 13 μm, giving a total imaging area of 13.3 mm x 13.3 mm. The camera is within a permanent vacuum and has a built in thermo-electric peltier cooler which is thermally stable, this allows the CCD to be maintained at a constant temperature of -70°C, with a precision of ±0.05°C. The low temperature reduces the dark current significantly with a typical value of 0.001 e^- $pixels^{-1}$ $seconds^{-1}$ improving on the previous set up by a magnitude of over $1x10^4$.

Figure 4-1 shows an example of an absorption spectrum (black lines) obtained from averaging 30 rows of the CCD. The red line in the figure is the background spectrum, which includes the dark current and offset, calculated by averaging 10 rows centered on the 50^{th} row below the measured spectrum. The background intensity is approximately 600 counts and the RMS of the variability in the background spectra is approximately 7 counts. For average signal strength of 22000 counts in the absorption spectrum the error on the spectra owing to electronic noise of 0.03%.

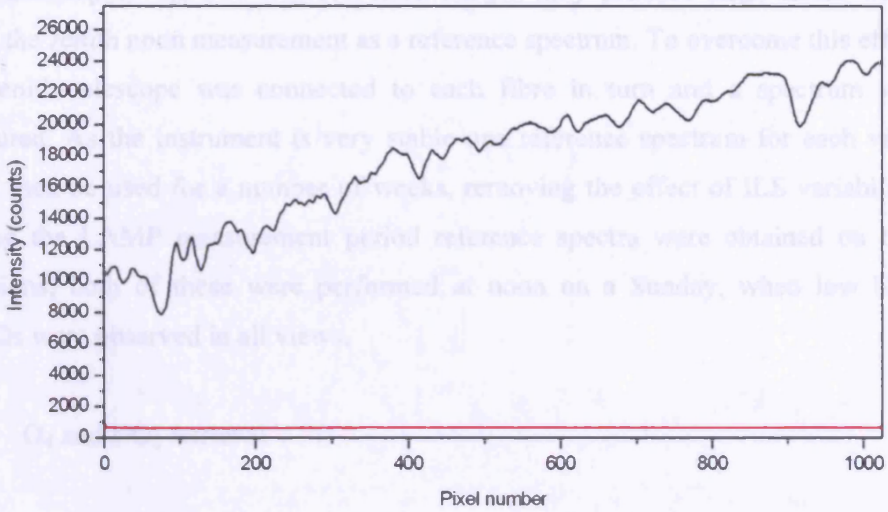

Figure 4-1: Absorption (black line) and background spectra (red line) measured by the CMAX-DOAS instrument with the new spectrometer and camera.

One major disadvantage with the new system is the variability of the instrument line shape across the CCD. Figure 4-2b shows the FWHM for a wavelength dependent Gaussian instrument line shape calculated using the WinDOAS software for each fibre. The FWHM increases considerably with increasing wavelength, from approximately 0.9 to 1.8. The variability in the line shape between each fibre is not as large as the variability across the CCD columns but differences are still evident when imaging a mercury line source through each fibre (Figure 4-2a).

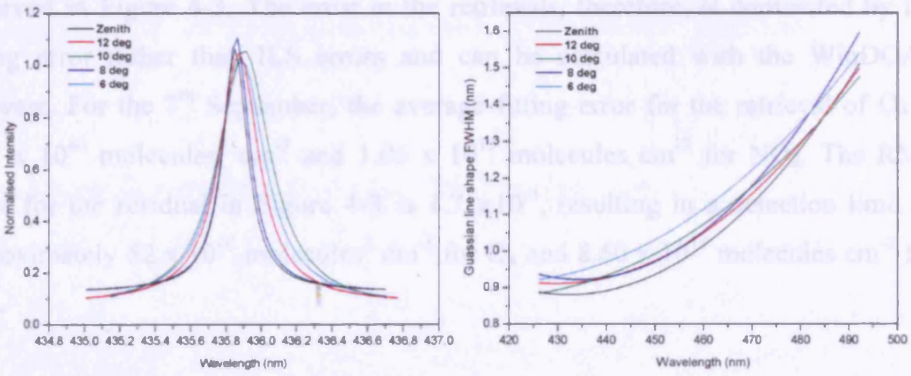

Figure 4-2: a) Mercury emission line spectra and b) Wavelength dependent Gaussian instrument line shape calculated using the WinDOAS software for each elevation angle fibre.

Variability in the ILS between fibre images may produce large errors when using the zenith noon measurement as a reference spectrum. To overcome this effect the zenith telescope was connected to each fibre in turn and a spectrum was measured. As the instrument is very stable one reference spectrum for each view could then be used for a number of weeks, removing the effect of ILS variability. During the LAMP measurement period reference spectra were obtained on two occasions, both of these were performed at noon on a Sunday, when low NO_2 DSCDs were observed in all views.

4.2.1 O_4 and NO_2 retrieval

For the retrieval of O_4 and NO_2 during this campaign, a wavelength range of 426 to 493 nm was used. This region includes two O_4 absorption bands at 477 nm and 447 nm and a strong absorption cross section for NO_2 (see section 2.6). Water vapour and ozone are also present in this wavelength region and are included within the fitting routine. A third order polynomial was also included in the fitting routine to remove the broadband structures. Figure 4-3 shows an example fit for O_4, NO_2, Ozone and water vapour from the 6° view for a one minute averaged spectrum obtained on the morning of 7th September 2007. The zenith reference spectrum was measured at noon on 9th September.

The effect of retrieving a reference spectrum from the same row as the off-axis measurements, thereby reducing the ILS error, is evident in the small residual observed in Figure 4-3. The error in the retrievals, therefore, is dominated by the fitting error rather than ILS errors and can be calculated with the WinDOAS software. For the 7th September, the average fitting error for the retrieval of O_4 is 43.7 x 10^{40} molecules^2 cm^{-5} and 1.05 x 10^{15} molecules cm^{-2} for NO_2. The RMS value for the residual in Figure 4-3 is 1.71×10^{-3}, resulting in a detection limit of approximately 52 x 10^{40} molecules^2 cm^{-5} for O_4 and 8.60 x 10^{14} molecules cm^{-2} for NO_2.

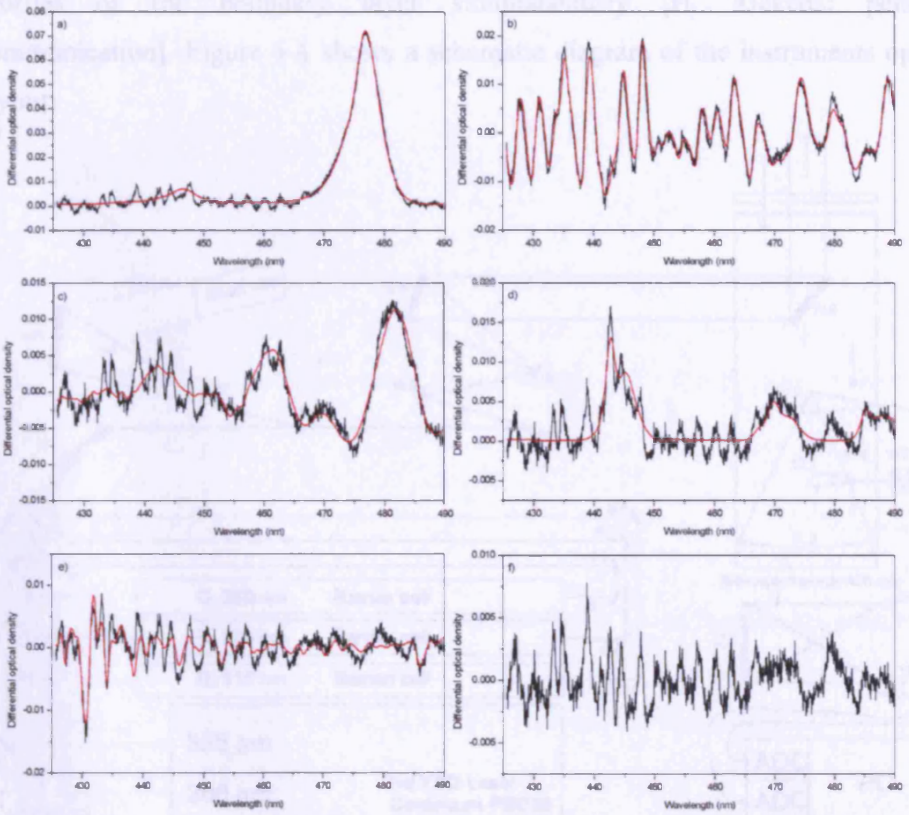

Figure 4-3: Example of the spectral retrieval of a) O_4 and b) NO_2 (294 K) on 7th September 2007.with a reference spectrum from the morning of 9th September. Include in the fitting routine are also c) O_3, d) H_2O, and e) Ring. The black lines represent the retrieved spectral signature and the red lines represent the fitted absorption cross section. An NO_2 cross section at 220 K, offset and polynomial (third order) is also included (not shown). The final residual for this fit (f) has a rms value of 1.71×10^{-3}. The differential slant column values for O_4, NO_2 and Ozone are 1.14×10^{40} molecules^2 cm^{-5}, 1.15×10^{17} molecules cm^{-2} and 6.90×10^{19} molecules cm^{-2} respectively.

4.3 Aerosols retrieval from the lidar instrument

4.3.1 Lidar instrument

The University of Manchester lidar instrument, deployed during the campaign, was situated on the ground below the location of the CMAX-DOAS head unit. The lidar instrument, built by Elight Systems, is designed to retrieve aerosol and ozone

profiles of the boundary layer simultaneously [H. Ricketts: personal communication]. Figure 4-4 shows a schematic diagram of the instruments optical layout.

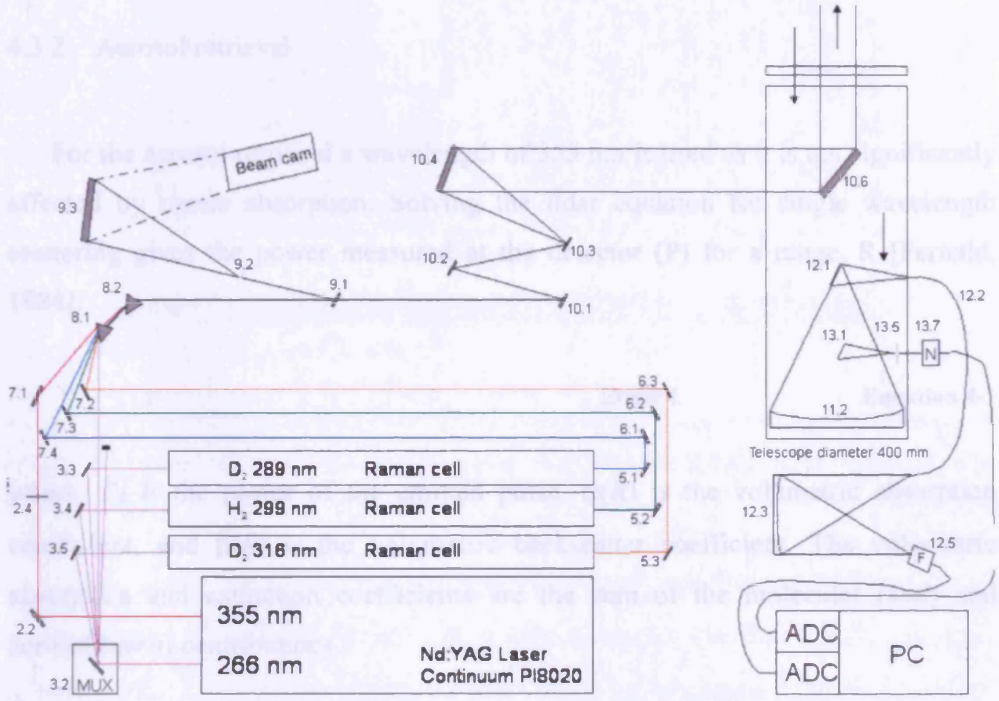

Figure 4-4: Optical diagram of the Elight Systems lidar instrument deployed during the LAMP campaign [Image: courtesy of H. Ricketts].

A laser supplies a pulse of energy at 1200 mJ and wavelength of 1064 nm, which is converted into wavelengths of 355nm and 266nm using combinations of second, third and fourth harmonic generators. The 266 nm pulse is then directed through three Raman cells containing different ratios of hydrogen and deuterium at predefined pressures, resulting in three wavelength changes of 289, 299 and 316 nm, owing to inelastic Raman scattering. The lidar pulse alternates in turn between the five wavelengths and the backscattered signal is collected by a 40 cm telescope. The telescope mirror focuses the backscatter signal onto two photomultiplier tubes (PMT), one for the near-field, which is passed through a broadband UV filter. The second PMT records the far-field signal after initially being focussed onto a diffraction grating to separate out the wavelengths of interest for each pulse. An analogue-to-digital converter then converts the signal into 4096 points with a range

resolution of 7.5 metres, providing aerosol retrieval up to an altitude of 5 km in cloud free conditions.

4.3.2 Aerosol retrieval

For the aerosol retrieval a wavelength of 355 nm is used as it is not significantly affected by ozone absorption. Solving the lidar equation for single wavelength scattering gives the power measured at the detector (P) for a range, R [Fernald, 1984].

Erreur ! **Equation 4-1**

where, P_0 *is* the power of the emitted pulse, $\alpha(R)$ is the volumetric absorption coefficient, and $\beta(R)$ is the volumetric backscatter coefficient. The volumetric absorption and extinction coefficients are the sum of the molecular (*mol*) and aerosol (*aero*) contributions.

$$\alpha(R)=\alpha_{mol}+\alpha_{aero} \quad \textbf{Equation 4-2}$$

$$\beta(R)=\beta_{mol}+\beta_{aero} \quad \textbf{Equation 4-3}$$

The molecular components of Equations 4-2 and 4-3 can be modelled using Rayleigh scattering theory. To determine the aerosol components a ratio of the total backscatter to the backscatter owing to molecules only, is calculated by choosing a point at high altitude, assumed to be free of aerosols. The aerosol volumetric backscatter coefficient (β_{aero}) can then be derived. Figure 4-5 shows an example of the backscatter measurements from the aerosol lidar deployed during the LAMP campaign on 6th September 2007. The backscatter coefficient increases in the lower troposphere over the day, owing to an increase in aerosols in this region. The boundary layer height can be determined from the altitude at the top of the aerosol layer.

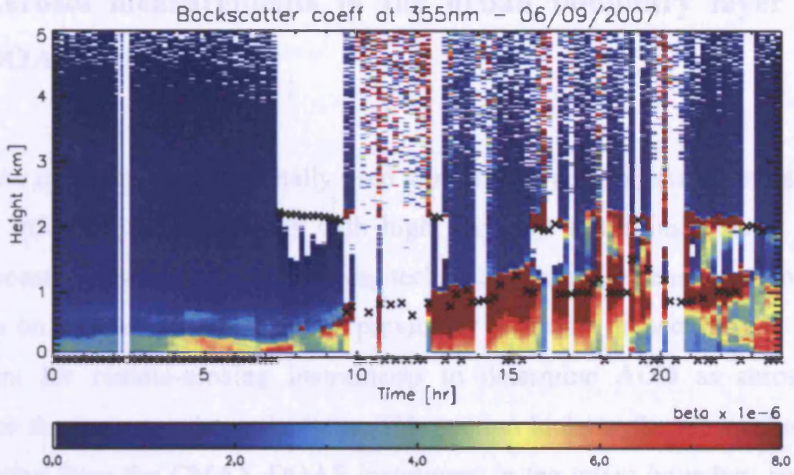

Figure 4-5: Backscatter coefficient (355 nm) calculated from measurements by the University of Manchester ozone and aerosol lidar over Leicester on 6th September 2007 [Image: courtesy of H. Ricketts].

To determine the AOD, knowledge of the aerosols extinction coefficient (α_{aero}) is required. The ratio of the extinction-to-backscatter coefficients, β_{aero} / α_{aero}, known as the Lidar Ratio (χ) can be determined by lab measurements. However, Vöelger *et al.* [1996] provided model based Lidar Ratios to be used for continental and marine environments according to the Global Aerosol Data Set. A lidar ratio of χ=55 steradians for continental air is used here.

The AOD is determined from the product of the aerosols extinction coefficient (α_{aero}) and the resolution of the lidar (ΔR).

$$AOD=\alpha_{aero}\times\Delta R \qquad \textbf{Equation 4-4}$$

During the LAMP campaign AOD measurements were averaged over 10 minutes, with a vertical resolution of 7.5 m, from 80 m to 5 km. The AOD retrieval below 80 m requires further analysis in the near-field data.

4.4 Aerosol measurements in the urban boundary layer by the DOAS technique

In situ monitors are traditionally used to measured aerosol properties as they can provide information on aerosols with high accuracy at the instruments location. More recently, however, remote sensing techniques have been employed to measure aerosols on a wider spatial scale, as previously discussed in section 1.6. It is also important for remote-sensing instruments to determine AOD as aerosols may influence the trace gas determinations. This section looks at the retrieval of aerosol information from the CMAX-DOAS instrument in the urban boundary layer along with aerosol measurements from the lidar instrument described in section 4.3 which was deployed alongside the CMAX-DOAS during the LAMP campaign.

The employment of DOAS systems to measure aerosol properties has previously been reported. Flentje *et al.*, [1997] performed measurements of gas species and the extinction coefficient using five spectral channels in the UV/visible wavelength region with a LP-DOAS instrument situated at Cape Arkona in Germany. The instrument was set up with two light paths of total path lengths 2750 km and 7030 km and the extinction coefficient was calculated from the intensity of the radiation measured by the short and long path lengths and difference in path length. The contributions to the extinction from Rayleigh scattering and absorption by trace gases were subtracted, resulting in extinction by aerosols only. The most common approach, however, to retrieve aerosol properties from DOAS systems is to observe the absorption of radiation in the O_4 bands in the UV, visible and near-infrared spectra.

DOAS retrievals of O_4 are often used to infer photon path lengths and as a tool for cloud detection from ground-based and satellite instruments. Clouds can shield the O_4 below the cloud layer when performing retrievals from satellite instruments. In general, the O_4 decreases with increasing altitude of the cloud, owing to the shielding of O_4 by the clouds [Acaretta *et al.*, 2004; Daniel *et al.*, 2003]. Tropospheric clouds may influence the ground-based DOAS retrievals of gases by enhancing the photon path length, owing to Mie scattering within the clouds [Van Roozendale *et al.*, 1994; Erle *et al.*, 1995; Wagner *et al.*, 1998, Pfeilsticker *et al*, 1999]. The O_4 profile is well known and almost constant within the troposphere,

therefore, an enhancement in the O_4 slant column may indicate an increase in path length owing to tropospheric clouds.

More recently, O_4 retrievals from LP-DOAS and MAX-DOAS instruments have been used to determine aerosol properties within the troposphere. A study on atmospheric absorption of O_4 using direct moonlight and zenith scattered sunlight, by Wagner *et al.*, [2002], involved a comparison between modelled and measured O_4 AMFs. The results show that the O_4 AMF is sensitive to changes in aerosol extinction. Wittrock *et al.*, [2004] demonstrated a good agreement between measured O_4 AMFs retrieved from a MAX-DOAS instrument, located at Ny-Ålesund and those modelled by the radiative transfer model, SCIATRAN. It was suggested that the AOD profile can be derived by varying the aerosol and albedo settings in the modelled O_4 calculations to match the O_4 DOAS measurements. This theory has since been evaluated in a series of papers by Wagner *et al.*, [2004] and Frieβ *et al.*, [2006].

The first of these studies looks at the use of MAX-DOAS systems to derive information on aerosols. A MAX-DOAS instrument, consisting of three movable telescopes at azimuthal angles of 5°, 185°, 250°, was deployed during the FORMAT II (Formaldehyde as a tracer for oxidation in the Troposphere) campaign in Italy in September 2003. Each telescope performs measurements at 3°, 6°, 10°, 18° and 90° elevation angles above the horizon and the O_4 DSCD were calculated from the spectral analysis between 335 and 367 nm. The results show that for an increasing aerosol load in the atmosphere the O_4 DSCS decrease overall, owing to the shorter light paths, as observed in Figure 4-6. In addition, the difference between the O_4 DSCDs at low elevation angles also decreases with increasing aerosol. The altitude of the aerosol layer also has an effect on the measured O_4 DSCDS.

A radiative transfer model (RTM) was used to model the O_4 AMFs during the measurement period. Four aerosol scenarios with varying altitude ranges and aerosol extinctions were used in the simulations. The results from the model runs agree well with the MAX-DOAS observations and demonstrate that MAX-DOAS O_4 measurements are very sensitive to aerosols near the surface. Additional work performed by Wagner *et al.*, [2004] on the magnitude of the Ring effect and relative intensity suggest that both of these may allow further information on aerosol properties to be derived from MAX-DOAS O_4 observations.

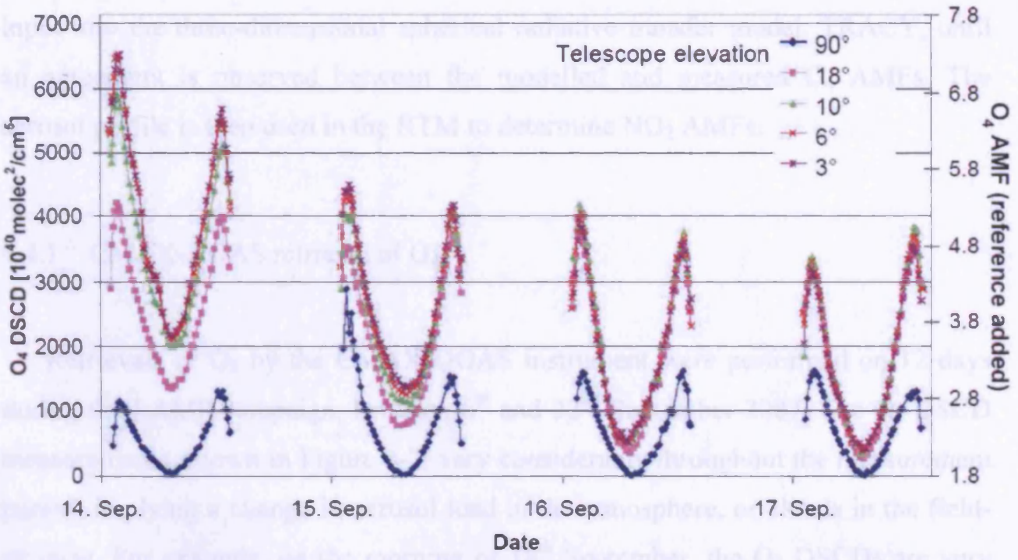

Figure 4-6: O_4 DSCDS and AMFs (calculated with a RTM) measured on 14th to 17th September 2003 for a telescope at 185° azimuth and elevation angles of 3°, 6°, 10°, 18° and 90° [Wagner *et al.*, 2004].

The second paper, by Freiß *et al.* [2006], focuses on an optimal estimation retrieval algorithm to determine aerosol properties using variations in the observed O_4 differential optical depths (DODs) and relative intensity at different viewing directions and wavelengths. The SCIATRAN model is used to simulate O_4 DODs and intensities at different solar zenith, elevation and azimuth angles, with varying aerosol scenarios. The outcomes of the model runs are then input into the optimal estimation model to retrieve the aerosol extinction profile. The results from the study demonstrate that O_4 from a single absorption band contains enough information to estimate the aerosol extinction in the lowermost 300 m of the atmosphere. For aerosols information at altitudes up to 3 km, multiple O_4 absorption bands are required. The precision of the AOD retrieval is greatly improved when including the variation of the observed intensity with viewing direction. At lower elevation angles an increase in the intensity is observed, owing to an increase in scattering by particles. The error in the retrieved AOD is similar when using only one or four O_4 bands with a precision in the AOD of 0.01 which is comparable to that of sun photometers and lidars, with the advantage that DOAS instruments are self-calibrating.

Sinreich *et al.*, [2005] demonstrated a simplified algorithm to retrieve aerosol extinction from MAX-DOAS O_4 measurements by varying an aerosol box profile,

input into the three-dimensional spherical radiative transfer model, TRACY, until an agreement is observed between the modelled and measured O_4 AMFs. The aerosol profile is then used in the RTM to determine NO_2 AMFs.

4.4.1 CMAX-DOAS retrieval of O_4

Retrievals of O_4 by the CMAX-DOAS instrument were performed on 12 days during the LAMP campaign, between 6th and 22nd September 2007. The O_4 DSCD measurements, shown in Figure 4-7, vary considerably throughout the measurement period, implying a change in aerosol load in the atmosphere, or clouds in the field-of view. For example, on the morning of 18th September, the O_4 DSCDs are very high with values up to 12000×10^{40} molecules^2 cm^{-5}. In addition, large separations are observed between the measurements from the low elevation angles on this day. The results from the lidar instrument on 18th September (Figure 4-7) demonstrate low AODs, with a maximum during the morning of AOD = 0.002. In comparison, the O_4 DSCDS on other days are much lower and in many cases do not have a significant separation between measurements from different elevation angles. The corresponding lidar AOD measurements show an increase in AOD on these occasions, compared to the 18th September. The results appear to agree with previous theories that for low elevation angles an increased aerosol load in the troposphere reduces the photon path length along the line-of-sight of the instrument, resulting in a decrease in O_4 DSCDS.

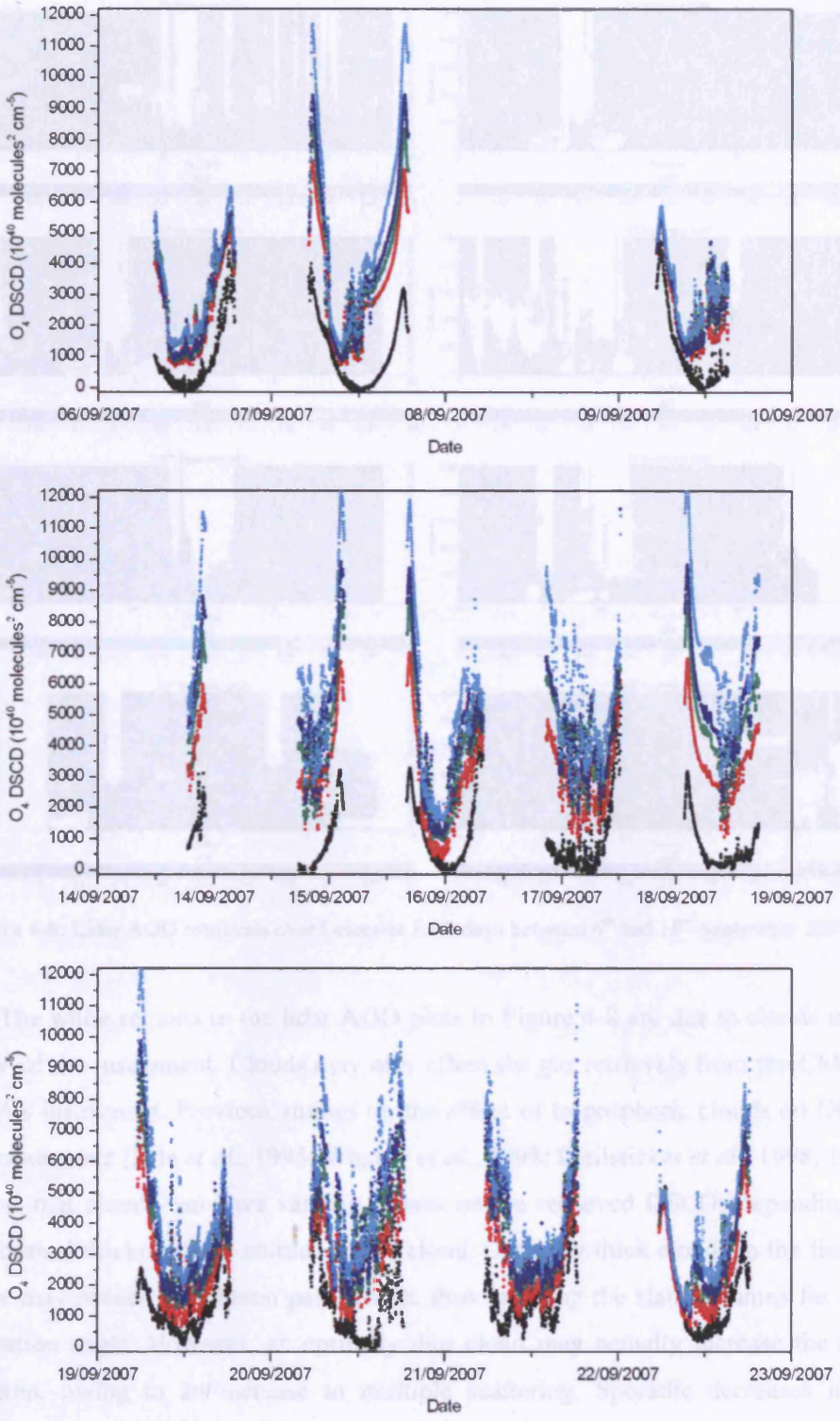

Figure 4-7: O_4 DSCDs measured by the zenith (black), 12° (red), 10° (green), 8° (dark blue), 6° (light blue) views on 11 days between 6th and 23rd September 2007.

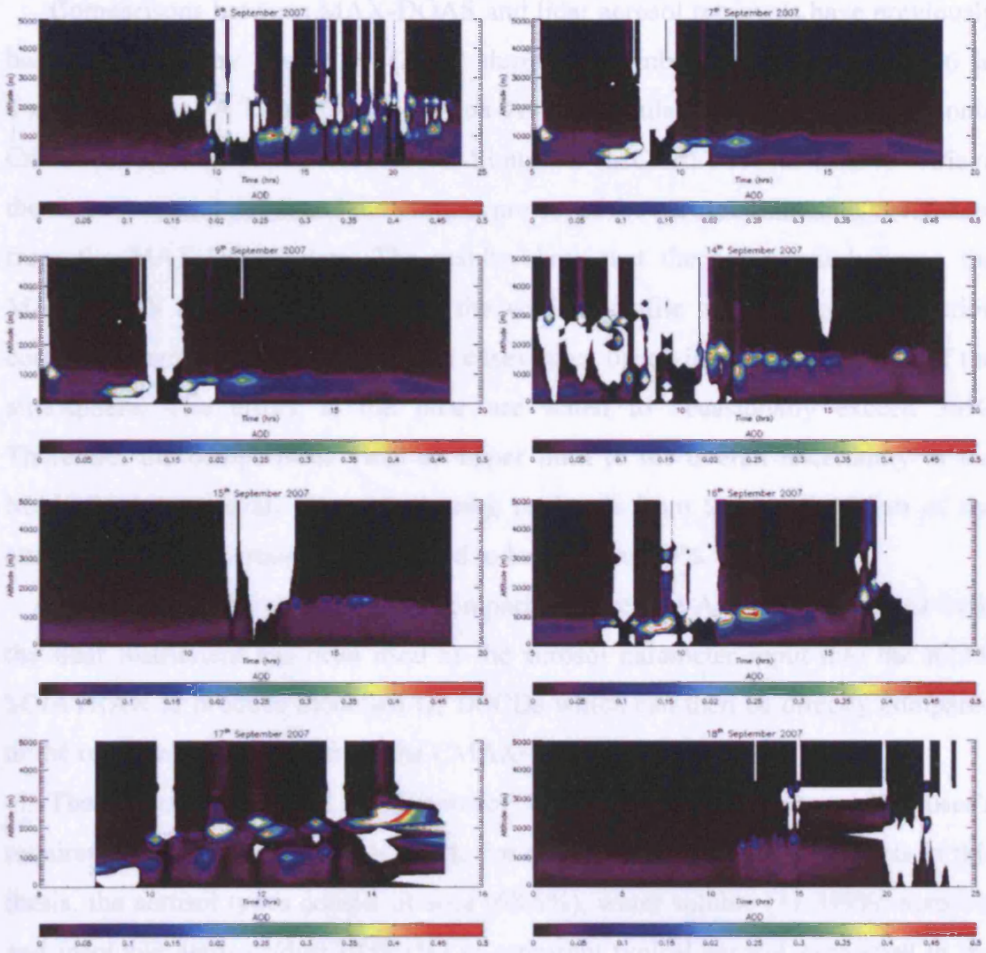

Figure 4-8: Lidar AOD retrievals over Leicester for 8 days between 6th and 18th September 2007.

The white regions in the lidar AOD plots in Figure 4-8 are due to clouds in the FOV of the instrument. Clouds may also effect the gas retrievals from the CMAX-DOAS instrument. Previous studies on the effect of tropospheric clouds on DOAS measurements [Erle *et al.*, 1995; Wagner *et al.*, 1998; Pfeilsticker *et al.*, 1998, 1999] report that clouds can have varying effects on the retrieved DSCDs depending on the optical thickness and altitude of the cloud. Optically thick clouds in the field of view may reduce the photon path length, thus reducing the slant columns for each elevation angle. However, an optically thin cloud may actually increase the slant column, owing to an increase in multiple scattering. Sporadic decreases in O_4 DSCD observed in the CMAX-DOAS data correspond to measurements of cloud from the lidar instrument, suggesting that optically thick clouds are present in the instruments field-of-view.

Comparisons between MAX-DOAS and lidar aerosol retrievals have previously been performed by Irie *et al.* (2007) during November and December 2006 in Tsukuba, Japan. A look-up-table of box AMFs calculated using the RTM Monte Carlo Atmospheric Radiative Transfer Simulator (MCARaTS) was used to retrieve the aerosol optical depth and the vertical profile of the aerosol extinction coefficient from the MAX-DOAS data. The results show that the agreement between the MAX-DOAS and lidar retrievals of the vertical profile of the aerosol extinction coefficient agree within 30% for most cases when observing the lowest 1 km of the atmosphere. The errors in the lidar are stated to occasionally exceed 30%. Therefore, the comparisons yield an upper limit to the overall uncertainty of the MAX-DOAS retrieval. When comparing retrievals from the bottom 2 km of the atmosphere the uncertainty is estimated to be less than 60%.

To perform a more quantitative comparison here, the AOD data retrieved from the lidar instrument has been used as the aerosol parameter input into the RTM, SCIATRAN to produce modelled O_4 DSCDs which can then be directly compared to the retrieved O_4 DSCDs from the CMAX-DOAS instrument.

The aerosol type and AOD/aerosol extinction can be set to the user's requirements in the SCIATRAN RTM. For the analysis of O_4 measurements in this thesis, the aerosol types consist of soot (68.6%), water soluble (31.399%) aerosols and insoluble aerosols/dust (0.001%) to represent typical aerosol properties in the urban boundary layer. The aerosol profile was set to 25 altitude levels, with altitudes of 200 m from 0 to 4 km and 250 m from 4 to 5 km, to reduce computational time. The lidar instrument measured the AOD every 7.5 m from 80 m up to 5 km. To derive the AOD within a 200/250 m layer, the sum of the AODs within the layer is calculated, resulting in larger AODs with a coarse vertical resolution.

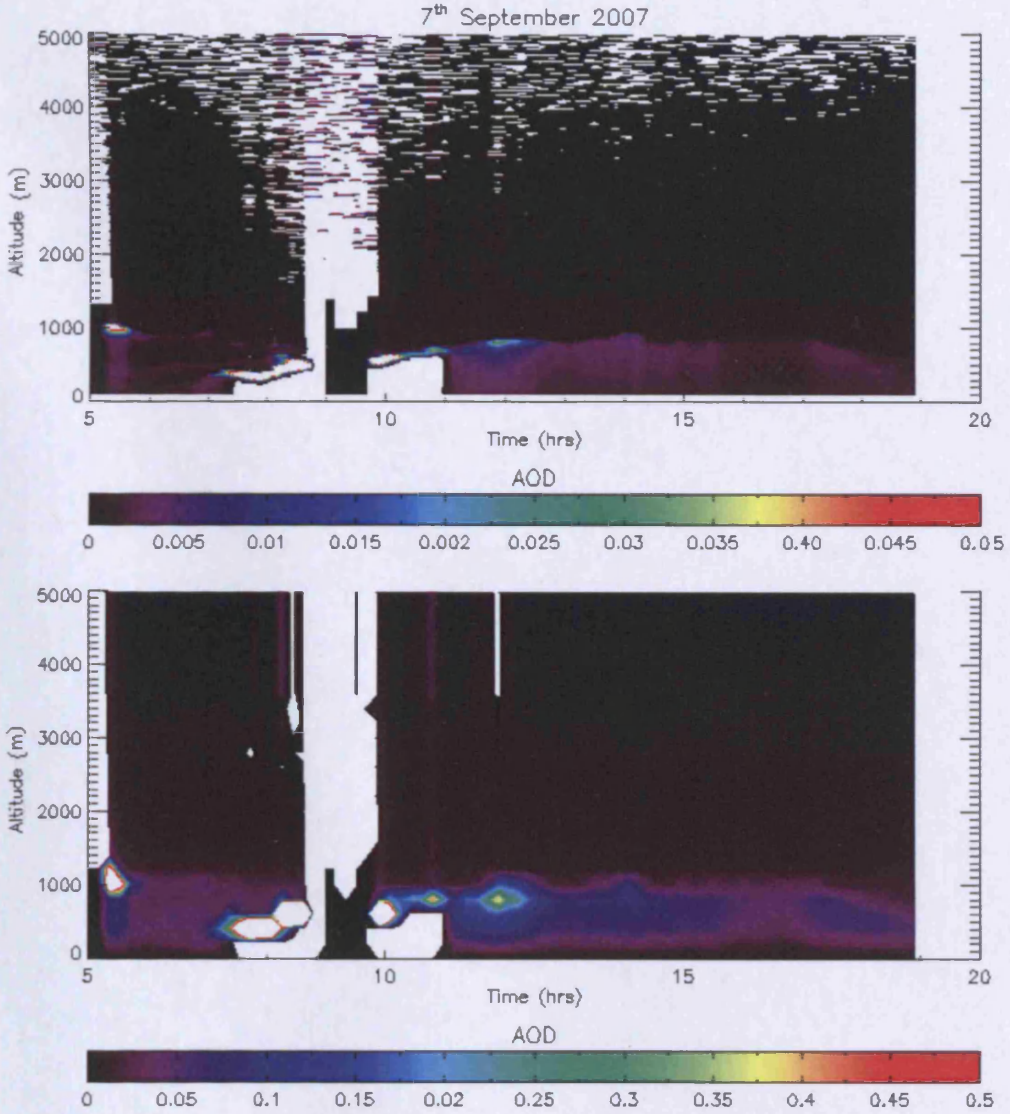

Figure 4-9: Top figure shows the AOD retrieved from the lidar with a vertical resolution of 7.5 m. Bottom figure shows the AOD integrated over 200 m from 0 to 4 km and 250 m from 4 to 5 km.

Figure 4-9 shows a plot of AOD retrieved by the lidar on 7th September 2007, with a vertical resolution of 7.5 m (top figure) and the total AODs over 25 altitude levels (bottom figure). The results demonstrate that the process retains most of the vertical structure in the AOD retrievals. A maximum altitude of 5 km is sufficient for the comparisons performed here as aerosols at higher altitudes do not significantly influence the retrievals in the boundary layer [Frieß *et al.*, 2006; Irie *et al.*, 2007].

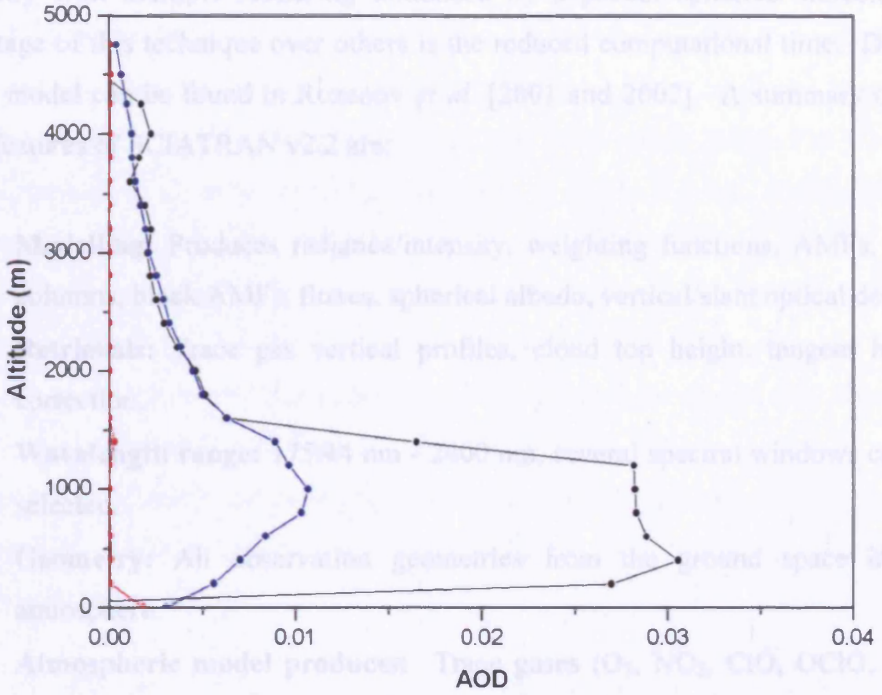

Figure 4-10: AOD measured by the lidar instrument for 31st August 2007. The black line represents the lidar AOD integrated over 200 m from 0 to 4 km and 250 m from 4 to 5 km. The blue line represents the lidar AOD corrected for the misalignment and the red line represents the AOD retrieval error.

Figure 4-10 shows the typical error on the retrieved AOD for the lidar instrument for the AOD integrated over 200 m from 0 to 4 km and 250 m from 4 to 5 km. In general, the lidar error is smaller than 1% of the total AOD. The blue line represents an offset in the retrieved AODs from the lidar, owing to a misalignment between the focal plane of the telescope and the detector. The offset at each altitude is approximately a third of the calculated AOD and should be subtracted from the measurement. However, the lidar data is still preliminary and offsets have not been calculated for all measurements.

4.4.2 Modelled O_4 slant columns with SCIATRAN

The radiative transfer model SCIATRAN (v2.2) was used to interpret the observations performed in this thesis. SCIATRAN was developed at the Institute of Environmental Physics at the University of Bremen and features full spherical

geometry with multiple scattering initialized by a pseudo-spherical model. The advantage of this technique over others is the reduced computational time. Details of the model can be found in Rozanov *et al.* [2001 and 2002]. A summary of the main features of SCIATRAN v2.2 are:

- **Modelling:** Produces radiance/intensity, weighting functions, AMFs, slant columns, block AMFs, fluxes, spherical albedo, vertical/slant optical depth.
- **Retrievals:** Trace gas vertical profiles, cloud top height, tangent height correction.
- **Wavelength range:** 175.44 nm - 2400 nm, several spectral windows can be selected.
- **Geometry:** All observation geometries from the ground space in the atmosphere.
- **Atmospheric model products:** Trace gases (O_3, NO_2, ClO, OClO, BrO, HCHO, SO_2, NO_3, O_4, O_2, H_2O, CO_2, CO, CH_4, and N_2O), aerosols, and clouds.
- **Earth surface:** Lambertian reflector with (wavelength dependent) albedo. The surface elevation with respect to the sea level can be specified.

For the analysis performed here, DSCDs of O_4 were calculated with the SCIATRAN RTM for each elevation angle, incorporating the input parameters summarised in Table 4-2.

Table 4-2: Summary of the main inputs in the SCIATRAN RTM for the calculation of O_4 DSCDs

Parameter	**Input**	**Comments**
Albedo	0.15	Typical value for urban area
Wavelength	477 nm	
Trace gas profile	Standard profiles	Appropriate to month and instrument latitude
Aerosol	AOD from lidar	Urban aerosol (Soot, water soluble, dust) 25 altitude levels (0 to 4 km: 200 m resolution. 4 to 5 km: 250 m resolution.

The wavelength setting in SCIATRAN is very important owing to the strong wavelength dependence of Rayleigh scattering in the atmosphere. In general, for increasing wavelengths the optical depth of the atmosphere decreases, hence an increase in the O_4 DSCDs [Wagner *et al.*, 2004; Frieß *et al.*, 2006]. The CMAX-DOAS retrieval of O_4 is performed in a window of 425 to 490 nm, which includes O_4 absorption bands at 447 nm and 477 nm. For this thesis, O_4 DSCDs were modelled at the maxima of the 477 nm wavelength band, to represent the strong O_4 band used in the CMAX-DOAS analysis. An albedo of 0.15 is used in the RTM, which is typical for an urban area, however differences in the albedo may introduce errors in the modelled O_4 DSCDs.

The effect of scattering owing to aerosols has wavelength dependence and the difference in AOD at two wavelengths (λ_0, λ) can be approximated using the Angström relation.

$$AOD_{\lambda} = AOD_{\lambda_0}\left(\frac{\lambda}{\lambda_0}\right)^{-\alpha} \qquad \textbf{Equation 4-5}$$

α is known as the Angström coefficient and can provide information on the particle size (the coefficient increases with smaller particle sizes).

González *et al.* [2003] retrieved AOD and Angström coefficients over Europe using data from the ATSR-2 radiometer on board the ESA satellite ERS-2, for August 1997. The results show that for industrial regions over Europe, the Angström coefficient ranges between 0.8 and 1.6. For the analysis performed here, the lidar retrieves AOD at 355 nm and the SCIATRAN RTM is modelling O_4 DSCDS at 458 nm. Using the Angström relation, the difference in AOD at 458 nm compared to 355 nm is 18 to 34 % for an Angström coefficient between 0.8 and 1.6. Therefore the AOD retrieved from the O_4 DSCDs is likely to be underestimated by 26% on average.

During LAMP, concurrent lidar and CMAX-DOAS measurement were performed on 8 days. The lidar measurements were integrated over a 10 minute period; therefore, modelled O_4 DSCDs were produced every 10 minutes and compared directly to the slant columns retrieved from the CMAX-DOAS instrument.

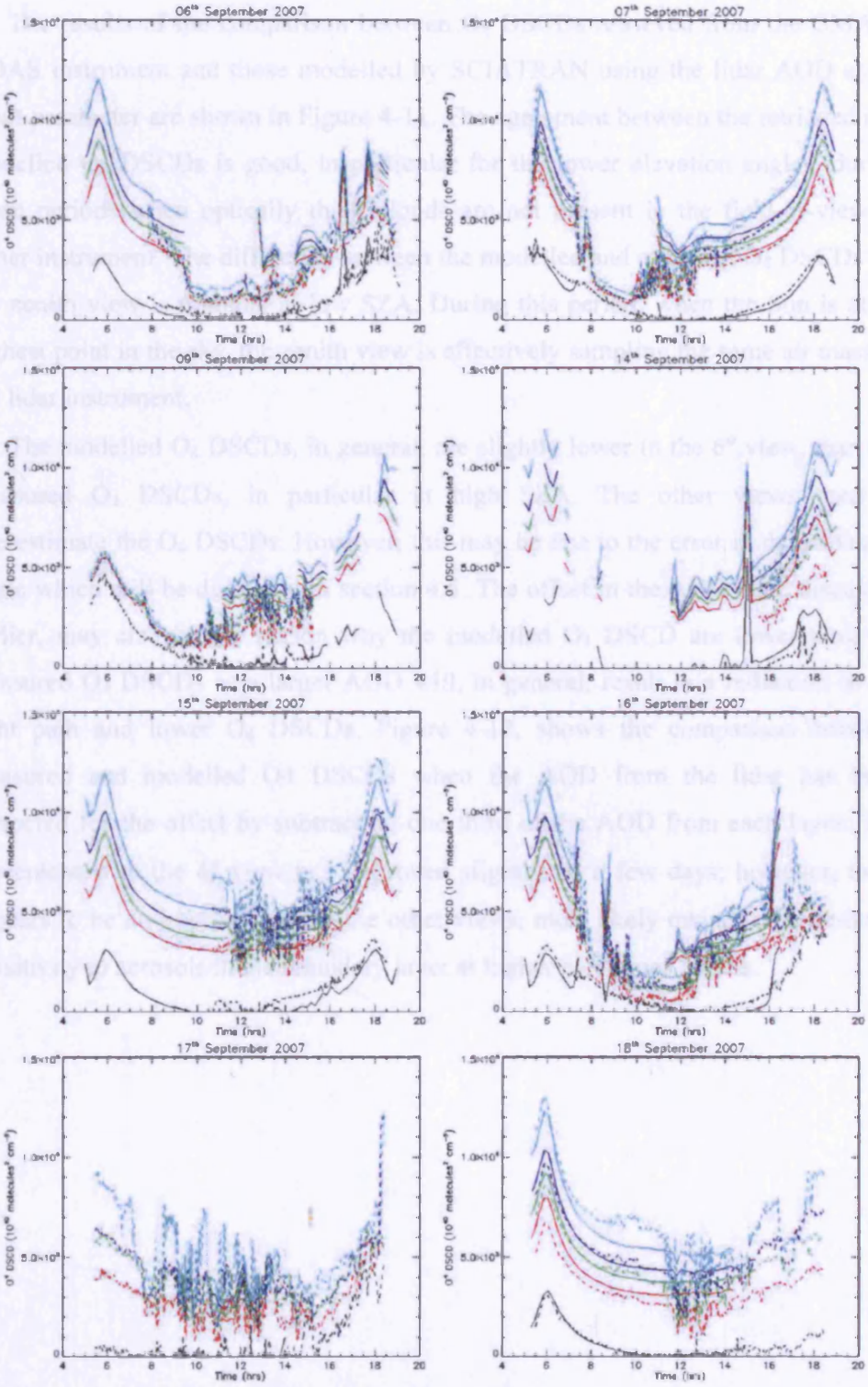

Figure 4-11: O_4 DSCDs retrieved from the CMAX-DOAS instrument (dashed lines) and modelled by SCIATRAN using the lidar AOD as an input parameter (solid lines), for the zenith (black), 12° (red), 10° (green), 8° (dark blue), 6° (light blue) views on 8 days between 6th and 18th September 2007.

The results of the comparison between O_4 DSCDs retrieved from the CMAX-DOAS instrument and those modelled by SCIATRAN using the lidar AOD as an input parameter are shown in Figure 4-11. The agreement between the retrieved and modelled O_4 DSCDs is good, in particular for the lower elevation angles, during those periods when optically thick clouds are not present in the field-of-view of either instrument. The difference between the modelled and retrieved O_4 DSCDs for the zenith view is minimal at low SZA. During this period, when the Sun is at its highest point in the sky, the zenith view is effectively sampling the same air mass as the lidar instrument.

The modelled O_4 DSCDs, in general, are slightly lower in the 6° view, than the measured O_4 DSCDs, in particular at high SZA. The other views tend to overestimate the O_4 DSCDs. However, this may be due to the error in the elevation angle which will be discussed in section 4.5. The offset in the AOD data, discussed earlier, may also be the reason why the modelled O_4 DSCD are lower than the measured O_4 DSCDs as a larger AOD will, in general, result in a reduction in the light path and lower O_4 DSCDs. Figure 4-12, shows the comparison between measured and modelled O4 DSCDs when the AOD from the lidar has been corrected for the offset by subtracting one third of the AOD from each layer. The agreement with the 6° view has improved slightly on a few days; however, there appears to be no improvement in the other views, most likely owing to the reduced sensitivity to aerosols in the boundary layer at higher elevations angles.

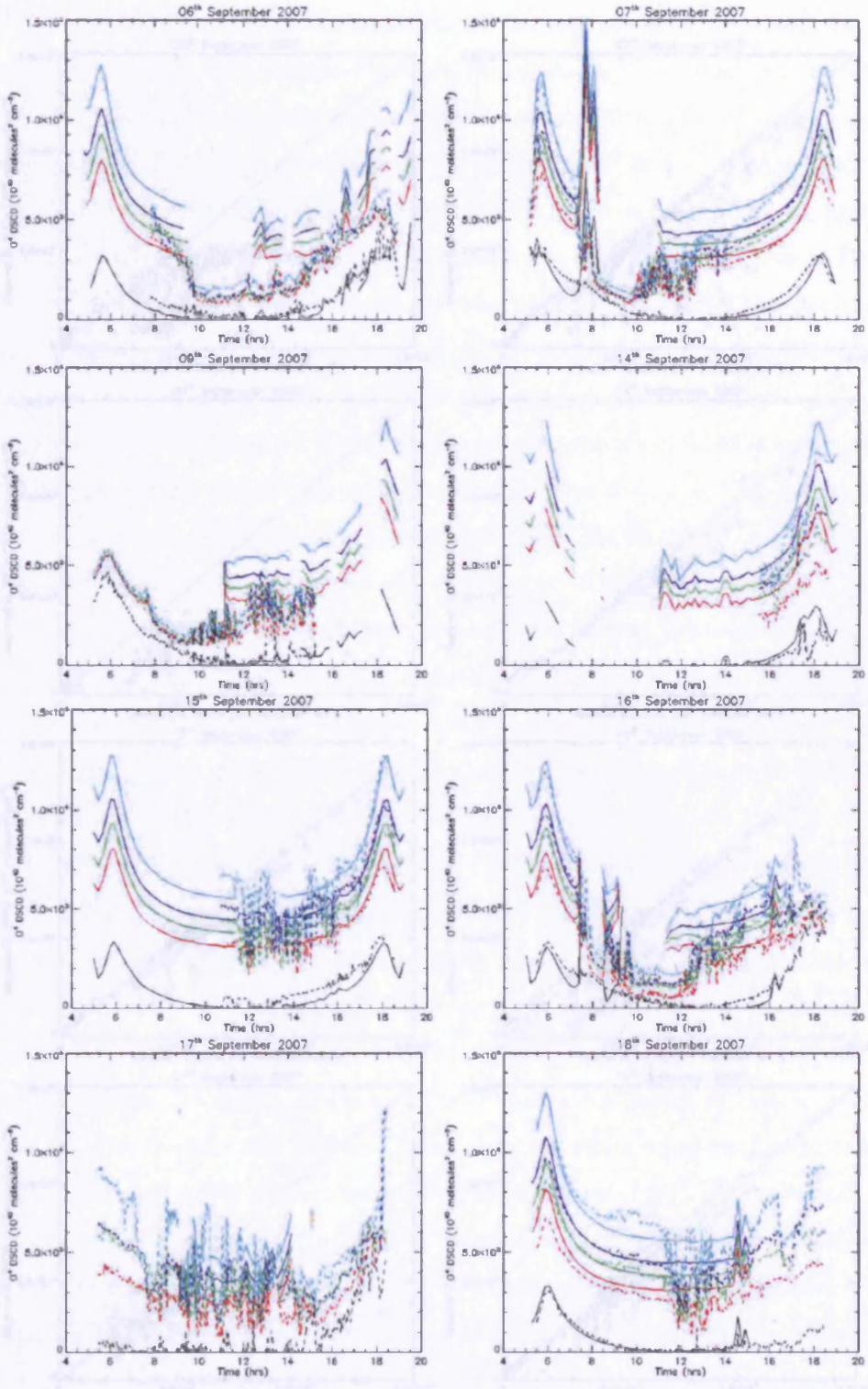

Figure 4-12: O_4 DSCDs retrieved from the CMAX-DOAS instrument (dashed lines) and modelled by SCIATRAN using the lidar AOD, which has been corrected for an offset, as an input parameter (solid lines), for the zenith (black), 12° (red), 10° (green), 8° (dark blue), 6° (light blue) views on 8 days between 6th and 18th September 2007.

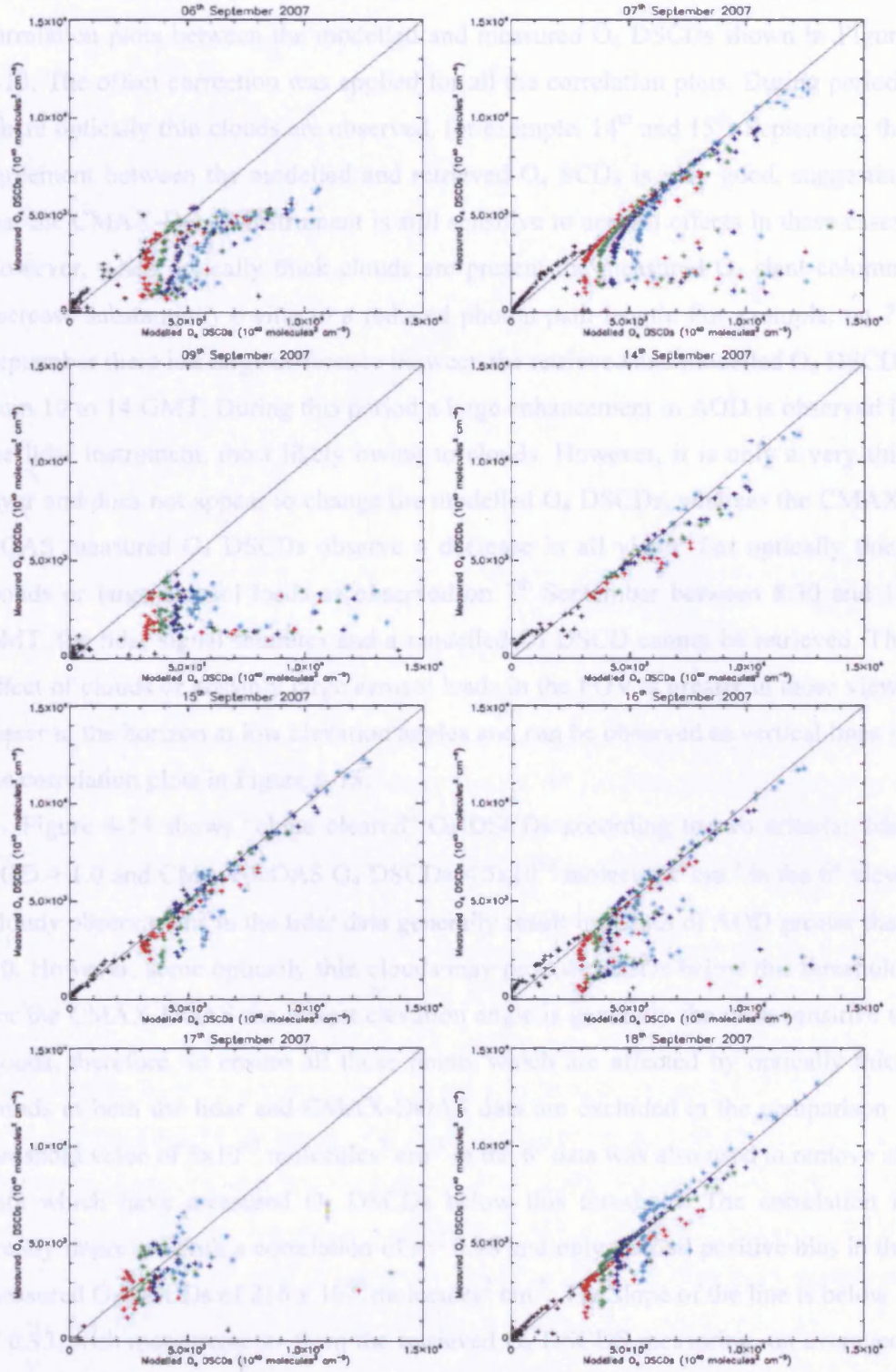

Figure 4-13: Comparison between measured O_4 DSCDs retrieved from the CMAX-DOAS instrument and modelled O_4 DSCDs by SCIATRAN using the lidar AOD as an input parameter (offset corrected), for the zenith (black), 12° (red), 10° (green), 8° (dark blue), 6° (light blue) views on 8 days between 6th and 18th September 2007. The grey lines represent the 1:1 line.

The effect of clouds on the retrieval of O_4 and aerosols is evident in the correlation plots between the modelled and measured O_4 DSCDs shown in Figure 4-13. The offset correction was applied for all the correlation plots. During periods where optically thin clouds are observed, for example, 14th and 15th, September, the agreement between the modelled and retrieved O_4 SCDs is very good, suggesting that the CMAX-DOAS instrument is still sensitive to aerosol effects in these cases. However, when optically thick clouds are present the measured O_4 slant columns decrease substantially owing to a reduced photon path length. For example, on 7th September there is a large difference between the retrieved and modelled O_4 DSCDs from 10 to 14 GMT. During this period a large enhancement in AOD is observed in the lidar instrument, most likely owing to clouds. However, it is only a very thin layer and does not appear to change the modelled O_4 DSCDs, whereas the CMAX-DOAS measured O_4 DSCDs observe a decrease in all views. For optically thick clouds or large aerosol loads as observed on 7th September between 8:30 and 10 GMT, the lidar signal saturates and a modelled O_4 DSCD cannot be retrieved. The effect of clouds or possibly large aerosol loads in the FOV is greater in those views closer to the horizon at low elevation angles and can be observed as vertical lines in the correlation plots in Figure 4-13.

Figure 4-14 shows "cloud cleared" O_4 DSCDs according to two criteria; lidar AOD > 1.0 and CMAX-DOAS O_4 DSCDs < $5x10^{43}$ molecules^2 cm^{-5} in the 6° view. Cloudy observations in the lidar data generally result in values of AOD greater than 1.0. However, some optically thin clouds may produce AODs below this threshold. For the CMAX-DOAS the lowest elevation angle is generally the most sensitive to clouds, therefore, to ensure all those points which are affected by optically thick clouds in both the lidar and CMAX-DOAS data are excluded in the comparison a threshold value of $5x10^{43}$ molecules^2 cm^{-5} in the 6° data was also used to remove all data which have measured O_4 DSCDs below this threshold. The correlation is greatly improved with a correlation of r = 0.98 and only a small positive bias in the measured O_4 DSCDs of 216×10^{40} molecules^2 cm^{-5}. The slope of the line is below 1 at 0.93, with measurements from the retrieved O_4 DSCDS measuring, on averaged, 7% lower than the modelled O_4 DSCDs using the lidar AOD as an input parameter.

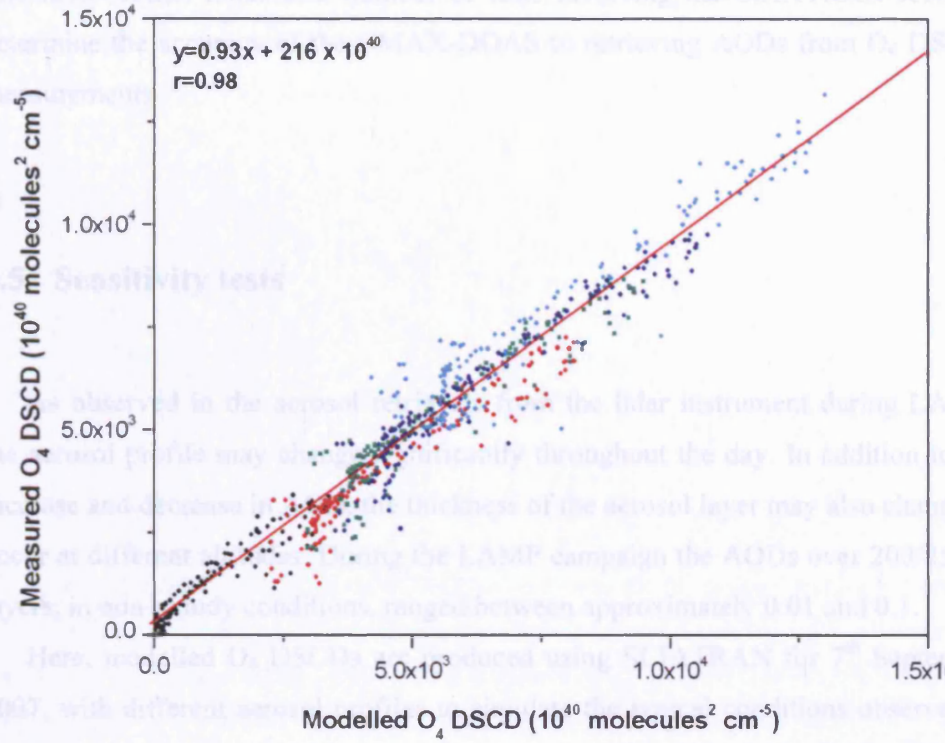

Figure 4-14: Comparison between measured O_4 DSCDs retrieved from the CMAX-DOAS instrument and modelled O_4 DSCDs by SCIATRAN using the lidar AOD (offset corrected) as an input parameter for the zenith (black), 12° (red), 10° (green), 8° (dark blue), 6° (light blue) views on 8 days between 6th and 18th September 2007. Cloudy measurements have been removed using the criteria described in the main text. The red line represents the linear regression of the correlation.

The good agreement between the measured O_4 DSCDs retrieved by the CMAX-DOAS instrument and those modelled by SCIATRAN using the lidar AOD as an input parameter, suggests that the CMAX-DOAS may be used to retrieve AOD, in the boundary layer by adjusting the aerosol profile in the SCIATRAN RTM until the modelled O_4 DSCDS agree with those measured by CMAX-DOAS. Optimal estimation [Seinreich *et al.*, 2005; Writtock *et al.*, 2002; Wagner *et al.*, 2002; 2004; Frieβ *et al.*, 2006;] or look-up-table methods [Leigh *et al.*, 2007; Irie *et al.*, 2007] have previously been used to vary the AOD profile and obtain an agreement between measured and modelled O_4 DSCDs or AMFs.

In addition to the absolute AOD, the aerosol profile shape may also change the observed O_4 DSCDs. Understanding how the profile shape effects the measurements may improve the accuracy of the AOD retrieval and reduce the number of profiles used in either the look-up-table or optimal estimation methods.

The next section looks at a number of tests involving the SCIATRAN RTM to determine the accuracy of the CMAX-DOAS to retrieving AODs from O_4 DSCDs measurements.

4.5 Sensitivity tests

As observed in the aerosol retrievals from the lidar instrument during LAMP, the aerosol profile may change significantly throughout the day. In addition to the increase and decrease in AOD, the thickness of the aerosol layer may also change or occur at different altitudes. During the LAMP campaign the AODs over 200/250 m layers, in non-cloudy conditions, ranged between approximately 0.01 and 0.1.

Here, modelled O_4 DSCDs are produced using SCIATRAN for 7th September 2007, with different aerosol profiles to simulate the typical conditions observed in Leicester, the results of which are used to determine the effect on the O_4 DSCDs.

4.5.1 Aerosol layer height

The effect of the aerosol layer height on the O_4 retrieval was investigated by calculating modelled O_4 DSCDs from SCIATRAN for each of the elevation angles used in the CMAX-DOAS retrieval. A box aerosol profile with a layer thickness of 100 m at altitudes between 200 m and 2 km and maximum AODs of 0.01 and 0.1 were used to simulate typical aerosol levels observed in Leicester.

The results of the simulations, shown in Figure 4-15 demonstrate that for very low AODs the layer height does not appear to have a large effect on the O_4 DSCDs, the standard deviation of the O_4 DSCDs for the 6° view is 3.92×10^{40} molecules^2 cm^{-5} at a SZA of 60°. When observing higher AODs, the effect is greater and the standard deviation of the O_4 DSCDs increases to 40.6×10^{40} molecules^2 cm^{-5}. In general, aerosols near the surface increase the optical depth of the atmosphere, thus reducing the measured O_4 DSCDs. However, when aerosol is present in layers at

different altitudes, the effect of multiple scattering may enhance the O_4 DSCDs for those views with scattering altitudes below or within the aerosol layer.

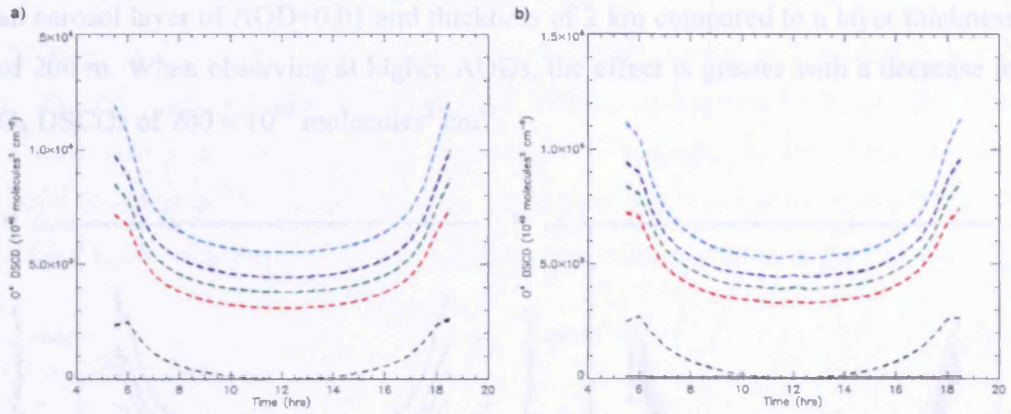

Figure 4-15: Modelled O_4 DSCDs by SCIATRAN at 477nm, for the zenith (black), 12° (red), 10° (green), 8° (dark blue), 6° (light blue). There are multiple lines at each viewing angle in the plot. The aerosol was modelled as a box profile with a maximum AOD of a) 0.01 and b) 0.1, and a layer thickness of 100 m at altitudes between 200 m and 2 km.

The results here suggest that the O_4 DSCDs do not appear to be sensitive to the height of the aerosol layer with AODs of the magnitude observed in Leicester. Averaging kernels produced by Frieβ *et al.* (2006) demonstrate that that the information on aerosols at higher altitudes is greatly improved when retrieving O_4 at different wavelengths.

4.5.2 Thickness of the aerosol layer

The thickness of the aerosol layer as retrieved by the lidar instrument during LAMP was observed to vary throughout the day, from approximately 600 m to 2 km, depending on the PBL height and cloud layers. Figure 4-16 show the results from a simulation of O_4 DSCDs from SCIATRAN, with an aerosol layer increasing in thickness from the surface, in 200 m steps, up to a maximum of 2 km, with a maximum AOD of 0.01 and 0.1

The results, presented in Figure 4-16, demonstrate the effect of the aerosol layer thickness on the modelled O_4 DSCDs is strong in comparison to the altitude of the aerosol layer, as shown in the previous test. As the layer thickness increases the O_4

DSCDs decrease owing to a reduction in the photon path length. The lower elevation angles show the greatest variation, with a decrease in AOD of approximately 400 x 10^{40} molecules^2 cm^{-5} for the O_4 DSCDs from the 6° view with an aerosol layer of AOD=0.01 and thickness of 2 km compared to a layer thickness of 200 m. When observing at higher AODs, the effect is greater with a decrease in O_4 DSCDs of 700 × 10^{40} molecules^2 cm^{-5}.

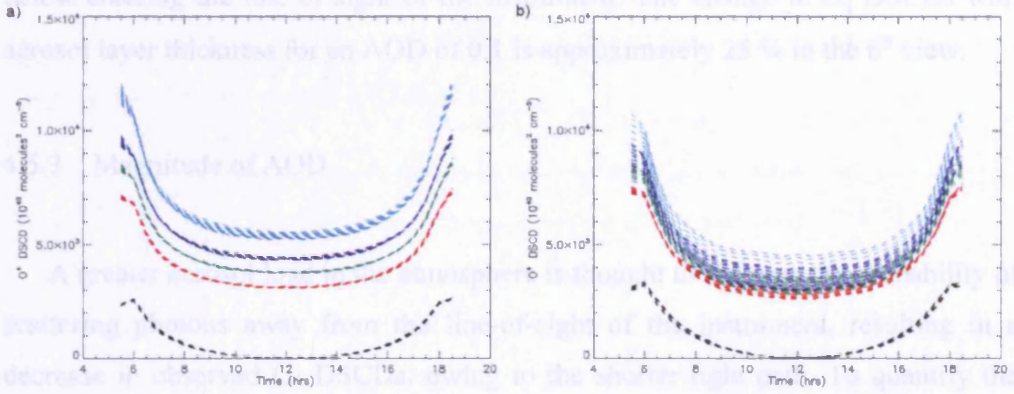

Figure 4-16: Modelled O_4 DSCDs by SCIATRAN, for the zenith (black), 12° (red), 10° (green), 8° (dark blue), 6° (light blue). The aerosol layer was modelled as a box profile with a maximum AOD of 0.01 and increased in thickness by 200 m up to 2 km.

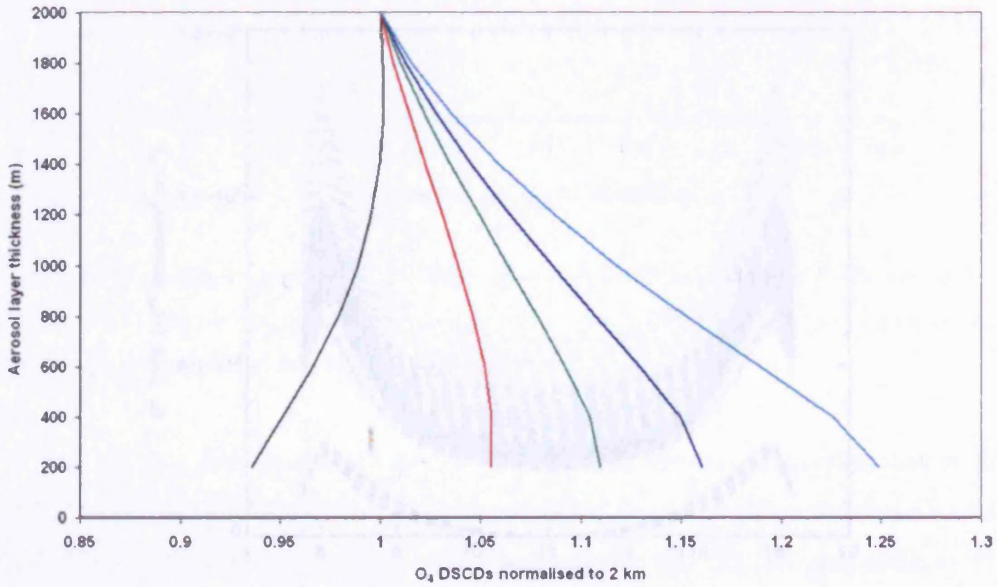

Figure 4-17: Modelled O_4 DSCDs by SCIATRAN, for the zenith (black), 12° (red), 10° (green), 8° (dark blue), 6° (light blue). The aerosol layer was modelled as a box profile with a maximum AOD of 0.01 and increased in thickness by 200 m up to 2 km.

In Figure 4-17, a plot of O_4 DSCDs modelled with SCIATRAN and normalised to the O_4 DSCDs at 2 km for each of the lower elevations angles is presented. The results show that the O_4 DSCDs simulated for the 6°, 8° , 10° and 12° views, decrease as the aerosol layer increases in thickness, owing to a reduction in the photon path length. However, the zenith observes an increase in O_4 DSCDs with aerosol, which may be caused by an increase in scattered photons from the layer below entering the line of sight of the instrument. The change in O_4 DSCDs with aerosol layer thickness for an AOD of 0.1 is approximately 25 % in the 6° view.

4.5.3 Magnitude of AOD

A greater aerosol load in the atmosphere is thought to increase the probability of scattering photons away from the line-of-sight of the instrument, resulting in a decrease in observed O_4 DSCDs, owing to the shorter light path. To quantify the effect on the different views of the CMAX-DOAS instrument, SCIATRAN was used to model O_4 DSCDs for a range of AODs with a 1 km layer thickness from the surface. The magnitude of the AOD was increased from 0.01 to 0.22 in steps of 0.01.

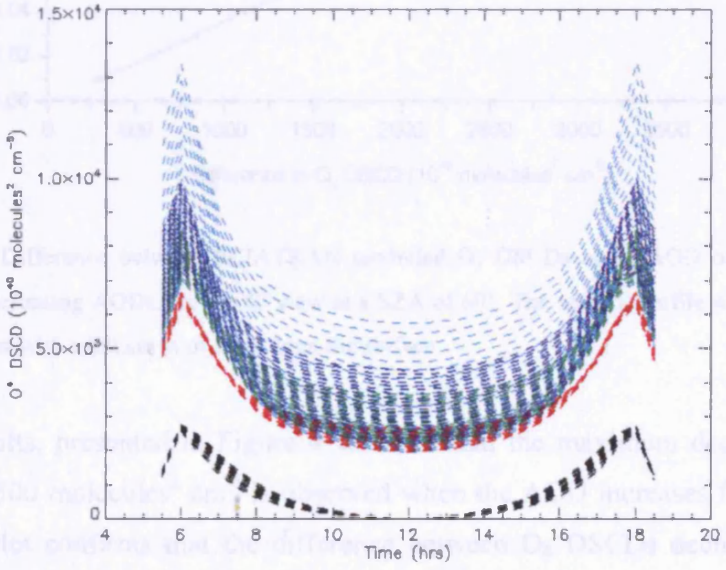

Figure 4-18: Modelled O_4 DSCDs by SCIATRAN, for the zenith (black), 12° (red), 10° (green), 8° (dark blue), 6° (light blue). The aerosol layer was modelled as a box profile with a 1 km thickness from the surface and the magnitude of the AOD increased in steps of 0.01 up to a maximum of 0.22.

From the results in Figure 4-18, it can be observed that an increase in AOD decreases the modelled O_4 DSCDs for all views, however, the sensitivity is greatly increased for lower elevation angles. As the AOD increases, additional aerosol scattering results in the difference between O_4 DSCDs at each view decreasing, until the views are independent of the direct photon light path. This effect has previously been seen in measurements by Wagner *et al*, [2004] and is also observed in the LAMP data (see section 4.4.2). The difference between the O_4 DSCDs modelled with an AOD of 0.01 and the O_4 DSCDs modelled at increasing aerosols loads was calculated for the 6° view at a SZA of 60°.

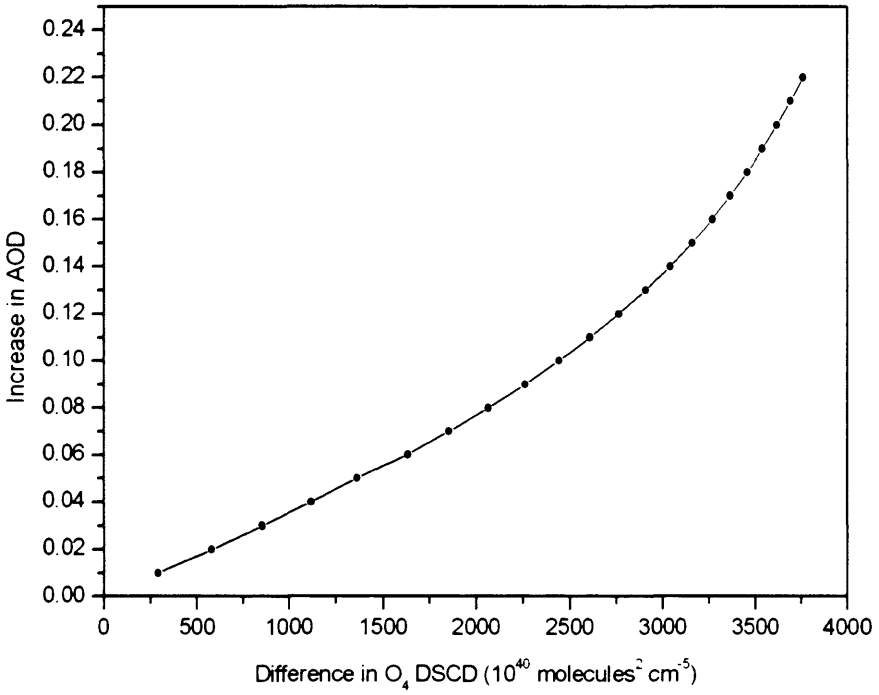

Figure 4-19: Difference between SCIATRAN modelled O_4 DSCDs at an AOD of 0.01 and O_4 DSCDs, for increasing AODs, for the 6° view at a SZA of 60°. The aerosol profile was modeled as an aerosol layer with a thickness of 1 km from the surface.

The results, presented in Figure 4-19 show that the maximum decrease in O_4 DSCD of 3500 molecules^2 cm^{-5} is observed when the AOD increases from 0.01 to 0.24. The plot confirms that the difference between O_4 DSCDs decreases as the magnitude of the AOD increase. For example, an increase in AOD of 0.01 between 0.01 and 0.02 decreases the O_4 DSCDs in the 6° view by 300×10^{40} molecules^2 cm^{-5}. However, for an increase in 0.01 between 0.22 and 0.23 the O_4 DSCDs only

decrease by approximately 70×10^{40} molecules^2 cm^{-5}, suggesting that the increase in photons owing to multiple scattering within the aerosol layer becomes comparable to the decrease in direct photon path length.

4.5.4 Elevation angle

As demonstrated previously, the sensitivity of the CMAX-DOAS to aerosols in the boundary layer can change significantly when measuring at different elevation angles, owing to the variation in photon path length. Therefore, an accurate elevation angle is important when comparing modelled and measured O_4 DSCDs. The telescopes within the head unit of the CMAX-DOAS instrument can be fixed to different elevation angles with an accuracy of approximately ±1.0°.

To calculate the effect of the elevation error on the O_4 DSCDs, modelled O_4 DSCDs were calculated for elevation angles of 6°, 5.9°, 5.8°, 5.7°, and 5.6° and 5.5° with an aerosols profile of AOD=0.01 and layer thickness of 1 km for the ground. The results of the modelled O_4 DSCDs for a change in elevation angle of up to 0.5° are shown in Figure 4-20.

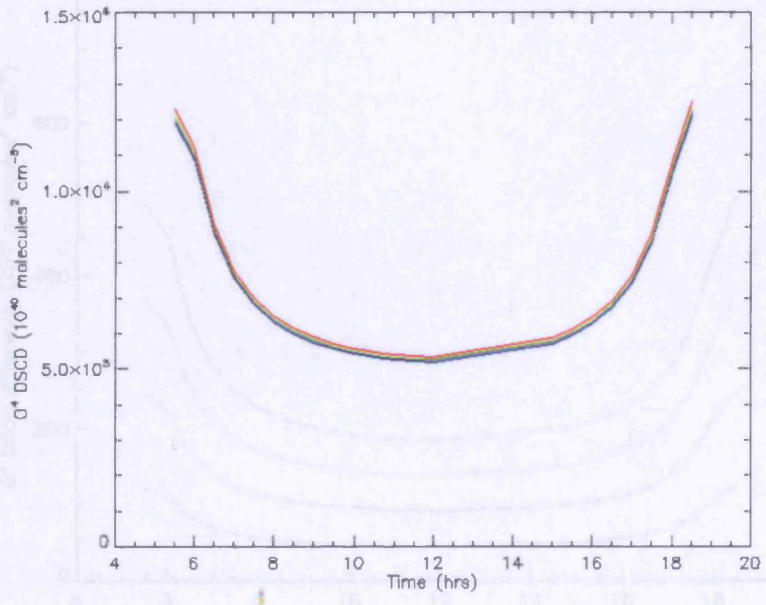

Figure 4-20: Modelled O_4 DSCDs by SCIATRAN, for five different elevation angles at 6° (black), 5.9° (purple), 5.8° (blue), 5.7° (red), 5.6°(green), and 5.5°(yellow). The aerosol layer was modelled as a box profile with a 1 km thickness and an AOD of 0.01.

To quantify the effect of elevation error, the difference between the O_4 DSCDs at 6° and those at the other elevation angles was determined. The results, presented in Figure 4-21, show for small SZAs the difference in O_4 DSCDs is almost constant and increases by approximately 50 $\times 10^{40}$ molecules^2 cm^{-5} for a decrease in elevation of 0.1°. Therefore, for an error in the elevation angle of ±1.0°, this results in an error in the modelled O_4 DSCDs of approximately ±500$\times 10^{40}$ molecules^2 cm^{-5}. In section 4.4.2, the results in Figure 4-13 show the retrieved O_4 DSCDs from CMAX-DOAS observe on average 5% smaller columns than the modelled O_4 DSCDs using the lidar AOD as an input parameter. For the 6° view, this results in the measured O_4 DSCDs observing smaller columns of approximately 300 to 600$\times 10^{40}$ molecules^2 cm^{-5}, depending on SZA angle compared to the modelled columns. Therefore, the error in the elevation angle may be an explanation for the differences observed and that the elevation angle for the 6° is actually at approximately 6.6°. However, there are other sources of error owing to the lidar ratio, the optical properties of aerosols and those introduced from the SCIATRAN modelling of O_4 DSCDs which may also introduce differences between the modelled and measured O_4 DSCDs.

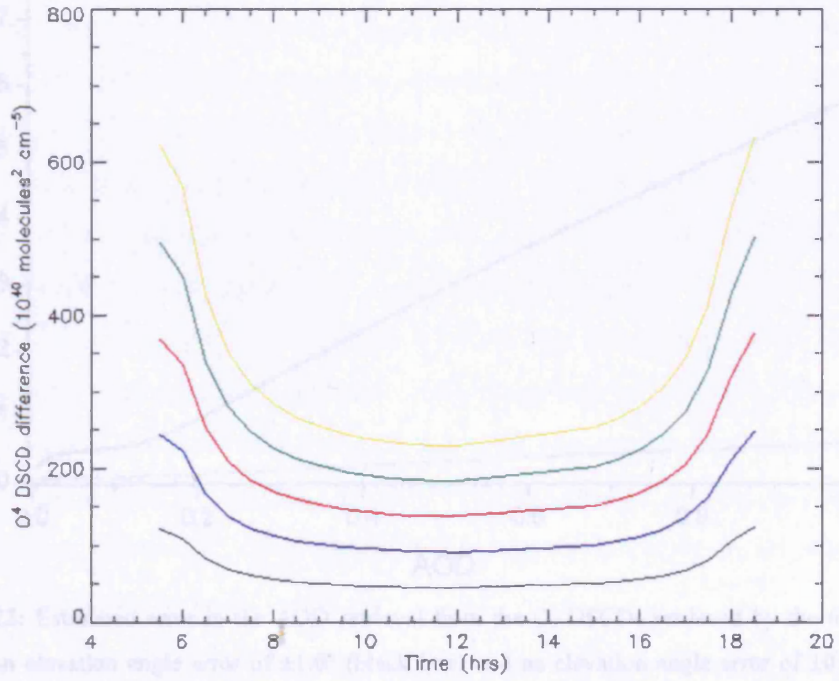

Figure 4-21: Difference in calculated O_4 DSCDs from SCIATRAN for a decrease in elevation angle from the 6° view of 0.1° (purple), 0.2° (blue), 0.3°(red), 0.4° (green) and 0.5°(yellow). The aerosol layer was modelled as a box profile with a 1 km thickness and an AOD of 0.01.

The error in the modelled O_4 DSCDs from the 6° view owing to the accuracy in the elevation angle (±1.0°) can be converted into an error in the AOD from the results in Figure 4-19, for a SZA of 60° and aerosol layer thickness of 1 km. A polynomial was fitted to the points in Figure 4-19, to determine the relationship between the change in O_4 DSCDs in the 6° view and the AOD magnitude, between 0.01 and 1.0. The error in the AOD was then calculated by assuming an error in the DSCDs of $\pm 500 \times 10^{40}$ molecules^2 cm^{-5}.

The result in Figure 4-22 show that the theoretical elevation error ranges between 0.01 to 0.55 for AODs between 0.01 and 1, retrieved from the O_4 DSCDs in the 6° view. The red line in the figure represents the theoretical error in AOD for an elevation angle error of ±0.1°. The error in the AOD is significantly reduced with a maximum of 0.05 for AODs of 1.0.

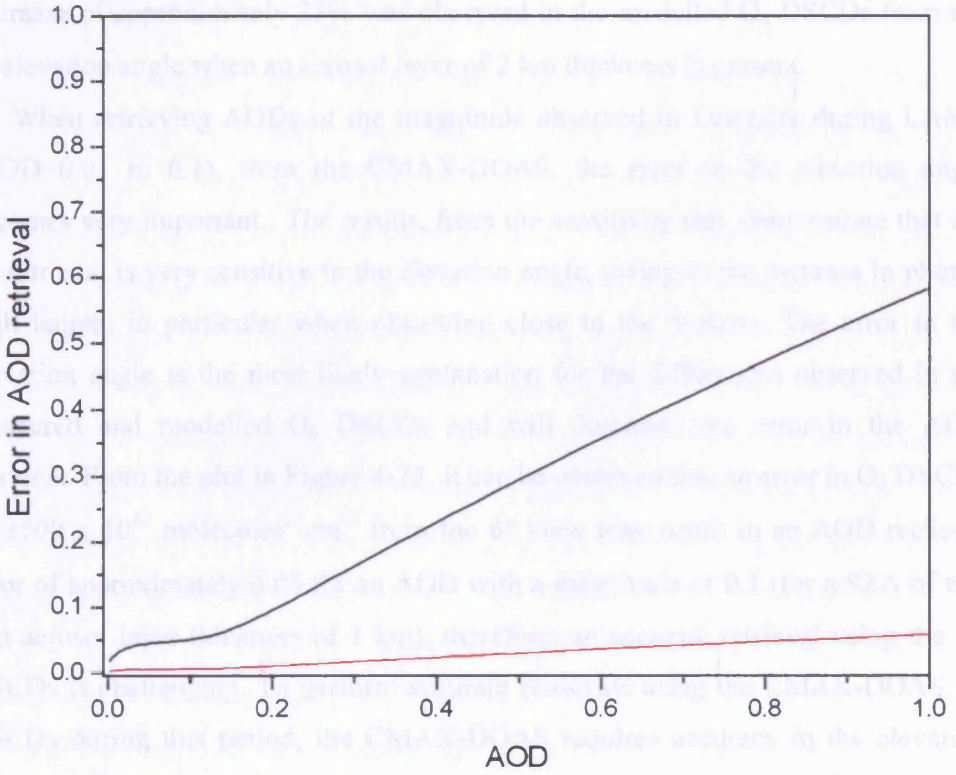

Figure 4-22: Estimated error in the AOD retrieval from the O_4 DSCDs retrieved by the 6° view, owing to an elevation angle error of ±1.0° (black line) and an elevation angle error of ±0.1° (red line).

4.5.5 Summary of sensitivity tests

When considering an optimal estimation algorithm or look-up-table method to retrieve aerosol information from DOAS instruments, the modelled O_4 DSCDs/AMFS are compared directly to the retrieved O_4 DSCDs/AMFs and adjusted accordingly with the aerosol input parameter. Using the RTM SCIATRAN, modelled O_4 DSCDs have been produced for a range of aerosol scenarios, typical for the urban boundary layer in Leicester during the LAMP campaign period, as determined by the lidar instrument. The results show, for aerosol levels of a maximum of 0.1 AOD, the aerosol layer altitude does not have a large effect on the retrieved O_4 DSCDs. However, the aerosol layer thickness does decrease the O_4 DSCDs for an increase in aerosol layer thickness from the ground. A maximum decrease of approximately 25% was observed in the modelled O_4 DSCDs from the 6° elevation angle when an aerosol layer of 2 km thickness is present.

When retrieving AODs of the magnitude observed in Leicester during LAMP (AOD=0.01 to 0.1), from the CMAX-DOAS, the error in the elevation angle becomes very important. The results, from the sensitivity test, demonstrate that the O_4 retrieval is very sensitive to the elevation angle, owing to the increase in photon path length, in particular when observing close to the horizon. The error in the elevation angle is the most likely explanation for the differences observed in the measured and modelled O_4 DSCDs and will dominate the error in the AOD retrieval. From the plot in Figure 4-22, it can be observed that an error in O_4 DSCDs of $\pm 500 \times 10^{40}$ molecules^2 cm^{-5} from the 6° view may result in an AOD retrieval error of approximately 0.05 for an AOD with a magnitude of 0.1 (for a SZA of 60° and aerosol layer thickness of 1 km), therefore, an accurate retrieval using the O_4 DSCDs is challenging. To perform accurate retrievals using the CMAX-DOAS O_4 DSCDs during this period, the CMAX-DOAS requires accuracy in the elevation angle of the telescope to be 0.1° or better.

4.6 CMAX-DOAS retrieval of NO_2 in the urban boundary layer

In the previous section, a number of sensitivity test were performed to determine the detection limit of the CMAX-DOAS to the retrieval of AOD using O_4 measurements. For the current system an optimal estimation method has not been performed to calculate the AOD from CMAX-DOAS. Therefore, aerosol profiles retrieved by the lidar are used to calculate AMFs for the CMAX-DOAS NO_2 retrievals during the LAMP campaign.

4.6.1 NO_2 air mass factors

Figure 4-23 presents tropospheric AMFs for each off-axis view, calculated by SCIATRAN for 8 days during the LAMP campaign. The total NO_2 AMFs were calculated using the same input parameters as summarised in Table 4-2. The stratospheric contribution to the total AMF is assumed to be equal for all elevation angles (Hönninger *et al.*, 2004a) and can be subtracted from the total AMF to yield a tropospheric NO_2 AMF. A similar approach is used in the DSCD retrievals of NO_2 from CMAX-DOAS. NO_2 in the atmosphere is present in the stratosphere, and in polluted regions, also in the tropospheric. The zenith view has greater sensitivity to trace gases in the stratosphere, owing to the small path length through the troposphere (see section 2.6.1). Thereby, subtracting the zenith DSCDs from the off-axis measurements yields a tropospheric NO_2 DSCD which can be divided by the appropriate tropospheric AMF to produce vertical column measurements of NO_2 in the troposphere. In addition to removing the stratospheric NO_2, however, a small component of tropospheric NO_2 measured by the zenith view is also removed.

The average tropospheric AMFs calculated at noon for the 8 days of measurements shown in Figure 4-23, are 3.6, 2.8, 2.3 and 1.9 for the 6°, 8°, 10° and 12° elevation angles with a standard deviation, owing to variations in the AOD profile over the 8 days of measurements, of approximately 0.03 to 0.3 at noon (0.7 to 6 %) depending on the viewing angle and SZAs, demonstrating that small changes in AODs over the LAMP period does not have a large effect on the retrieved NO_2 AMFs. The sharp peaks observed in Figure 4-21 are caused by clouds in the field of view of the lidar, producing anomalies in the calculated AMFs.

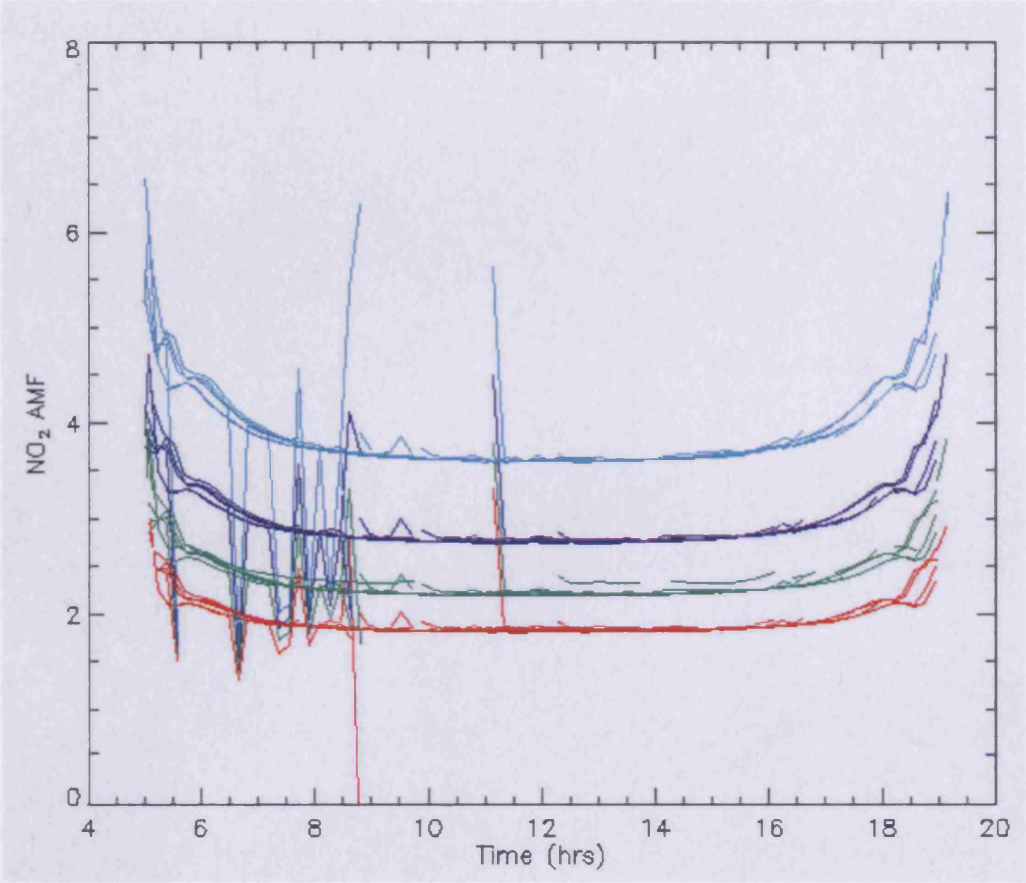

Figure 4-23: Tropospheric NO_2 AMFs for 12° (red), 10° (green), 8° (dark blue), 6° (light blue) views, calculated during 8 days in September 2007 with the RTM SCIATRAN.

As previously discussed in section 2.6.1, a geometric approach can be used to determine the AMF of a tropospheric absorber near the surface and below the scattering altitude, for single scattering events. It has been suggested that the AMF may be approximated to 1/sin (α), where α is the elevation angle of the viewing telescope [Hönninger *et al.*, 2004a]. For the telescope views in the CMAX-DOAS instrument, this approximation results in tropospheric NO_2 AMFs of 9.6, 7.2, 5.8, 4.8 for the 6°, 8°, 10° and 12° elevation angles. Comparing the geometrical AMFs to those calculated with SCIATRAN, show that the geometrical approach over estimates the NO_2 by more than 2.5 times. The result suggests that, even for the low AODs observed in Leicester, multiple scattering should be accounted for when calculating AMFs for DOAS instruments.

The accuracy of the NO_2 AMFs calculated with SCIATRAN associated with the error in the CMAX-DOAS elevation angles was determined by calculating

tropospheric NO_2 AMFs for elevation angles of 6°, 5.9°, 5.8°, 5.7°, and 5.6°. The results, presented in Figure 4-24, show that an error of 0.5° in the elevation angle of the telescope will only change the calculated tropospheric NO_2 AMFs by up to 8%. Hence, for the CMAX-DOAS instrument, this will result in accuracy in the NO_2 AMFs of approximately 16%.

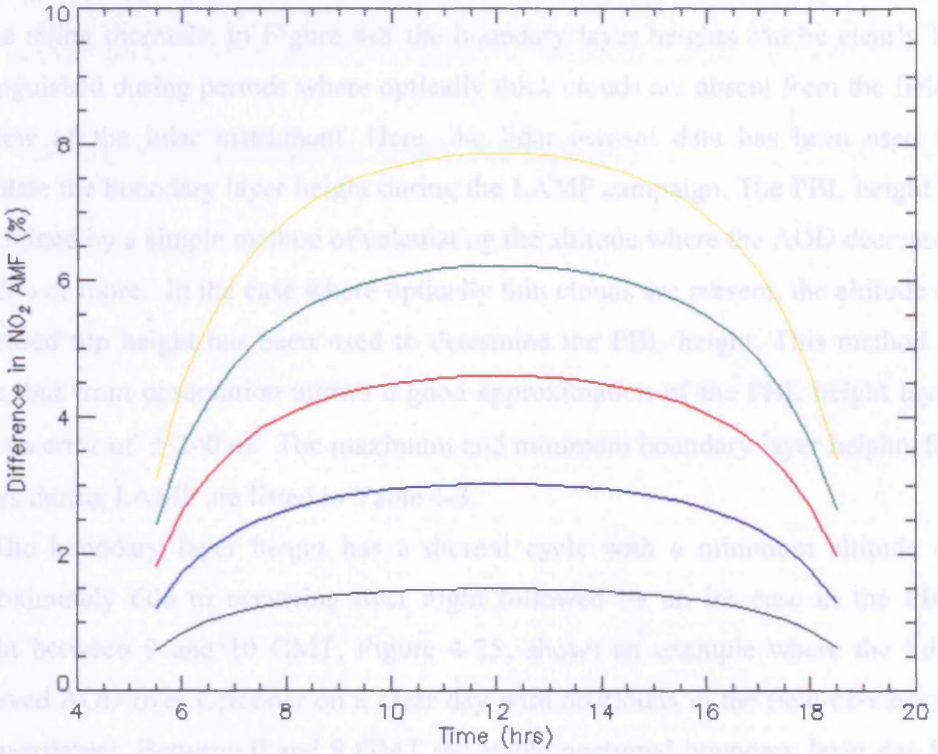

Figure 4-24: Percentage difference in calculated tropospheric AMFs from SCIATRAN for a decrease in elevation angle from the 6° view of 0.1° (black), 0.2° (blue), 0.3°(red), 0.4° (green) and 0.5°(yellow) for 7th September 2007.

4.6.2 NO_2 concentration within the urban boundary layer

The vertical tropospheric column densities of NO_2 are calculated by dividing the retrieved NO_2 DSCDs by the calculated tropospheric AMFs from SCIATRAN. If the assumption is made that the tropospheric NO_2 observed by CMAX-DOAS lies within the boundary layer, the concentration of NO_2 may be calculated by integrating the vertical tropospheric column densities over the boundary layer height.

Sinreich *et al.*, [2005] calculated the boundary layer height from the ratio of the modelled NO_2 AMFs at 2° and 20° elevation angles as a function of NO_2 box profile height, which was varied in the AMF calculations. The measured SCD ratio at 2° and 20° gave a value of 6, which corresponds to a box profile height of 1500 m (±300 m). The boundary layer height may also be calculated from the AOD retrieval. The top of the boundary layer forms an inversion layer which acts as a lid to the rising thermals. In Figure 4-8 the boundary layer heights can be clearly be distinguished during periods where optically thick clouds are absent from the field-of-view of the lidar instrument. Here, the lidar aerosol data has been used to calculate the boundary layer height during the LAMP campaign. The PBL height is determined by a simple method of calculating the altitude where the AOD decreases by 75% or more. In the case where optically thin clouds are present, the altitude of the cloud top height has been used to determine the PBL height. This method is basic, but from observation allows a good approximation of the PBL height layer with an error of ± 200 m. The maximum and minimum boundary layer heights for 8 days during LAMP are listed in Table 4-3.

The boundary layer height has a diurnal cycle with a minimum altitude of approximately 600 m occurring over night followed by an increase in the PBL height between 9 and 10 GMT. Figure 4-25, shows an example where the lidar retrieved AOD over Leicester on a clear day with no clouds in the field-of-view of the instrument. Between 0 and 9 GMT the stable nocturnal boundary layer can be observed between the surface and 400m, with a residual layer above. After 9 GMT the altitude of the PBL increases forming a mixing layer with an altitude of approximately 1800 m. The entrainment layer, which acts as a lid on the rising thermals can be observed at the top of the mixing layer. Between 9 and 15 GMT the thermals can still be observed as spikes in the AOD, between the PBL and the free-troposphere. After 15 GMT however, the entrainment zone becomes stable.

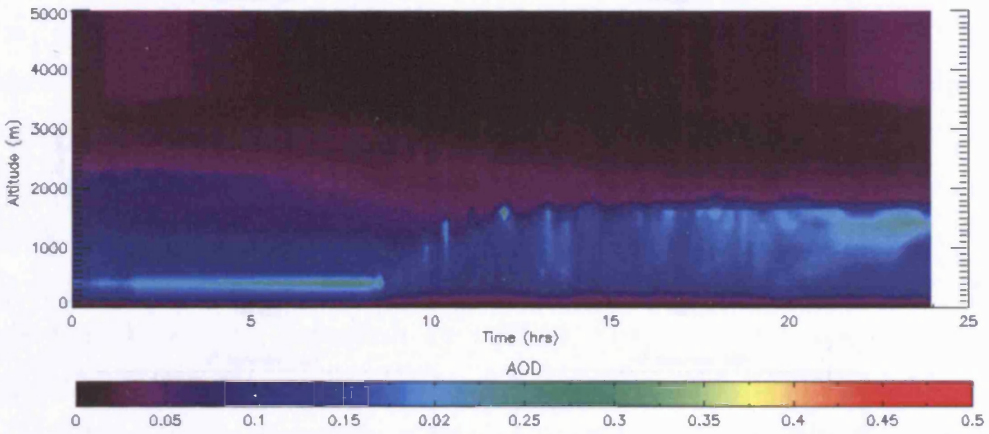

Figure 4-25: Lidar AOD retrievals over Leicester for 31st August 2007.

Table 4-3: Summary of the PBL heights calculated from the lidar instrument during LAMP

Date	Minimum PBL height (m)	Maximum PBL height (m)
06/07/09	600	1600
07/07/09	1000	1200
09/07/09	1200	1600
14/07/09	600	1800
15/07/09	1200	1800
16/07/09	1000	1200
17/07/09	1000	2000
18/07/09	1400	2000

Figure 4-26 shows NO_2 concentrations in the urban boundary layer over Leicester, measured by the 12° (red), 10° (green), 8° (dark blue), 6° (light blue) views of the CMAX-DOAS instrument for 8 days during the LAMP campaign. The total error in the calculation of NO_2 within the boundary layer arises from the error in the PBL height and the fitting error for the NO_2 columns and is approximately 27% for all elevation angles.

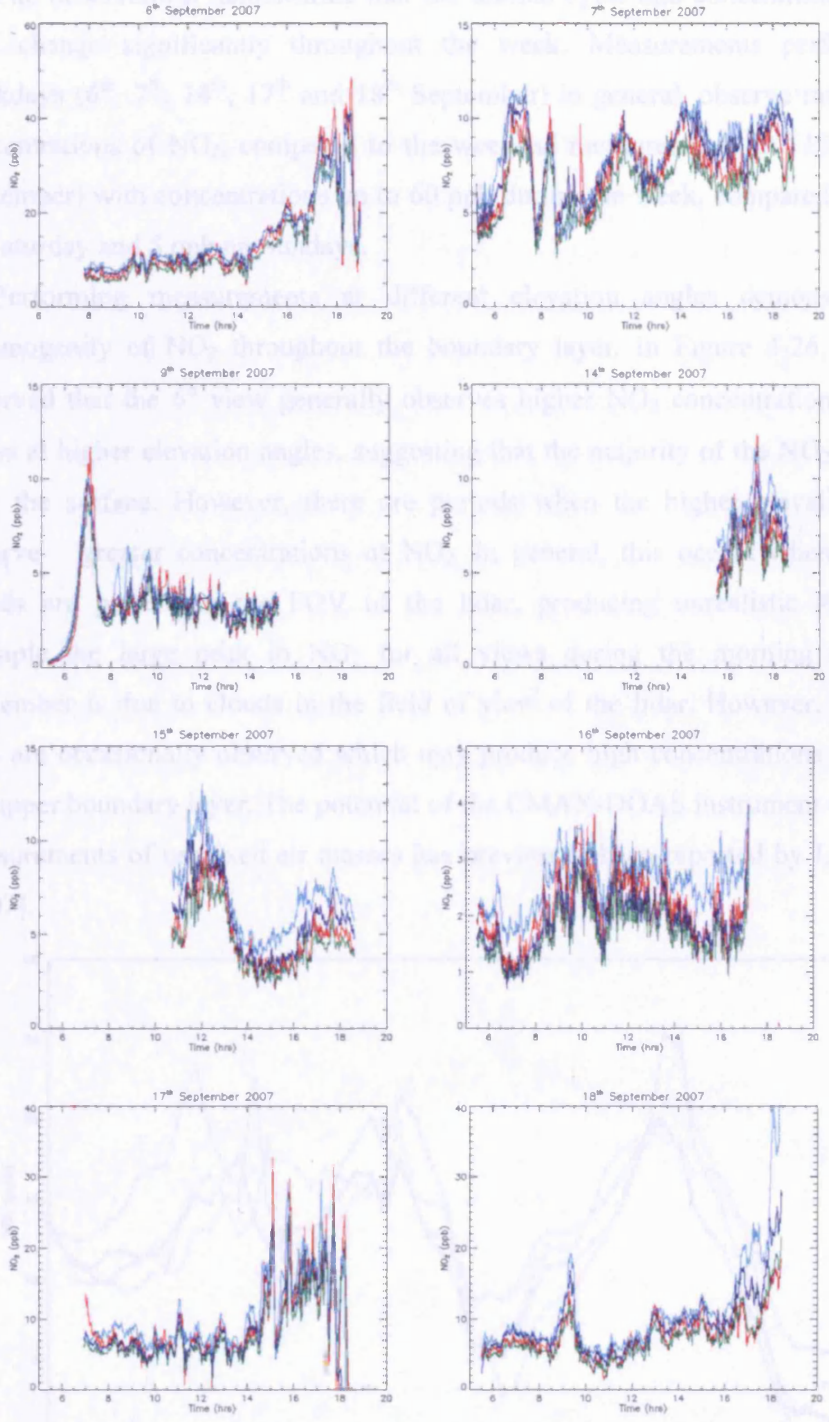

Figure 4-26: NO_2 concentrations derived using the CMAX-DOAS system in the urban boundary layer for 8 days during the LAMP campaign. The different colours represent measurements by the 12° (red), 10° (green), 8° (dark blue), 6° (light blue) views.

The observations demonstrate that the diurnal cycle and concentration of NO_2 may change significantly throughout the week. Measurements performed on weekdays (6^{th}, 7^{th}, 14^{th}, 17^{th} and 18^{th} September) in general, observe much higher concentrations of NO_2, compared to the weekend measurements (9^{th} 15th and16^{th} September) with concentrations up to 60 ppb during the week, compared to 10 ppb on Saturday and 5 ppb on Sundays.

Performing measurements at different elevation angles demonstrates the inhomogenity of NO_2 throughout the boundary layer. In Figure 4-26, it can be observed that the 6° view generally observes higher NO_2 concentrations than the views at higher elevation angles, suggesting that the majority of the NO_2 is located near the surface. However, there are periods when the higher elevation angles observe greater concentrations of NO_2. In general, this occurs when there are clouds are present in the FOV of the lidar, producing unrealistic AMFs. For example the large peak in NO_2 for all views during the morning of the 9^{th} September is due to clouds in the field of view of the lidar. However, plumes of NO_2 are occasionally observed which may produce high concentrations of NO_2 in the upper boundary layer. The potential of the CMAX-DOAS instrument to perform measurements of unmixed air masses has previously been reported by Leigh *et al.* [2007].

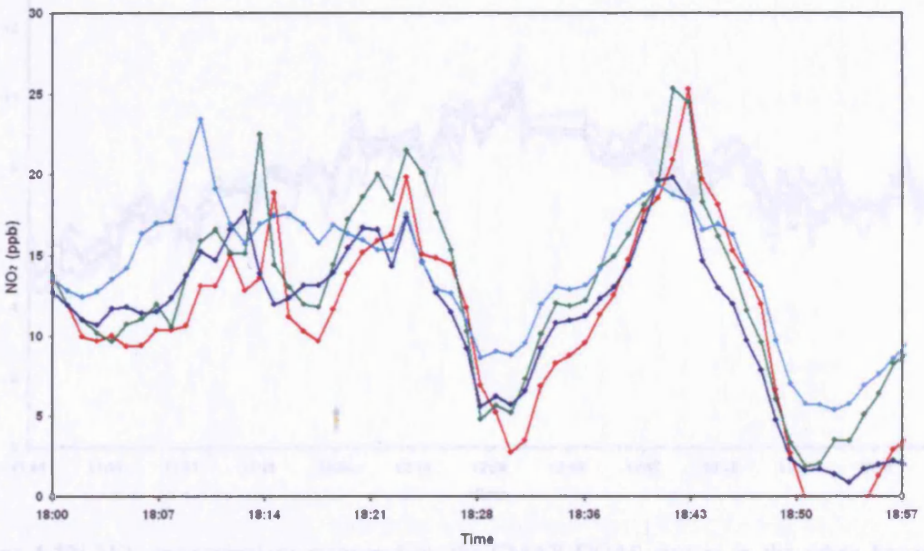

Figure 4-27: NO_2 concentrations measured by the CMAX-DOAS system in the urban boundary layer between 18:00 and 19:00 GMT on 17^{th} September 2007. The different colours represent measurements by the 12° (red), 10° (green), 8° (dark blue), 6° (light blue) views.

Figure 4-27 shows the NO_2 concentrations measured by each view for one hour between 18:00 and 19:00 GMT on 17th September 2007. Individual plumes of NO_2 can be observed as distinct peaks in the data. For example, at 18:11 GMT a peak in NO_2 of 24 ppb is observed in the lowest view which then decreases sharply over the next few minutes. During this period, peaks in NO_2 are also observed in the 8°, 10° and 12° views suggesting a plume of NO_2 is rising within the boundary layer. Between 18:30 and 18:44 GMT, a steady rise in NO_2 is observed in all views simultaneously. However, higher concentrations are measured in the 10° and 12° views which may result from the transport of NO_2 to higher altitudes.

A similar result is observed on 7th September (Figure 4-28), where an increase in NO_2 was observed between 11:00 and 12:30 GMT, with a maximum of 13 ppb measured in the 10° view. At approximately 12:15 GMT on this day a fire was reported at a site in the city centre. The direct emission of NO from the fire and subsequent reaction with HO_2/RO_2 leads to an increase in NO_2 over background levels. The wind was prominently in a northerly direction during this period, resulting in plumes of NO_2 being transported through each view of the CMAX-DOAS instrument.

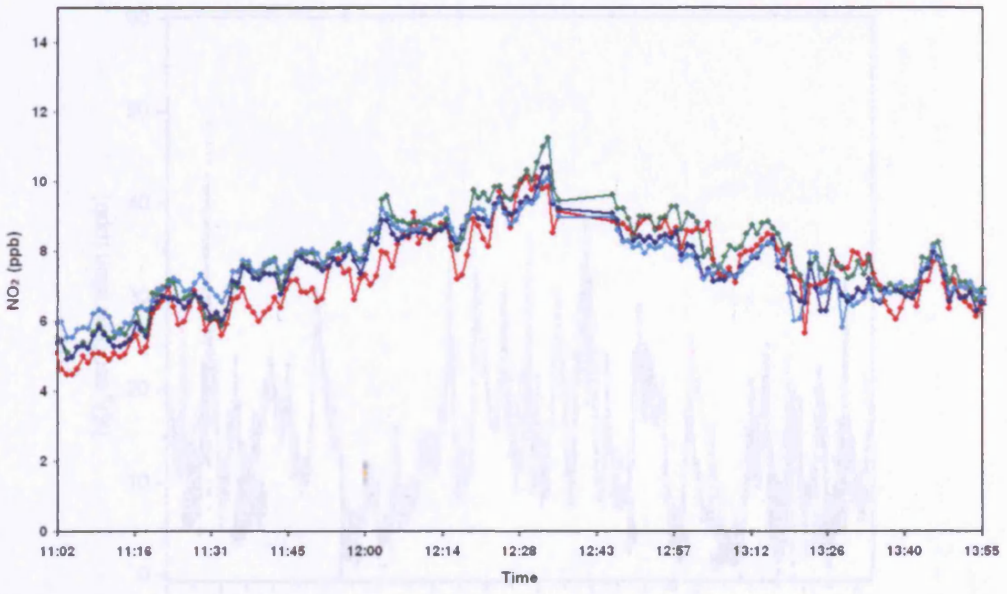

Figure 4-28: NO_2 concentrations measured by the CMAX-DOAS system in the urban boundary layer between 11:00 and 14:00 GMT on 7th September 2007. The different colours represent measurements by the 12° (red), 10° (green), 8° (dark blue), 6° (light blue) views.

4.6.3 Comparison of NO_2 measurements from CMAX-DOAS and *in situ* monitors

During the LAMP campaign, measurements of NO_2 were also performed by chemiluminescence monitors run by Leicester City Council, on site and around the city centre for the duration of the measurement period; along with photolysis measurements of NO_2 by the NO_{xy} instrument, up to 12th September (BBCEAS NO_2 data is currently not available for analysis). The results from section 4.6.2 demonstrate that the 6° view has the greatest sensitivity to NO_2 at the near surface, therefore, is suitable for comparisons with the *in situ* data.

Figure 4-29 shows a plot of the NO_2 concentration measured by the CMAX-DOAS instrument, and two chemiluminescence monitors, located on site and within the city centre. The city centre monitor is located approximately 2 km north of the CMAX-DOAS instrument, between two large buildings and away from any major roads to allow hourly averaged measurements of urban background NO_2 in Leicester. The monitor located on site has the same design as the one in the city centre and performs 15 minute averaged measurements of NO_2.

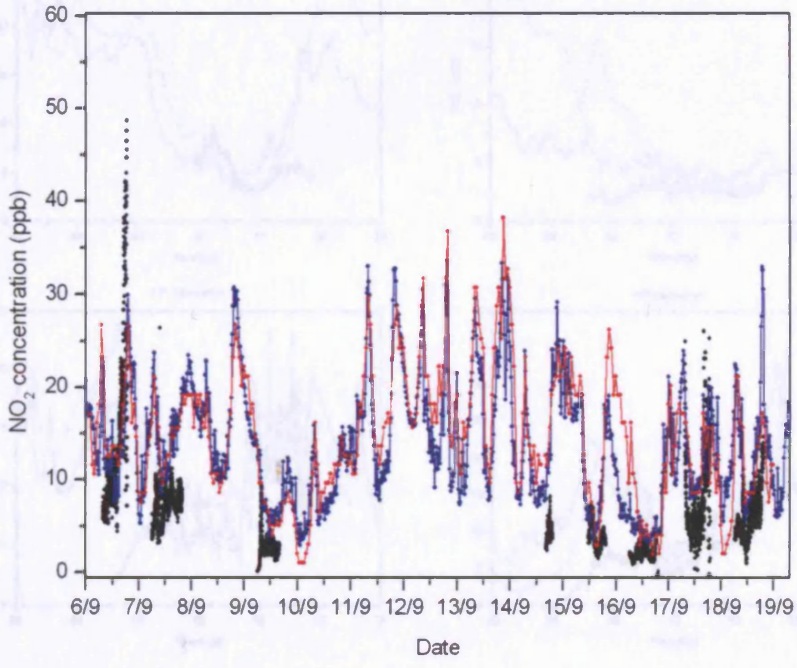

Figure 4-29: NO_2 concentrations for the period between 6th and 19th September measured by the 6° view of the CMAX-DOAS instrument (black line), the chemiluminescence monitor on site (blue line), and a chemiluminescence monitor situated within the city centre (red line).

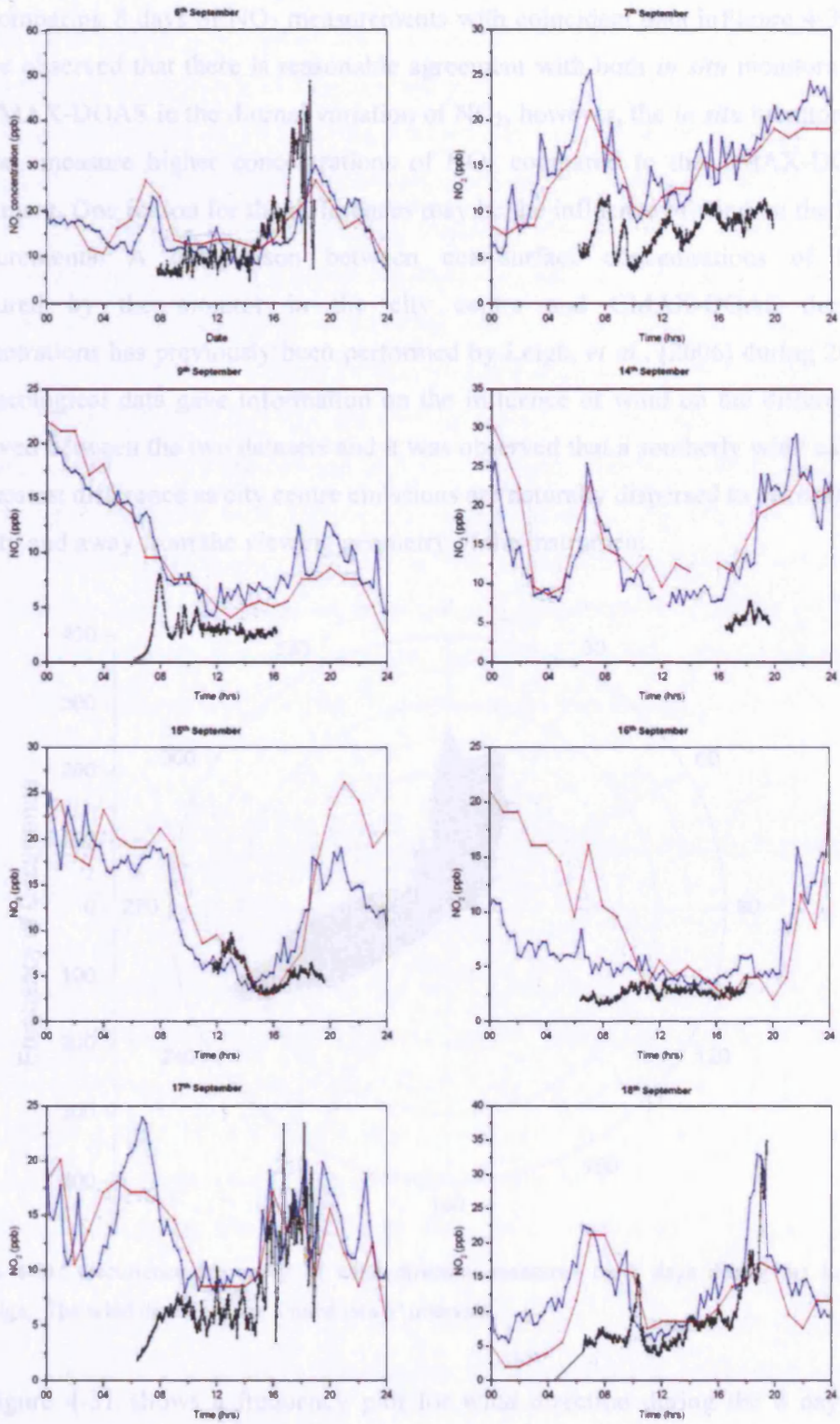

Figure 4-30: NO_2 concentrations for 8 days in September measured by the 6° view of the CMAX-DOAS instrument (black line), the chemiluminescence monitor on site (blue line), and a chemiluminescence monitor situated within the city centre (red line).

Comparing 8 days of NO_2 measurements with coincident data in Figure 4-30, it can be observed that there is reasonable agreement with both *in situ* monitors and the CMAX-DOAS in the diurnal variation of NO_2, however, the *in situ* monitors, in general, measure higher concentrations of NO_2 compared to the CMAX-DOAS instrument. One reason for the differences may be the influence of wind on the NO_2 measurements. A comparison between near-surface concentrations of NO_2 measured by the monitor in the city centre and CMAX-DOAS derived concentrations has previously been performed by Leigh, *et al.*, [2006] during 2004. Meteorological data gave information on the influence of wind on the differences observed between the two datasets and it was observed that a southerly wind causes the greatest difference as city centre emissions are naturally dispersed to the north of the city and away from the viewing geometry of the instrument.

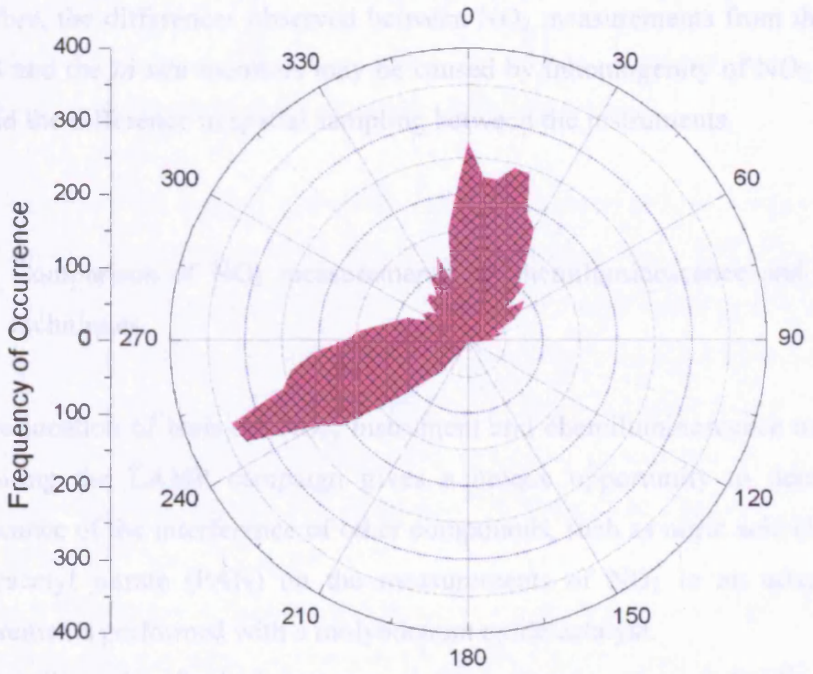

Figure 4-31: Occurrence frequency of wind direction measured on 8 days during the LAMP campaign. The wind directions are binned into 5° intervals.

Figure 4-31 shows a frequency plot for wind direction during the 8 days of coincident measurements. The wind direction was binned in 5° bins for data between 5 and 22 GMT to represent the wind direction during measurements performed by the CMAX-DOAS instrument. The results from the analysis show

that the wind direction during the 8 days was predominantly from a northerly or westerly/south-westerly direction and the differences between the measurements cannot be directly attributed to wind influences.

The inhomogenity of NO_2 across Leicester is evident in Figure 4-30 where differences in NO_2 concentration are observed by the two chemiluminescence monitors. For example, on 16th September the city centre monitor observes twice the concentration of NO_2 during the morning, than the monitor on the campaign site for the same period. This day falls on a Sunday and in general there are much lower NO_2 concentrations at the weekend owing to the reduction in traffic and industry. However, the high peak in NO_2 observed by the city centre monitor suggests an increase in traffic, most like owing to a festival event that took place in the city centre on this day. The result demonstrates that local emissions within the vicinity of the monitor have a strong effect on the concentration of NO_2 measured. Therefore, the differences observed between NO_2 measurements from the CMAX-DOAS and the *in situ* monitors may be caused by inhomogenity of NO_2 across the city and the difference in spatial sampling between the instruments.

4.6.4 Comparison of NO_2 measurements by chemiluminescence and photolytic techniques

The location of both the NO_{xy} instrument and chemiluminescence monitors on site during the LAMP campaign gives a unique opportunity to determine the significance of the interference of other compounds, such as nitric acid (HNO_3) and peroxyacetyl nitrate (PAN) on the measurements of NO_2 in an urban area by measurements performed with a molybdenum oxide catalyst.

Sampling tubes for both instruments were placed next to each other to ensure the instruments were measuring the same air. The NO_{xy} instrument performs measurements of NO_2 every minute. The data was then averaged over 15 minute intervals to allow for a direct comparison to measurements performed by the chemiluminescence monitor on site.

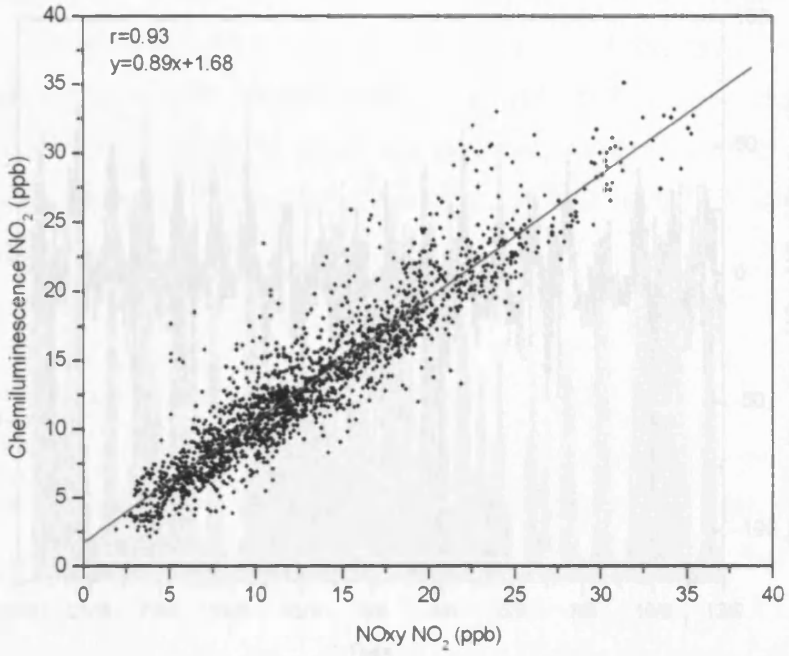

Figure 4-32: Correlation of NO_2 measurements by the chemiluminescence monitor and the NO_{xy} instrument. The red line represents the linear regression of the correlation.

Figure 4-32 shows the correlation of NO_2 concentrations measured by the chemiluminescence monitor and the NO_{xy} instrument from 23rd August to 12th September 2007. The agreement is very good, with a correlation coefficient of 0.93 and only a small offset of 1.68 ppb in the chemiluminescence measurements. In Figure 4-33 and Figure 4-34 the percentage difference between NO_2 measurements from the chemiluminescence monitor and the NO_{xy} instrument are shown along with ozone measurements for 23rd August to 12th September 2007 and for a zoomed in period from 24th to 30th August 2007.

The results show that the chemiluminescence monitors on average measure 5% greater NO_2 than the NO_{xy} instrument during the LAMP campaign, with a standard deviation of 24%. The greatest difference is observed during the afternoon when the ozone concentration increases. Dunlea *et al.*, [1999] also observed enhancements in the NO_2 measured by chemiluminescence detectors, equipped with molybdenum converters, compared to a TILDAS and a DOAS instrument when ozone levels peaked and concluded that the interference is most likely caused by reactive nitrogen species that are produced photochemically along with ozone, such as HNO_3.

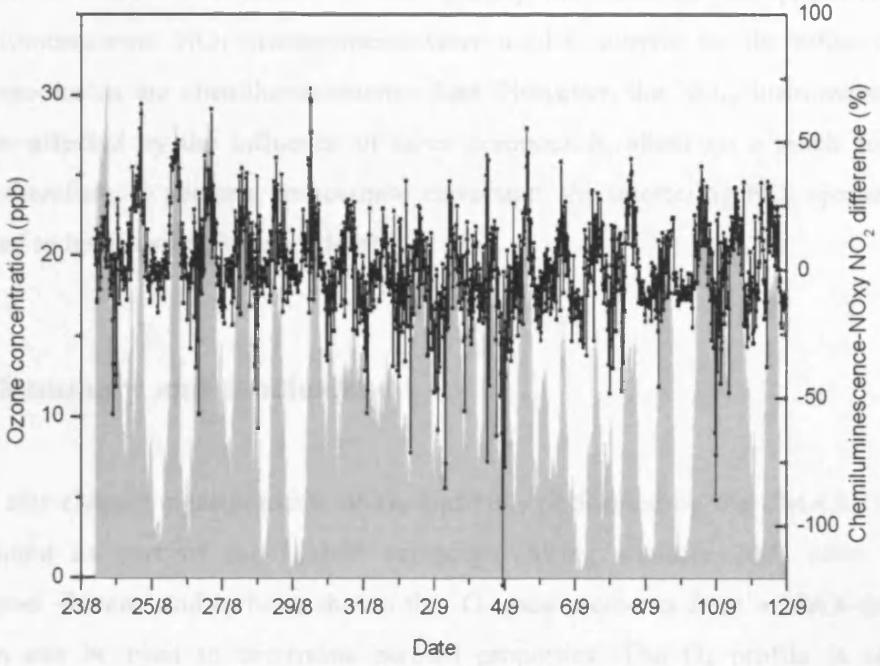

Figure 4-33: Percentage difference of NO_2 measurements by the chemiluminescence monitor and the NO_{xy} instrument from 23rd August to 12th September 2007. The grey shading represents the ozone concentration measured over the same period.

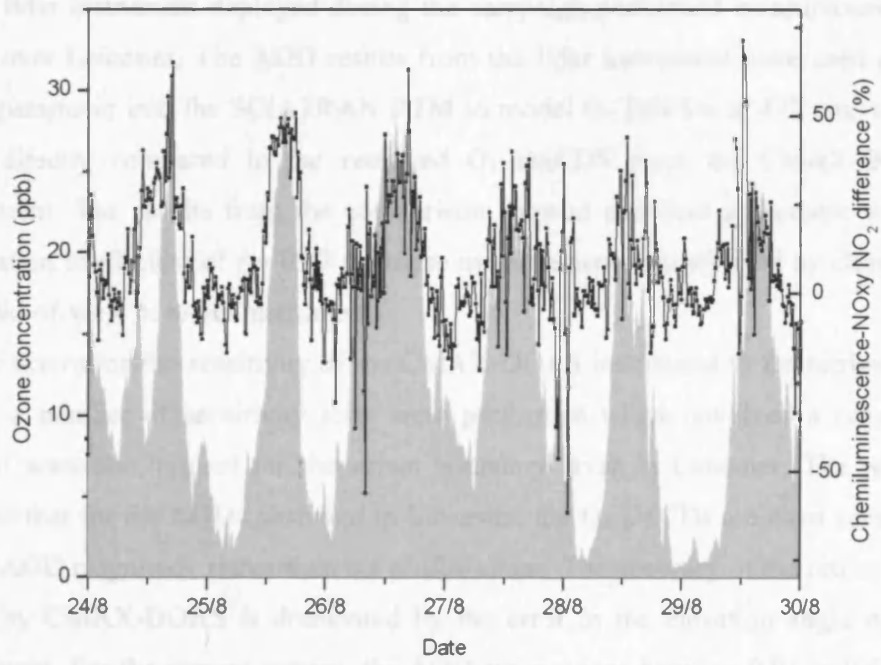

Figure 4-34: Percentage difference of NO_2 measurements by the chemiluminescence monitor and the NO_{xy} instrument from 24th to 30th August 2007. The grey shading represents the ozone concentration measured over the same period.

In a study by Ordóñez, *et al.*, [2006] the ratio of the photolytic to chemiluminescence NO_2 measurements were used to correct for the influence of other species in the chemiluminescence data. However, the NO_{xy} instrument may also be affected by the influence of other compounds, albeit on a much smaller scale, therefore, to perform an accurate correction, the interfering NO_y species are required to be measured independently.

4.7 Summary and conclusions

In this chapter measurements of O_4 and NO_2 performed by the CMAX-DOAS instrument as part of the LAMP campaign during summer 2007 have been presented. Recent studies have shown that O_4 measurements from a MAX-DOAS system can be used to determine aerosol properties. The O_4 profile is almost constant within the troposphere; therefore, any variation in the O_4 slant column may indicate an increase or decrease in photon path length owing to tropospheric clouds or aerosols.

A lidar instrument deployed during the campaign performed measurements of AOD over Leicester. The AOD results from the lidar instrument were used as an input parameter into the SCIATRAN RTM to model O_4 DSCDs at 477 nm, which were directly compared to the retrieved O_4 DSCDS from the CMAX-DOAS instrument. The results from the comparison showed excellent agreement with a correlation coefficient of $r = 0.97$ for those measurements not effected by clouds in the field-of-view of either instrument.

To determine the sensitivity of the CMAX-DOAS instrument to the retrieval of AOD, a number of sensitivity tests were performed which involved a range of aerosol scenarios, typical for the urban boundary layer in Leicester. The results showed that for the AODs observed in Leicester, the O_4 DSCDs are most sensitive to the AOD magnitude rather than the profile shape. The accuracy of the retrieval of AOD by CMAX-DOAS is dominated by the error in the elevation angle of the instrument. For the current system, the AOD error ranges between 0.01 to 0.55 for AODs between 0.01 and 1 when retrieving AOD from O_4 DSCDs at one viewing angle and a single wavelength. The potential of the CMAX-DOAS instrument to

retrieving AOD could be very good, although it would require accuracy in the elevation angle of 0.1°. Combining measurements from different wavelengths and viewing direction may also enable derivation of the aerosol size, as previously suggested by Frieβ *et al*, [2004].

Using the aerosol data from the lidar instrument, AMFs for NO_2 were calculated by the SCIATRAN RTM and concentrations of NO_2 in the boundary layer over Leicester derived. The largest error source in the derived NO_2 concentrations was the calculation of the boundary layer height from the lidar AOD measurements with an error of approximately 27% for all elevation angles. Comparisons of the CMAX-DOAS NO_2 measurements with *in situ* monitors likely demonstrate the inhomogeneity of NO_2 across the city owing to local emission sources.

Finally, a comparison of NO_2 measurements from different *in situ* instruments was performed to determine the significance of other nitrogen compounds interfering with measurements performed with a molybdenum oxide catalyst. The results show that the molybdenum oxide catalyst on average overestimates the NO_2 by 5%, with a standard deviation of 24% owing to the conversion of reactive nitrogen species to NO_2.

Chapter 5

Intercomparison of OMI tropospheric NO_2 columns with CMAX-DOAS and *in situ* measurements

Satellite retrieved products are often compared to ground based or airborne data to assess the accuracy and precision of the satellite data by independent means. In addition, the results of an intercomparison can be used as a diagnostic tool in the improvement of retrieval algorithms.

The validation strategy is important, as poor validation will compromise the quality of the satellite retrieved products. A simple approach to validation is a comparison exercise concluding in the difference between the satellite data and a reference set of 'validated' data. However, this is not sufficient to determine the usefulness of the data for its intended scientific applications. What needs to be identified is how well the satellite data represents known geophysical features that are observed by other instruments or deduced from our understanding. The validation programme, in general, involves an initial validation before public release of a new product or after release of a near-real-time (NRT) product. Following this is a detailed geophysical validation for different scenarios and the verification of precision after the improvement of a retrieval algorithm. Finally, a long term validation is performed to evaluate trends and degradation of the instrument.

The comparison with *in situ* and other ground based measurements is important for the purpose of validation as it can benefit from knowledge on the local geophysical parameters and allow a large number of possible co-locations, with varying atmospheric scenarios, potentially improving the significance of the validation. However, the validation of satellite instruments with ground based

observation techniques yield different samplings of the atmosphere on a spatial and temporal scale which may reduce reliability and introduce biases.

In this chapter, retrieved tropospheric VCDs of NO_2 from the Ozone Monitoring Instrument (OMI) are compared to coincident tropospheric columns retrieved from the CMAX-DOAS instrument and *in situ* near-surface measurements from chemiluminescence detectors in and around Leicester city centre. A field-of-view (FOV) weighted estimate for the OMI-equivalent urban NO_2 was calculated for each coincidence by including background emissions from a nearby *in situ* monitor, situated in a rural area. The final part of this chapter presents seasonal and weekly cycles of NO_2 in an urban and rural environment measured by the OMI and *in situ* monitors.

5.1 Retrieval of NO_2 over Leicester from CMAX-DOAS

During the period of measurements analysed in this chapter, the CMAX-DOAS instrument was set-up as described in Chapter 3, with five telescopes fixed at elevation angles of 90° (zenith), 15°, 10°, 5° and 2°. The DOAS technique was performed in the wavelength region 431 to 508 nm [Leigh *et al.*, 2006] to derive DSCDs of NO_2, O_3, H_2O and O_4. Tropospheric NO_2 DSCDs are derived using a zenith reference spectrum for each viewing angle and then subtraction of the concurrent zenith differential slant column for each measurement in the off-axis views, removing the stratospheric signal, along with a small signal from tropospheric absorbers. The average detection limits are 3.2×10^{15}, 4.2×10^{15} and 4.7×10^{15} molecules cm^{-2} for the 15°, 10° and 5° views respectively when using a zenith reference spectrum [Leigh *et al.*, 2006]. For the comparisons performed in this chapter, data from the 5° viewing angle was used. The retrieval of VCDs at higher elevation angles are less affected by aerosols however, the sensitivity to tropospheric absorbers will decrease. The 2° view has the greatest sensitivity to tropospheric absorbers. However, the error on the retrieved slant columns for the 2° elevation angle is 10.3% compared to 5% for the other elevation angles owing to the low signal to noise ratio for the 2° elevation angle. NO_2 VCDs are derived from the

AMFs calculated with the SCIATRAN RTM. Previous analysis of NO_2 AMFs in Chapter 4 demonstrated that small variations in AOD do not significantly change the calculated NO_2 AMFs, giving a standard deviation of 0.7 to 6% depending on the elevation angle and SZA, for AODs between 0.01 and 0.1. Therefore, a typical AOD profile obtained from the lidar data with a maximum AOD of 0.05 was used in the AMF calculations in this chapter, for the 5° view.

The largest contribution to the measured CMAX-DOAS NO_2 column amount is located in the PBL. In Chapter 4, the PBL height was determined from lidar aerosol measurements and ranged between 600 and 2000 m over Leicester, during summer. The height of the PBL depends on many factors such as weather conditions and time of year [Medeiros *et al.*, 2005]. Aerosol data was not available during the period of data capture used in this chapter and given the uncertainty in calculating the PBL height over Leicester from CMAX-DOAS O_4 aerosol measurements, tropospheric VCDs retrieved from CMAX-DOAS are used in the comparisons performed in this chapter rather than estimated PBL mixing ratios.

5.2 Previous work on the validation of tropospheric NO_2 from space

NO_2 is an important tropospheric trace gas when monitoring pollution in the UBL. Public exposure to NO_2 in the urban environment is a health concern, a public policy concern and subject to several EU directives on pollution levels [DEFRA, 2003]. At present, the majority of monitoring of NO_2 uses sparse networks of *in situ* monitors. In addition to *in situ* NO_2 monitoring networks, remote sensing of the troposphere from satellites and ground based remote sensing instruments could provide measurements of tropospheric NO_2 on much larger scales.

Spectroscopic techniques are a useful method for detecting NO_2 and other strong atmospheric absorbers. The first tropospheric NO_2 column measurements obtained on a global scale were performed by the Global Ozone Monitoring Experiment (GOME) launched onboard the ESA ERS-2 in April 1995 [Burrows *et al.*, 1999; Leue *et al.*, 2001; Martin *et al.*, 2002].

One advantage of measurements of NO_2 from space is the possibility of observing pollution 'hot spots', high concentrations of NO_2 over industrial regions. Beirle *et al.*, [2003] produced weekly cycles of tropospheric NO_2 columns retrieved from GOME for different regions of the world. Industrial regions and cities in the USA, Europe and Japan show a clear decrease of approximately 25 to 50% in tropospheric NO_2 on a Sunday compared to observed weekly levels. Regions in the Middle East show a different cycle owing to other social working patterns, with weekly minimums on Friday and Saturday. In China there is no indication of a weekly cycle which may indicate that the emissions from China are dominated by heavy industry and power plants whereas in the USA and Europe it is transport which mainly contributes to the NO_2 sources.

A study of tropospheric NO_2 measurements in the Po river basin (northern Italy) from GOME was performed by Petritoli *et al.* [2004] and included comparisons with *in situ* stations within the Po Valley and a zenith viewing DOAS instrument located on peak of Mount Cimone. Under particular meteorological conditions the agreement between the GOME measured tropospheric columns of NO_2 and those measurements made at the near-surface showed a good correlation for high pollution episodes. A similar study by Ordóñez *et al.* [2006] included a comparison of GOME tropospheric NO_2 columns with measurements of NO_2 from 99 ground stations in the Lombardy region. The *in situ* measurements were scaled to tropospheric vertical columns using 3 monthly averaged profile shapes of NO_2 calculated by the Model of Ozone and Related tracers 2 (MOZART-2). The agreement between the GOME and ground based columns was very good, with a correlation coefficient of $r = 0.78$ for slightly polluted stations. Schaub *et al.*, [2006] produced tropospheric columns, to be compared to NO_2 columns retrieved from GOME measurements, from integrated measurements of NO_2 by *in situ* stations at different altitude levels in Switzerland. For clear sky conditions the comparison shows good agreement with a correlation coefficient of $r = 0.7$. The study also demonstrated that the GOME columns were systematically smaller than the equivalent ground based columns. Blond *et al.*, [2007] performed an intercomparison of *in situ* NO_2 measurements and model results from the CHIMERE chemistry transport model with SCIAMACHY NO_2 tropospheric columns for 2003. The 439 stations across Western Europe, used in the study, were categorised into urban, suburban, and rural stations and their annual means

compared to the annual mean of co-located SCIAMACHY tropospheric columns, which are simultaneously available in a model grid box (n = 176). The correlation was low (r = 0.43), however, when the comparison is limited to the 29 rural sites the agreement is much better (r = 0.9). Blond *et al.*, suggested that urban sites were unlikely to be suitable for validation of satellite tropospheric NO_2 retrievals with low spatial resolution, such as SCIAMACHY.

In this chapter, a comparison is performed of retrieved NO_2 tropospheric vertical columns from the NASA-AURA Ozone Monitoring Instrument with those from the Concurrent Multi-Axis Differential Optical Absorption Spectroscopy (CMAX-DOAS) instrument installed on the University campus for the period December 2005 to March 2006. The OMI tropospheric columns are then compared to a set of data from *in-situ* chemiluminescence monitors for 2005 and 2006, operated by the Leicester City Council.

The previous studies of comparisons between ground based and satellite measurements of tropospheric NO_2, discussed above, have been performed over large regions, which include many cities and towns and heavily polluted areas. Here, the first results from the validation over a small city in central England with an area of approximately 73 km^2 are presented. Observations of trace gases on a city scale, from space, are limited by the spatial resolution of the instrument. The spatial resolution of OMI improves on that of previous instruments and potentially makes it suitable for measurements of air quality on an urban scale [Levelt *et al.*, 2006].

5.3 The AURA Satellite

The Ozone Monitoring Instrument operates onboard the NASA Earth Observing System (EOS) Aura satellite launched on 19th June 2004 into a sun synchronous polar orbit (98^{o} inclination) with a period of approximately 100 minutes and an altitude of 705 km, crossing the equator between 13.40 and 13.50, local time. The Aura mission is designed to research the chemistry and dynamics of the Earths atmosphere, such as ozone, air quality and climate.

The four instruments onboard Aura measure greenhouse gases in the troposphere and UTLS regions. Aura also retrieves information on absorbing and

reflecting aerosols and water vapour. Table 5-1 contains a summary of the instruments onboard the Aura satellite, along with the species they detect.

Table 5-1: Summary of the instruments onboard Aura and the species they measure in the atmosphere.

Name	Instrument	Spectral range	Species measured
HIRDLS (HIgh Resolution Dynamics Limb Sounder)	Scanning infrared limb sounder	6.12 to 17.76 μm	Global distribution of temperature and profiles of O_3, H_2O, CH_4, N_2O, NO_2, HNO_3, N_2O_5, CFC11, CFC12, $ClONO_2$, and aerosols.
MLS (Microwave Limb Sounder	Microwave limb-sounding radiometer/spectrometer	Millimetre and submillimetre-wavelengths	Profiles of OH, HO_2, H_2O, O_3, HCl, ClO, HOCl, BrO, HNO_3, N_2O, CO, HCN, CH_3CN, volcanic SO_2), cloud ice, temperature and geopotential height
OMI (Ozone Monitoring Instrument)	Nadir-viewing wide-field-imaging spectrometer	270 - 500 nm	Columns of O_3 NO_2, SO_2, BrO, OClO, aerosols and cloud top pressure.
TES (Tropospheric Emission Spectrometer)	High-spectral-resolution infrared-imaging Fourier transform spectrometer	3.2 to 15.4 μm	Profiles of Temperature, O_3, NO_2, CO, HNO_3, CH_4

5.4 OMI instrument

5.4.1 Objectives

The OMI was built by Dutch Space/TNO-TPD in the Netherlands, in co-operation with Finnish subcontractors VTT. A team constituting of Dutch (KNMI), US (NASA) and Finnish (FMI) scientists were established to develop retrieval algorithms, monitor in-flight instrument calibration, operational handling of the instrument and conducting data validation.

The OMI is designed to measure total column ozone, ozone profile, surface UV irradiance, aerosols and cloud characteristics, and the column amounts of trace gases at high spatial resolution. The measurements will indicate whether the ozone layer is recovering and the aerosol and cloud measurements will provide information on the Earth's radiation budget and climate change. Global measurements of tropospheric gases will offer information on air quality and transport across the globe. The combination of OMI data with the MLS, HIRDLS and TES data sets will improve on the data retrieved and extract more information on trace gases in the atmosphere.

5.4.2 Pointing geometry

OMI is a nadir viewing spectrometer that measures upwelling radiance in the ultraviolet and visible wavelength range between 270 and 500 nm [Levelt *et al.*, 2006]. The instrument has two CCD detectors, one in the UV (270-365nm) and one in the VIS (350-500 nm) wavelength range. The UV wavelength range is divided in two channels: UV-1 (270-310 nm) and UV-2 (310-365 nm). The spectral resolution is 0.52 and 0.45 nm in the UV-1 and UV-2 channels and 0.63 in the visible channel.

The CCDs are two dimensional arrays, which enable the instrument to instantaneously record spectra across the whole wavelength range for 60 discrete pixels along a 114° swath (see Figure 5-1). The large swath corresponds to a 2600 km wide spatial sampling for one orbit, enabling global coverage in just one day. Figure 5-2 shows the size of the OMI cross track ground pixel size as a function of

distance from nadir. At nadir the ground pixel size is 13 km (along track) x 24 km (cross track); this increases to approximately 13 km x 150 km for the outermost swath angles (57°). OMI combines the spectral advantages of SCIAMACHY and GOME with the global coverage of TOMS.

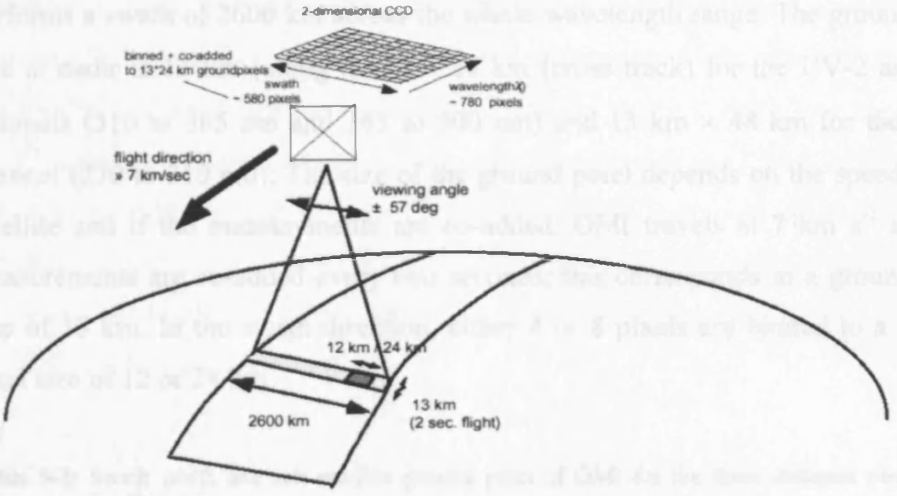

Figure 5-1: Coverage of OMI. The large swath width of 2600 km means OMI can cover the whole globe in one day. At higher latitudes more overpasses are available [Levelt *et al.*, 2006].

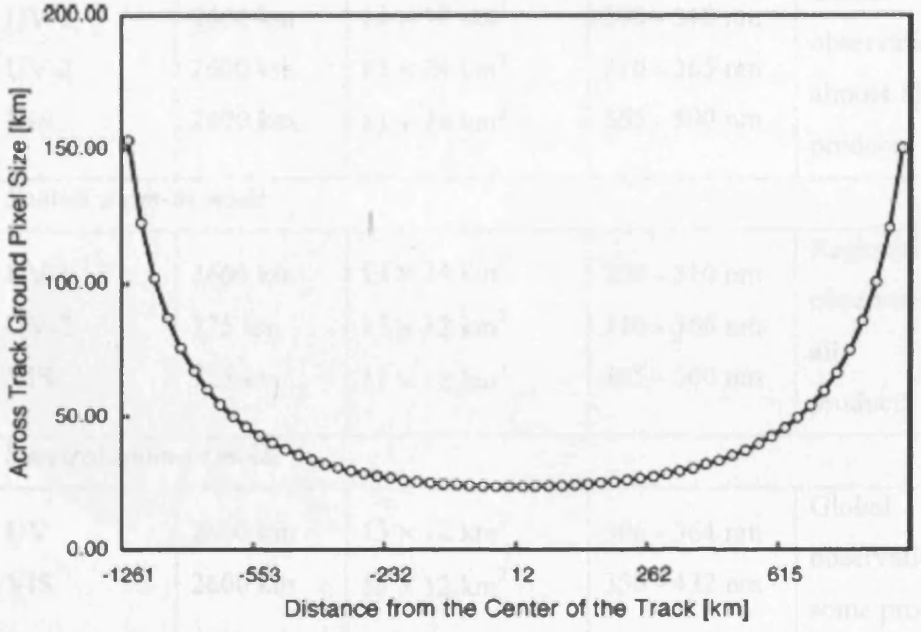

Figure 5-2: OMI cross track ground pixel size as a function of distance from nadir [Levelt *et al.*, 2006].

5.4.3 Measurement modes

OMI has three measurement modes: the global measurement mode, the spatial zoom-in measurement mode and the spectral zoom-in measurement mode

The normal operation mode is the global measurement mode, for which OMI performs a swath of 2600 km across the whole wavelength range. The ground pixel size at nadir is 13 km (along track) × 24 km (cross track) for the UV-2 and VIS channels (310 to 365 nm and 365 to 500 nm) and 13 km × 48 km for the UV-1 channel (270 to 310 nm). The size of the ground pixel depends on the speed of the satellite and if the measurements are co-added. OMI travels at 7 km s^{-1} and the measurements are co-added every two seconds; this corresponds to a ground pixel size of 13 km. In the swath direction, either 4 or 8 pixels are binned to a ground pixel size of 12 or 24 km.

Table 5-2: Swath width and sub-satellite ground pixel of OMI for the three different observation modes [Levelt *et al.*, 2000].

Observation mode	**Swath width**	**Nadir ground pixel size**	**Spectral range**	**Application**
Global mode				
UV-1 UV-2 VIS	2600 km 2600 km 2600 km	13 × 48 km^2 13 × 24 km^2 13 × 24 km^2	270 - 310 nm 310 - 365 nm 365 - 500 nm	Global observations of almost all OMI products
Spatial zoom-in mode				
UV-1 UV-2 VIS	2600 km 725 km 725 km	13 × 24 km^2 13 × 12 km^2 13 × 12 km^2	270 - 310 nm 310 - 365 nm 365 - 500 nm	Regional observations of all OMI products
Spectral zoom-in mode				
UV VIS	2600 km 2600 km	13 × 12 km^2 13 × 12 km^2	306 - 364 nm 350 - 432 nm	Global observation of some products

In the spatial zoom mode the spatial resolution can be reduced to 13 km x 12 km. This small pixel size allows OMI to observe in between clouds and is useful for regional studies. The spectral zoom mode decreases the spectral range while observing the ground with at resolution of 13 km x 12 km. A reduction in spectral range enables the swath width to be fixed at 2600 km; therefore, daily global coverage is still possible with an increased spatial resolution, however the wavelength range is limited to 306 to 432 nm. A summary of the observation modes and spectral and spatial ranges is listed in Table 5-1.

A measurement also contains some information outside the 13×12/24 km region owing to the intrinsic field of view (IFOV). The IFOV is defined as the FWHM of the pixel response curve when a point source is moving with the swath or flight direction. The IFOV of an OMI pixel is approximately 3 km in the swath direction and 10 km in the flight direction.

5.4.4 Geolocation

The geolocation of the observation is determined from the elevation and azimuth angles for each pixel line-of-sight and the time of the measurement using the SDP toolkit [Levelt *et al.*, 2006]. The science requirements state that the geolocation of the pixels should have an accuracy of 1/10th of the ground pixel. This has been tested by generating a false colour RGB image, derived from the OMI radiance measurements (Red=465-485nm, Green=405-415 nm, Blue=340-360 nm].

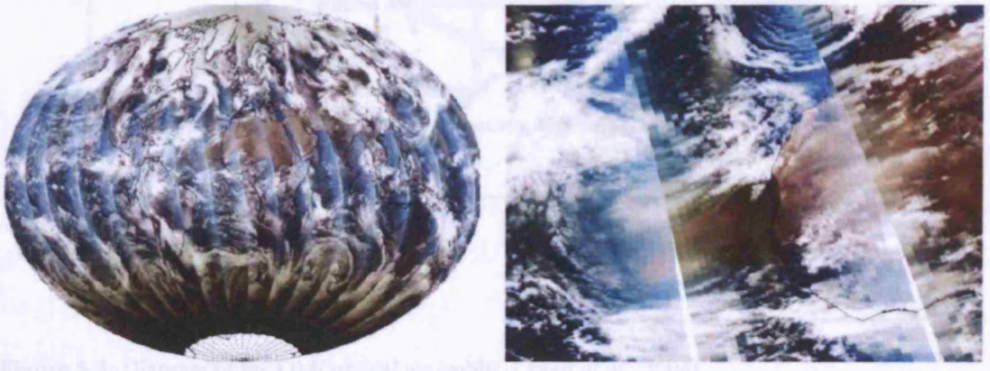

Figure 5-3: False colour RGB plot from OMI radiances on May 16, 2005 for the whole globe and the Sahara desert. Dust storms and its outflow can be seen above the Sahara dessert. [Levelt *et al.*, 2006].

Figure 5-3 shows a false colour RGB plot from OMI radiances on May 16, 2005. The image on the left shows a global RGB plot and the image on the right is from the Sahara desert, where dust storms can be observed. The world map alignment was determined to be: latitude = 8°/1000 ± 0.3°/1000 and longitude = -3°/1000 ± 0.3°/1000, where 1° /1000 = 111 m. This is within the accuracy required.

5.4.5 Instrument design

The OMI spectrometer consists of a telescope, mirrors, UV and visible detectors and calibration systems. Figure 5-4 shows the main components of the spectrometer. The upwelling radiation from the Earth is imaged onto the entrance slit of the spectrometer and reflected from the primary mirror through a polarisation scrambler. The polarisation scrambler effectively depolarises the signal. OMI is sensitive to polarised light, owing to the dependence on the optical properties of the mirrors and gratings. Although, the dependence on the optical properties can be corrected pre-flight by determining the polarisation response of the instrument.

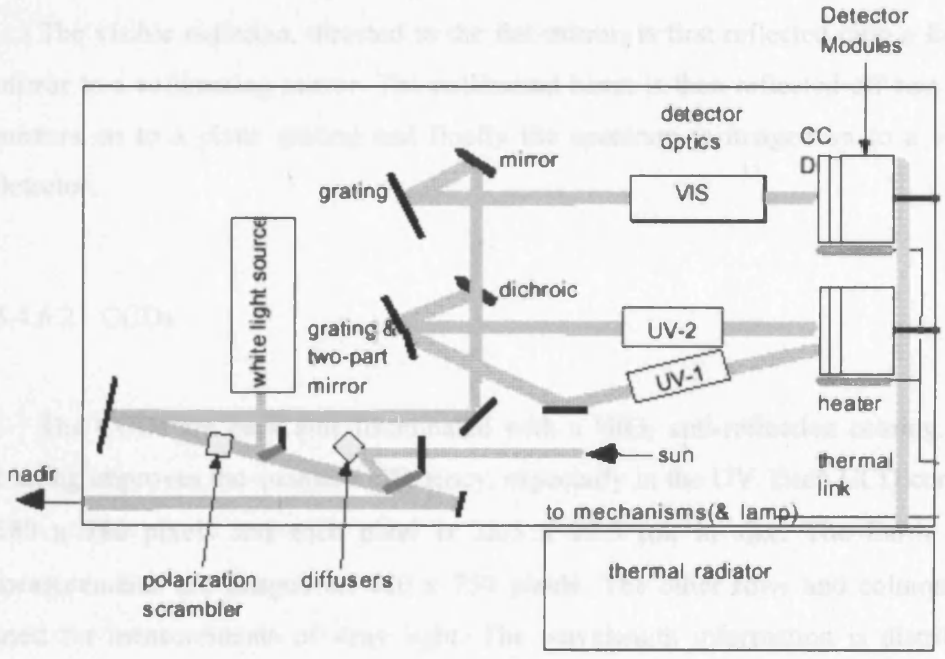

Figure 5-4: Diagram of the OMI optical assembly [Levelt *et al.*, 2006].

The radiation is then reflected off a secondary mirror, which has a coating that restricts the transmission of stray light above 500 nm, onto a dichroic mirror, which contains a multilayer coating of dielectrics, this coating reflects light from the UV region onto a folding mirror and the visible light to a flat mirror

5.4.6 Optical Assembly

5.4.6.1 UV and visible channels

The UV radiation incident on the flat mirror is reflected to a plano convex fused silica lens that collimates the beam in the direction of a grating which forms a spectrum detected by the two UV channels. The UV channel is split in to two sub channels UV-1 and UV-2 to avoid problems owing to stray light. The stray light originating from wavelengths between 310 and 380 nm may exceed the actual signal from light at lower wavelengths. Splitting the channels will improve the signal in the UV-1 wavelength range.

The visible radiation, directed to the flat mirror, is first reflected onto a folding mirror to a collimating mirror. The collimated beam is then reflected off two more mirrors on to a plane grating and finally the spectrum is imaged on to a visible detector.

5.4.6.2 CCDs

The CCDs are back side illuminated with a HfO_2 anti-reflection coating. This coating improves the quantum efficiency, especially in the UV. Each CCD contains 580 x 780 pixels and each pixel is 22.5 x 22.5 μm in size. The Earth shine measurements are imaged on 480 x 750 pixels. The other rows and columns are used for measurements of stray light. The wavelength information is distributed along the 480 rows and the spatial information along the 750 columns. The signal from each pixel is transferred to the storage region, this is known as a 'frame transfer'. The storage array is the same size as the detector array. While the storage array is being read, the detector array is able to image another spectrum. This

increases the temporal resolution of the instrument and also reduces the 'smear effect' although this may still cause some problems and is corrected for in the data processing. In the read out area each pixel is separately processed. To reduce the read out time the pixels are binned into 4 or 8 rows, this reduces the ground pixel size. The exposure time of the CCD is 0.4 seconds. Co-addition of 5 exposures results in a 2 second interval in which measurements are performed in the flight direction.

The read out area has an excess of 17 pixels on each end of the CCD which are covered and hence, not illuminated by light. These extra rows and columns are used to measure the dark current and electronics offset. To reduce the dark current the detectors are operated at -10 °C and to avoid ice formation on the surface of the detectors, out gassing of the instrument was performed soon after launch. The detectors however, will deteriorate over time due to radiation damage, so shielding is added to reduce the damage.

Owing to the design of the optics there is distortion in both the spatial and spectral direction. The curvature in the in the spatial direction is very small but may introduce errors as the pixels in the same row may have slightly different viewing angles, hence, varying pixel sizes. In the spectral direction a much larger curvature in the columns is observed. The distortion in the columns has been accurately calculated. In the UV-1 band, the maximum distortion is approximately between 0.2 and 9 pixels. For the UV-2 band the maximum distortion increases from 0.25 to 17 pixels. The effect is less prominent in the visible region with a distortion of 0.3 to 2 pixels.

5.4.7 Instrument Calibration

Instrument calibration is defined as the correction of the observed data or final spectrum into a physically meaningful absolute quantity. The calibration can be performed pre-flight and onboard, after launch. The OMI instrument includes two calibration devices onboard, a White Light Source (WLS) and Light Emitting Diodes (LEDs) [Dobber *et al.*, 2006].

The WLS, a Tungsten Halogen lamp, onboard OMI is used to determine the CCD detector properties, such as non-linearity of the pixels (see section 3.1.4) and

to perform a radiometric calibration and monitor throughput of the instrument to determine degradation of the instrument. The WLS is measured during flight once per week.

The LEDs, situated in front of the detectors in the UV and visible channels are used to identify bad pixels and obtain the relative gain values. The detector electronics consist of a 12 bit analogue to digital converter (ADC) which is proportional to the electron charge produce by the photons. The gain is a ratio of the number of electrons per pixel to the number of counts per pixel. The gain can be switched between a function of rows and a function of wavelength. Switching to a function of wavelength results in more gain, therefore, increasing the signal to noise ratio, which is of use in the UV region.

5.4.8 Wavelength Calibration

The wavelength calibration of the OMI is performed in a similar way to the CMAX-DOAS (see section 3.4.1), with the use of Fraunhofer lines in the radiance (terrestrial) and irradiance (solar) spectrum. The wavelength calibration may change during an orbit owing to thermal effects and the stability is expected to be of the order of 0.02 pixels for the irradiance spectra and 0.04 to 0.05 pixels for the radiance spectra. The calibration itself is accurate to 0.01 pixels. The spectral slit function was measured pre-launch for each pixel on the CCD and is assumed to stay constant throughout the lifetime of the instrument. Standard Gaussian line shapes profiles represent the line-shape for the UV-1 band and broadened Gaussians for the UV-2 and visible bands.

5.4.9 Data processing

The OMI data goes through a number of steps of processing, which is performed at the NASA Goddard Space Flight Center and at KNMI in the Netherlands. The main data products from the processing are:

Level 0 – Raw instrument data

Level 1 – Geolocated/Calibrated

Level 2 – Geophysical parameters

Level 3 – Gridded data

The level 0 product consists of raw instrument data at the original resolution. The data is then processed by KNMI using the ground data processing software (GDPS) developed by Dutch Space and is commissioned by the Netherlands Agency for Aerospace Programs (NIVR) [van den Oord *et al.*, 2006]. A 100 minute orbit of OMI produces 0.5 GB of raw data that is processed by the GDPS to Level 1 data. The level 0 data is first reformatted and with additional engineering data forms the Level 1a data package. The second step in the level 0 to level 1 processing includes radiometrically corrected and calibrated radiances, geolocated, at full instrument resolution (level 1b).

The level 2 product contains the geophysical parameters which are derived from the radiometrically calibrated and geolocated radiances. Each file contains one orbit of data and most of the level 2 products will be at 13 x 24 km^2 (nadir pixel size) resolution. The level 2 spectral surface UV irradiance and weighted irradiance (290 to 400 nm) are produced using the enhanced version of TOMS Surface UV-B flux algorithm. The radiance products are used in radiative transfer models.

There are four level 2 ozone products retrieved using different methods, two for total column ozone, the ozone profile, and tropospheric total ozone column. OMI also provides aerosol information using the near-UV and multi-wavelength methods which are used for the retrieval of aerosol characteristics over the ocean and land. Retrievals of trace gases are performed for NO_2, BrO, HCHO, OClO, and SO_2, using the DOAS technique (see Chapter 2). The slant column densities are determined from a polynomial function applied to the ratio of the measured Earth radiance to the solar irradiance data. The OMI algorithm is based on the following equation:

$$\frac{I(\lambda)}{F(\lambda)} = P(\lambda)\exp\left[-N_s\sigma(\lambda, T_{eff})\right] \tag{4.1}$$

where I is the radiance, F is the solar irradiance, P is the low order polynomial N_s is the slant column density of ozone, σ is the absorption cross section, λ, wavelength and T_{eff} the effective temperature. The fit parameters and the polynomial coefficients are determined using a nonlinear, least squares fit.

The OMI level 2 product also provides cloud pressure and effective cloud fraction (C_{eff}) measurements from two cloud retrieval algorithms. Clouds have varying effects on retrievals from space. Clouds may obscure gas located below the cloud, decreasing measurement sensitivity. Secondly, owing to the high albedo of clouds, they generally increase the sensitivity to gas above the cloud layer. The Rotational Raman Scattering method (OMCLDRR) is based on the least squares fitting of the Ring spectrum in the range 392-398 nm [Joiner and Vasilkov, 2006]. The O_2-O_2 algorithm (OMCLDO2) is based on DOAS fitting of the absorption spectrum of the O_2-O_2 band at 477 nm [Acarreta *et al.*, 2004] . In this study, the OMCLDO2 cloud product is used to identify cloudy pixels. Sneep *et al.*, [2006] produced a first validation of the OMCLDO2 product using MODIS/Aqua data. The results show that the effective cloud fraction error meets the OMI scientific requirement of ≤ 0.1.

The level 3 products contain daily global averaged data from the level 2 files, re-gridded at resolutions of, 0.25 deg x 0.25 deg, 0.5 deg x 0.5 deg, or 1 deg x 1 deg.

In addition to the operational data products, the OMI near-real-time (NRT) and very-fast-delivery data (VFD) are also produced. The NRT product is available within 3 hours after the observation and contains data for total and tropospheric NO_2 columns and ozone total columns. The main difference between the NRT product and the operational product is that the predicted altitude and ephemeris data is used in the NRT processing, which may cause some errors in the geolocation parameters [Boersma *et al.*, 2006]. The VFD products, available within 30 minutes of the observation, include images of total ozone columns and UV data [Leppelmeier *et al.*, 2006]. Retrievals of the operational products are also performed by independent science groups from the level 1b data.

5.5 OMI NO_2 retrieval algorithm

5.5.1 Tropospheric NO_2 columns

The retrieval of the level 2 operational NO_2 product from OMI is based on the DOAS method described in chapter 2. The algorithm for the retrieval of total column and tropospheric NO_2 from OMI data is described in detail by Bucsela *et al.* [2006]. Briefly, the algorithm is divided into three processes, each performed separately. The first process performs a least squares fitting on the ratio of the earthshine radiance spectrum to a solar irradiance spectrum. A fitting window of 405 to 465 nm is used to include the strongest NO_2 absorption features and avoids some of the Ring (Raman scattering) structure. In the second process, the NO_2 SCDs retrieved from the DOAS fit are converted to vertical column densities (VCDs) by the use of air mass factors (AMFs), which are computed for both stratospheric and tropospheric NO_2, under clear and cloudy, polluted and unpolluted conditions. The stratospheric AMF is applied to the retrievals to compute an initial estimate of the NO_2 VCD. Thirdly, a smoothing algorithm is then applied to the data within ± 12 hours and over a 10° latitude band and zonal planetary wave smoothing (up to wave-2), to extract the "unpolluted" field, consisting mostly of the stratospheric NO_2. If the initial VCD exceeds the unpolluted value then the AMF is corrected to one appropriate for elevated levels of tropospheric NO_2 and a new VCD calculated for total and tropospheric NO_2.

The publicly released NO_2 operational product used in this thesis contains datasets of the observed total column, the tropospheric column (NO_2 vertical column between ground and the estimated mean tropopause pressure of 150 mb), the polluted column (magnitude of the column above the background, integrated from ground to 250 mb), the unpolluted column (polluted column subtracted from the total column) and an estimate of the column hidden by the clouds within the FOV of the instrument known as the ghost column. The ghost column is calculated from the measured column and an *a priori* NO_2 profile. However care must be taken when using the ghost column as the uncertainty increases as the cloud fraction increases, in particular for cloud fractions greater than 0.4.

5.5.2 Errors

The main sources of error in the OMI NO_2 retrieval algorithm arise from uncertainties in the AMF. The calculation of the AMF is affected by the assumed profile shape of NO_2 in the atmosphere and also the OMI cloud fraction and cloud top pressure. The cloud algorithm is sensitive to aerosols, therefore, aerosol effects are included indirectly in the AMF calculation and their relative contribution to the total error budget is expected to be small. However, the omission of aerosols in the AMF calculation may still have an effect, particularly over heavily polluted regions. The relative errors in the tropospheric column density estimate are also larger than the total column errors. Therefore, the error in tropospheric NO_2 columns can be as large as 60% in the presence of clouds/aerosols and pollution [Boersma *et al.*, 2004].

5.6 Striping effects

Owing to some hot transient pixels in the OMI CCDs and large dark current signals, which increase the noise at certain wavelengths, stripes have occurred in the L2 data products. Stripe patterns with peak to peak amplitudes of 20 % are commonly found in the operational NO_2 column density data. The striping has more of an effect on weaker absorbers, such as BrO, HCHO and ClO, owing to the peak to peak magnitude of the striping becoming comparable to the column amounts. However, the striping also has an effect on stronger absorbers such as NO_2. An example of this can be seen in the level 2 NO_2 data in Figure 5-5. In general, the stripe pattern is very similar if the data has been processed with the same solar irradiance spectrum, suggesting the origin of the stripes is in the irradiance spectra rather than in the earthshine radiance spectra.

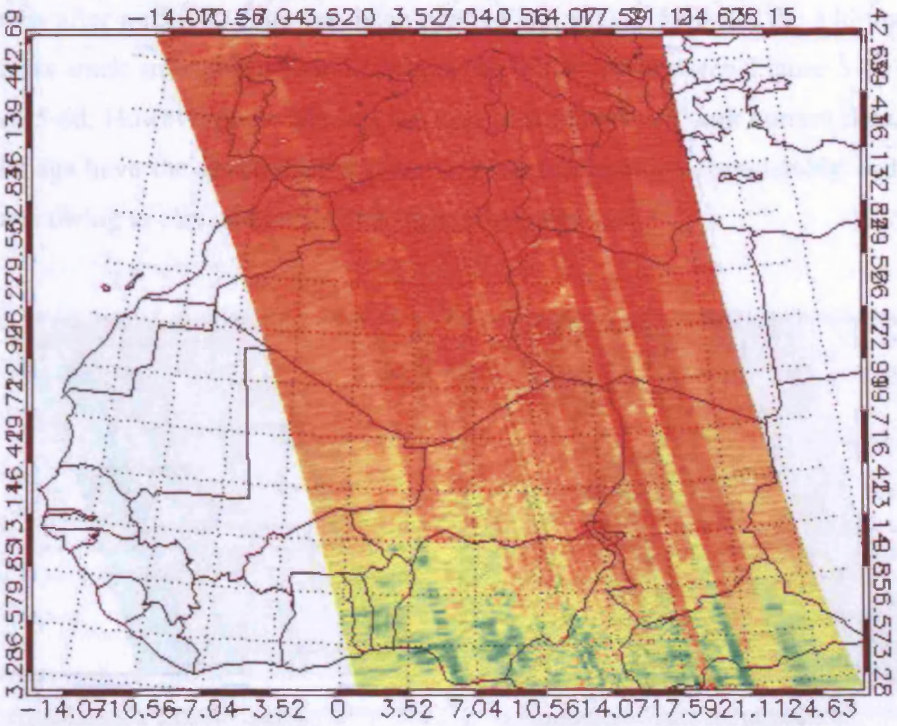

Figure 5-5: OMI NO_2 column amounts. The vertical striping effect owing to hot pixels and large dark current is clearly visible [Veihelmann *et al.*, 2006].

To correct for striping effects, several improvements have been performed to the retrieval algorithm [Veihelmann *et al.*, 2006]. Firstly the hot transient pixels are identified and a correction factor for the dark current in applied. In addition, time averaging the irradiance spectra using a median filter also reduces the effect of stripes.

A further addition is an experimental cross-track smoothing procedure. The stripe patterns in the column density data are identified as those values that deviate from the along-track median by more than the along-track standard deviation. A low order polynomial function is then fitted to the stripe pattern and dividing the stripe pattern by the polynomial function brings the stripe patterns of all orbits to a common baseline. For each row, the irradiance spectrum is selected that causes the stripe with the smallest possible amplitude or no stripe at all

The effects of the de-striping techniques can be observed in Figure 5-6. Figure 5-6a, shows NO_2 vertical columns when no striping has been applied. Figure 5-6b shows the NO_2 vertical columns after the hot transient pixels are identified and a correction factor for the dark current applied. Figure 5-6c shows the NO_2 vertical

columns after a median filter has been applied and Figure 5-6d has the addition of the cross track smoothing. Small changes are observed between Figure 5-6c and Figure 5-6d. However, reprocessing the data using improved dark current data and pixel flags have the greatest effect, the striping has reduced considerably and the features owing to elevated levels of NO_2 are more obvious.

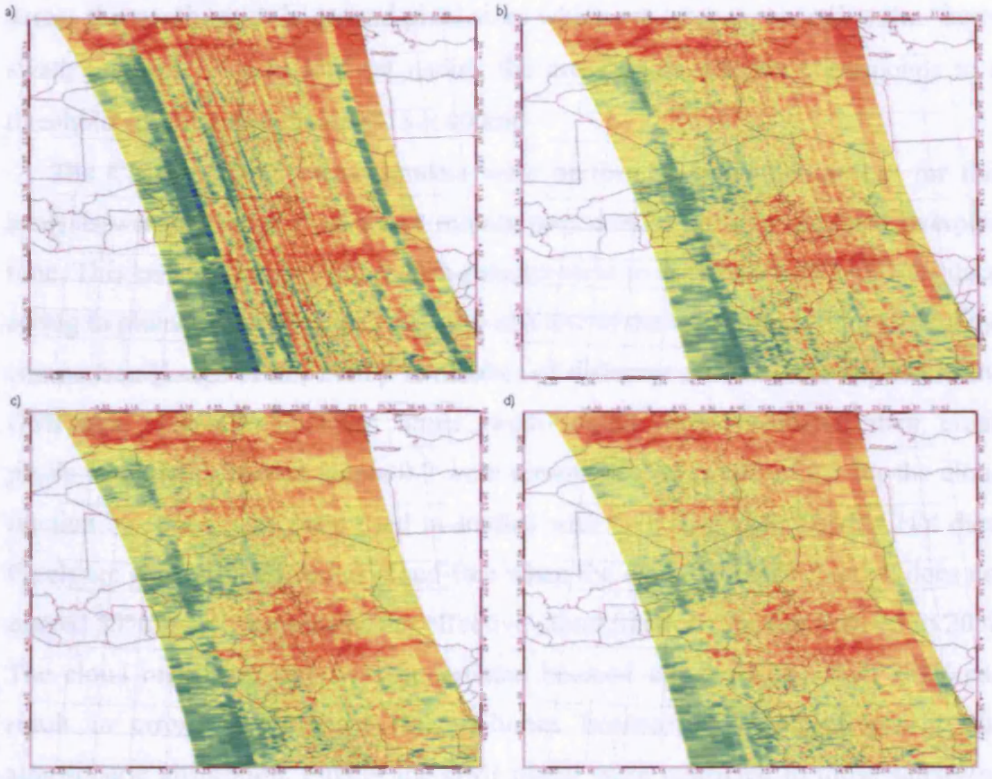

Figure 5-6: OMI NO_2 vertical columns for a) nominal data, reprocessed data using b) the dark current corrections c) median filtered irradiance spectra and d) cross-track smoothing correction.

5.7 Comparison of OMI and CMAX-DOAS NO_2 measurements

5.7.1 Co-location thresholds applied to OMI data

Coincident OMI and CMAX-DOAS tropospheric columns over Leicester were compared for the period when continuous CMAX-DOAS data were available. A

coincidence was defined as an overlap between an "inner swath" OMI pixel and a circle of radius 5 km centred to the *in situ* monitor in the city centre (52.63 N, 1.13 W). The circle includes the main built-up area of the city and major road systems in terms of estimated NO_2 concentrations as defined by a map of city emissions (not shown). The OMI pixels towards the edge of the swath, with cross track positions of 0 to 10 and 50 to 59, have not been included in the analysis because viewing angles across the swath result in ground pixel sizes which are large compared to the "inner swath" size of 13×24 km^2 (at nadir); the cross-track criterion corresponds to a threshold size of approximately 13×40 km^2

The CMAX-DOAS measurements were performed every minute but for this analysis were averaged over a five minute period either side of the OMI overpass time. This ensures that any short term enhancement in the CMAX-DOAS NO_2 data, owing to plumes passing across the field-of-view of the telescope, will not affect the comparison [Leigh *et al.*, 2007]. A number of different criteria were applied to the OMI data. First, all coincident "inner swath" pixels were considered, then, cloud pixels with cloud fraction above 0.2 were removed; a threshold of 0.2 for the cloud fraction has previously been used in studies with GOME and SCIAMACHY data. Pixels are generally defined as cloud-free when the cloud radiance fraction does not exceed 50%, which corresponds to effective cloud fractions smaller than 15 to 20%. The cloud restriction tests was undertaken because clouds in the OMI FOV can result in erroneous retrieved NO_2 columns because of cloud effects on the atmospheric absorption. Finally the OMI pixels were restricted to those satisfying the first two conditions but also having at least 90% of the Leicester circle within the OMI pixel. An important aspect of this comparison is that relevant CMAX-DOAS data were only available for the winter months from December 2005 to March 2006.

5.7.2 Results

The results in Figure 5-7 show correlations between OMI and CMAX-DOAS tropospheric NO_2 columns for the three cases considered. The black circles in Figure 5-8 show all pixels that satisfy the "inner swath" criterion. The calculated correlation coefficient, R, is relatively poor at 0.1. The red crosses are those for

which further cloud clearing has been performed. The best correlation is obtained for the strictest filtering of the OMI data (r = 0.45) where at least 90% of the Leicester circle within the OMI pixel.

Figure 5-7 shows that although there is a reasonable agreement between the two sets of data a positive offset is present in the OMI NO_2 VCD of 1.67×10^{15} molecules cm^{-2} and the CMAX-DOAS instrument often retrieves OMI NO_2 VCD twice as large as the OMI during this period over the winter. The VCDs from CMAX-DOAS are retrieved using an AMF calculated with an aerosol setting similar to that measured in September 2007, with an AOD of 0.05 up to 1500 m. During winter time the aerosol levels can be high owing to the combustion of fossil fuels for heating with the addition of low temperatures and stagnant air masses. Leigh *et al.* [2007] derived air mass factors (AMF) for NO_2 for each of the viewing angles of the CMAX-DOAS instrument, by inputting an aerosol box profile of 0.1 optical depth from the surface to 1500 m.

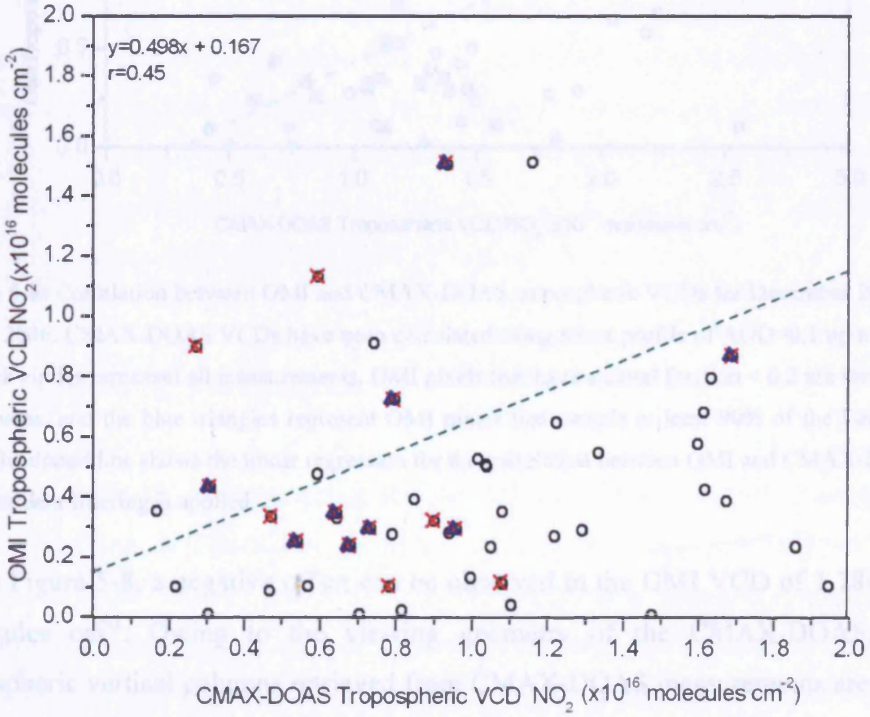

Figure 5-7: Correlation between OMI and CMAX-DOAS tropospheric VCDs for December 2005 to March 2006. Black circles represent all measurements. OMI pixels that have a cloud fraction < 0.2 are shown as red crosses, and the blue triangles represent OMI pixels that sample at least 90% of the Leicester area. The dotted line shows the linear regression for the correlation between OMI and CMAX-DOAS when strident filtering is applied.

Figure 5-8 shows the results of the comparison between OMI and CMAX-DOAS using AMFs calculated by SCIATRAN with the settings used by Leigh *et al.* [2007]. The results show that the agreement is much better, the correlation coefficient has increased to r=0.64 when observing those pixels with the strictest filtering of the OMI data.

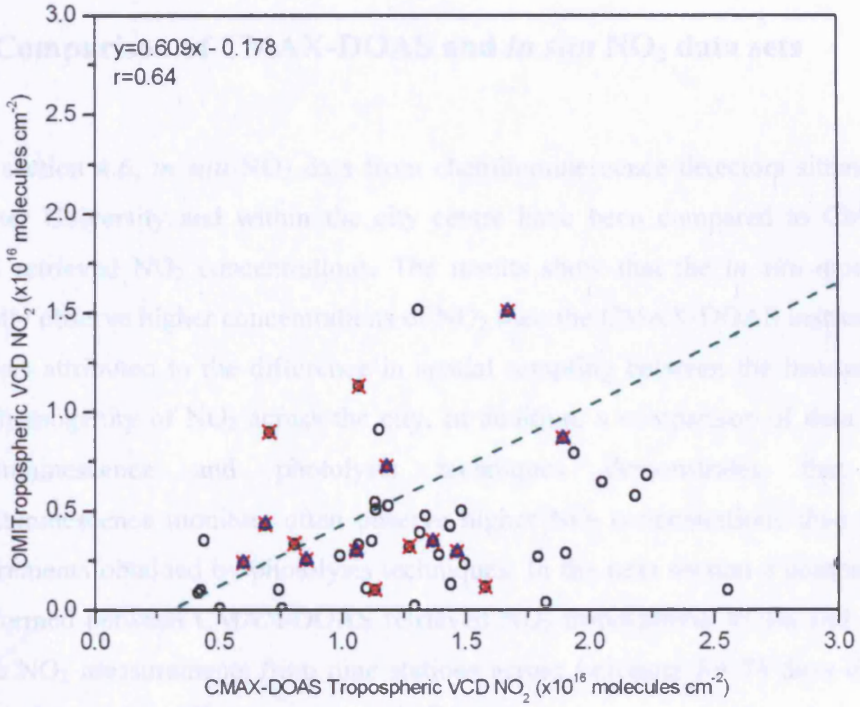

Figure 5-8: Correlation between OMI and CMAX-DOAS tropospheric VCDs for December 2005 to March 2006. CMAX-DOAS VCDs have been calculated using a box profile of AOD=0.1 up to 1500 m Black circles represent all measurements. OMI pixels that have a cloud fraction < 0.2 are shown as red crosses, and the blue triangles represent OMI pixels that sample at least 90% of the Leicester area. The dotted line shows the linear regression for the correlation between OMI and CMAX-DOAS when strident filtering is applied.

In Figure 5-8, a negative offset can be observed in the OMI VCD of 1.78×10^{15} molecules cm^{-2}. Owing to the viewing geometry of the CMAX-DOAS, the tropospheric vertical columns retrieved from CMAX-DOAS measurements are only representative of a small area across the OMI pixel. At nadir, when the pixel size is smallest (13×24 km^2), the area of Leicester still only contributes to approximately 25% of the total OMI pixel coverage. There are two different NO_2 sources contributing to the tropospheric NO_2 column measured by OMI. One is from the city centre and the other from the background NO_2. The background source of NO_2

is explored further in section 5.9. A further improvement in the correlation may be possible if using measurements of AOD from the MODIS instrument onboard the AQUA satellite to determine the NO_2 AMFs for CMAX-DOAS. However, this has not performed in the work here.

5.8 Comparison of CMAX-DOAS and *in situ* NO_2 data sets

In section 4.6, *in situ* NO_2 data from chemiluminescence detectors situated at Leicester University and within the city centre have been compared to CMAX-DOAS retrieved NO_2 concentrations. The results show that the *in situ* monitors generally observe higher concentrations of NO_2 than the CMAX-DOAS instrument. This was attributed to the difference in spatial sampling between the instruments and inhomogenity of NO_2 across the city. In addition, a comparison of data from chemiluminescence and photolysis techniques demonstrates that the chemiluminescence monitors often observe higher NO_2 concentrations than those measurements obtained by photolysis techniques. In the next section a comparison is performed between CMAX-DOAS retrieved NO_2 tropospheric VCDs and near-surface NO_2 measurements from nine stations across Leicester for 74 days during the period December 2nd 2005 to March 13th 2006

5.8.1 Categorising in situ monitors

Many of the *in situ* monitoring stations in Leicester are located close to the roadside and may be affected by the traffic density. The measurements from these stations, therefore, do not necessarily represent the spatially averaged concentration of NO_2 across Leicester. A mean concentration of NO_2 was calculated for each of the *in situ* stations between the local time of 11am and 2 pm to represent the concentration during the OMI overpass. The stations were then categorised according to the levels of NO_2 measured (Table 5-3). Those stations with mean concentrations in excess of 30 ppb (group 3) were located close to the roadside, in areas where high traffic density occurs. Group 2 monitors were located between 2

and 8 m from the roadside and in areas with less traffic, and the group 1 monitors were situated between 6.5 and 35 m from the road.

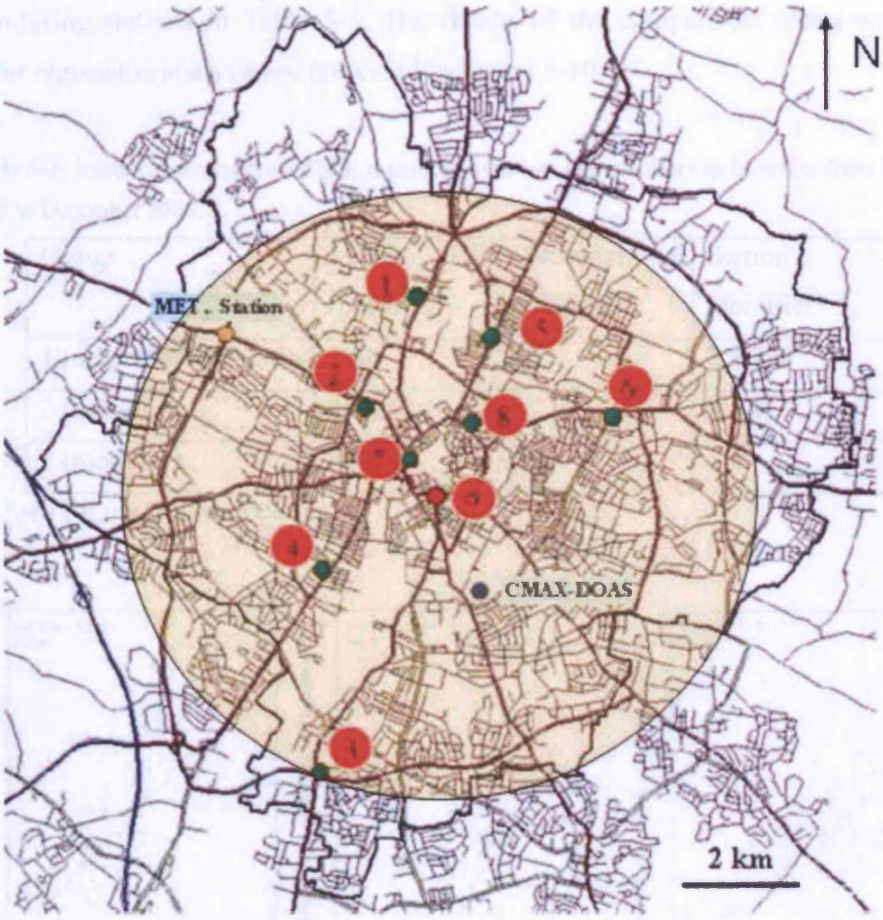

Figure 5-9: Location of chemiluminescence NO_2 monitoring stations in Leicester (red) and the CMAX-DOAS (blue). The orange circle represents a 5 km radius area around the centre of the city that encompasses Leicester.

5.8.2 Comparison of CMAX-DOAS NO_2 with in situ measurements

The *in situ* monitoring stations perform measurements every 15 minutes (or 1 hour in the case of monitor 9 in the city centre), over a 24 hour period. However, the CMAX-DOAS instrument can only obtain measurements during daylight hours. For the comparison between CMAX-DOAS and *in situ* NO_2 data sets only those measurements by the chemiluminescence monitors obtained during the period when CMAX-DOAS was operating were included in the analyses. The vertical columns

from the CMAX-DOAS instrument were derived using AMFs calculated with the settings used by Leigh *et al.* [2007]. Daily averages were then calculated for all sets of data, along with the standard deviation for each of the three groups of *in situ* monitoring stations in Table 5-3. The results of the comparison, along with the linear regression analysis are presented in Figure 5-10.

Table 5-3: Mean concentrations of NO_2 measured by the *in situ* monitors in Leicester from January 2005 to December 2006.

Group	Mean NO_2 (ppb)	Number of stations	Station identifier*
1 (urban background)	<20	4	2,4,7,9
2 (urban)	20<30	3	1,5,8
3 (roadside)	>30	2	3,6

*see Figure 5-9 for location

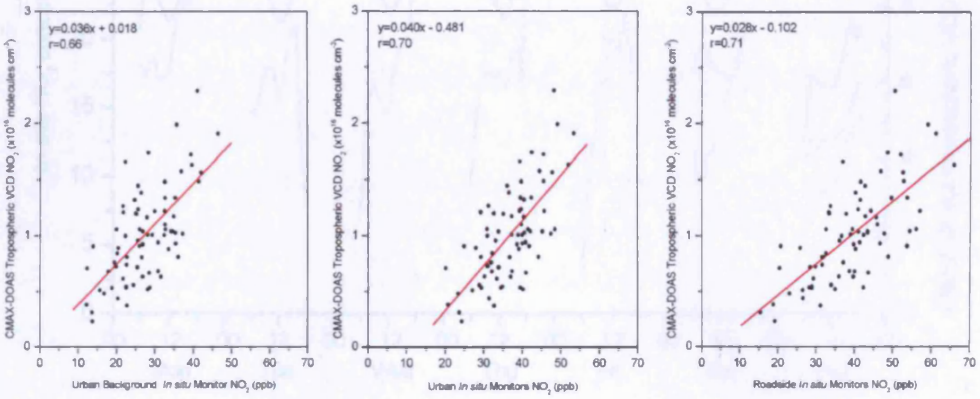

Figure 5-10: Daily averaged NO_2 concentrations from the three groups of in situ monitoring stations (Table 1) and the CMAX-DOAS retrieved NO_2 VCD for December 2005 to March 2006.

The results show, for those stations operating near to the roadside (group 3) and in areas of heavy traffic density (group 2), that there is a positive offset between CMAX-DOAS and *in situ* measurements; such that the *in situ* instrument measure a strong NO_2 signal even when CMAX-DOAS is measuring low values. This would be expected, as the monitoring stations measure NO_2 near to the surface, whereas CMAX-DOAS measures NO_2 throughout the boundary layer. The agreement, however, is still very good with correlation coefficients of $r = 0.68$ and $r = 0.71$ for group 2 and group 3 monitoring stations respectively.

In contrast to the correlations with group 2 and group 3 monitoring stations, the comparison with measurements from monitoring stations in group 1, defined as "urban background", show no positive bias in the *in situ* measurements. In fact there is a very small positive bias in the CMAX-DOAS measurements. The agreement is also very good, with a correlation coefficient of $r = 0.66$. The results show that the measurements from those stations situated close to the roadside, or in areas where the traffic density is high, display a greater influence from emissions owing to vehicles.

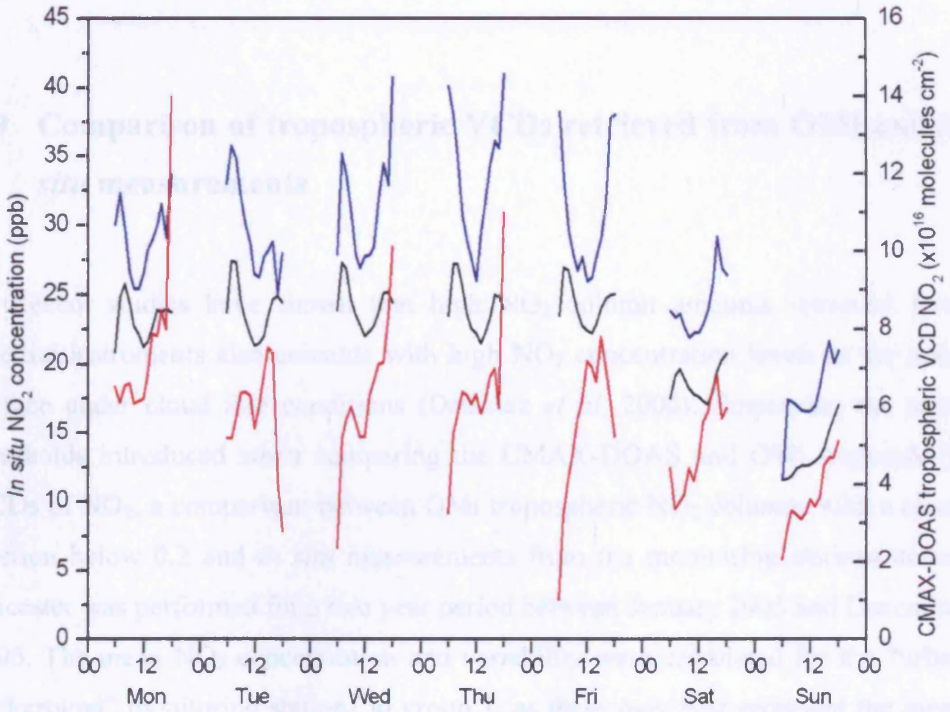

Figure 5-11: Average VCDs of NO_2 in Leicester for each hour of the week as measured by the CMAX-DOAS instrument (red lines) and measurements of NO_2 concentration from the group 1 *in situ* monitors (blue lines), for December 2005 to March 2006. The black lines represent the average concentration of NO_2 measured by the group 1 *in situ* monitors from 6am to 6pm for 2005 to 2006.

Hourly averaged measurements have been produced for each day of the week for coincident measurements between the CMAX-DOAS and the group 1 *in situ* monitors for December 2005 to March 2006. The results in Figure 5-11 show that both sets of data generally observe peaks in NO_2 during the morning and evening, during weekdays, coinciding with the local rush hour traffic. Saturdays and Sundays show different diurnal cycles owing to the reduced traffic density. During early

morning and late evening the two sets of data do not agree as well. This may be due to sampling differences as there are a reduced number of coincident measurements during these periods over the winter months owing to the CMAX-DOAS instrument only operating when the light levels are sufficient enough to retrieve measurements. The change in the PBL height may also cause differences between the morning and evening. The black lines in Figure 5-11 show the diurnal cycle from two years of averaged data between 6am and 6pm for the group 1 *in situ* monitors. The peaks in NO_2 during the week days are evident.

5.9 Comparison of tropospheric VCDs retrieved from OMI and *in situ* measurements

Recent studies have shown that high NO_2 column amounts retrieved from satellite instruments also coincide with high NO_2 concentration levels at the near-surface under cloud free conditions (Ordóñez *et al.* 2006). Employing the same thresholds introduced when comparing the CMAX-DOAS and OMI tropospheric VCDs of NO_2, a comparison between OMI tropospheric NO_2 columns with a cloud fraction below 0.2 and *in situ* measurements from the monitoring stations across Leicester was performed for a two year period between January 2005 and December 2006. The mean NO_2 concentration and variability were calculated for the "urban background" monitoring stations in group 1, as these may best represent the mean level of NO_2 at Leicester city scales.

5.9.1 FOV-weighted comparison

Figure 5-12 shows a comparison between the mean NO_2 measured by the *in situ* monitoring stations in group 1 and OMI tropospheric NO_2 columns. The horizontal bars illustrate the variability of near surface NO_2 measurements across the stations in group 1. The tropospheric NO_2 VCDs correlate reasonably well (r = 0.43, n = 150) with the near-surface NO_2 measurements when cloud clearing is implemented but there is quite some scatter. Near-surface measurements,

particularly in urban areas, are subject to variation owing to spatial and temporal inhomogeneity of boundary layer NO_2. These variations may account for some of the differences that are observed between the OMI tropospheric NO_2 VCDs and ground based measured NO_2. The two observation techniques yield different samplings of the atmosphere on a spatial scale, which can introduce biases. Emissions of NO_2 retrieved by OMI over Leicester originate from the polluted city centre and the surrounding area.

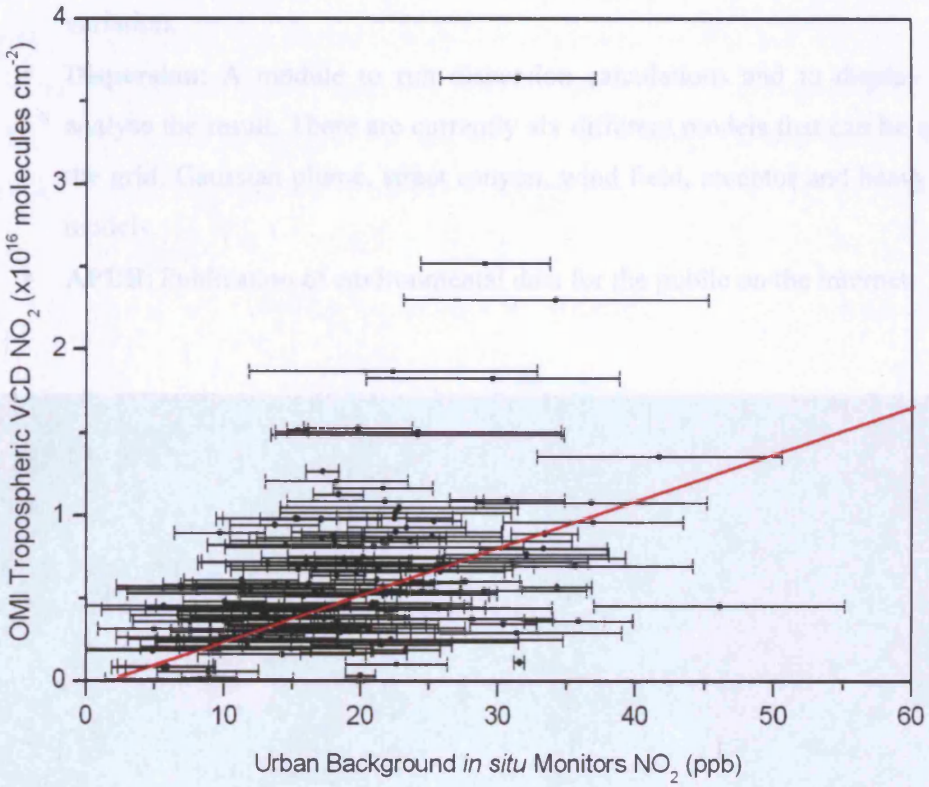

Figure 5-12: Correlation between OMI tropospheric VCDs and the mean near surface NO_2 concentrations from group 1 *in situ* monitoring stations for January 2005 to December 2006. The horizontal bars for ach point represent the variability of NO_2 concentration across the group 1 in situ monitors and the red line represents the linear regression analysis.

The variation in emissions across Leicestershire can be observed in Figure 5-13. The figure on the left shows NO_x emissions calculated with the Airviro model for 5th December 2005 at 13:00 GMT for a 1 km x 1 km grid. The Airviro model is a web based integrated system for air quality management designed by the Swedish

Meteorological and Hydrological Institute (SMHI). The main modules of the model are:

- **Indico**: Data collection and time series. Data are collected automatically from instruments measuring meteorology, air quality and other variables relevant to air pollution.
- **Indico validation**: Supports validation of measured data.
- **EDB**: An emission database that describes emissions to air and water in an area with many sources emitting several substances with different time variation.
- **Dispersion**: A module to run dispersion calculations and to display and analyse the result. There are currently six different models that can be used, the grid, Gaussian plume, street canyon, wind field, receptor and heavy gas models.
- **APUB**: Publication of environmental data for the public on the internet

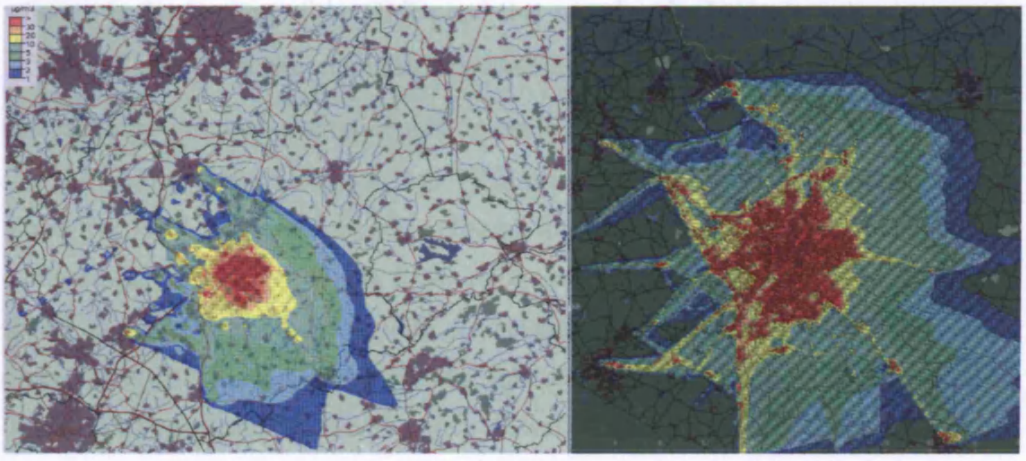

Figure 5-13: NO_x emissions over Leicestershire (left) and the Leicester city (right) calculated with the Airviro model for 5th December 2005 at 13:00 GMT.

For the results in Figure 5-13, a Gaussian model has been used to derive the distribution of pollutants near-surface over Leicester. The model does not support simulations of NO_2 alone; therefore, NO_x has been modelled here. One hour mean values are simulated, as the wind is generally constant during such a period. The plot on the right in Figure 5-13 shows the same simulation as the plot on the left, but

on a grid of 250 m x 250 m for Leicester city centre and the immediate surroundings. Both simulations demonstrate the variability of NO_x over Leicester. In particular, in can be observed that the city centre is a large emission source, which disperses towards the surrounding area. The region in red in both plots in Figure 5-13 encompasses an area approximately 5 km in radius, as shown in Figure 5-9.

To estimate the equivalent near-surface NO_2 concentration sampled by OMI, background NO_2 measurements were obtained from an *in situ* monitor, situated in Market Harborough (52.55° N, 0.77 W°), approximately 38 km south east of Leicester city centre. The station was chosen as it is situated in a rural site, generally upwind of Leicester, and is relatively close to the city, but outside of the 5 km radius area classed as the polluted region. The FOV-weighted near-surface NO_2 ($FWNS_{NO_2}$) can be expressed by the following equation:

$$FWNS_{NO_2} = \alpha.NS_{NO_2}^{city} + (1-\alpha).NS_{NO_2}^{bkg} \qquad \textbf{Equation 5-1}$$

where α is the fraction of the OMI pixel that samples the Leicester urban area and $NS_{NO_2}^{city}$ and $NS_{NO_2}^{bkg}$ are the coincident near-surface measurements of NO_2 from the city monitors and the background monitor in Market Harborough.

The FOV-weighted near-surface NO_2 measurements have been compared to cloud-free OMI NO_2 tropospheric columns for 2005 and 2006. The results of the comparison, presented in Figure 5-14, show that the agreement is very good for the spring and summer months with correlation coefficients of 0.83 and 0.64 respectively. During the winter months, however, the correlation is very poor (r = 0.04). OMI generally retrieves much lower concentrations of NO_2 than that represented by the near-surface NO_2 measurement. This is particularly true for the months December and January. In the autumn season, the majority of points remain close to the best fit line for spring and the correlation is good (r = 0.6); however, there are occurrences when high concentrations of NO_2 are measured from the ground when OMI measures low tropospheric NO_2 columns. All but one of those coincidences occurs in November, which suggests that the atmospheric conditions in late autumn and winter are such that it is difficult to retrieve NO_2 close to the surface from satellite based instruments.

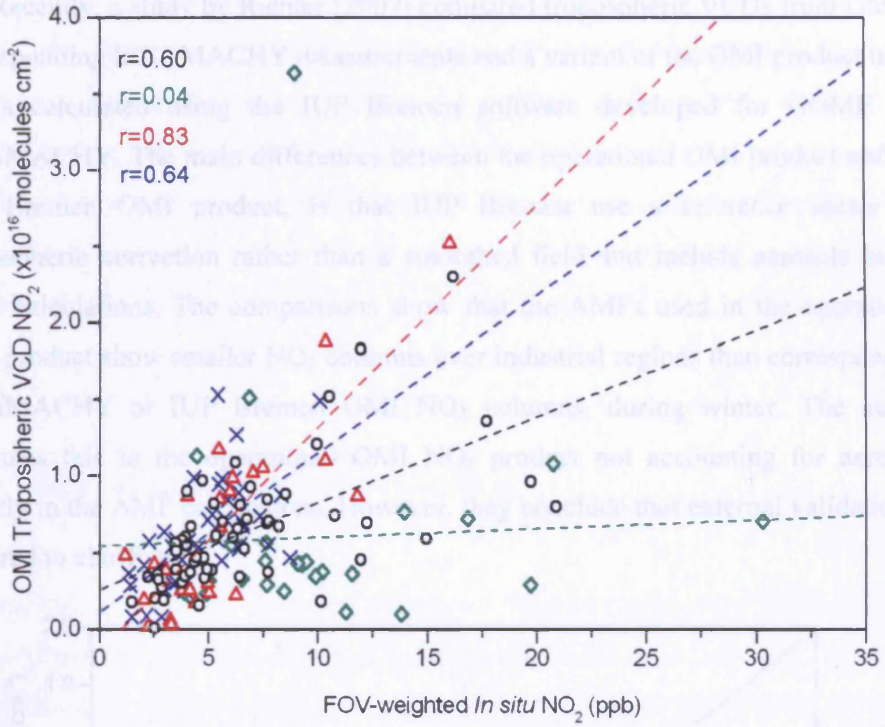

Figure 5-14: Correlation between OMI NO_2 tropospheric VCDs (cloud fraction <0.2) and the FOV-weighted mean near-surface NO_2 concentrations, for January 2005 to December 2006. The different symbols represent the seasons, autumn (black circles), winter (green diamonds), spring (red triangles) and summer (blue crosses). The dashed lines represent the linear regression for each season.

The retrieved column from OMI depends on the *a priori* profile shape used in the AMF calculations. During winter, local emissions in Leicester are generally high, but the OMI instrument may yield lower values as the a priori may not reflect the high levels observed coupled with the decrease in vertical sensitivity of OMI towards the surface [Eskes *et al.*, 2003].

Another possible explanation for the divergence during these months is the effect of aerosol on the AMF calculations. An increase in aerosols during winter results in an overestimation in the cloud fraction and a lower cloud height, which tends to increase the light path through the troposphere, hence, an increase in the tropospheric AMF and a lower retrieved column than in reality. Therefore, the

indirect effect of aerosols on the cloud retrieval may only partly compensate for the exclusion of aerosols in the AMF calculations [Boersma *et al.*, 2004].

Recently, a study by Richter [2007] compared tropospheric VCDs from OMI to corresponding SCIAMACHY measurements and a variant of the OMI product using AMFs calculated using the IUP Bremen software developed for GOME and SCIAMACHY. The main differences between the operational OMI product and the IUP Bremen OMI product, is that IUP Bremen use a reference sector for stratospheric correction rather than a smoothed field and include aerosols in the AMF calculations. The comparisons show that the AMFs used in the operational OMI product show smaller NO_2 columns over industrial regions than corresponding SCIAMACHY or IUP Bremen OMI NO_2 columns, during winter. The author attributes this to the operational OMI NO_2 product not accounting for aerosols directly in the AMF calculations. However, they conclude that external validation is required to clarify this.

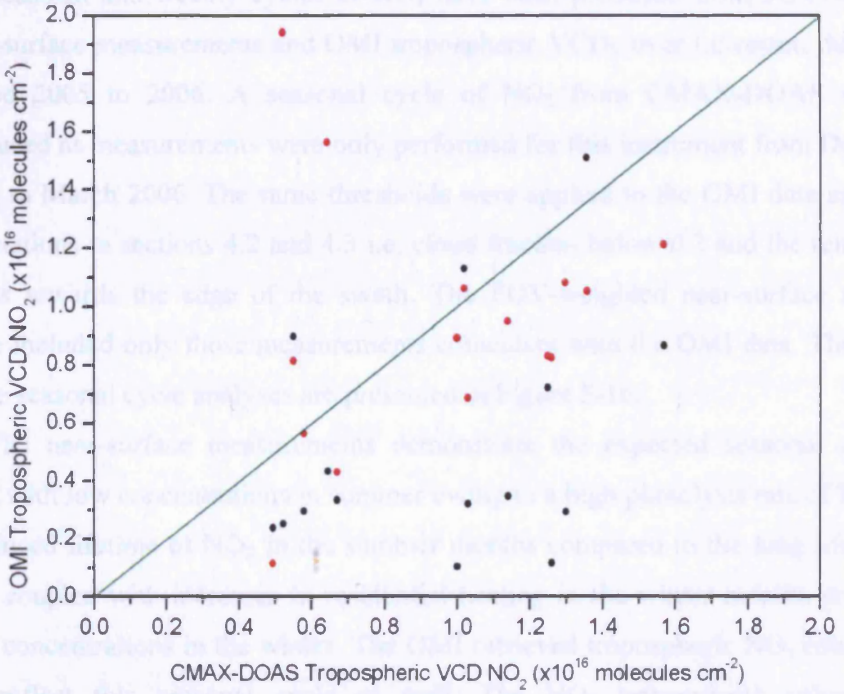

Figure 5-15: Correlation between OMI and CMAX-DOAS tropospheric NO_2 VCDs for December 2005 to March 2006. CMAX-DOAS VCDs have been calculated using a box profile of AOD=0.1 up to 1500 m. Black points represent the OMI operational product for tropospheric NO_2 VCDs with a cloud fraction < 0.2. The red points are the equivalent coincidences for the Bremen retrieval of tropospheric NO2 VCDs. The green line represents the 1:1 line.

Figure 5-15 shows a comparison of OMI and CMAX-DOAS tropospheric NO_2 VCDs for the operational product (black points) and the Bremen retrieval (red points) for all OMI data with a cloud fraction below 0.2 from December 2005 to March 2006. The results show that the Bremen retrieval of tropospheric NO_2 VCDs appear much higher and to fall closer to the 1:1 line, shown in green, however the correlation has not improved overall. Further validation with a long time series of data is required to determine whether accounting for aerosols directly in the AMF and using a reference sector for stratospheric correction results in an accurate retrieval of tropospheric NO_2 VCDs.

5.10 Seasonal and weekly cycles of NO_2

Seasonal and weekly cycles of NO_2 have been produced from FOV-weighted near-surface measurements and OMI tropospheric VCDs over Leicester, during the period 2005 to 2006. A seasonal cycle of NO_2 from CMAX-DOAS was not produced as measurements were only performed for this instrument from December 2005 to March 2006. The same thresholds were applied to the OMI data as for the correlations in sections 4.2 and 4.3 i.e. cloud fraction below 0.2 and the removal of pixels towards the edge of the swath. The FOV-weighted near-surface seasonal cycle included only those measurements coincident with the OMI data. The results of the seasonal cycle analyses are presented in Figure 5-16.

The near-surface measurements demonstrate the expected seasonal cycle of NO_2, with low concentrations in summer owing to a high photolysis rate of NO_2 and a reduced lifetime of NO_2 in the summer months compared to the long lifetime of NO_2 coupled with increases in residential heating in the winter months producing high concentrations in the winter. The OMI retrieved tropospheric NO_2 columns do not reflect this seasonal cycle as well. The NO_2 tropospheric columns are significantly lower during January and December than expected, as previously discussed in section 4.3, suggesting that OMI is underestimating the NO_2 tropospheric columns during winter. Higher NO_2 for spring compared to autumn is observed by both sets of sensors.

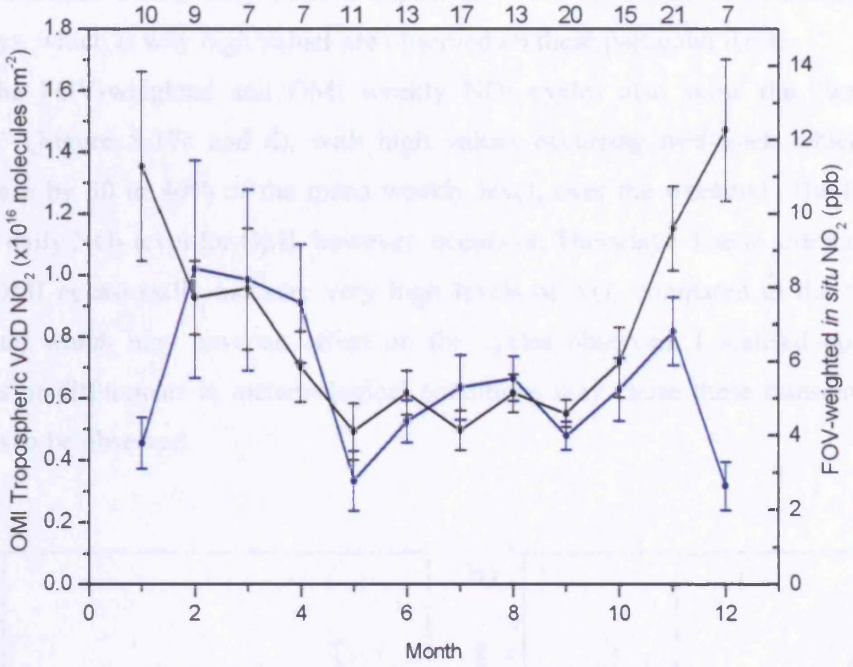

Figure 5-16: Monthly averages of NO_2 for 150 cloud free days (clf <0.2) between January 2005 and December 2006 for OMI tropospheric columns (blue) and coincident mean FOV-weighted *in situ* data from group 1 monitors in Leicester (black), the error bars show the standard deviation on the mean. The number of cloud free observation for each month is shown at the top of the plot.

Time average weekly cycle of NO_2 measurements from the ground based monitors and OMI has been examined for all cloud free days (OMI cloud fraction $\leq$ 0.2) during 2005 and 2006. For each day of the week, the mean is calculated and normalised to the total mean value of all the days. Results are presented in Figure 5-17a and Figure 5-17b which show normalised near-surface NO_2 measurements, coincident with OMI, for each day of the week for group 1 monitors and the rural background monitor. The error bars on the plots show the standard deviation on the daily mean. A noticeable decrease in NO_2 at the weekend compared to the mean weekly level is observed in both the urban and rural datasets; however, there is a large decrease in the rural measurements on Tuesdays and Wednesdays, comparable to that of the weekend values. The rural site is generally less affected by anthropogenic emissions; there is also a decrease of average NO_2 from urban to rural concentrations as expected (not shown). Hence, the rural measurements may not actually demonstrate a strong weekly cycle but may be influenced by emissions

from vehicles during busy periods especially from commuters on Mondays and Fridays, which is why high values are observed on these particular days.

The FOV-weighted and OMI weekly NO_2 cycles also show the "weekend effect" (Figure 5-17c and d), with high values occurring mid-week which then decrease by 30 to 40% of the mean weekly level, over the weekend. The highest mean daily NO_2 level for OMI, however, occurs on Thursday. The *in situ* monitors and OMI occasionally measure very high levels of NO_2 compared to the weekly median, which may have an affect on the cycles observed. Localised pollution events or differences in meteorological conditions may cause these transient high values to be observed.

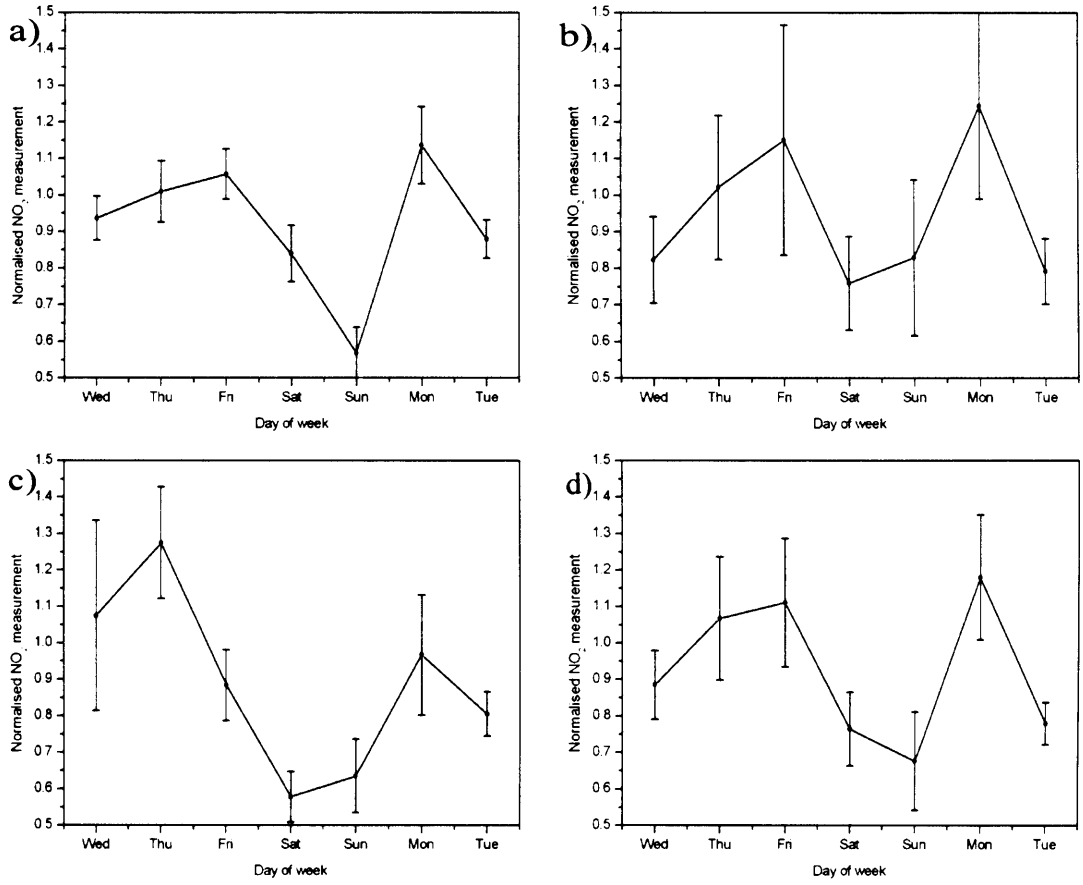

Figure 5-17: Weekly cycle of NO_2 over Leicester for all cloud free days during 2005 and 2006 for a) group 1 *in situ* stations, b) the rural background station, c) OMI VCD retrievals and d) FOV-weighted measurements. The mean is calculated for each day and normalised to the mean weekly value. The error bars show the standard deviation on the mean.

Weekly cycles have also been produced from CMAX-DOAS data for the winter period during December 2nd 2005 to March 15th 2006, presented in Figure 5-18a, along with coincident *in situ* monitor measurements from group 1 monitoring stations in Leicester (Figure 5-18b). The "weekend effect" during this period is more noticeable than those from the FOV-weighted and OMI cycles in Figure 5-17. CMAX-DOAS and the *in situ* stations in Leicester show a decrease in NO_2 on Saturday of approximately 5 to 15%, owing to the reduction in industrial activity, but possible increase in traffic due to shopping and short trips and a significant decrease of approximately 30 to 40% on Sunday. The FOV-weighted and OMI measurements both include NO_2 emissions from the rural background, therefore, the anthropogenic cycles, which are very clear in the city measurements, may have less of an effect when a background source is also measured. The weekly cycle may also be dependent on the season, owing to the difference in the lifetime of NO_2 in the boundary layer from summer to winter. However, a longer time series of NO_2 data than that used in this study will be required to perform a reasonable analysis of the seasonal variation on the weekly cycle.

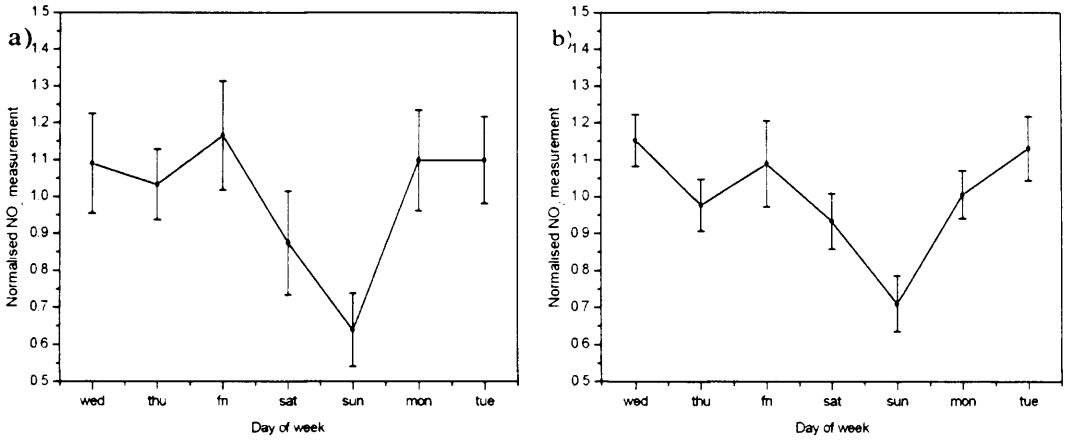

Figure 5-18: a) Weekly cycle of NO_2 over Leicester observed by a) CMAX-DOAS and b) group 1 *in situ* monitors for December 2nd 2005 to March 15th 2006.

5.11 Summary and conclusions

In this chapter, vertical tropospheric column densities of NO_2 from CMAX-DOAS, for the period December 2005 to March 2006 over Leicester, UK have been retrieved for the comparison with OMI tropospheric NO_2 columns. The VCDs for the CMAX-DOAS were derived from tropospheric NO_2 AMF calculations by the SCIATRAN RTM. Initially, the AMFs were calculated assuming an aerosol profile similar to that retrieved by the lidar instrument, with an AOD of 0.002, as described in Chapter 4. However, the results of the comparison between the OMI and CMAX-DOAS instrument, showed that an improvement between the correlation can be obtained when using an aerosol profile with a greater aerosol load (AOD=0.1) for these winter months, giving a correlation coefficient of r=0.64 when the OMI data is cloud-cleared and where at least 90% of the Leicester circle is within the OMI pixel. The NO_2 data from the CMAX-DOAS instrument has previously been validated with near-surface NO_2 measurements from chemiluminescence monitors located in the city centre, with good agreement [Leigh *et al.*, 2006; 2007]. The *in situ* chemiluminescence monitors, were classified into three different groups, according to the mean concentration level of NO_2. The groups of monitors that best represent the concentration of NO_2 across Leicester from correlations with the CMAX-DOAS instrument were the "urban background" group with mean NO_2 levels below 20 ppb.

Comparisons between ground based and space based instruments are challenging, owing to the large difference in spatial sampling and time correlations, which can introduce biases. The agreement between CMAX-DOAS measurements of NO_2 over Leicester, with retrieved tropospheric NO_2 columns from OMI is good when cloud clearing has been applied but the correlation is further improved, with a correlation coefficient of 0.64, when only those pixels that sample at least 90% of the Leicester area were included in the analyses.

The correlation of near-surface NO_2 measurements with OMI tropospheric NO_2 columns demonstrate that NO_2 emissions from a polluted urban area cannot be simplistically linked to the column measurement by a satellite instrument. A strong positive bias in the near-surface NO_2 measurements, with large scattering was observed when comparing ground-based *in situ* NO_2 with tropospheric columns

from OMI for January 2005 to December 2006, under cloud free conditions. The satellite footprint of OMI over Leicester includes a large area surrounding the city. Therefore, a fraction of the NO_2 emissions sampled by an OMI pixel originates from the surrounding background area. A correction to the near-surface measurement was performed by multiplying the near-surface measurement of NO_2 by the fraction of the OMI pixel sampling the city and adding the fraction sampling the background. The background measurement was obtained from an *in situ* monitor situated in a rural area 38 km south of the city centre. The FOV-weighted estimate for the OMI-equivalent urban NO_2 near-surface measurements improved the correlation considerably, in particular for spring and summer with correlation coefficients of $r = 0.83$ and $r = 0.64$, respectively. During the winter months, OMI still retrieves much lower concentrations of NO_2 than that apparently represented by the near-surface NO_2 measurement, even with the background correction applied. The differences observed may be due to the exclusion of aerosols in the operational OMI NO_2 product which may cause lower tropospheric columns to be observed over industrial regions in winter.

The seasonal cycle of NO_2 also demonstrates that the OMI appears to be underestimating the tropospheric column amounts during the winter months. The FOV-weighted near-surface data show the expected seasonal cycle with low concentrations in the summer and high concentrations in the winter, however the cycle is not as obvious in the OMI data. The FOV-weighted near-surface seasonal cycle included only those measurements coincident with the OMI data; therefore, differences could not be attributed to the reduced number of observations by OMI compared to the *in situ* monitors.

NO_2 data from all three instruments were binned into daily means and normalised to the median weekly value, to produce weekly cycles of NO_2. A reduction in NO_2 emissions is observed in the OMI and FOV-weighted *in situ* NO_2 at the weekend, owing to the decrease in traffic and industry. However, the CMAX-DOAS data demonstrates a much clearer cycle, with almost constant weekly levels and a large reduction in NO_2 on a Sunday. Repeating the analysis with *in situ* data from the "urban background" monitors, without any background correction, also reveals a clearer weekly cycle. The result may demonstrate that the large OMI pixel, in this case, is dominated by background sources of NO_2, which do not display such a strong anthropogenic cycle.

The study has shown that OMI is able to detect tropospheric NO_2 over polluted regions such as Leicester in the UK, if particular attention is paid to the sampling area of the pixel and cloud clearing is implemented. The methods developed allow an interpretation of the OMI retrievals for measuring NO_2 at the surface over urban areas and demonstrate the use of utility of satellite instruments as part of an air quality monitoring system on a regional scale.

Chapter 6

Halogen oxide measurements in the marine boundary layer

Reactive halogen species (RHS) are believed to contribute to the destruction of ozone within the MBL, initiated by reactions with HO_x and NO_x. In the MBL RHS precursors are thought to be emitted from intertidal macroalgae at low tide and halides present in sea salt aerosols. During low tide at daytime, photolysis reactions lead to elevated levels of halogen oxides. Previous measurement campaigns have used *in situ* and LP-DOAS techniques to perform direct measurements of halogen oxides (IO, BrO, OIO) and their precursors. Modelling studies have also been performed to understand the role of halogens in the MBL (von Glasow et al., 2002a, 2002b, 2004). However, the impact of halogens on marine oxidation chemistry is still not clearly understood and the quantification of these effects requires measurements of halogen oxides within the marine boundary layer. The CMAX-DOAS instrument offers an opportunity to perform measurements within a marine environment for a number of concurrent views, enabling the vertical and horizontal distribution of halogen oxides to be determined.

During September 2006 a measurement campaign to observe and quantify a range of reactive halogen species (RHS) was held in Roscoff in Brittany, France (48.72° N, 3.97° W). The campaign is part of the Reactive Halogens in the Marine Boundary Layer (RHaMBLe) program funded by NERC UKSOLAS. RHaMBLe is a two year project which includes three core activities. One of the core activities is the Roscoff campaign, which primarily focused on measurements of ultra-fine particle formation and RHS in a region with intertidal macroalgae.

In this chapter, an overview of the measurement campaign in Roscoff is given along with the first measurements IO by a MAX-DOAS system in the mid-latitude MBL along with a correlation with IO data retrieved by a LP-DOAS instrument

deployed alongside the CMAX-DOAS system during the campaign. Finally the results from the retrieval of BrO and NO_2 are presented.

6.1 Previous measurements of RHS in the Marine Boundary Layer

Optical absorption techniques such as DOAS have been used extensively over the past decade to measure RHS in the MBL. In Mace Head, Ireland, a number of measurement campaigns to study halogen oxides have been performed. The Mace Head Atmospheric Research Station operated by Galway University is located on the west coast of Ireland (53°19' N, 9°54' W) and is predominantly influenced by air masses from the clean marine region of the North Atlantic Ocean.

During a campaign in spring 1997 at Mace Head, two different LP-DOAS instruments performed the first measurements of IO in the coastal MBL [Alicke *et al.*, 1999, Allan *et al.*, 2000]. During four days between 5th and 8th May, 1997, Alicke *et al.* [1999] reported IO concentrations consistently above the instrument detection limit of 0.9 ppt, up to a maximum of 6.7 ppt. The observations also show that the diurnal variation of IO follows the solar radiation. Allan *et al.* [2000] also observed high levels of IO up to approximately 3 ppt from 8th to 12th May, 1997 with an average daytime concentration of 1.17 ppt.

Allan *et al.*, [2000] reported measurements of IO using the same LP-DOAS instrument during two other campaigns in Tenerife (June to July 1997) and Cape Grim in Tasmania (January to February 1999). In Tenerife, the IO levels were above the instrument detection limit on all five days of measurements, with peak concentrations up to 3.5 ppt observed at midday. The emission of iodocarbons, often proposed as a source of RHS, in the measurement region is thought to be negligible and it is suggested, therefore, that these levels represent the background concentration found in the subtropical North Atlantic. Cape Grim received air masses from the clean marine region of the southern ocean and also from the north coast of Tasmania. The IO levels at Cape Grim were much lower than observed at both Mace Head and Tenerife and generally did not exceed the detection limit. However, on two of three days where high IO concentrations were observed, the air mass originated from an easterly direction over the coast of North Tasmania.

Table 6-1: Mixing ratios (m.r.) and detection limits (D.L.) measured by LP-DOAS at Dagebüll, Lillia and Mace Head [Peters *et al.*, 2005].

	Species	Av.D.L.	Min Max D.L.	Av.m.r.	Max m.r. ± 2σ
Brittany 2003	NO_2	0.23 ppb	0.09 0.73 ppb	1.02 ppb	(5.40±0.26) ppb
	O_3	1.2 ppb	0.7 4.6 ppb	42.67 ppb	(88.89±5.01) ppb
	IO	0.23 ppt	0.13 0.96 ppt	0.75 ppt	(7.7±0.5) ppt
	BrO	0.67 ppt	0.37 2.36 ppt	0.75 ppt	(3.99±1.30) ppt[b]
	OIO	1.84 ppt	0.69 5.80 ppt	−0.24 ppt	(13.3±4.96) ppt[b]
	I_2	7.58 ppt	2.84 23.95 ppt	−0.82 ppt	(23.29±10.6) ppt[b]
North Sea 2002	NO_2	0.02 ppb	0.01 0.05 ppb	1.9 ppb	(8.10±0.02) ppb
	O_3	2.8 ppb	1.8 23 ppb	37.25 ppb	(59.3±2.6) ppb
	IO	0.28 ppt	0.18 0.65 ppt	0.35 ppt	(1.90±0.65) ppt
	BrO	1.47 ppt	0.6 4.08 ppt	0.2 ppt	(2.98±1.36) ppt[b]
	OIO	2.75 ppt	1.18 12.19 ppt	4.27 ppt	(15.26±6.65) ppt[b]
Mace Head 1998	NO_2	0.07 ppb	0.02 0.6 ppb	0.6 ppb	(6.54±0.07) ppb
	O_3	4.3 ppb	1.4 15.5 ppb	32.35 ppb	(44±3.9) ppb
	IO	0.91 ppt	0.3 6 ppt	0.48 ppt	(7.2±0.3) ppt
	BrO	2.45 ppt	0.88 9.45 ppt	−1.28 ppt	(4.1±4.2) ppt[b]
	OIO[a]	3.22 ppt	1.78 5.12 ppt	0.69 ppt	(9.19±1.25) ppt
	I_2[a]	9.99 ppt	7.6 27.6 ppt	6.6 ppt	(61.29±12.09) ppt

[a] Re-analysis Mace Head 1998 data
[b] No identification in the spectrum

A study by Peters *et al.* [2005] show results from the measurement of RHS in three different European costal regions using a LP-DOAS instrument (see Table 6-1). The measurements at Dagebüll, Germany, Lillia in Brittany and Mace Head (1998 campaign) show enhanced levels of IO at all three sites, with concentrations up to 7.7 ppt in Brittany. A strong correlation of IO concentration with low tide was also observed in the Lillia data which suggests that the primary contributor to the RHS is from exposed macroalgae. In the literature, two explanations can be formed. Carpenter *et al.*, [1999] measured peak concentrations of both CH_2I_2 and IO with a LP-DOAS instrument and gas chromatograph mass spectrometer (GCMS) at Mace Head during low tide. The atmospheric measurements along with results from a 2-D model incorporating horizontal and vertical dispersion, suggest the total flux of iodine atoms in Mace Head was dominated by the photolysis of CH_2I_2 from sources offshore as well as coastal.

However, during a third campaign (NAMBLEX) in Mace Head in August 2002 Saiz-Lopez and Plane [2004] indicated that I_2 may actually be the dominant source of coastal iodine at Mace Head from DOAS observations. During the measurement period the I_2 mixing ratio varied from below the detection limit to a maximum of 93 ppt during the night owing to the increased lifetime of I_2. During the night IO was

also observed up to a maximum of 7 ppt. The authors suggest that a likely route for the production of IO at night is from the reaction of I_2 and NO_3 to yield INO_3 and iodine atoms which may then react with O_3 to form IO. The peaks in I_2 during the day and night always coincide with low tide which suggests that the source is emitted from macroalgae under stress. Measurements of OIO were obtained simultaneously with the I_2 measurements and also show a maximum at night, with a concentration of 10.8 ppt.

During the NAMBLEX campaign in Mace Head in August 2002 BrO was also measured by LP-DOAS for six days of the campaign. A maximum concentration of BrO occurred during the day with a sharp increase at dawn, most likely owing to inorganic bromine species photolysing to produce Br atoms which react with ozone to yield BrO. Further peaks in BrO occur around noon and also in late afternoon. The average BrO daytime concentration of 2.3 ppt is thought to be sufficient to increase ozone depletion in the MBL.

A broad band cavity ringdown spectrometer (BBCRDS) from Cambridge University was also deployed at Mace Head in 2002 to measure NO_3, N_2O_5, I_2 and OIO [Bitter *et al.*, 2005]. The effective absorption path of approximately 10 km allows sensitive measurements of the target gas species. For OIO and I_2 a detection limit of 4 ppt and 20 ppt respectively could be achieved with an integration time of 10 minutes. The mixing ratios of these compounds were generally below the detection limits for most of the campaign, however, higher concentrations of 13 ± 4 ppt and 94 ± 13 ppt for OIO and I_2, respectively, were observed around sunset at low tide.

DOAS retrievals of trace gases in the MBL are generally performed with LP-DOAS instruments. More recently, however, MAX-DOAS instruments have been employed to provide measurements of BrO at varying altitudes, yielding information on the vertical gas profile.

Hönninger *et al.* [2004b] performed measurements of BrO and SO_2 with a MAX-DOAS instrument at the world's largest salt pan, Salar de Uyuni in Southern Altiplano, Bolivia during October to November 2002. The MAX-DOAS instrument retrieved slant columns from four elevation angles (5°, 10°, 20° and 90° above the horizon) in the UV wavelength range. Concentrations of BrO were retrieved from the 5° slant column measurements by assuming a mixing layer height of 1 ± 0.5 km.

BrO levels of up to 20 ppt were observed and coincided with local ozone depletion events.

A study on the south east coast of Hudson Bay involved coincident measurements of halogen oxides and other trace gases by MAX-DOAS and LP-DOAS instruments during Spring 2001 [Hönninger *et al.*, 2004c]. The MAX-DOAS system consisted of a scanning telescope which took sequential measurements of scattered sunlight at elevation angles of 5°, 10°, 20° and 90 °, with an integration time of approximately 5 minutes for each elevation angle at noon. The LP-DOAS instrument was set up almost parallel to the MAX-DOAS system with an azimuth angle between the two views of < 10°. Simultaneous measurements of BrO were obtained between 19th April and 8th May 2001. In addition the LP-DOAS instrument performed measurements of ozone, OClO, IO, OBrO and OIO. The results from the study showed that many of the peaks in BrO (up to 30 ppt), observed by both instruments coincided with a decrease in ozone and in one particular case complete ozone depletion was observed after sunset.

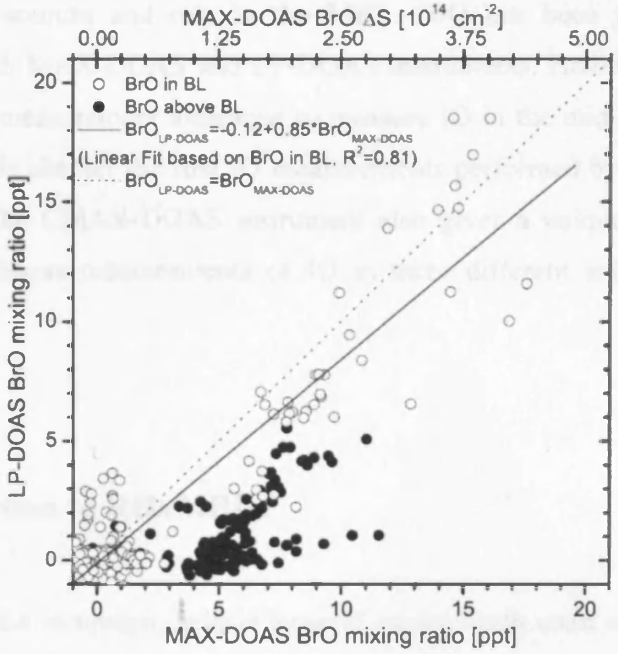

Figure 6-1: Concentration of BrO retrieved from 5° slant column densities of the MAX-DOAS (assuming BL height of 1 km) and coincident LP-DOAS measurements on the south east coast of Hudson Bay. The solid points represent the MAX-DOAS measurents of BrO above the BL, and the open circles represent the measurement of BrO below the BL. [Hönninger *et al.*, 2004c]

A comparison between the LP-DOAS and MAX-DOAS retrieved concentrations of BrO was performed for all coincident measurements. The concentration of BrO from MAXDOAS was derived from the 5° slant column densities by assuming a BrO layer of 1 km at the surface. The results from the comparison are shown in Figure 6-1. The MAX-DOAS measurements have been categorised into points above the boundary layer (when there is an enhancement in the BrO slant columns, but no difference between the 5 ° 10 ° and 20 ° views) and those within the boundary layer, where there is an enhancement in the BrO slant columns for the 5 ° view only. A good agreement is found between the LP-DOAS and MAX-DOAS measurements for events when BrO is observed at high concentrations within the boundary layer alone.

The campaigns and studies discussed in this section include measurements of halogen oxides in various marine environments. The results suggest that intertidal macroalgae is the primary source of IO and sea salt aerosols are a significant source of BrO. Therefore studying these species within a coastal location is important to determine their sources and role in the MBL. BrO has been previously been measured by both MAX-DOAS and LP-DOAS instruments. However, to date, the most successful measurement technique to measure IO in the mid-latitude MBL is LP-DOAS. In this chapter the first IO measurements performed by a MAX-DOAS are presented. The CMAX-DOAS instrument also gives a unique opportunity to perform simultaneous measurements of IO in three different azimuthal viewing directions.

6.2 Introduction to RHaMBLe

The RHaMBLe campaign, held in Roscoff on the north coast of France during September 2006 (see Figure 6-4), involved the deployment of a number of *in situ* and remote sensing instruments from seven institutions. A summary of the instruments participating in the Roscoff RHaMBLe campaign is given in Table 6-2.

The site of the campaign at Roscoff was selected as it is known to have a dense coverage of macroalgae which is exposed during low tide, as shown in Figure 6-2).

Figure 6-2: Photographs taken from the top of the mobile lab pointing north. The photographs show the change in tide over 3 hours.

6.2.1 Meteorological conditions during the RHaMBLe campaign

Meteorological data was sampled every minute from two separate stations on site during the RHaMBLe campaign. The data presented in this chapter is measured by the University of Manchester meteorological station.

Figure 6-3 shows a frequency plot of wind direction on the left, measured every minute during the campaign and the plot on the right shows a histogram of wind speed, binned to 0.5 ms^{-1} intervals. The wind direction throughout the campaign was predominantly from a south westerly direction and occasionally from a southerly or easterly direction. There was no prolonged period where air was sampled from the northerly clean Atlantic region.

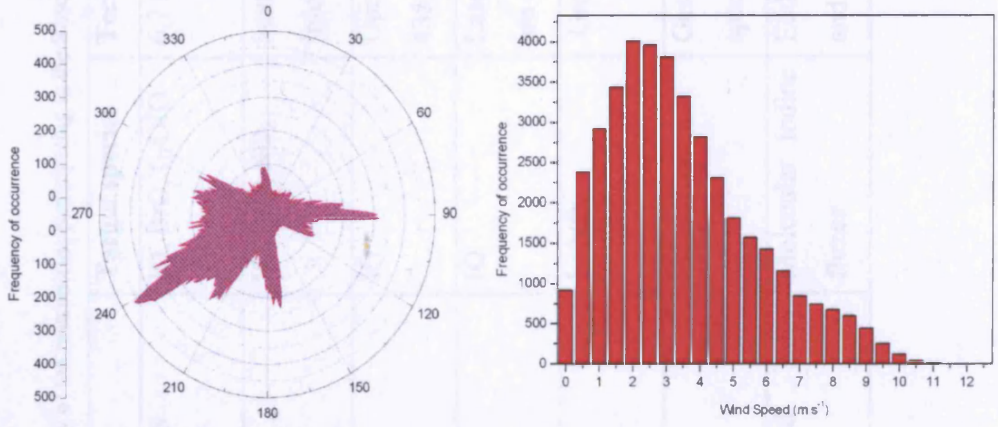

Figure 6-3: Frequency plot of a) wind direction (1° binned) and b) wind speed (0.5 ms^{-1} binned) for the duration of the Roscoff RHaMBLe campaign. Meteorological data is sampled every minute from the University of Manchester meteorological station.

Table 6-2: Summary of the instruments participating in the Roscoff RHaMBLe campaign.

Instrument	**Target species**	**Technique**	**Detection limit**	**Institution**
Long path-DOAS	IO, BrO, I_2, OIO	6.7 km and 2.5 km paths	0.6 ppt (IO), 50 ppt-(NO_2)	University of Leeds
CMAX-DOAS	IO, BrO, NO_2	Scattered light - 7 axis, DSCDs (molecules cm^{-2})	7×10^{14} (NO2), 3×10^{13} (IO), 9×10^{13} (BrO)	University of Leicester
2 x BBCRDS	IO	Open-path CRDS instrument at 435 nm	10 ppt (Bristol)	University of Cambridge/ Bristol
FAGE-LIF	IO	Laser Induced Fluorescence at 445 nm (300 s integration)	0.3ppt (300 s integration)	University of Leeds
BBCEAS	I_2, NO_3	Green LED source	15 ppt (I_2) 2.5 ppt (NO_3)	University of Cambridge
GC-MS	Iodocarbons	Gas chromatograph with mass spectrometric detection		University of York
REA (Relaxed Eddy Accumulation)	Molecular iodine fluxes	Eddies sampled according to updrafts and downdrafts.		University of Manchester/ York

Table 6.2: Continued

Eddy Correlation/ particle number concentration	Aerosols/Fluxes	Aerosol measurements particle number concentration (>2 nm and > 10 nm diameter) and size distributions from 3 nm		University of Manchester
NO_{xy} instrument	NO, NO_2	Diode based blue light converter	~3 ppt (NO), 6ppt (NO_2), 3ppt (NOy) (10 minute data cycle)	University of York
Ozone monitor	O_3	UV absorption technique	1 ppb	University of York
Radiometers	J values, Actinic flux	0.5 second integration time		University of Leicester
Meteorological data		Temperature, wind speed, wind direction, humidity		University of Leeds/ Manchester

6.3 CMAX-DOAS set up during the RHaMBLe campaign.

The CMAX-DOAS system was set up as described in Chapter 3, with the head unit attached to the top of a mast approximately 5 m above the ground, fixed to the side of a mobile lab. The mast could be moved up and down, to a maximum height of 10 m by the use of a pump, which allowed access to the telescopes. In addition to the five telescopes incorporated into the head unit pointing north at elevation angles of 2°, 5°, 10°, 15°, and 90° (zenith), two more telescopes were attached to the side of the unit. One of the telescopes was permanently fixed at an elevation of 5° and an azimuth angle of 60° west throughout the campaign. The second telescope was originally used as an additional zenith view which allowed a self-consistency test to be performed on the instrument. The telescope was then moved and permanently fixed at an elevation angle of 5° and 60° east (see red lines in Figure 6-4). Fibres from each telescope are input into a multi-track fibre and connected to the spectrometer, housed within the mobile lab.

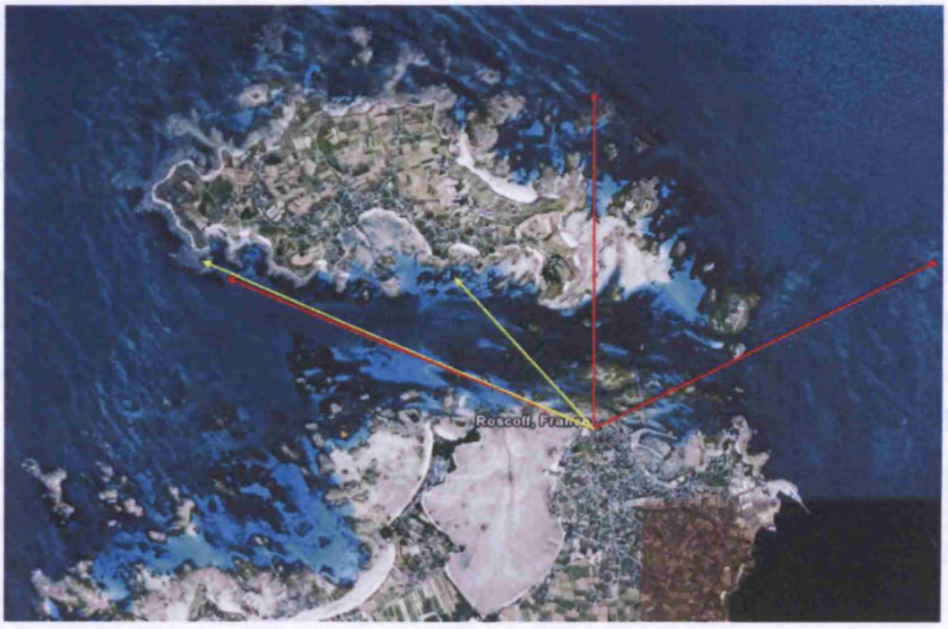

Figure 6-4: RHaMBLe campaign measurement site in Roscoff, France. The red lines represent the viewing direction of the CMAX-DOAS telescopes and the yellow lines represent the viewing directions of the LP-DOAS instrument.

During the campaign a number of problems were encountered which affected the quality of the data. The most serious of these was a power failure resulting in oil from the vacuum pump entering the camera housing and specks forming on the CCD. The oil on the CCD produced large structures on the spectra of a magnitude comparable to the optical density of the IO retrieval and the IO absorption structure cannot be extracted separately from the noise, resulting in spectra from the 10°, 15° and the original zenith to be discarded during this experiment.

In addition, temperature fluctuations from the heat produced by the instruments situated inside the mobile lab affected the mechanical and optical components of the spectrometer. The temperature changes expanded and contracted the gratings and mirrors resulting in wavelength shifts in the spectra. Foam padding was placed around the spectrometer and camera to reduce the effect of temperature, however, the consequence of the temperature and oil effects still resulted in spectra with low S/N. In Chapters 4 and 5, the zenith view spectrum at noon is used as the reference for the other views as it has the smallest path length through the atmosphere, hence observes the least absorption by gases. The second zenith view was not as affected by the oil on the CCD as much as the original zenith and theoretically could be used as the reference spectrum, however, the shift in wavelength appears to be large along the rows and is not uniform across all fibres; therefore, the spectra measured in the second zenith view cannot be used as reference spectra for the off-axis measurements in the DOAS analysis. For the analysis performed here, the spectrum recorded in each view at noon is used as the reference for that view.

To improve the S/N the spectra have been averaged over 15 minute intervals. A spectrum is recorded every minute, therefore, averaging over 15 minutes results in a reduction of noise on the spectra by $1/\sqrt{15}$ (approximately a factor of 4). The wavelength shift in the spectra was corrected by linearly shifting each spectrum to fit the noon spectrum before spectral averaging. However, small changes in the instrument line shape across the CCD columns may result in additional structures in the averaged spectra.

6.4 CMAX-DOAS retrieval of IO in the MBL

During the campaign, the retrieval of IO was performed on 17 days between 5th and 26th September. A wavelength window of 25 nm from 434 to 459 nm was used for the analysis (see section 2.6). This wavelength region includes three IO bands at and avoids the strong Fraunhofer structure between 425 and 433 nm. Within the selected wavelength region absorption features of NO_2 (at 294 K and 220 K), O_4, ozone and water vapour are also present and are included in the DOAS fitting routine. A third order polynomial is used to fit the broadband features owing to scattering.

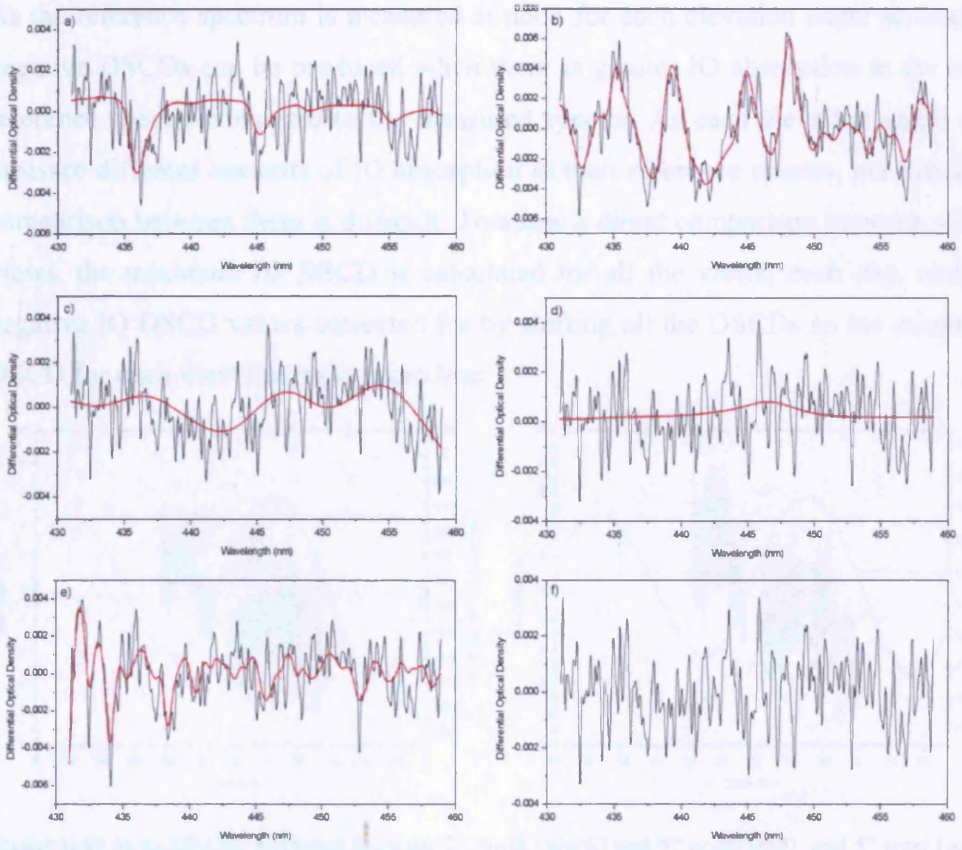

Figure 6-5: Spectral retrieval of a) IO and b) NO_2 (294 K) on 8th September 2006 at 18:00 GMT from the 2° view. Include in the fitting routine are also c) O_3, d) O_4, and e) Ring. H_2O, NO_2 (220 K), an offset and 3rd order polynomial are also included (not shown). The black lines represent the retrieved spectral signature and the red lines represent the fitted absorption cross section. The residual for this fit (f) has an rms value of 2.23×10^{-3}. The DSCD values for IO and NO_2 are 1.79×10^{14} molecules cm^{-2} and 3.20×10^{16} molecules cm^{-2} respectively.

Figure 4-3 shows an example fit for IO, NO_2, ozone and O_4 from the 2° north view for a spectrum obtained at 18:00 GMT on 8th September 2006, the reference spectrum in this case was measured at noon in the 2° view. The O_4 is particularly weak in this wavelength range compared to the bands used in Chapters 4 and 5 as the wavelength region was chosen on the strength of the IO bands. The residual in this retrieval is much larger compared to those in the retrievals from Chapter 4 and 5 owing to the increase in noise levels on the spectra (see sections 4.2.1), resulting in detection limit of approximately 2.2 x 10^{13} molecules cm^{-2} for IO and 6.75 x 10^{14} molecules cm^{-2} for the NO_2 DSCD. Nonetheless there appears to be a good indication that IO is measured in these experiments.

The DOAS analysis was used to derive DSCDs for IO from each viewing angle. As the reference spectrum is measured at noon for each elevation angle separately, negative DSCDs can be produced when there is greater IO absorption in the noon reference spectra compared to the measured spectra. As each elevation angle may measure different amounts of IO absorption in their reference spectra, performing a comparison between them is difficult. To allow a direct comparison between all the views, the minimum IO DSCD is calculated for all the views, each day, and the negative IO DSCD values corrected for by shifting all the DSCDs so the minimum DSCD for each view lies on the zero line.

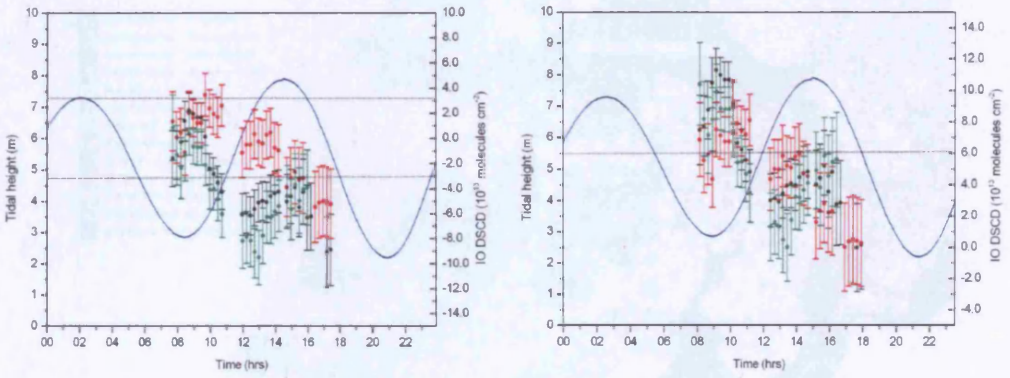

Figure 6-6: a) IO DSCDs retrieved from the 2° north (black) and 5° north (red) and 5° west (green) elevation angles on 5th September 2007 and b) DSCDs of IO with the negative offset in all views corrected for. The error bars represent the fitting error on the IO retrieval and the grey line represents the average detection limit for the 2° north view.

An example of the offset correction is presented in Figure 6-6 for 5th September 2006. The left hand plot in the figure shows the retrieved IO DSCDs for the 2° north

(black) and 5° north (red) and 5° east (green) elevation angles. Correcting for the negative offset allows a comparison to be performed of the IO absorption in all views. From the plot on the right it can be observed that the 2° view measures the largest IO DSCD and the 5° east view sees an increase in IO absorption when the northerly views have reached a minimum. The grey lines in Figure 6-6 show the average detection limit of approximately $\pm 3\times10^{13}$ molecules cm^{-2} when no correction has been applied, resulting in a detection limit of approximately 6×10^{13} molecules cm^{-2} after the negative offset has been corrected for.

6.5 Distribution of IO in the MBL from the CMAX-DOAS measurements

The location of IO precursors are thought to be heterogeneously distributed over ocean and costal regions owing to the diverse coverage of the macroalgae. The addition of extra azimuthal views on the CMAX-DOAS instrument allows the first simultaneous measurements of IO in three viewing directions.

Figure 6-7: Macroalgae distribution map around Roscoff, France. [image courtesy of CNRS Station Biologique de Roscoff].

Figure 6-7 shows a map of the location of various species of macroalgae around Roscoff. Previous studies have demonstrated that emissions of RHS, such as CH_3I, C_2H_5I, CH_2ICl, CH_2IBr and CH_2I_2 from macroalgae, in particular *Laminaria digitata* and *Laminaria saccharina* [McFiggans *et al.*, 2004], are quickly photolysed to yield iodine atoms [Carpenter *et al.*, 1999; 2001; O'Dowd *et al.*, 2002]. From the map it can be observed that the *Laminaria* species are generally located to the north and west of Roscoff, around the small rocky islands and Ile de Batz.

The results from the retrieval of IO for 17 days during the RHaMBLe campaign are presented in Figure 6-8. The 5° east telescope was only fixed into position from 13th September onwards. The plots in Figure 6-8 demonstrate during the RHaMBLe campaign the CMAX-DOAS often measured IO above the average detection limit of approximately 6x 10^{13} molecules cm^{-2} and an anti-correlation with tide was present, in agreement with the theory that IO precursors are emitted by macroalgae when exposed at low tide. High DSCDs of IO are often observed when the low tide corresponds with solar noon, presumably owing to the rapid photolysis of IO precursors such as CH_2I_2 and possibly I_2.

The results in Figure 6-8 also show, during some days, the peaks in IO DSCD occur at different times and at with different magnitudes, depending on the view from which measurements were obtained. On a number of days the IO DSCDs measured by the 2° elevation angle are much lower than from the 5° views. The 2° view has a greater sensitivity to absorption in the lowermost level of the MBL, therefore, this result suggests that the IO is present at higher altitudes in the MBL.

Whalley *et al.*, [2007] observed IO levels, up to concentrations of 20 ppt (300 s integration), with the FAGE-LIF on the 7th and 8th September in Roscoff. The authors suggest that the high concentrations of IO indicate either a strong IO source near to the instruments inlet, or that the IO levels were sustained in the MBL. The results from the CMAX-DOAS suggest the latter may be the case here.

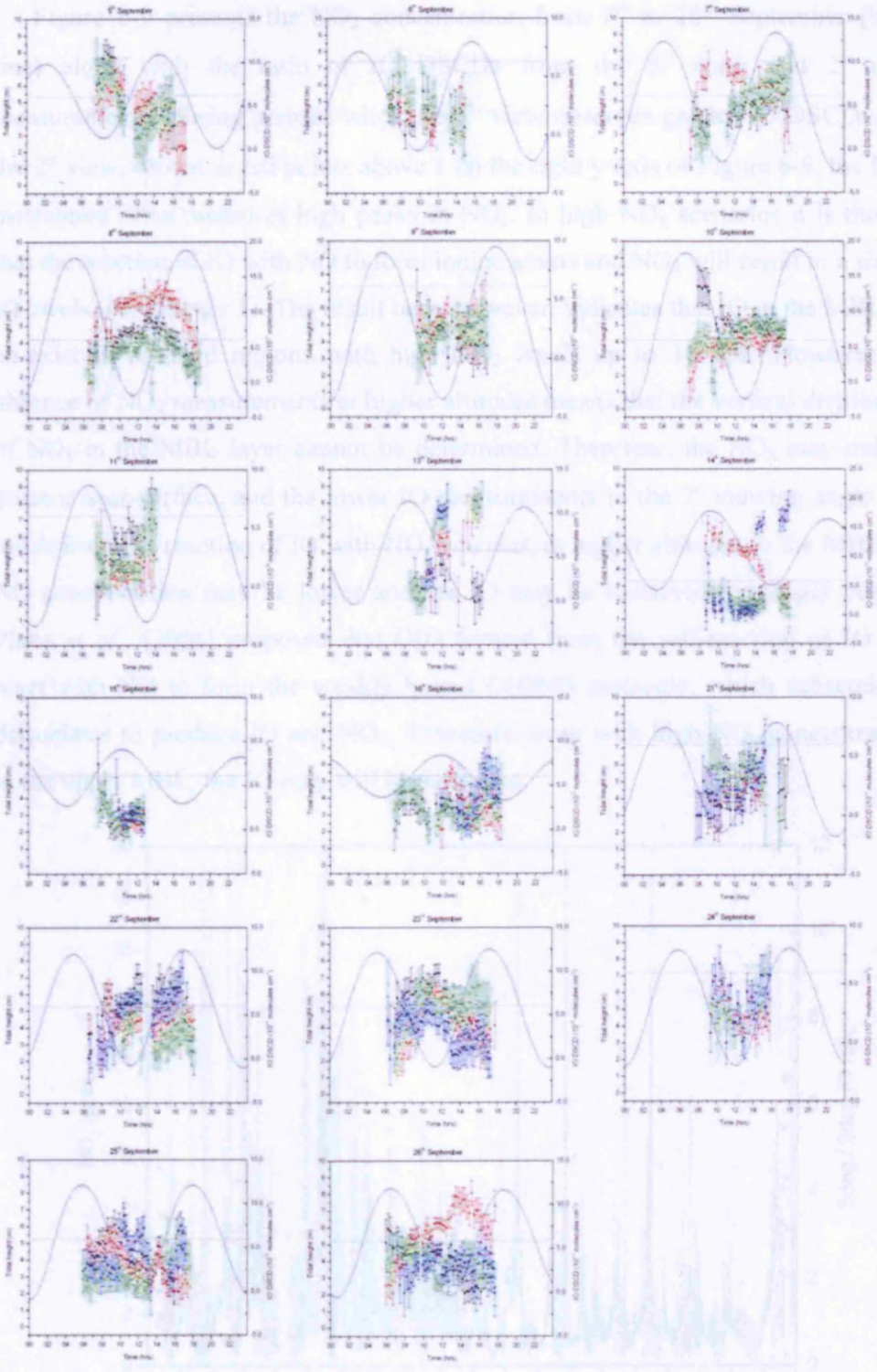

Figure 6-8: IO DSCDs measured during the RHaMBLe campaign. The coloured dots represent the 2° north (black) and 5° north (red), 5° west (green) and 5° east (blue) views. The error bars show the fitting error for each measurement. The navy blue line represents the tidal height and the grey line represents the average detection limit for the 2° north view.

Figure 6-9 presents the NO_2 concentration from 7th to 26th September (black line) along with the ratio of IO DSCDs from the 5° north and 2° north measurements. During periods when the 5° view observes greater IO DSCDs than the 2° view, shown as red points above 1 on the right y-axis of Figure 6-9, the NO_{xy} instrument often measures high peaks in NO_2. In high NO_x scenarios it is thought that the reaction of IO with NO to form iodine atoms and NO_2 will result in a sink in IO levels (see chapter 1). The result here, however, indicates that IO in the MBL can co-exist in polluted regions with high NO_2 levels up to 10 ppb. However, the absence of NO_x measurements at higher altitudes means that the vertical distribution of NO_x in the MBL layer cannot be determined. Therefore, the NO_x may only be present near-surface, and the lower IO measurements in the 2° viewing angle may result from the reaction of IO with NO, whereas, at higher altitudes in the MBL, the NO concentration may be lower and the IO may be sustained for longer periods. Plane *et al.*, [2006] proposed that OIO formed from the self-reaction of IO may react with NO to form the weakly bound OIONO molecule, which subsequently dissociates to produce IO and NO_2. Therefore, even with high NO_x concentrations in the upper MBL, the IO may still be sustained.

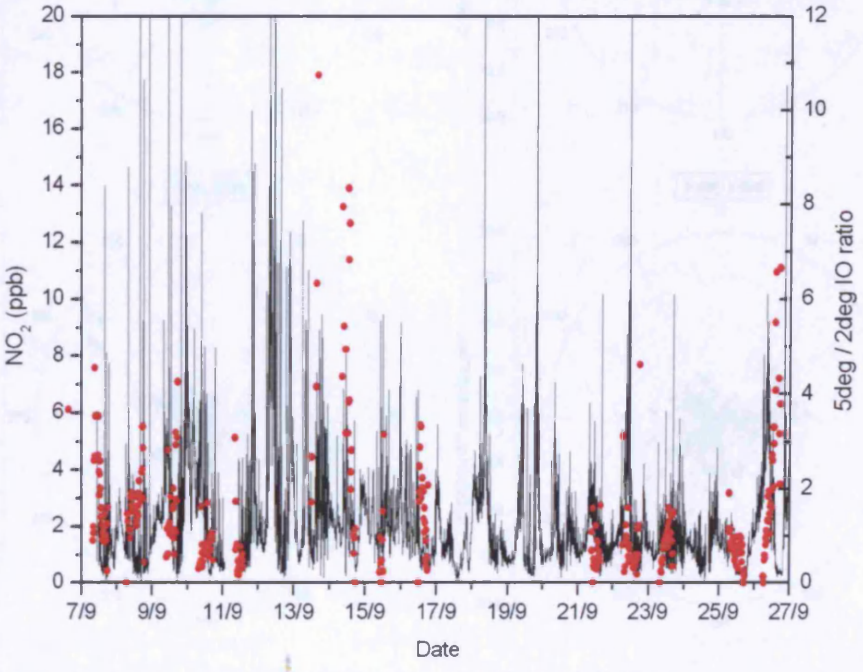

Figure 6-9: Plot of NO_2 concentration measured by the NO_{xy} instrument (black lines) along with the ratio of IO DSCDs from the 5° north and 2° north CMAX-DOAS measurements (red points) for 7th to 26th September 2006.

6.5.1 Using CMAX-DOAS observations to determine source regions of IO

The variability in the retrieved IO DSCDs from each of the 5° viewing angles demonstrates the heterogeneous distribution of IO and its precursors within the MBL around Roscoff. The plots in Figure 6-10 show the retrieved IO DSCDs from CMAX-DOAS as a function of wind direction for the 2° north view and all the 5° north views. The 5° west and the 2° views show similar results, with large IO values observed when the wind is coming from an easterly or south/south-westerly direction. Easterly winds generally occurred during the first half of the campaign, hence the 5° east view, installed from 13th September onwards does not show many correlations with wind direction coming from the east.

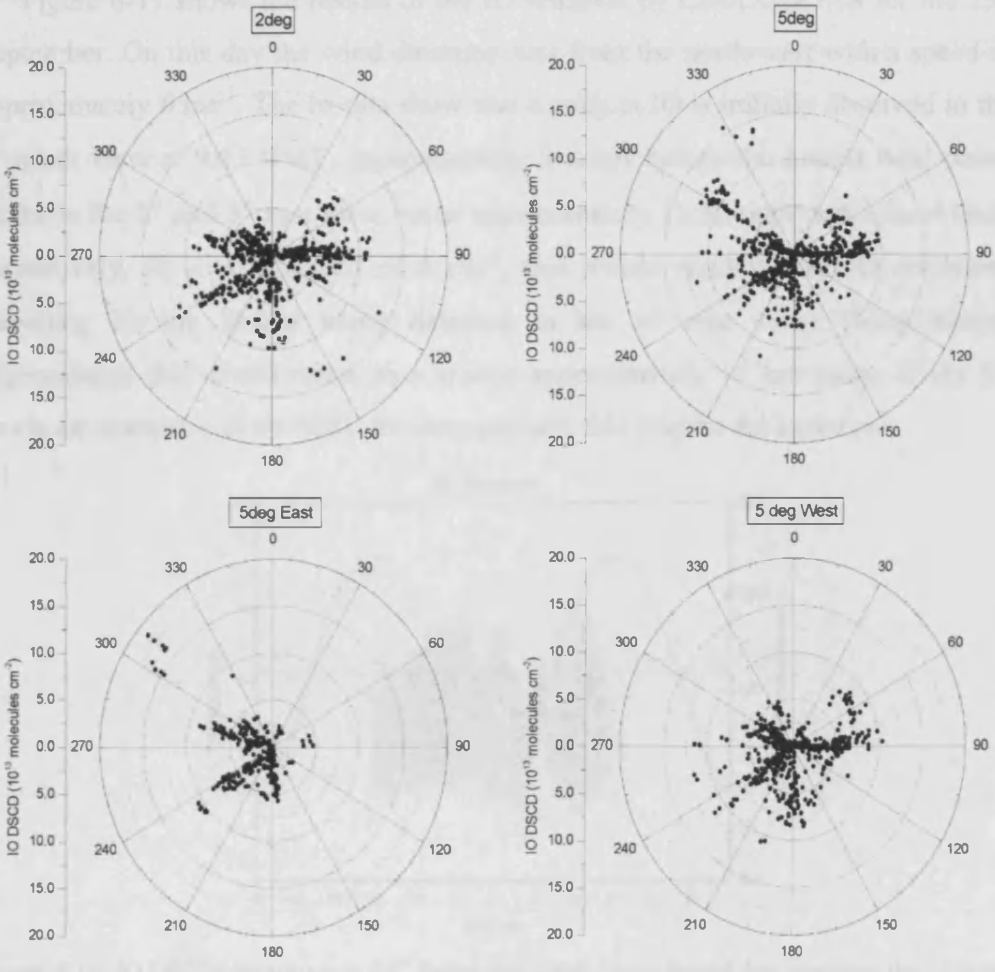

Figure 6-10: 15 minute averaged IO DSCDs from the CMAX-DOAS instrument as a function of wind direction, for the 2° north ,5° north, 5° east and 5° west viewing angles.

The 5° east view appears to observe high concentrations of IO when the wind is coming across the Atlantic from a north-westerly direction. This is also the case for the 5° north view. The higher IO DSCDs observed in the 5° east and 5° north views compared to 5° west view may imply that there is a source of IO far out from the coast line towards the north-westerly region that is upwelled higher into the MBL and observed by the 5° northerly view, followed by the easterly view. This is explored further in the next section.

6.5.1.1 Case studies: 22nd to 25th September 2006

Figure 6-11 shows the results of the IO retrieval by CMAX-DOAS for the 25th September. On this day the wind direction was from the north-west with a speed of approximately 6 ms^{-1}. The results show that a peak in IO is initially observed in the 5° north view at 9.45 GMT, approximately 3 hours before the lowest tidal point. Peaks in the 2° and 5° east view occur approximately 15 minutes and 1 hour later, respectively. At a wind speed of 6 ms^{-1}, this would result in the IO emissions travelling 22 km before being detected in the 5° east view. Using simple trigonometry this would relate to a source approximately 16 km away. If the IO levels are sustained in the MBL for long periods, this may be the case here.

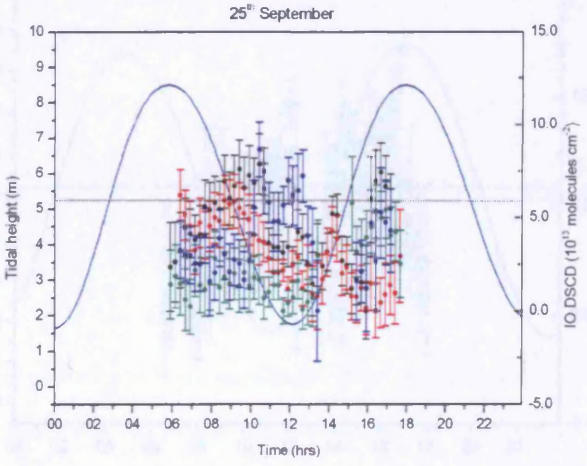

Figure 6-11: IO DSCDs measured on 25th September 2006. The coloured dots represent the 2° north (black) and 5° north (red), 5° west (green) and 5° east (blue) views. The error bars show the fitting error for each measurement. The navy blue line represents and the grey line represents the average detection limit for the 2° north view.

However, peaks in IO may also result from local sources close to the shoreline. For example, if macroalgae is close to the shoreline in the northerly direction, the north viewing angle may observe a peak in the IO first as the macroalgae is exposed and the IO builds up. Towards the east however, the macroalgae may be located further from the shoreline and were not exposed until low tide. For example, on 22nd September 2006, a similar result is observed to that on the 25th September, with a sharp peak in IO from the 2° and 5° north viewing angles at approximately 8.30 GMT (there is no data for the 5° west view until 10 GMT). The wind originated from the south during the morning of 22nd September; therefore, any IO produced from a source close to the coast in the northerly direction will not be transported through the easterly or westerly views. However, the east viewing angle observes a peak in IO around 2 hours later, suggesting that the macroalgae may be located further from the shoreline in the easterly direction and is not exposed until low tide. An interesting feature on this day is the second peak in IO observed by the 2° north viewing angle just after low tide, which coincides with a peak in the 5° west view. The wind direction slowly moved round to a south westerly direction during this period, therefore the IO may be transported from the 5° west view towards the northerly view, however there is not a similar peak observed in the 5° north view and this requires further investigation.

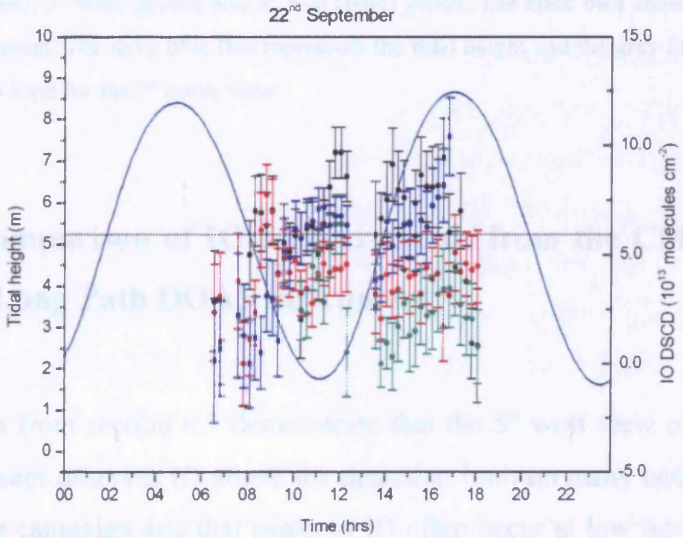

Figure 6-12: IO DSCDs measured on 22nd September 2006. The coloured dots represent the 2° north (black) and 5° north (red), 5° west (green) and 5° east (blue) views. The error bars show the fitting error for each measurement. The navy blue line represents the tidal height and the grey line represents the average detection limit for the 2° north view.

On the 23rd September 2006 a southerly wind was observed throughout the day. A southerly wind should result in similar IO diurnal cycles in all 5° views if the IO sources were homogeneously distributed. However, the IO observed in the 5° west view remains almost constant until high tide, whilst the IO observed by the other views decrease just after low tide (see Figure 6-13). The differences may indicate more abundant sources present near the coast in the westerly region of the sea surrounding Roscoff, which are exposed for longer periods during low tide.

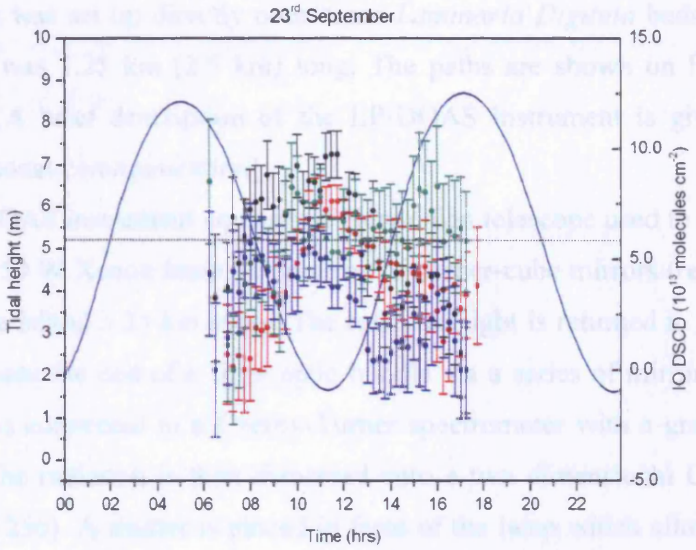

Figure 6-13: IO DSCDs measured on 23rd September 2006. The coloured dots represent the 2° (black) and 5° (red), 5° west (green) and 5° east (blue) views. The error bars show the fitting error for each measurement. The navy blue line represents the tidal height and the grey line represents the average detection limit for the 2° north view.

6.6 Intercomparison of IO measurements from the CMAX-DOAS and a Long Path DOAS instrument

The results from section 6.7 demonstrate that the 5° west view of the CMAX-DOAS instrument observes IO above the detection limit on many occasions during the RHaMBLe campaign and that peaks in IO often occur at low tide. As the west view was pointing along the same direction as the LP-DOAS instrument, for most of the campaign, it provides a good opportunity to perform an intercomparison between the two instruments

6.6.1 LP- DOAS instrument

The LP-DOAS instrument was deployed during the RHaMBLe campaign to perform measurements of I_2, IO, OIO as well as NO_3 and BrO. The instrument was situated approximately 100 m east of the main campaign site and was initially set up with a long path of 3.35 km (6.7 km total) which was directed towards the edge of the island, Ill de Batz. In addition to the long path, towards the end of the campaign a shorter path was set up directly over some *Laminaria Digitata* beds to the same island which was 1.25 km (2.5 km) long. The paths are shown on Figure 6-4 as yellow lines. A brief description of the LP-DOAS instrument is given here [A. Mahajan: personal communication].

The LP-DOAS instrument consists of Newtonian telescope used to collimate the light from a 450 W Xenon lamp, to an array of corner-cube mirrors (retro-reflector) situated on the island 3.35 km away. The reflected light is returned to the telescope and focused onto the end of a fibre optic bundle via a series of mirrors. The fibre optic bundle is connected to a Czerny-Turner spectrometer with a grating of 1200 lines mm^{-1}. The radiation is then dispersed onto a two dimensional CCD detector array (1024 x 256). A shutter is placed in front of the lamp which allows the signal to be switched on and off in intervals.

Spectra are obtained in three different configurations. The first is an atmospheric spectrum measured from the reflected signal, which contains scattered light and absorption features. The second is a scattered light spectrum only, obtained by blocking the signal from the lamp and the third is a spectra including scattered light, atmospheric absorption and a lamp spectrum. After processing the spectra, the majority of the lamp structure and the scattered light are removed leaving a normalised processed spectrum which is used to derive a differential optical density spectrum by applying a high pass Fast Fourier Transform (FFT) to smoothen the spectrum. A low pass FFT is then applied and an inverse transformation performed to calculate the broad band structure of the spectrum (I_0'). The logarithm of the broad band structure divided by the smoothed spectrum gives the differential optical density spectrum (see section 2.3). The DOAS fitting routine also includes the lamp spectra, to remove any residual structures and improve the fit.

6.6.2 Results of comparison

A comparison has been performed between the 15 minute averaged IO DSCDs, retrieved by the CMAX-DOAS instrument in the 5° east view and IO concentrations measured every minute by the LP-DOAS instrument, whilst at a path length of 6.7 km. Figure 6-14 shows the results of the comparison for six days during the RHaMBLe campaign when coincident measurements were performed. The results show that the CMAX-DOAS retrievals of IO appear to show prolonged enhancements, compared to the sharp peaks observed by the LP-DOAS instrument.

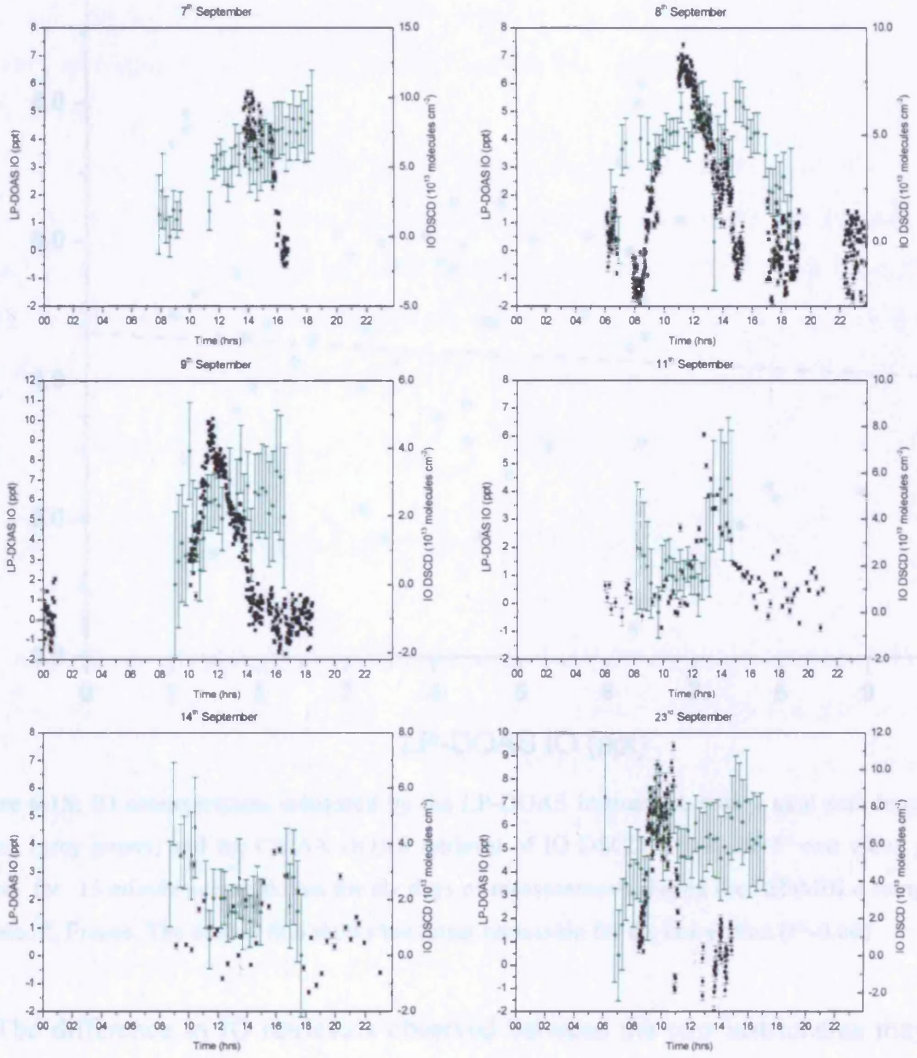

Figure 6-14: IO concentrations measured by the LP-DOAS instrument, with a total path length of 6.7 km (black points) and the CMAX-DOAS retrieval of IO DSCDs from the 5° east view, green points) for six days during the RHaMBLe campaign in Roscoff, France.

The correlation, shown in Figure 6-15, shows the agreement between IO concentrations measured the LP-DOAS and the retrieved IO DSCDs from the 5° east viewing angle of the CMAX-DOAS instrument. The LP-DOAS measurements were averaged over 15 minute intervals to allow a direct comparison with the CMAX-DOAS measurements. The correlation, shown as a dashed line in the figure has a correlation coefficient of r=-0.06, suggesting that there does not appear to be a relationship between the two sets of measurements.

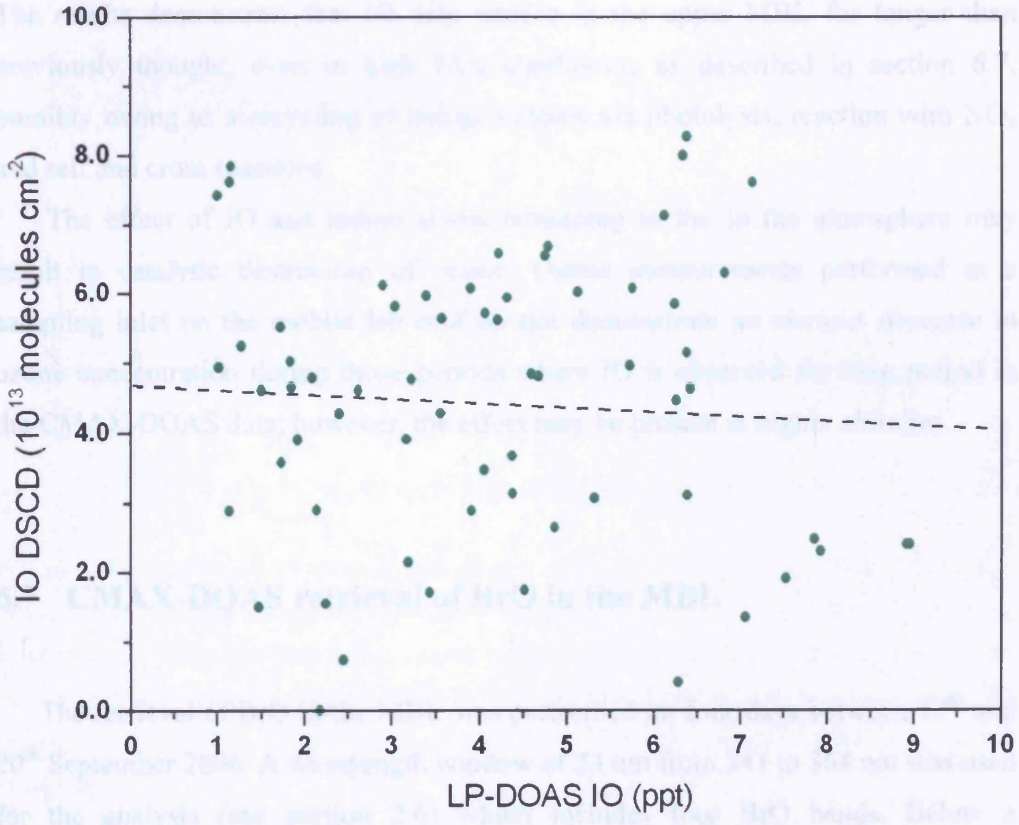

Figure 6-15: IO concentrations measured by the LP-DOAS instrument, with a total path length of 6.7 km (grey points) and the CMAX-DOAS retrieval of IO DSCDs from the 5° east view, green points) for 15 minute averaged data for six days of measurements during the RHaMBLe campaign in Roscoff, France. The dashed line shows the linear regression for the correlation (r=-0.06)

The difference in IO retrievals observed between the two instruments may be attributed to the different sampling altitudes. The LP-DOAS instrument performs measurements along a horizontal path up to 3.35 km away and approximately 3 to 10 m above the sea level, depending on tidal height. The CMAX-DOAS instrument, however, is initially position at a height of approximately 8 to 15 meters above the

sea level and an elevation angle of 5°. At a distance of 3.35 km, the CMAX-DOAS 5° west view is sampling at an altitude of approximately 300 m above the sea level. At a few meters above the sea bed, the LP-DOAS may observe a sharp increase in IO as the tide recedes and more seaweed is exposed. Conversely, the CMAX-DOAS instrument measures IO much higher in the atmosphere. In addition, the scattering point of the photons for the CMAX-DOAS instrument is more than likely to be a farther distance than the position of the LP-DOAS retro-reflector, possibly resulting in CMAX-DOAS observing IO emission from sources behind the island, Ill de Batz. The results demonstrate that IO may remain in the upper MBL for longer than previously thought, even in high NO_x conditions, as described in section 6.7, possibly owing to a recycling of halogen atoms via photolysis, reaction with NO_x and self and cross reactions.

The effect of IO and iodine atoms remaining in the in the atmosphere may result in catalytic destruction of ozone. Ozone measurements performed at a sampling inlet on the mobile lab roof do not demonstrate an obvious decrease in ozone concentration during those periods where IO is observed for long period in the CMAX-DOAS data; however, the effect may be present at higher altitudes.

6.7 CMAX-DOAS retrieval of BrO in the MBL

The retrieval of BrO in the MBL was performed on four days between 17th and 20th September 2006. A wavelength window of 23 nm from 341 to 364 nm was used for the analysis (see section 2.6) which includes four BrO bands. Below a wavelength of approximately 340 nm the signal to noise decreases rapidly, resulting in large errors in the retrievals. Within the selected wavelength region absorption cross sections of NO_2 (at 294 K and 220 K), O_4, ozone and OClO and a third order polynomial are also included in the DOAS fitting routine.

Figure 4-3 shows an example fit for BrO, NO_2 (294 K), Ozone and O_4 from the 2° view for a spectrum obtained at 07:30 GMT on 19th September 2006, the reference spectrum in this case was measured at noon in the 2° view. The residual for the retrieval of BrO is larger than for IO owing to the decrease in intensity in the

UV wavelength region. The detection limit for BrO calculated from the residual is approximately 8.6 x 10^{13} molecules cm^{-2}.

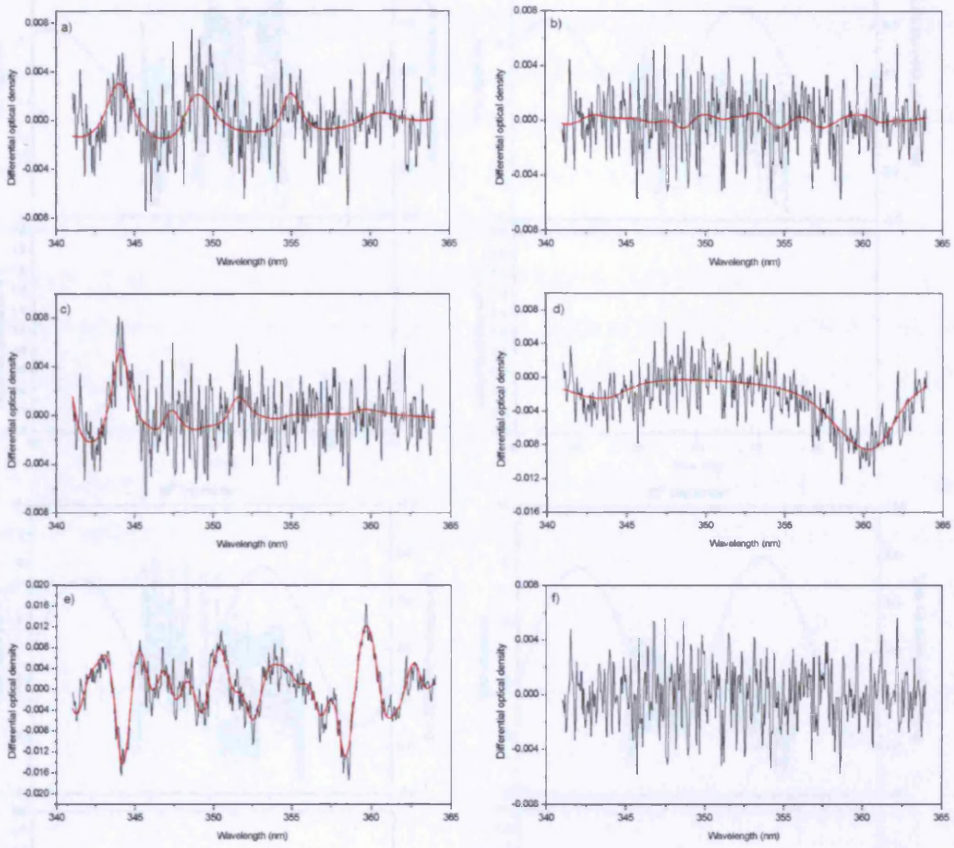

Figure 6-16: Example of the spectral retrieval of a) BrO on 19th September 2006 at 07:30 GMT. Include in the fitting routine are also b) NO_2 (294 K), c) O_3, d) O_4, and e) Ring. OClO, NO_2 at 220 K, an offset and a third order polynomial are also included (not shown). The black lines represent the retrieved spectral signature and the red lines represent the fitted absorption cross section. The residual for this fit (f) has an rms value of 3.35 x 10^{-3}. The DSCD values for BrO is 6.3 x 10^{14} molecules cm^{-2}.

6.7.1 Correlations with tidal measurements and solar radiance

Figure 6-17 shows the results of the BrO retrieval for the 2°, 5°, 5° east and 5° west views on four days between 17th and 20th September 2006, along with tidal height data. Also shown in Figure 6-17 are plots of actinic flux integrated over 380 to 700 nm, measured by a radiometer situated next to the CMAX-DOAS head unit. The results show elevated levels of BrO on all four days, suggesting that that CMAX-DOAS instrument is sufficiently sensitive to the detection of BrO.

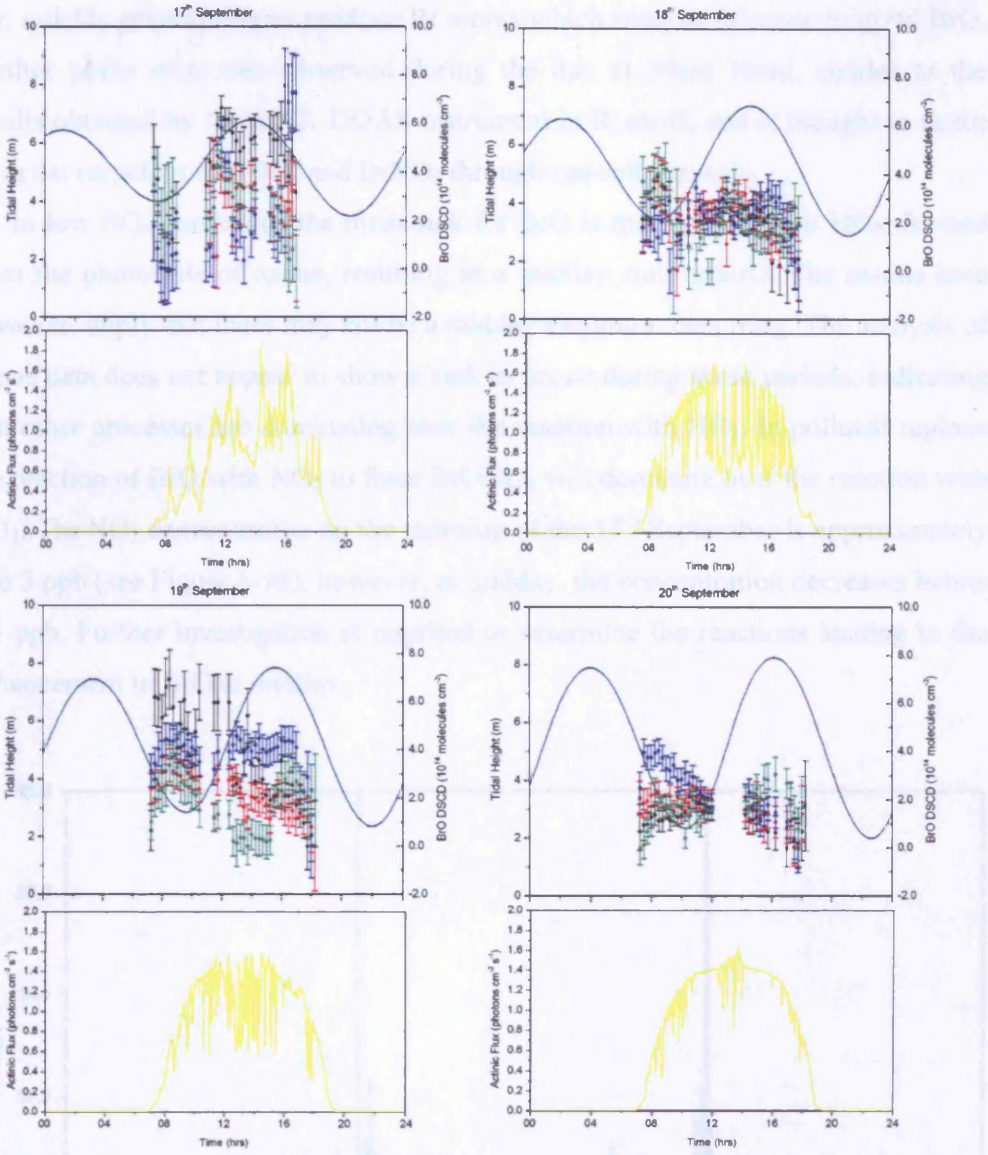

Figure 6-17: Plots of total actinic flux and BrO DSCDs, measured on four days during the RHaMBLe campaign, represented by yellow lines. The coloured dots represent the 2° (black) and 5° (red), 5° west (green) and 5° east (blue) views. The error bars show the fitting error for each measurement. The navy blue line represents the tidal height.

The results in Figure 6-17 show that the BrO DSCDs do increase at low tide; however, peaks are also observed when the tidal height is at a maximum and possibly correlate with the actinic flux. An increase in BrO is observed on 18th and 19th September just after dawn, in agreement with previous measurements of BrO by a LP-DOAS instrument in Mace Head [Saiz-Lopez *et al.*, 2004, 2006b]. The authors attribute the enhancement to inorganic bromine species, such as Br_2, and

IBr, quickly photolysing to produce Br atoms which react with ozone to yield BrO. Further peaks were also observed during the day at Mace Head, similar to the results obtained by the MAX-DOAS instrument in Roscoff, and is thought to occur from the recycling of HOBr and $BrNO_3$ through sea-salt aerosols.

In low NO_x conditions the main sink for BrO is the reaction with HO_2, formed from the photolysis of ozone, resulting in a midday sink in BrO. The results here however, imply that there may not be a midday minimum occurring. The analysis of ozone data does not appear to show a sink in ozone during these periods, indicating that other processes are dominating over the reaction with HO_2. In polluted regions the reaction of BrO with NO_2 to form $BrONO_2$ will dominate over the reaction with HO_2. The NO_2 concentration on the morning of the 17th September is approximately 2 to 3 ppb (see Figure 6-18), however, at midday, the concentration decreases below 0.5 ppb. Further investigation is required to determine the reactions leading to the enhancement in BrO at midday.

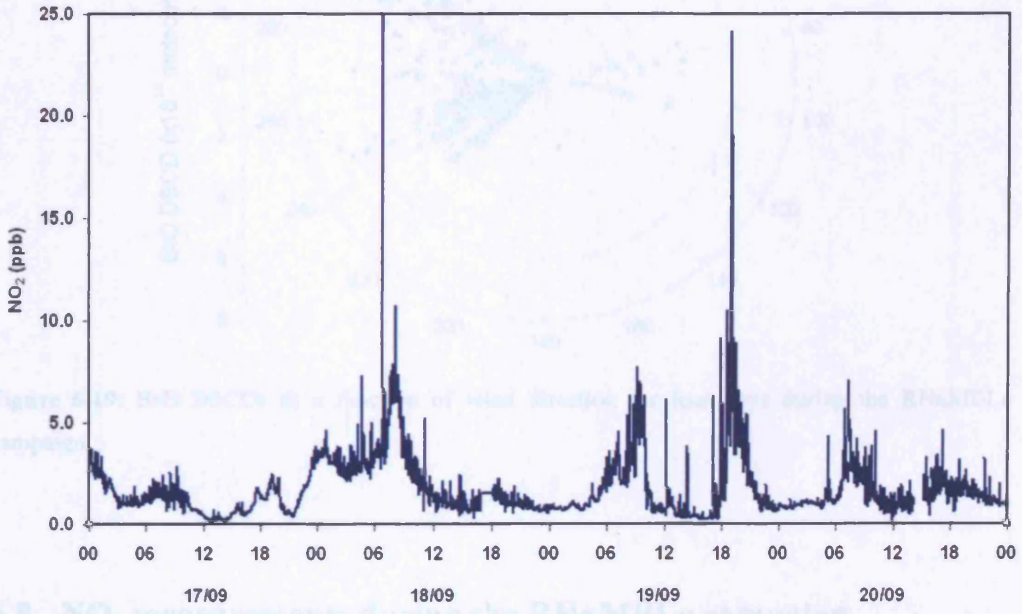

Figure 6-18: Plot of NO_2 measured by the NOxy instrument on four days during the RHaMBLe campaign from 17h to 20th September 2006.

The variation in BrO observed from different viewing angles is evident in the four days of data presented here. Saiz-Lopez *et al.* [2006] observed an increase in BrO with wind speed, possibly owing to wind-driven production of sea-salt

aerosols, however, this result is not obvious when analysing the wind data for the four days of measurements performed.

The correlation of BrO DSCDs with wind direction, shown in Figure 6-19, demonstrates that the peaks of BrO in different views do no appear to show any strong correlation with wind direction, either. The result for BrO is contrary to the IO observations discussed in section 6.7, where a correlation with wind data is observed, implying that the BrO precursors do not have a major source in macroalgae and are more likely to originate from sea-salt aerosols. However, it is challenging to infer information from only four days of measurements and a longer dataset is required to allow for varying scenarios.

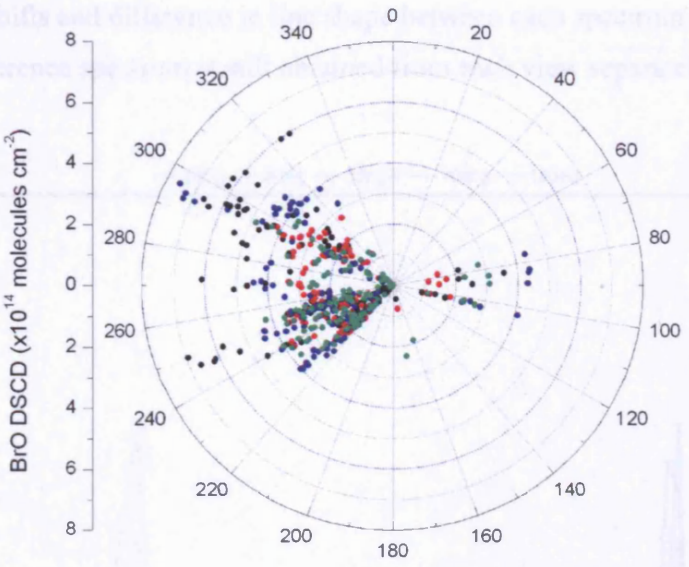

Figure 6-19: BrO DSCDs as a function of wind direction for four days during the RHaMBLe campaign.

6.8 NO_2 measurements during the RHaMBLe campaign

The NO_2 observations relating to IO and BrO have previously been discussed in sections 6.7 and 6.9. In this section, observations of NO_2, retrieved from the CMAX-DOAS instrument will be presented. The set up of the CMAX-DOAS, with seven telescopes pointing at different elevation and azimuth angles gives an

opportunity to observe plumes of NO_2 in the vertical and horizontal direction. In Chapter 4, NO_2 plumes were observed in the vertical plane as they passed through each viewing angle resulting in high concentrations of NO_2 in the upper boundary layer over Leicester. Leigh *et al.*, 2007 demonstrated the ability of the CMAX-DOAS instrument to measure plumes in the horizontal direction from the observations by two telescopes placed at an elevation angle of 15° and pointing 20° east and 20 ° west of the permanent viewing geometries.

NO_2 is a strong absorber in the atmosphere and with a highly structured absorption cross-section in the visible wavelength range. The retrieval of NO_2, therefore, is much less affected by noise than IO and 1 minute averaged spectra can be used in the analysis here, for all viewing angles. However, owing to the wavelength shifts and difference in line shape between each spectrum imaged on the CCD, the reference spectrum is still obtained from each view separately, at noon.

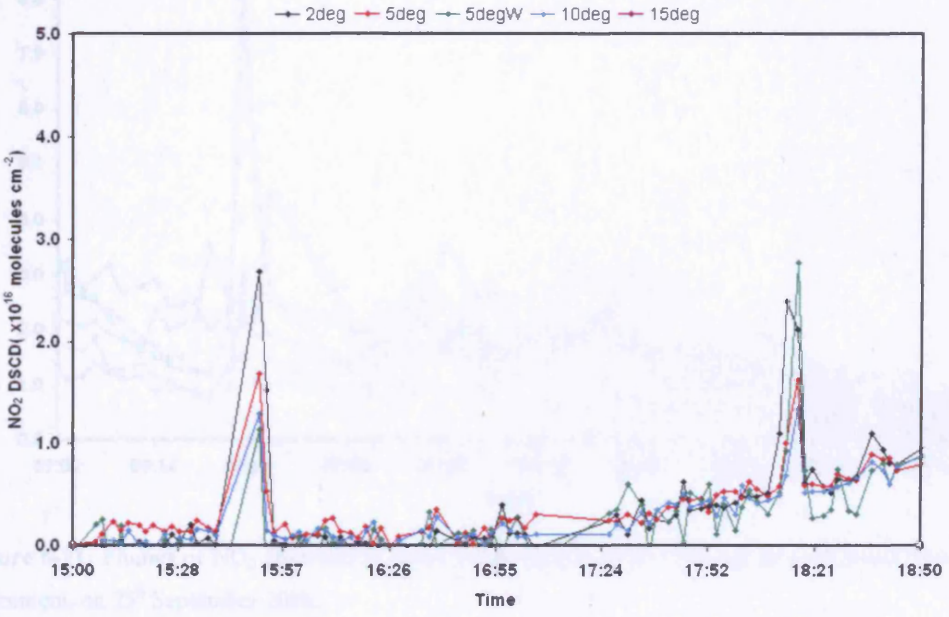

Figure 6-20: Plumes of NO_2 observed as peaks in the NO_2 DSCDs observed by the CMAX-DOAS instrument, on 8th September 2006.

Figure 6-20 shows the results of the NO_2 retrieval from the 2°, 5° 10° 15° and 5° west views of the CMAX-DOAS instrument, for a period during 8th September 2006. The NO_2 DSCDs are very small apart from two distinct peaks observed at 15:30 and 18:13 GMT. The first of these lasts approximately 15 minutes and is

observed in all views simultaneously, with a maximum observed in the 2° view. The results indicate that the source is from local emissions near to the head unit. The second peak lasts approximately 11 minutes and is detected by the 2° view first, followed by the other views a few minutes later. Similar peaks are observed by the NO_{xy} instrument at the same time, with concentrations increasing from below 1 ppb to 2 ppb in the first peak and over 3 ppb in the second peak. No enhancement was observed in the NO_2 retrieved from the LP-DOAS NO_2 measurements. The most likely source of the NO_2 is emission from a tour bus that stopped by the campaign site for a few minutes at this time. The wind during these periods was from an easterly direction, therefore, the LP-DOAS, which is situated east of the site, may not observe the emissions.

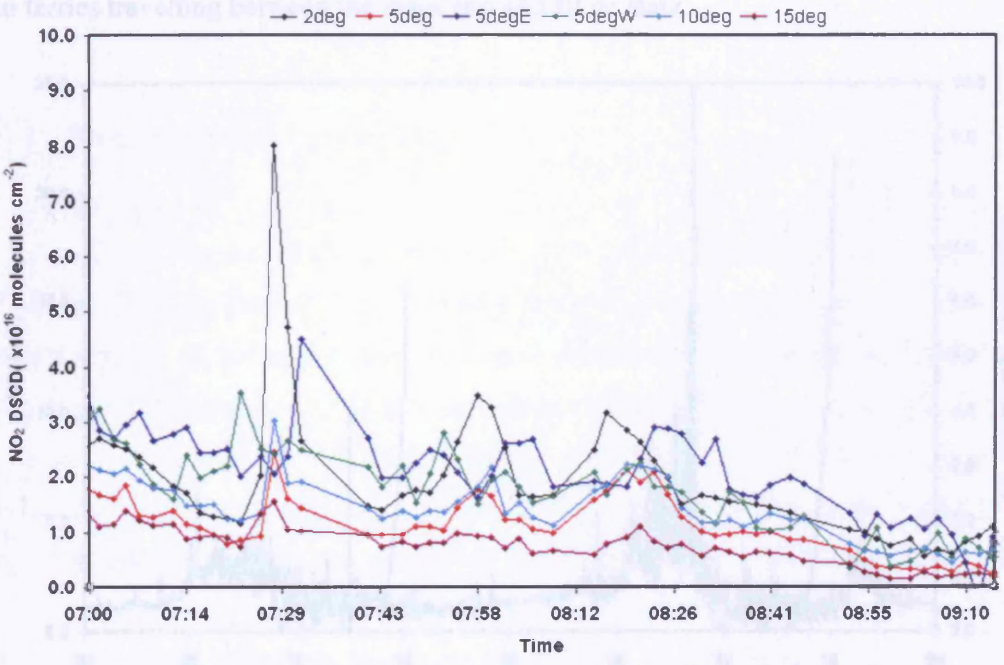

Figure 6-21: Plumes of NO_2 observed as peaks in the NO_2 DSCDs observed by the CMAX-DOAS instrument, on 25^h September 2006.

On 25th September, the results of the CMAX-DOAS NO_2 retrieval, shown in Figure 6-21, indicate that plumes of NO_2 are travelling from west to east, and detected by each telescope in turn. An initial peak in NO_2 is observed by the 5° west view at 7.23 GMT, followed by peaks in all northerly viewing telescopes at 7.28 am GMT and the 5° east view at 7:32 GMT. Approximately 30 minutes and 45 minutes later, two more events occur, with peaks in all viewing directions, however, the NO_2

DSCDs are much lower during these events. The source of the emissions in this case, is more likely to be from over the sea, rather than local coastal emissions. The period between each peak allows an estimate to be calculated of the distance between the instrument and the emission source. Using the second plume as an example, the time between taken for the plume to travel through the 5° west view to the 5° north view is 3 minutes. The wind speed at this point was approximately 5 ms^{-1} from a westerly direction, giving a source distance of $(180 \times 5)/\tan 60° \approx 520$ m. During the initial event a small aircraft was observed flying from west to east between the coast of Roscoff and Ill de Batz. Emissions from the aircraft are the most likely source of the NO_2 plumes. Similar events, with short enhancements in the retrieved NO_2 are observed on other days during the campaign and correspond to ferries travelling between the mainland and Ill de Batz.

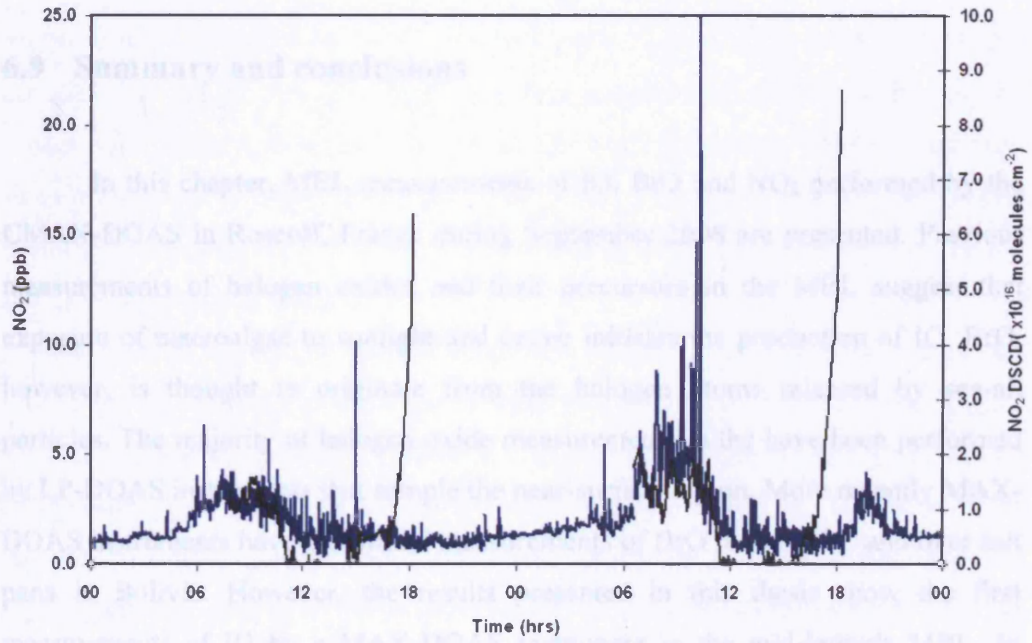

Figure 6-22: NO_2 retrieved from the 2° view of the CMAX-DOAS instrument (black lines) and NO_2 concentrations measured by the NO_{xy} instrument (blue lines), from 21st to 22nd September 2006. The large DSCDs observed in the CMAX-DOAS data in the evenings are caused by the stratospheric contribution to the slant column measurement.

In general, the NO_2 observed in the MBL throughout the campaign was very low with concentrations measured by the NO_{xy} instrument of a few ppb. However, peaks are occasionally observed owing to emissions from ferries and aircraft. There

are also a few occasions when prolonged emissions of NO_2 are observed. Figure 6-22 shows two days of NO_2 measurements performed by the NO_{xy} instrument, shown as blue lines and the 2° view of the CMAX-DOAS instrument (black lines), for 21st and 22nd September. Between 6 and 12 GMT for both days the NO_2 concentration reaches levels above 4 ppb and on some occasions sharp peaks can be observed over 25 ppb. A broad enhancement in NO_2 in the mornings can also be observed in the CMAX-DOAS data. Finally, the stratospheric component of the NO_2 slant column measurement can be observed as a large increase in NO_2 DSCD at dusk, which increases with SZA, owing to the increase in path length in the stratosphere. The wind direction for both days is from a south/south-westerly direction; bring polluted air masses from the continent, over the campaign site.

6.9 Summary and conclusions

In this chapter, MBL measurements of IO, BrO and NO_2 performed by the CMAX-DOAS in Roscoff, France during September 2006 are presented. Previous measurements of halogen oxides and their precursors in the MBL suggest that exposure of macroalgae to sunlight and ozone initiates the production of IO. BrO, however, is thought to originate from the halogen atoms released by sea-alt particles. The majority of halogen oxide measurements in the have been performed by LP-DOAS instruments that sample the near-surface region. More recently MAX-DOAS instruments have performed measurements of BrO in the MBL and over salt pans in Bolivia. However, the results presented in this thesis show the first measurements of IO by a MAX-DOAS instrument in the mid-latitude MBL. In addition, the CMAX-DOAS instrument is able to perform simultaneous measurements with a number of concurrent views, potentially allowing the measurement of the vertical and horizontal distribution of halogen oxides, and the determination of their source regions.

6.9.1 IO

Despite the problems encountered during the campaign, which affected the quality of the data, the results shown in this chapter have demonstrated that the CMAX-DOAS system is capable of measuring IO in the MBL. The results demonstrate that IO emissions are anti-correlated with tidal height, in agreement with previous measurements and the theory that IO precursors are emitted by macroalgae when exposed at low tide. The largest IO emissions appear to be observed when the lowest tide corresponded with solar noon.

Analysis of the IO retrievals for different elevation angles shows that IO may exist in high concentrations, in a polluted MBL, with NO_2 concentrations up to 10 ppb, possibly owing to a reaction between OIO and NO, which quickly dissociates to produce IO and NO_2, or via the recycling of halogen atoms in the MBL. The higher DSCDs measured by the 5° elevation angle of the CMAX-DOAS instrument compared to the 2° elevation angle, possibly suggest that the NO_x may only be present near-surface, therefore, IO may be removed from lower altitudes and only remain sustained at higher altitudes in the MBL. The results suggest that further investigation is required to determine the effect of polluted air masses on the halogen oxides in the MBL.

Case studies were performed for three days during the campaign when the wind direction was coming from the north-west over the Atlantic region and from a southerly direction, over the continent. The observations of IO by the azimuthal telescopes during these periods show periods where plumes of IO appear to be transported through each viewing direction in turn and are correlated with wind data, suggesting that there are sources of IO far from the coast line that may be upwelled higher into the MBL in addition to local sources near the coast.

Results from an intercomparison of CMAX-DOAS and LP-DOAS IO measurements for six days during the campaign do not show a strong correlation. The LP-DOAS IO measurements increase sharply with low tide, whereas the CMAX-DOAS show a much broader enhancement in the IO levels. The differences were attributed to the CMAX-DOAS instrument measuring at a higher altitude and sampling different air masses.

6.9.2 BrO

The measurement of BrO by passive DOAS instruments is challenging owing to the low signal detected from the scattered sunlight in the UV region. However, the results appear to show elevated BrO levels during all four days of measurements. The results of the analysis show, in contrast to IO, BrO does not appear to have a strong anti-correlation with tidal height. The diurnal cycle shows an enhancement in BrO just after dawn attributed to the photolysis of inorganic bromine species. However, a midday minimum in BrO, caused by the reaction of HO_2, formed from the photolysis of ozone, does not appear to present in the data and further investigation is required.

6.9.3 NO_2

In comparison to the NO_2 measured in the urban boundary layer in Chapters 4 and 5, the concentrations retrieved in the marine boundary layer are much lower, as expected, owing to a decrease in traffic and industrial sources. Nonetheless, the CMAX-DOAS system is sufficiently sensitive to identify specific sources. Sharp peaks in NO_2 concentration were often observed throughout the day in measurements from the NO_{xy} instrument and the CMAX-DOAS instrument. The set-up of the CMAX-DOAS instrument, with seven different views also gives a unique opportunity to measure plumes of NO_2 as they are transported through the different viewing geometries and appear to be due to specific sources.

The analysis of NO_2 plumes concentrated on two days of measurements. The first of these days showed an increase in NO_2 in all views simultaneously. A similar peak was observed in the NO_{xy} instrument, but not measured by the LP-DOAS instrument, indicating that the emissions came from a local source around the campaign site. On the second day the CMAX-DOAS instrument detected a plume of NO_2 travelling through each view in turn. From the wind speed measurements and the time taken to travel through each view the location of the source was measured and attributed to emissions from a small aeroplane.

Chapter 7

Conclusions and future work

The work performed in this thesis involved measurements of trace gases and aerosols within the boundary layer, the lowermost layer of the atmosphere, which is directly influenced by emissions from the surface. The measurements were performed by the Concurrent Multi-Axis Differential Optical Absorption Spectroscopy (CMAX- DOAS) instrument. CMAX-DOAS is a scattered light DOAS instrument with up to seven viewing directions that is capable of measuring gas species with a temporal resolution of a minute or less.

The two main aims of this thesis were:

1) Perform measurements of NO_2 and O_4 in the urban boundary layer to monitor air quality over Leicester and perform a comparison of aerosol retrievals from the lidar and CMAX-DOAS system.

2) Perform measurements of IO and BrO in the marine boundary layer to determine their sources and improve knowledge on the role of halogens in oxidative processes.

Both of these aims were performed with a view to understanding the spatial (vertical and horizontal) and temporal distribution of trace gases and aerosols in the urban and marine boundary layers.

The first of these aims, presented in Chapter 4, involved measurements of NO_2 and O_4 over Leicester during a measurement campaign in Summer 2007. The primary focus of the campaign was to perform a comparison of the aerosol retrievals between the CMAX-DOAS and the lidar instrument, which were deployed long side each other during the campaign. The study also involved a number of sensitivity tests with simulated O_4 DSCDs from the SCIATRAN radiative transfer model

(RTM). In addition, a comparison of NO_2 measurement techniques was performed to determine the influence of nitrogen compounds on measurement of NO_2 by *in situ* monitors with molybdenum oxide catalytic converters.

In Chapter 5, a comparison of tropospheric vertical columns from the Ozone Monitoring Instrument (OMI) with *in situ* data and a CMAX-DOAS dataset of NO_2 measurements from December 2005 to March 2006 were performed. The majority of NO_2 measurements in urban regions are *in situ* and do not benefit from the spatial sampling of the CMAX-DOAS instrument or satellite instruments. However, validation of remote sensing techniques is important to perform accurate retrievals. A field-of-view (FOV) weighted estimate for the OMI-equivalent near-surface urban NO_2 was calculated, by including background emissions from a nearby *in situ* monitor, situated in a rural area. The chapter concluded with seasonal and weekly cycles of NO_2 in an urban and rural environment measured by the OMI and *in situ* monitors.

A summary of the main results from the measurements performed in the urban boundary layer are given here:

1. The AOD measurements from the lidar instrument were used as an input parameter to the modelled O_4 DSCDs and a comparison performed between the measured O4 DSCDs from CMAX-DOAS and the modelled O_4 DSCDs. The agreement is excellent with a correlation coefficient of r = 0.98 for cloud free measurements. The AODs observed in Leicester during the summer were low and ranged between 0.01 and 0.1.

2. Sensitivity tests performed by modelling O_4 DSCDs for various aerosol scenarios demonstrate that the O_4 DSCDs retrieved from the CMAX-DOAS are sensitive to both the aerosol layer thickness and magnitude of the AOD, but not aerosol layers at elevated altitudes. The error for the retrieval of AODs from the CMAX-DOAS O_4 DSCDs is dominated by the error in the elevation angle. The error in AOD ranges between 0.01 to 0.55 for AODs between 0.01 and 1 when retrieving AOD from O_4 DSCDs at one viewing angle and a single wavelength.

3. Comparisons of the CMAX-DOAS NO_2 measurements with *in situ* monitors demonstrate the inhomogeneity of NO_2 across the city owing to local emission sources and a comparison of *in situ* techniques show that molybdenum oxide catalyst appear to convert reactive nitrogen species to NO_2, resulting in a higher measured concentration than is actually present.

4. The comparison between the OMI and CMAX-DOAS instrument over winter 2005/2006 show the agreement improves when using an aerosol load of AOD=0.1 to calculate the NO_2 AMFs, instead of AOD=0.05 as an average measured during the summer. The best correlation was obtained when only those pixels that sample at least 90% of the Leicester area were included in the analyses, with a correlation coefficient of 0.64.

5. Applying a FOV-weighted estimate for the OMI-equivalent urban NO_2 near-surface measurements improved the correlations, in particular for spring and summer, with correlation coefficients of $r = 0.83$ and $r = 0.64$ respectively.

6. The FOV-weighted near-surface data show the expected seasonal cycle with low concentrations in the summer and high concentrations in the winter. However, during the winter months, OMI retrieves much lower concentrations of NO_2 than that apparently represented by the near-surface NO_2 measurement. The differences are attributed to the exclusion of aerosols in the operational OMI NO_2 product.

7. A "weekend effect", where a reduction in NO_2 emissions occurs at the weekend owing to the decrease in traffic and industry, is observed in the NO_2 measurements from both the OMI and FOV-weighted *in situ* NO_2.

The second aim of this thesis, presented in Chapter 6, involved measurements of BrO and IO in the MBL in Roscoff, France as part of the Reactive Halogens in the Marine Boundary Layer (RHaMBLe) program. The current theory is that reactive halogen species (RHS) contribute to the destruction of ozone within the marine

boundary layer initiated by reactions with HO_x and NO_x. In the marine boundary layer RHS precursors are thought to be emitted from intertidal macroalgae at low tide and halides present in sea salt aerosols.

The CMAX-DOAS instrument was set up with two additional telescopes pointing in easterly and westerly directions to determine the source regions of RHS and horizontal distribution of IO and BrO. A comparison of IO measurements was also performed with a LP-DOAS instrument directed along the same view as the westerly viewing telescope. Finally measurements of NO_2 were performed to observe plumes of NO_2 and their sources identified.

A summary of the main results from the measurements performed in the marine boundary layer are given here:

1. The results have demonstrated that the CMAX-DOAS system is capable of measuring IO in the MBL. The analysis showed that IO often peaks at low tide in agreement with the theory that macroalgae emits iodine precursors when exposed at low tide. In addition, the analysis from different elevation angles show, in contrast to previous observations, that IO levels are possibly sustained for long periods (up to a few hours) and may exist in high concentrations, in a polluted MBL. A similar result was observed when comparing IO measurements from CMAX-DOAS with IO from the LP-DOAS instrument.

2. Observations of IO by the azimuthal telescopes show possible plumes of IO transported through each viewing direction in turn which are closely correlated with wind direction. The results suggest sources of IO far from the coast line that may be lifter higher into the MBL, in addition to sources close to the shoreline.

3. The results from the BrO analysis show that the CMAX-DOAS instrument observes elevated BrO DSCDs in the MBL, suggesting that the instrument is capable of measuring trace gases in the UV region where the signal is low.

4. The retrieval of NO_2 in the MBL shows that the NO_2 concentration is much lower than the levels observed in the UBL in Leicester. The low concentrations allow the instrument to identify specific sources of NO_2 which were also observed by the *in situ* NO_{xy} instrument and attributed to local sources near the campaign site.

7.1 Recommendations for future work

The main results from this thesis, summarised in the previous section, demonstrate the ability of the CMAX-DOAS instrument to retrieve information on gases and aerosols in both the urban and marine boundary layer. However, improvements can be made and some recommendations are given here along with suggestions for future studies:

The results from the sensitivity tests and comparisons between measurements from the lidar and CMAX-DOAS instruments in Chapter 4 show that the error in the retrieval for AOD in the currently set-up is approximately 0.01 to 0.55 for AODs between 0.01 and 1. However, the instrument has the potential to retrieve aerosols to an accuracy of 0.005 for all AODs if the elevation angle is known to a precision of 0.1° or better.

The advantage of additional telescopes is evident from the results obtained during the RHaMBLe campaign. The new CMAX-DOAS set-up, described in Chapter 4, consists of a multi track fibre that can be connected with up to 14 telescopes at once, enabling the system to perform measurements with a range of elevation and azimuth views. For an urban area, such as Leicester, the additional views will allow the variability of NO_2 and aerosols across the city to be determined, which will improve the validation of satellite instruments.

In the marine boundary layer, additional elevation angles may allow the IO and BrO vertical distribution to be measured. In a study by Saiz-Lopez *et al.* [2007], a 1-D chemical transport model (CTM) was used to investigate the vertical gradients of BrO and IO in the boundary layer at Halley Station, Antarctica.

The results from the modelled IO mixing ratios, shown in Figure 7-1, demonstrate that IO has a strong vertical gradient in the Antarctic boundary layer. With a number of telescopes pointing at different elevation angles the CMAX-DOAS instrument may be able to measure the vertical gradient of IO and BrO in the MBL.

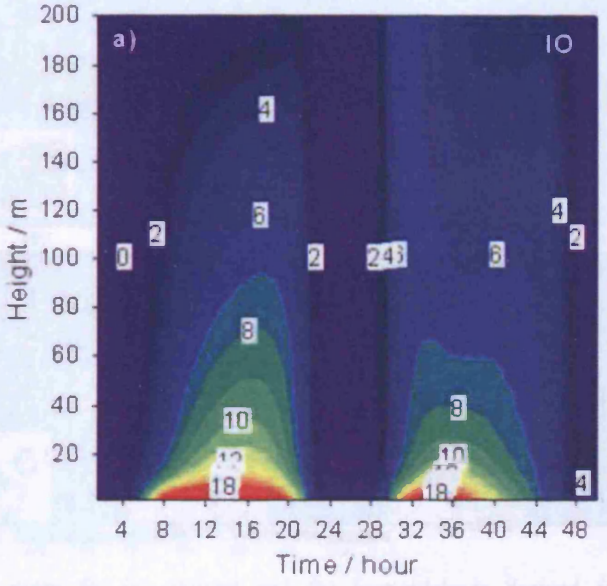

Figure 7-1: Two day model of the IO mixing ratios at Halley, Antarctica. The numbers represent the mixing ratios of IO in ppt [Saiz-Lopez *et al.*, 2007].

The observations of IO and BrO in the MBL have demonstrated the ability of the CMAX-DOAS instrument to measuring weak absorbers in the atmosphere. Two trace gases that are of particular importance in the boundary layer are glyoxal (CHOCHO) and formaldehyde (HCHO). These two gases are formed from the oxidation of hydrocarbons form both anthropogenic and biogenic sources and can be used as an indicator for volatile organic compounds and the formation of photochemical smog [Volkamer *et al.*, 2005].

HCHO has been reported from space for some time [Chance *et al.*, 2000], however, CHOCHO has only recently been observed from both ground and space-based instruments [Volkamer *et al.*, 2005; Kurosu *et al.*, 2005; Wittrock *et al.*, 2006; Beirle *et al.*, 2006; Sinreich *et al.*, 2007 ; Kurosu *et al.*, 2006].

The results from the study of HCHO and CHOCHO from space show that HCHO is strongly correlated with biomass burning events and CHOCHO is also

elevated over intense burning regions but is also correlated with anthropogenic and biogenic emissions. In fact, measurements of CHOCHO from SCIAMACHY and OMI have indicated a large source of CHOCHO over areas having strong biogenic emissions in the tropics (see Figure 7-2).

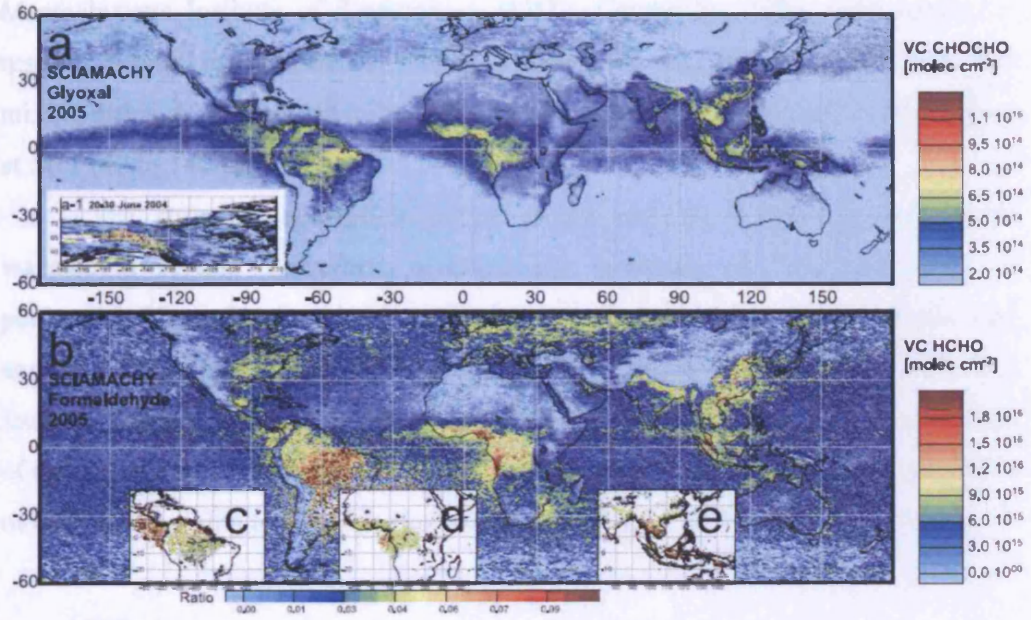

Figure 7-2: Yearly mean for (a) glyoxal and (b) formaldehyde derived from SCIAMACHY observations in 2005 [Wittock *et al.*, 2006].

The retrieval of HCHO from passive ground-instruments is challenging as HCHO absorbs in the UV region, hence, the signal to noise ratio is low when using solar radiation as the light source. However, the retrieval of BrO in the marine boundary layer by CMAX-DOAS has demonstrated the ability of the instrument to detecting species in the UV regions. From the instrument set-up during RHaMBLe, typical rms values for the residual in the UV regions are approximately of 3 x 10^{-3}. Assuming a similar instrument set-up and residual value when a retrieving HCHO using the three main absorption bands between 337 to 357 nm, this relates to a detection limit of approximately 1.3 x 10^{16} molecules cm^{-2} for the HCHO slant columns. Heckel *et al.* [2005] reported slant column amounts between 1 x 10^{16} molecules cm^{-2} and 12 x 10^{16} molecules cm^{-2} when retrieving HCHO with a MAX-DOAS instrument over the Po-Valley region of Italy, suggesting that the CMAX-

DOAS instrument could retrieve HCHO above the detection limit in polluted regions.

Previous retrievals of CHOCHO have been performed with a LP-DOAS instrument in Mexico City [Volkamer *et al.*, 2005] with mixing ratios detected from < 0.15 ppb to 1.82 ppb and by two ground-based MAX-DOAS instrument at Massachusetts Institute of Technology (MIT), Cambridge, USA, and onboard a research vessel in the Gulf of Maine [Sinreich *et al.*, 2007], where CHOCHO mixing ratios were observed to be up to 2.5 times larger over the Gulf of Maine than at MIT (40 to 140 ppt).

The strongest absorption bands of glyoxal are located in the visible wavelength region. Therefore, simultaneous retrievals of NO_2 may also be performed. Figure 7-4 shows the results from the retrieval of CHOCHO (black line) and NO_2 (blue line) during the LAMP campaign on the 7th September 2007. The retrieval was performed over the wavelength region 435 to 460 nm and an example of the CHOCHO fit is shown in Figure 7-3. The residual for this fit has an rms value of 6.75 x 10^{-4} giving a detection limit of approximately1.35 x10^{15} molecules cm^{-2}.

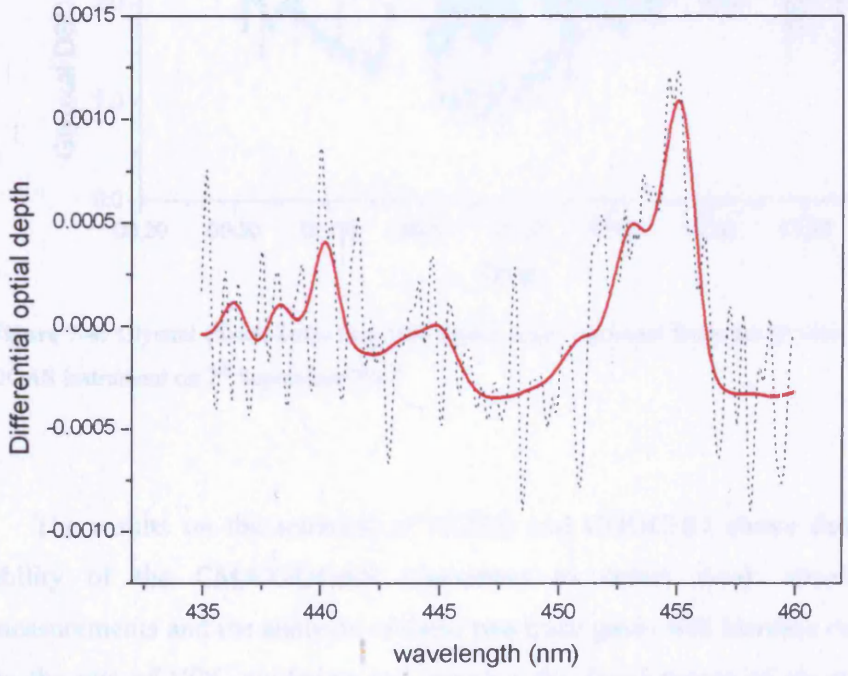

Figure 7-3: Example of the spectral retrieval of glyoxal on 7th September 2007 at 8:21 GMT. The black dashed line represents the retrieved spectral signature and the red line represents the fitted glyoxal absorption cross section.

The results shown in Figure 7-4, demonstrate that the NO_2 and CHOCHO follow a similar diurnal cycle. The O_4 measurements on this day confirm that the large peak in NO_2 and CHOCHO DSCDs between 8.30 and 9.30 cannot be attributed to clouds, and most likely arise from vehicle emissions during the rush hour traffic period. The simultaneous increase in both the NO_2 and CHOCHO is in agreement with previous observations by Volkamer *et al.*, [2005] owing to the reaction of NO with peroxy radicals from the photolysis and oxidation of CHOCHO and other VOCs.

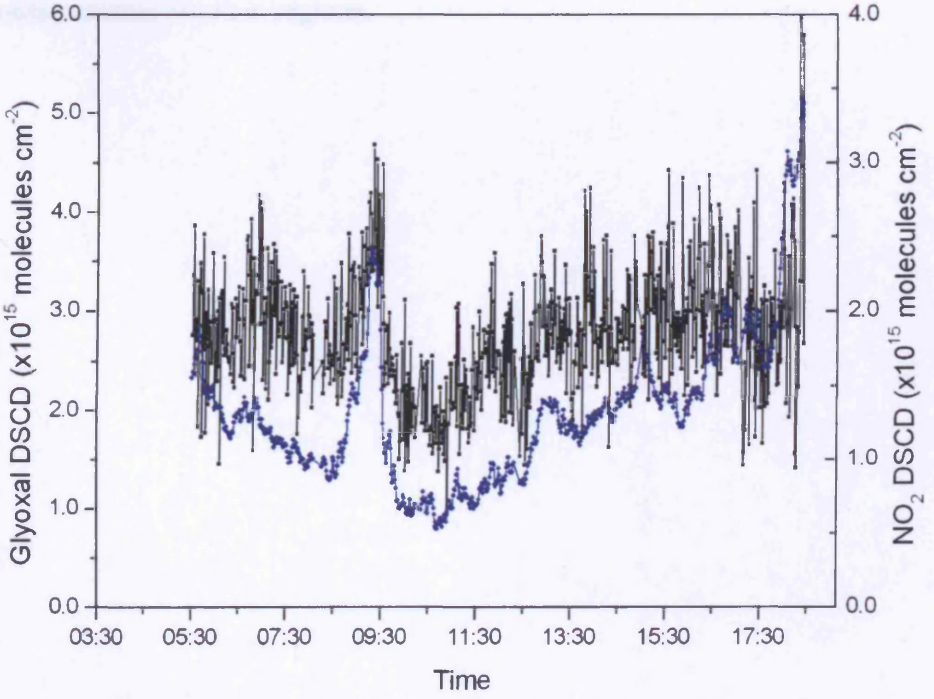

Figure 7-4: Glyoxal (black lines) and NO_2 (blues lines) retrieved from the 6° view of the CMAX-DOAS instrument on 7th September 2007.

The results on the retrieval of HCHO and CHOCHO above demonstrate the ability of the CMAX-DOAS instrument to detect weak absorbers. Future measurements and the analysis of these two trace gases will increase our knowledge on the rate of VOC oxidation and improve the development of air quality control policies. In addition, the data will provide an additional source for the validation of space-based measurements.

The methods developed in this thesis allow an interpretation of the OMI retrievals for measuring NO_2 at the surface over urban areas. So far, this has only been performed on measurements over Leicester. Its application to other national and international cities/sites would serve to further support the use of satellite instruments as part of an air quality monitoring system. The launch of GOME-2 in 2006 and the potential future launch of the TROPOMI in 2014/2015 will provide additional satellite datasets and continue the long term monitoring of the troposphere. TROPOMI, in particular, will provide measurements of trace gases and aerosols in the atmosphere with a spatial resolution of 10 x 10 km^2, making it ideal for measurements in urban regions.

Appendix

Table A1: Specifications of the gratings used in the CMAX-DOAS system.

Line Density (l/mm)	**Blaze Wavelength (nm)**	**Type**	**Peak Efficiency(%)**	**Reciprocal Dispersion (nm/mm)***	**Multichannel Array Bandpass(nm)****	**Primary Wavelength region(nm)*****
1200	350	Ruled	80	3.2	81	200-1400
600	400	Ruled	85	6.5	165	250-1300
300	500	Ruled	80	12.8	325	250-1150

* at blaze wavelength.

** across a 1 inch array, with grating centered at blaze wavelength.

*** wavelength region where grating efficiency is ≥20%

References

Acarreta, J. R., P. Stammes and W. H. Knap (2004). "First retrieval of cloud phase from SCIAMACHY spectra around 1.6 μm." *Atmospheric Research,* 72(1-4): 89-105.

Afe, O. T., A. Richter, B. Sierk, F. Wittrock and J. P. Burrows (2004). "BrO emission from volcanoes: A survey using GOME and SCIAMACHY measurements." *Geophysical Research Letters,* Vol. 31, doi:10.1029/2004GL020994,

Alicke, B., K. Hebestreit, J. Stutz and U. Platt (1999). "Iodine oxide in the marine boundary layer." *Nature*, 397(6720): 572.

Aliwell, S. R., M. Van Roozendael, P. V. Johnston, A. Richter, T. Wagner, D. W. Arlander, J. P. Burrows, D. J. Fish, R. L. Jones and K. K. Tørnkvist (2002). "Analysis for BrO in zenith-sky spectra: An intercomparison exercise for analysis improvement." *Journal of Geophysical Research,* 107: 4199.

Allan, B. J., G. McFiggans, J. M. C. Plane and H. Coe (2000). "Observations of iodine monoxide in the remote marine boundary layer." *Journal of Geophysical Research*, 105(D11): 14363-14370.

Ashworth, S. H., B. J. Allan and J. M. C. Plane (2002). "High resolution spectroscopy of the OIO radical - Implications for the ozone-depleting potential of iodine." *Geophysical Research Letters,* 29(10): 65-1.

Ayers, G. P. and R. W. Gillett (2000). "DMS and its oxidation products in the remote marine atmosphere: implications for climate and atmospheric chemistry." *Journal of Sea Research* ,43(3-4): 275-286.

Ayers, G. P., R. W. Gillett, J. M. Cainey and A. L. Dick (1999). "Chloride and Bromide Loss from Sea-Salt Particles in Southern Ocean Air." *Journal of Atmospheric Chemistry*, 33(3): 299-319.

Balis, D., J. C. Lambert, M. Van Roozendael, R. Spurr, D. Loyola, Y. Livschitz, P. Valks, V. Amiridis, P. Gerard and J. Granville (2007). "Ten years of GOME/ERS 2 total ozone data-: The new GOME data processor(GDP) version 4: 2. Ground-based validation and comparisons with TOMS V 7/V 8." *Journal of Geophysical Research*, 112(D7).

Barrie, L. A., J. W. Bottenheim, R. C. Schnell, P. J. Crutzen and R. A. Rasmussen (1988). "Ozone destruction and photochemical reactions at polar sunrise in the lower Arctic atmosphere." *Nature*, 334(6178): 138-141.

Beirle, S., U. Platt, M. Wenig and T. Wagner (2003). "Weekly cycle of NO 2 by GOME measurements: a signature of anthropogenic sources." *Atmospheric Chemistry and Physics*, 3: 2225-2232.

Beirle, S., R. Volkamer and F. Wittrock (2006). "DOAS Retrieval of Glyoxal from Space." *Proceedings of the ESA Atmospheric Science Conference,* 2006.

Berden, G., R. Peeters and G. Meijer (2000). "Cavity ring-down spectroscopy: Experimental schemes and applications." *International Reviews in Physical Chemistry* 19(4): 565-607.

Bey, I., D. J. Jacob, R. M. Yantosca, J. A. Logan, B. D. Field, A. M. Fiore, Q. Li, H. Y. Liu, L. J. Mickley and M. G. Schultz (2001). "Global modeling of tropospheric chemistry with assimilated meteorology- Model description and evaluation." *Journal of Geophysical Research,* 106(D19): 23073-23096.

Bitter, M., S. M. Ball, I. M. Povey and R. L. Jones (2005). "A broadband cavity ringdown spectrometer for in-situ measurements of atmospheric trace gases." *Atmospheric Chemistry and Physics,* 5: 2547-2560.

Blacet, F. E. (1952). "Photochemistry in the Lower Atmosphere." *Industrial & Engineering Chemistry*, 44(6): 1339-1342.

Blond, N., K. F. Boersma and H. J. Eskes (2007). "Intercomparison of SCIAMACHY nitrogen dioxide observations, in situ measurements and air quality modeling results over Western Europe." *Journal of Geophysical Research,* 112(D10).

Bloss, W. J., J. D. Lee, C. Bloss, K. Wirtz, M. Martin-Reviejo, M. Siese, D. E. Heard and M. J. Pilling (2003). "Validation of the calibration of a laser-induced fluorescence instrument for the measurement of OH radicals in the atmosphere." *Atmospheric Chemistry and Physics,* 4: 571-583.

Boersma, K. F., H. J. Eskes, J. P. Veefkind and E. J. Brinksma (2006). "Near-real time retrieval of tropospheric NO_2 from OMI." *Atmospheric Chemistry and Physics Discussions,* 6(6): 12301-12345.

Bogumil, K., J. Orphal, T. Homann, S. Voigt, P. Spietz, O. C. Fleischmann, A. Vogel, M. Hartmann, H. Kromminga and H. Bovensmann (2003). "Measurements of molecular absorption spectra with the SCIAMACHY pre-flight model: instrument characterization and reference data for atmospheric remote-sensing in the 230–2380 nm region." *Journal of Photochemistry & Photobiology*, 157(2-3): 167-184.

Bovensmann, H., J. P. Burrows, M. Buchwitz, J. Frerick, S. Noël, V. V. Rozanov, K. V. Chance and A. P. H. Goede "SCIAMACHY: Mission Objectives and Measurement Modes." *Journal of the Atmospheric Sciences*, 56(2): 127-150.

Brunekreef, B. and S. T. Holgate (2002). "Air pollution and health." *The Lancet,* 360(9341): 1233-1242.

Bucsela, E. J., E. A. Celarier, M. O. Wenig, J. F. Gleason, J. Pepijn Veefkind, K. Folkert Boersma and E. J. Brinksma (2006). "Algorithm for NO_2 vertical column retrieval from the ozone monitoring instrument." *IEEE transactions on geoscience and remote sensing,* 44(5): 1245-1258.

Burrows, J. P., M. Weber, M. Buchwitz, V. Rozanov, A. Ladstätter-Weißenmayer, A. Richter, R. DeBeek, R. Hoogen, K. Bramstedt and K. U. Eichmann (1999) "The Global Ozone Monitoring Experiment (GOME): Mission Concept and First Scientific Results." *Journal of the Atmospheric Sciences,* 56(2): 151-175.

Carpenter, L. J. (2003). "Iodine in the marine boundary layer." *Chemical Reviews,* 103(12): 4953-4962.

Carpenter, L. J., K. Hebestreit, U. Platt and P. S. Liss (2001). "Coastal zone production of IO precursors: a 2-dimensional study." *Atmospheric Chemistry and Physics,* 1: 9-18.

Carpenter, L. J., W. T. Sturges and S. Penkett (1999). "Short-lived alkyl iodides and bromides at Mace Head, Ireland- Links to biogenic sources and halogen oxide production." *Journal of Geophysical Research,* 104(D1): 1679-1690.

Chance, K. (1998). "Analysis of BrO measurements from the Global Ozone Monitoring Experiment." *Geophysical Research Letters,* 25(17): 3335-3338.

Chance, K., P. I. Palmer, R. J. D. Spurr, R. V. Martin, T. P. Kurosu and D. J. Jacob (2000). "Satellite observations of formaldehyde over North America from GOME." *Geophysical Research Letters,* 27(21): 3461-3464.

Chance, K. and R. J. D. Spurr (1997). "Ring effect studies: Rayleigh scattering, including molecular parameters for rotational Raman scattering, and the Fraunhofer spectrum." *Applied Optics*, 36(21): 5224-5230.

Chapman S. (1930), "A theory of upper atmospheric ozone" *Royal Meteorological Society,* 3. 103- 117.

de Vries, J., E. C. Laan, R. W. M. Hoogeveen, R. T. Jongma, I. Aben, H. Visser, E. Boslooper, H. Saari, M. Dobber and P. Veefkind (2007). "TROPOMI: solar backscatter satellite instrument for air quality and climate." *Proceedings of SPIE* 6744: 674409.

Dickerson, R. R., K. P. Rhoads, T. P. Carsey, S. J. Oltmans, J. P. Burrows and P. J. Crutzen (1999). "Ozone in the remote marine boundary layer- A possible role for halogens." *Journal of Geophysical Research*, 104(D17): 21385-21396.

Dobber, M. R., R. J. Dirksen, P. F. Levelt, G. H. J. van den Oord, R. H. M. Voors, Q. Kleipool, G. Jaross, M. Kowalewski, E. Hilsenrath and G. W. Leppelmeier (2006). "Ozone monitoring instrument calibration." *IEEE Transactions on Geoscience and Remote Sensing*, 44(5): 1209-1238.

Dunlea, E. J., S. C. Herndon, D. D. Nelson, R. M. Volkamer, F. San Martini, P. M. Sheehy, M. S. Zahniser, J. H. Shorter, J. C. Wormhoudt and B. K. Lamb (2007). "Evaluation of nitrogen dioxide chemiluminescence monitors in a polluted urban environment." *Atmospheric Chemistry and Physics*, 6, 3163–3180.

Eisinger, M., J. P. Burrows and A. Richter (1996). "Studies on the precision of GOME irradiance and radiance products and GOME measurements of OClO and BrO over Antarctica." *GOME Geophysical Validation Campaign. Final results workshop proceedings,* ESA WPP-108.

Eskes, H. J. and K. F. Boersma (2003). "Averaging kernels for DOAS total-column satellite retrievals." *Atmospheric Chemistry and Physics*, 3: 1285-1291.

Farman, J. C. and R. J. Murgatroyd (1985). "Ozone photochemistry in the antarctic stratosphere in summer." Quarterly Journal of the Royal Meteorological Society 111(470): 1013-1025.

Fayt, C. and M. van Roozendael (2001). "WinDOAS 2.1–Software user manual." Uccle, Belgium, BIRA-IASB.

Fernald, F. G. (1984). "Analysis of atmospheric lidar observations- Some comments." *Applied Optics,* 23(5): 652.

Ferrare, R., S. Ismail, E. Browell, V. Brackett, M. Clayton, S. Kooi, S. H. Melfi, D. Whiteman, G. Schwemmer and K. Evans (2000). "Comparison of aerosol optical properties and water vapor among ground and airborne lidars and Sun photometers during TARFOX." *Journal of Geophysical Research,* 105: 9917-9933.

Fish, D. J. and R. L. Jones (1995). "Rotational Raman scattering and the ring effect in Zenith-sky spectra." *Geophysical Research Letters,* 22(7): 811-814.

Flentje, H., R. Dubois, J. Heintzenberg and H. J. Karbach (1997). "Retrieval of aerosol properties from boundary layer extinction measurements with a DOAS system." *Geophysical Research Letters*, 24(16): 2019-2022.

Frieß, U., M. P. Chipperfield, H. Harder, C. Otten, U. Platt, J. Pyle, T. Wagner and K. Pfeilsticker (1999). "Intercomparison of measured and modelled BrO slant column amounts for the arctic winter and spring 1994/95." *Geophysical Research Letters,* 26(13): 1861-1864.

Frieß, U., K. Kreher, P. V. Johnston and U. Platt "Ground-Based DOAS Measurements of Stratospheric Trace Gases at Two Antarctic Stations

during the 2002 Ozone Hole Period." *Journal of the Atmospheric Sciences*, 62(3): 765-777.

Frieß, U., P. S. Monks, J. J. Remedios, A. Rozanov, R. Sinreich, T. Wagner and U. Platt (2006). "MAX-DOAS O_4 measurements: A new technique to derive information on atmospheric aerosols: 2. Modeling studies." *Journal of Geophysical Research*, 111.

Frieß, U., T. Wagner, I. Pundt, K. Pfeilsticker and U. Platt (2001). "Spectroscopic Measurements of Tropospheric Iodine Oxide at Neumayer Station, Antarctica." *Geophysical Research Letters*, 28(10): 1941-1944.

Gonzalez, C.R., M. Schaap, G. de Leeuw, P.J.H. Builtjes, and M. van Loon (2003). "Spatial variation of aerosol properties over Europe derived from satellite observations and comparison with model calculations." *Atmospheric Chemistry & Physics*, *3*, 521–533.

Grainger, J. F. and J. Ring (1962). "Anomalous Fraunhofer line profiles." *Nature*, 193(762): 45.

Greenblatt, G. D., J. J. Orlando, J. B. Burkholder and A. R. Ravishankara (1990). "Absorption measurements of oxygen between 330 and 1140 nm." *Journal of Geophysical Research*, 95: 18577-18582.

Hausmann, M. and U. Platt (1994). "Spectroscopic measurement of bromine oxide and ozone in the high Arctic during Polar Sunrise Experiment 1992." *Journal of Geophysical Research*, 99(D12): 25399-25414.

Haywood, J. and O. Boucher (2000). "Estimates of the direct and indirect radiative forcing due to tropospheric aerosols: A review." *Review of Geophysics*, 38(4): 513-543.

Heard, D. E., K. A. Read, J. Methven, S. Al-Haider, W. J. Bloss, G. P. Johnson, M. J. Pilling, P. W. Seakins, S. C. Smith and R. Sommariva (2006). "The North

Atlantic Marine Boundary Layer Experiment (NAMBLEX). Overview of the campaign held at Mace Head, Ireland, in summer 2002." *Atmospheric Chemistry and Physics*, 6(8): 2241-2272.

Hebestreit, K., J. Stutz, D. Rosen, V. Matveiv, M. Peleg, M. Luria and U. Platt (1999). "DOAS Measurements of Tropospheric Bromine Oxide in Mid-Latitudes." *Science*, 283(5398): 55.

Hegels, E., (1998): Global distribution of atmospheric bromine oxide from GOME on the earth observing satellite ERS-2." *Geophysical Research Letters*, 25: 3127-3130.

Hendrick, F., M. Van Roozendael, A. Kylling, A. Petritoli, A. Rozanov, S. Sanghavi, R. Schofield, C. von Friedeburg, T. Wagner and F. Wittrock (2006). "Intercomparison exercise between different radiative transfer models used for the interpretation of ground-based zenith-sky and multi-axis DOAS observations." *Atmospheric Chemistry and Physics*, 6: 93-108.

Holben, B. N., Y. J. Kaufman, T. F. Eck, I. Slutsker, D. Tanre, J. P. Buis, A. Setzer, E. Vermote, and J. Reagan, (1998), "AERONET- A federated instrument network and data archive for aerosol characterization" *Remote Sensing of Environment*, v. 66, p. 1-16.

Hönninger, G., (2002)," Halogen Oxide Studies in the Boundary Layer by Multi Axis Differential Optical Absorption Spectroscopy and Active Long path DOAS" *PhD Thesis*

Hönninger, G., C. von Friedeburg and U. Platt (2004a). "Multi axis differential optical absorption spectroscopy (MAX-DOAS)." *Atmospheric Chemistry and Physics*, 4: 231-254.

Hönninger, G., H. Leser, O. Sebastian and U. Platt (2004b). "Ground-based Measurements of Halogen Oxides at the Hudson Bay by Active Long Path DOAS and Passive MAX-DOAS." *Geophysical Research Letter*, 31.

Hönninger, G., N. Bobrowski, E. R. Palenque, R. Torrez and U. Platt (2004c). "Reactive bromine and sulfur emissions at Salar de Uyuni, Bolivia." *Geophysical Research Letter*,31.

Irie, H., Y. Kanaya, H. Akimoto, H. Iwabuchi, A. Shimizu and K. Aoki "Performance of MAX-DOAS measurements of aerosols at Tsukuba, Japan: a comparison with lidar and sky radiometer measurements." *Atmospheric Chemistry and Physics Discussions*, 7: 9769-9793.

Joiner, J. and A. P. Vasilkov (2006). "First results from the OMI rotational Raman scattering cloud pressure algorithm." *IEEE Transactions on Geoscience and Remote Sensing*, 44(5): 1272-1282.

Kiehl, J. T. and K. E. Trenberth (1997). "Earth's annual global mean energy budget." *Bulletin American Meteorological Society*, 78(2): 197-208.

Kley, D. and M. McFarland (1980). "Chemiluminescence detector for NO and NO_2." *Atmospheric Technology*, 12.

Kromminga, H., J. Orphal, P. Spietz, S. Voigt and J. P. Burrows (2003). "New measurements of OClO absorption cross-sections in the 325–435 nm region and their temperature dependence between 213 and 293 K." *Journal of Photochemistry & Photobiology, A: Chemistry*, 157(2-3): 149-160.

Kurosu, T. P., K. Chance, X. Liu, R. Volkamer, T. M. Fu, D. Millet, D. J. Jacob and P. Levelt (2007). "Seasonally resolved global distributions of glyoxal and formaldehyde observed from the Ozone Monitoring Instrument on EOS Aura." *International Symposium on Remote Sensing*, Brazil, 21-26 April 2007, INPE, p. 6461-6464.

Kurucz, R. L. and B. Bell (1995). "Atomic line list." *Smithsonian Astrophysical Observatory*, April 15, 1995.

Langridge, J. M., S. M. Ball and R. L. Jones (2006). "A compact broadband cavity enhanced absorption spectrometer for detection of atmospheric NO_2 using light emitting diodes." *The Analyst*, 131(8): 916-922.

Leigh, R. J., G. K. Corlett, U. Friess and P. S. Monks (2006). "Concurrent multiaxis differential optical absorption spectroscopy system for the measurement of tropospheric nitrogen dioxide." *Applied Optics*, 45(28): 7504-7518.

Leigh, R. J., G. K. Corlett, U. Friess and P. S. Monks (2007). "Spatially resolved measurements of nitrogen dioxide in an urban environment using concurrent multi-axis differential optical absorption spectroscopy." *Atmospheric Chemistry and Physics*, 7: 4751-4762.

Leppelmeier, G. W., O. Aulamo, S. Hassinen, A. MÄLkki, T. Riihisaari, R. Tajakka, J. Tamminen and A. Tanskanen (2006). "OMI Very Fast Delivery and the Sodankylä Satellite Data Centre." *IEEE Transactions on Geoscience and Remote Sensing*, 44(5): 1283.

Leue, C., M. Wenig, T. Wagner, O. Klimm, U. Platt and B. Jähne (2001). "Quantitative analysis of NO x emissions from Global Ozone Monitoring Experiment satellite image sequences." *Journal of Geophysical Research*, 106(D6): 5493-5506.

Levelt, P. F., G. H. J. van den Oord, M. R. Dobber and A. Malkki (2006). "The ozone monitoring instrument." *IEEE Transactions on Geoscience and Remote Sensing*, 44(5): 1093-1101.

Levenberg, K. (1944). "A method for the solution of certain nonlinear problems in least squares." *Quarterly of Applied Mathematics*, 2: 164-168.

Marquardt, D. W. (1963). "An Algorithm for Least-Squares Estimation of Nonlinear Parameters." *Journal of the Society for Industrial and Applied Mathematics*, 11(2): 431-441.

Martin, R. V., K. Chance, D. J. Jacob, T. P. Kurosu, R. J. D. Spurr, E. Bucsela, J. F. Gleason, P. I. Palmer, I. Bey and A. M. Fiore (2002). "An improved retrieval of tropospheric nitrogen dioxide from GOME." *Journal of Geophysical Research*, 107(10.1029): 9-1.

McFiggans, G., H. Coe, R. Burgess, J. Allan, M. Cubison, M. R. Alfarra, R. Saunders, A. Saiz-Lopez, J. M. C. Plane and D. Wevill (2004). "Direct evidence for coastal iodine particles from Laminaria macroalgae–linkage to emissions of molecular iodine." *Atmospheric Chemistry and Physics*, 4: 701-713.

McFiggans, G., J. M. C. Plane, B. J. Allan, L. J. Carpenter, H. Coe and C. O'Dowd (2000). "A modeling study of iodine chemistry in the marine boundary layer." *Journal of Geophysical Research*, 105(D11): 14371-14386.

Medeiros, B., A. Hall and B. Stevens "What Controls the Mean Depth of the PBL?" *Journal of Climate*, 18(16): 3157-3172.

Mie, G. (1908). "Beitrage zur Optik truber Medien, speziell kolloidaler Metallosungen." *Annals of Physics*, 25(3): 377.

Molina, M. J. and F. S. Rowland (1974). "Stratospheric sink for chlorofluoromethanes - Chlorine atom catalysed destruction of ozone." *Nature*, 249(5460): 810-812.

Monks, P. S. (2005). "Gas-phase radical chemistry in the troposphere." *Chemical Society Reviews*, 34(5): 376-395.

Murphy, D. M., J. R. Anderson, P. K. Quinn, L. M. McInnes, F. J. Brechtel, S. M. Kreidenweis, A. M. Middlebrook, M. Posfai, D. S. Thomson, and P. R. Buseck (1998), "Influence of sea-salt on aerosol radiative properties in the Southern Ocean marine boundary layer" *Nature*, v. 392, p. 62-65.

Navas, M. J., A. M. Jiménez and G. Galán (1999). "Air analysis: determination of hydrogen peroxide by chemiluminescence." *Atmospheric Environment*, 33(14): 2279-2283.

Noxon, J. F. (1975). "Nitrogen Dioxide in the Stratosphere and Troposphere Measured by Ground-Based Absorption Spectroscopy." *Science*, 189 (4202): 547-549.

Noxon, J. F., E. C. Whipple Jr and R. S. Hyde (1979). "Stratospheric NO2. I-Observational method and behavior at mid-latitude." *Journal of Geophysical Research*, 84: 5047-5065.

O'Dowd, C. D., J. L. Jimenez, R. Bahreini, R. C. Flagan, J. H. Seinfeld, K. Hameri, L. Pirjola, M. Kulmala, S. G. Jennings and T. Hoffmann (2002). "Marine aerosol formation from biogenic iodine emissions." *Nature*, 417(6889): 632-636.

Ordonez, C., A. Richter, M. Steinbacher, C. Zellweger, H. Nüß, J. P. Burrows and A. S. H. Prévôt (2006). "Comparison of 7 years of satellite-borne and ground-based tropospheric NO_2 measurements around Milan, Italy." *Journal of Geophysical Research*, 111.

Oriel, (2001) The Book of Photon Tools, in *http://www.oriel.com*, Oriel corporation.

Perliski, L. M. and S. Solomon (1993). "On the evaluation of air mass factors for atmospheric near-ultraviolet and visible absorption spectroscopy." *Journal of Geophysical Research*, 98(D6): 10-363.

Perner, D. and U. Platt (1979). "Detection of nitrous acid in the atmosphere by differential optical absorption." *Geophysical Research Letters*, 6(12): 917-920.

Perner, D. and U. Platt (1980). "Absorption of light in the atmosphere by collision pairs of oxygen/O2/2." *Geophysical Research Letters*, 7: 1053-1056.

Peters, C., S. Pechtl, J. Stutz, K. Hebestreit, G. Hönninger, K. G. Heumann, A. Schwarz, J. Winterlik and U. Platt (2005). "Reactive and organic halogen species in three different European coastal environments." *Atmospheric Chemistry and Physics*, 5: 3357-3375.

Petritoli, A., P. Bonasoni, G. Giovanelli, F. Ravegnani, I. Kostadinov, D. Bortoli, A. Weiss, D. Schaub, A. Richter and F. Fortezza (2004). "First comparison between ground-based and satellite-borne measurements of tropospheric nitrogen dioxide in the Po basin." *Journal of Geophysical Research*, 109.

Pfeilsticker, K., F. Erle and U. Platt (1997). "Absorption of Solar Radiation by Atmospheric O_4." *Journal of the Atmospheric Sciences*, 54(7): 933-939.

Pfeilsticker, K., H. Bösch, C. Camy-Peyret, R. Fitzenberger, H. Harder, and H. Osterkamp (2001), First Atmospheric Profile Measurements of UV/Visible O_4 Absorption Band Intensities: Implications for the Spectroscopy, and the Formation Enthalpy of the O_2-O_2 Dimer, *Geophys. Res. Lett.*, *28*(24), 4595–4598.

Piters, A. J. M., K. Bramstedt, J. C. Lambert and B. Kirchhoff (2006). "Overview of SCIAMACHY validation: 2002–2004." *Atmospheric Chemistry and Physics*, 6: 127-148.

Pitts, J. N. and B. J. Finlayson-Pitts (1986). Atmospheric Chemistry: Fundamentals and Experimental Techniques, *John Wiley & Sons*.

Plane, J. M. C., D. M. Joseph, B. J. Allan, S. H. Ashworth and J. S. Francisco (2006). "An experimental and theoretical study of the reactions OIO+ NO and OIO+ OH." *Journal of Physical Chemistry*, 110(1): 93-100.

Platt, U. (1994). "Differential Optical Absorption Spectroscopy(DOAS)." *Air Monitoring by Spectroscopic Techniques*.

Platt, U. and G. Hönninger (2003). "The role of halogen species in the troposphere." *Chemosphere*, 52(2): 325-338.

Platt, U. and C. Janssen (1995). "Observation and role of the free radicals NO 3, ClO, BrO and IO in the troposphere." *Faraday Discussions*, 100: 175-198.

Platt, U., L. Marquard, T. Wagner and D. Perner (1997). "Corrections for zenith scattered light DOAS." *Geophysical Research Letters*, 24(14): 1759-1762.

Platt, U. and G. K. Moortgat (1999). "Heterogeneous and Homogeneous Chemistry of Reactive Halogen Compounds in the Lower Troposphere." *Journal of Atmospheric Chemistry*, 34(1): 1-8.

Platt, U., D. Perner and H. W. Pätz (1979). "Simultaneous measurement of atmospheric CH_2O, O_3, and NO_2 by differential optical absorption." *Journal of Geophysical Research*, 84(C10): 6329-6335.

Rayleigh, L. (1899). "On the transmission of light through an atmosphere containing small particles in suspension, and on the origin of the blue of the sky." *Philosophical Magna*, 47: 375-384.

Richter, A. and J. P. Burrows (2002). "Tropospheric NO2 from GOME measurements." *Advances in Space Research*, 29(11): 1673-1683.

Richter, A., J. P. Burrows, H. Nuess, C. Granier and U. Niemeier (2005). "Increase in tropospheric nitrogen dioxide over China observed from space." *Nature*, 437(7055): 129-132.

Richter, A., F. Wittrock, A. Ladstätter-Weißenmayer and J. P. Burrows (2002). "Gome measurements of stratospheric and tropospheric BrO." *Advances in Space Research*, 29(11): 1667-1672.

Rothman, L. S., A. Barbe, D. Chris Benner, L. R. Brown, C. Camy-Peyret, M. R. Carleer, K. Chance, C. Clerbaux, V. Dana and V. M. Devi (2003). "The

HITRAN molecular spectroscopic database: edition of 2000 including updates through 2001." *Journal of Quantitative Spectroscopy and Radiative Transfer*, 82(1-4): 5-44.

Rozanov, A., H. Bovensmann, A. Bracher, S. Hrechanyy, V. Rozanov, M. Sinnhuber, F. Stroh and J. P. Burrows (2005). "NO_2 and BrO vertical profile retrieval from SCIAMACHY limb measurements: Sensitivity studies." *Advances in Space Research*, 36(5): 846-854.

Saiz-Lopez, A., K. Chance, X. Liu, T. P. Kurosu and S. P. Sander (2007). "First observations of iodine oxide from space." *Geophysical Research Letters*, 34.

Saiz-Lopez, A. and J. M. C. Plane (2004). "Novel iodine chemistry in the marine boundary layer." *Geophysical Research Letters*, 31(4).

Saiz-Lopez, A., J. M. C. Plane, A. S. Mahajan, P. S. Anderson, S. J. B. Bauguitte, A. E. Jones, H. K. Roscoe, R. A. Salmon, W. J. Bloss and J. D. Lee, (2007), "On the vertical distribution of boundary layer halogens over coastal Antarctica: implications for O_3, HO_x, NO_x and the Hg lifetime.", *Atmospheric Chemistry and Physics Discussions*, 7, 9385-9417.

Saiz-Lopez, A., J. M. C. Plane, G. McFiggans, P. I. Williams, S. M. Ball, M. Bitter, R. L. Jones, C. Hongwei and T. Hoffmann (2006a). "Modelling molecular iodine emissions in a coastal marine environment: the link to new particle formation." *Atmospheric Chemistry and Physics*, 6: 883-895.

Saiz-Lopez, A., J. A. Shillito, H. Coe and J. M. C. Plane (2006b). "Measurements and modelling of I_2, IO, OIO, BrO and NO_3 in the mid-latitude marine boundary layer." *Atmospheric Chemistry and Physics*, 6: 1513-1528.

Saiz-Lopez, A., R. W. Saunders, D. M. Joseph, S. H. Ashworth and J. M. C. Plane (2004). "Absolute absorption cross-section and photolysis rate of I_2." *Atmospheric Chemistry and Physics*, 4: 1443-1450.

Sander, R., Y. Rudich, R. von Glasow and P. J. Crutzen (1999). "The role of BrNO 3 in marine tropospheric chemistry: A model study." *Geophysical Research Letters*, 26(18): 2857-2860.

Sanders, R. W., S. Sloomon, J. P. Smith, L. Perliski, H. L. Miller, G. H. Mount, J. G. Keys and A. L. Schmeltekopf (1993). "Visible and near-ultraviolet spectroscopy at McMurdo Station, Antarctica 9: Observations of OClO from April to October 1991." *Journal of Geophysical Research*, 98(D4): 7219-7228.

Sandstrom, T. (1995). "Respiratory effects of air pollutants: experimental studies in humans." *European Respiratory Journal*, 8(6): 976-995.

Schall, C. and K. G. Heumann (1993). "GC determination of volatile organoiodine and organobromine compounds in Arctic seawater and air samples." *Analytical and Bioanalytical Chemistry* ,346(6): 717-722.

Schaub, D., K. F. Boersma, J. W. Kaiser, A. K. Weiss, D. Folini, H. J. Eskes and B. Buchmann (2006). "Comparison of GOME tropospheric NO_2 columns with NO_2 profiles deduced from ground-based *in situ* measurements." *Atmospheric Chemistry and Physics*, 6: 3211-3229.

Seinfeld, J. H. and S. N. Pandis (1998). "Atmospheric chemistry and physics: from air pollution to climate change." *John Wilsey & Sons*

Sinreich, R., U. Frieß, T. Wagner and U. Platt (2005). "Multi axis differential optical absorption spectroscopy (MAX-DOAS) of gas and aerosol distributions." *Faraday Discussions*, 130: 153-164.

Sinreich, R., R. Volkamer, F. Filsinger, U. Frieß, C. Kern, U. Platt, O. Sebastián and T. Wagner (2006). "MAX-DOAS detection of glyoxal during ICARTT 2004." *Atmospheric Chemistry and Physics*, 6: 9459-9481.

Sneep, M., D. Ityaksov, I. Aben, H. Linnartz and W. Ubachs (2006). "Temperature-dependent cross sections of O_2–O_2 collision-induced absorption resonances at 477 and 577nm." *Journal of Quantitative Spectroscopy and Radiative Transfer*, 98(3): 405-424.

Solomon, S. (1990). "Progress towards a quantitative understanding of Antarctic ozone depletion." *Nature*, 347(6291): 347-354.

Solomon, S., G. H. Mount, R. W. Sanders, R. O. Jakoubek and A. L. Schmeltekopf (1988). "Observations of the Nighttime Abundance of OClO in the Winter Stratosphere Above Thule, Greenland." *Science*, 242(4878): 550-555.

Solomon, S., A. L. Schmeltekopf and R. W. Sanders (1987). "On the interpretation of zenith sky absorption measurements." *Journal of Geophysical Research*, 92: 8311-8319.

Spietz, P., J. C. Gómez Martín and J. P. Burrows (2005). "Spectroscopic studies of the I_2/O_3 photochemistry Part 2. Improved spectra of iodine oxides and analysis of the IO absorption spectrum." *Journal of Photochemistry & Photobiology, A: Chemistry*, 176(1-3): 50-67.

Steinbacher, M., C. Zellweger, B. Schwarzenbach, S. Bugmann, B. Buchmann, C. Ordóñez, A. S. H. Prevot and C. Hueglin (2007). "Nitrogen oxide measurements at rural sites in Switzerland: Bias of conventional measurement techniques." *Journal of Geophysical Research*, 112(D11).

Stier, P., J. Feichter, S. Kinne, S. Kloster, E. Vignati, J. Wilson, L. Ganzeveld, I. Tegen, M. Werner and Y. Balkanski (2005). "The aerosol-climate model ECHAM 5-HAM." *Atmospheric Chemistry and Physics*, 5(4): 1125-1156.

Stull, R. B. (1988). An Introduction to Boundary Layer Meteorology, *Springer*.

Stutz, J., K. Hebestreit, B. Alicke and U. Platt (1999). "Chemistry of Halogen Oxides in the Troposphere: Comparison of Model Calculations with Recent Field Data." *Journal of Atmospheric Chemistry* 34(1): 65-85.

Takamura, T., Y. Sasano and T. Hayasaka (1994). "Tropospheric aerosol optical properties derived from lidar, sun photometer, and optical particle counter measurements." *Applied Optics*, 33(30): 7132-7140.

Theys, N., M. Van Roozendael, F. Hendrick, C. Fayt, C. Hermans, J. L. Baray, F. Goutail, J. P. Pommereau and M. De Maziere (2007). "Retrieval of stratospheric and tropospheric BrO columns from multi-axis DOAS measurements at Reunion Island (21? S, 56? E)." *Atmospheric Chemistry and Physics*, 7: 4733-4749.

Tørnkvist, K. K., D. W. Arlander and B. M. Sinnhuber (2002). "Ground-Based UV Measurements of BrO and OClO over Ny-Ålesund during Winter 1996 and 1997 and Andøya during Winter 1998/99." *Journal of Atmospheric Chemistry*, 43(2): 75-106.

Tuckermann, M., R. Ackermann, C. GÖLz, H. Lorenzen-Schmidt, T. Senne, J. Stutz, B. Trost, W. Unold and U. Platt (1997). "DOAS-observation of halogen radical-catalysed arctic boundary layer ozone destruction during the ARCTOC-campaigns 1995 and 1996 in Ny-Alesund, Spitsbergen." *Tellus B*, 49(5): 533-555.

van den Oord, G. H. J., N. C. Rozemeijer, V. Schenkelaars, P. F. Levelt, M. R. Dobber, R. H. M. Voors, J. Claas, J. de Vries, M. ter Linden and C. De Haan (2006). "OMI level 0 to 1 b processing and operational aspects." *IEEE Transactions on Geoscience and Remote Sensing*, 44(5): 1380-1397.

Van Der A, R. J., D. Peters, H. Eskes, K. F. Boersma, M. Van Roozendael, I. De Smedt and H. M. Kelder (2006). "Detection of the trend and seasonal

variation in tropospheric NO_2 over China." *Journal of Geophysical Research*, 111(D 12).

van Roozendael, M., C. Hermans and Y. Kabbadj (1995). "Ground-based measurements of stratospheric OClO, NO_2 and O_3 at Harestua, Norway (60 N, 10 E) during SESAME." *European rocket and balloon programmes and related research.*

Vandaele, A. C., C. Hermans, P. C. Simon, M. Carleer, R. Colin, S. Fally, M. F. Merienne, A. Jenouvrier and B. Coquart (1998). "Measurements of the NO_2 absorption cross-section from 42 000 cm-1 to 10 000 cm-1 (238-1000 nm) at 220 K and 294 K." *Journal of Quantitative Spectroscopy and Radiative Transfer 59*(3): 171-184.

Vandaele, A.C., C. Fayt, F. Hendrick, C. Hermans, F. Humbled, M. Van Roozendael, M. Gil, M. Navarro, O. Puentedura, M. Yela, G. Braathen, K. Stebel, K.K. Tornkvist, P. Johnston, K. Kreher, F. Goutail, A. Mieville, J.P. Pommereau, S. Khaikine, A. Richter, H. Oetjen, F. Wittrock, S. Bugarski, U. Friess, K. Pfeilsticker, R. Sinreich, T. Wagner, G. Corlett, and R. Leigh, An intercomparison campaign of ground-based UV-Visible measurements of NO2, BrO and OClO slant columns. Methods of analysis and results for NO_2., *Journal of Geophysical Research-Atmospheres,* (2004JD005423RR), 2005.

Veihelmann, B., P. F. Levelt, P. Stammes and J. P. Veefkind (2007). "Simulation study of the aerosol information content in OMI spectral reflectance measurements." *Atmospheric Chemistry and Physics,* 7: 3115-3127.

Voelger, P., J. Boesenberg and I. Schult (1996). "Scattering properties of selected model aerosols calculated at UV-wavelengths- Implications for DIAL measurements of tropospheric ozone." *Contributions to Atmospheric Physics*, 61(9): 177-187.

Volkamer, R., P. Spietz, J. Burrows and U. Platt (2005). "High-resolution absorption cross-section of glyoxal in the UV–vis and IR spectral ranges." *Journal of Photochemistry & Photobiology, A: Chemistry*, 172(1): 35-46.

Wada, R., J. M. Beames and A. J. Orr-Ewing (2007). "Measurement of IO radical concentrations in the marine boundary layer using a cavity ring-down spectrometer." *Journal of Atmospheric Chemistry*, 58(1): 69-87.

Wagner, T., J. P. Burrows, T. Deutschmann, B. Dix, C. von Friedeburg, U. Frieß, F. Hendrick, K. P. Heue, H. Irie and H. Iwabuchi (2007). "Comparison of Box-Air-Mass-Factors and Radiances for Multiple-Axis Differential Optical Absorption Spectroscopy (MAX-DOAS) Geometries calculated from different UV/visible Radiative Transfer Models." *Atmospheric Chemistry and Physics*, 7: 1809-1833.

Wagner, T., B. Dix, C. von Friedeburg, U. Friess, S. Sanghavi, R. Sinreich and U. Platt (2004). "MAX-DOAS O 4 measurements: A new technique to derive information on atmospheric aerosols-Principles and information content." *Journal Geophysical Research*, 109.

Wagner, T., C. Leue, M. Wenig, K. Pfeilsticker and U. Platt (2001). "Spatial and temporal distribution of enhanced boundary layer BrO concentrations measured by the GOME instrument aboard ERS-2." *Journal of Geophysical Research*, 106(D20): 24225-24236.

Wagner, T., F. Wittrock, A. Richter, M. Wenig, J. P. Burrows and U. Platt (2002). "Continuous monitoring of the high and persistent chlorine activation during the Arctic winter 1999/2000 by the GOME instrument on ERS-2." *Journal of Geophysical Research* 107: 8267.

Wayne, R. P., I. Barnes, P. Biggs, J. P. Burrows, C. E. Canosa-Mas, J. Hjorth, G. Le Bras, G. K. Moortgat, D. Perner and G. Poulet (1991). "Nitrate radical.

Physics, chemistry, and the atmosphere." *Atmospheric Environment*, 25(1): 209.

Whalley, L. K., K. L. Furneaux, T. Gravestock, H. M. Atkinson, C. S. E. Bale, T. Ingham, W. J. Bloss and D. E. Heard (2007). "Detection of iodine monoxide radicals in the marine boundary layer using laser induced fluorescence spectroscopy." *Journal of Atmospheric Chemistry*, 58(1): 19-39.

Wilkins, E. T. (1954). "Air Pollution and the London Fog of December, 1952." *The Journal of the Royal Society for the Promotion of Health*, 74(1): 1.

Wilmouth, D. M., T. F. Hanisco, N. M. Donahue and J. G. Anderson (1999). "Fourier transform ultraviolet spectroscopy of the A2PI3/2 - X2PI3/2 transition of BrO." *Journal Physical Chemistry*, 103(45): 8935-8945.

Wittrock, F., R. Mueller, A. Richter, H. Bovensmann and J. P. Burrows (2000). "Measurements of iodine monoxide(IO) above Spitsbergen." *Geophysical Research Letters*, 27(10): 1471-1474.

Wittrock, F., H. Oetjen, A. Richter, S. Fietkau, T. Medeke, A. Rozanov and J. P. Burrows (2003). "MAX-DOAS measurements of atmospheric trace gases in Ny-Alesund." *Atmospheric Chemistry and Physics Discussions*, 3: 6109-6145.

Wittrock, F., A. Richter, H. Oetjen, J. P. Burrows, M. Kanakidou, S. Myriokefalitakis, R. Volkamer, S. Beirle, U. Platt and T. Wagner (2006). "Simultaneous global observations of glyoxal and formaldehyde from space." *Geophysical Research Letters*, 33.

von Glasow, R., R. Sander, A. Bott, and P. J. Crutzen, (2002a). "Modelling halogen chemistry in the marine boundary layer 1. Cloudfree MBL." *Journal of Geophysical Research.*, 107(D17), 4341, doi:10.1029/2001JD000942

von Glasow, R., R. Sander, A. Bott, and P. J. Crutzen, (2002b). "Modelling halogen chemistry in the marine boundary layer 2. Interactions with sulfur and the cloud-covered MBL", *Journal of Geophysical Research.*, 107(D17), 4323, doi:10.1029/2001JD000943.

von Glasow, R., von Kuhlmann, R., Lawrence, M. G., Platt, U., and Crutzen, P. J. (2004). "Impact of reactive bromine chemistry in the troposphere." *Atmospheric Chemistry and Physics*, 4, 2481–2497.